

Linkage of E2F1 transcriptional network and cell proliferation with respiratory chain activity in breast cancer cells

Kazunori Mori,¹ Tetsu Uchida,¹ Motonori Fukumura,² Shigetoshi Tamiya,¹ Masato Higurashi,¹ Hirosato Sakai,¹ Fumihiko Ishikawa¹ and Motoko Shibamura¹

Departments of ¹Molecular Biology; ²Medicinal Chemistry, Showa University School of Pharmacy, Tokyo, Japan

Key words

Breast neoplasm, cell cycle, E2F1 transcription factor, electron transport, reactive oxygen species

Correspondence

Motoko Shibamura, Division of Cancer Cell Biology, Department of Molecular Biology, Showa University School of Pharmacy, 1-5-8 Hatanodai, Shinagawa-ku, Tokyo 142-8555, Japan.
Tel: +81-3-3784-8209; Fax: +81-3-3784-6850;
E-mail: smotoko@pharm.showa-u.ac.jp

Funding Information

This study was supported by JSPS KAKENHI Grant Numbers 26460399 and 21570205 and the Private University High Technology Research Center Project matching fund by a subsidy from MEXT.

Received December 5, 2015; Revised April 8, 2016;
Accepted April 18, 2016

Cancer Sci 107 (2016) 963–971

doi: 10.1111/cas.12953

Mitochondria are multifunctional organelles; they have been implicated in various aspects of tumorigenesis. In this study, we investigated a novel role of the basal electron transport chain (ETC) activity in cell proliferation by inhibiting mitochondrial replication and transcription (mtR/T) using pharmacological and genetic interventions, which depleted mitochondrial DNA/RNA, thereby inducing ETC deficiency. Interestingly, mtR/T inhibition did not decrease ATP levels despite deficiency in ETC activity in different cell types, including MDA-MB-231 breast cancer cells, but it severely impeded cell cycle progression, specifically progression during G2 and/or M phases in the cancer cells. Under these conditions, the expression of a group of cell cycle regulators was downregulated without affecting the growth signaling pathway. Further analysis suggested that the transcriptional network organized by E2F1 was significantly affected because of the downregulation of E2F1 in response to ETC deficiency, which eventually resulted in the suppression of cell proliferation. Thus, in this study, the E2F1-mediated ETC-dependent mechanism has emerged as the regulatory mechanism of cell cycle progression. In addition to E2F1, FOXM1 and BMYB were also downregulated, which contributed specifically to the defects in G2 and/or M phase progression. Thus, ETC-deficient cancer cells lost their growing ability, including their tumorigenic potential *in vivo*. ETC deficiency abolished the production of reactive oxygen species (ROS) from the mitochondria and a mitochondria-targeted antioxidant mimicked the deficiency, thereby suggesting that ETC activity signaled through ROS production. In conclusion, this novel coupling between ETC activity and cell cycle progression may be an important mechanism for coordinating cell proliferation and metabolism.

Cell proliferation is a process that simultaneously demands macromolecular synthesis in a greater amount and ATP supply at a higher rate to increase the total biomass and, finally, divide the cells into two daughter cells.⁽¹⁾ To meet these demands, actively dividing cells utilize mitochondria as biosynthetic organelles rather than powerhouses, which are primarily involved in oxidative phosphorylation (OXPHOS).⁽²⁾ However, this does not necessarily mean that OXPHOS function is not important for actively dividing cells such as cancer cells. Indeed, OXPHOS still makes a significant contribution to ATP supply in cancer cells,⁽³⁾ thereby supporting cancer cell proliferation and survival.

In some cases, mitochondria appear to play more active roles in tumorigenesis; for example, upon the activation of oncogenes, the cancer cells exploit the electron transport chain (ETC) and elevate the production of reactive oxygen species (ROS).^(4–6) In some hereditary cancers, truncated mitochondrial enzymes caused by mutations may have direct oncogenic properties that affect tumor susceptibility.⁽⁷⁾

In addition, it is also possible that basal activities of mitochondria may play some fundamental role in cancer cells, such as sustaining their proliferation potential, given that cell proliferation is degraded greatly when mitochondrial replication and transcription (mtR/T) are inhibited.⁽⁸⁾ Because the inhibition of mtR/T primarily leads to deficient OXPHOS function,^(4,9–11) this proliferation defect could be explained simply by an insufficient production of ATP. However, we recently discovered that ATP levels remained normal under mtR/T inhibition in several cancer cell types, but their proliferation was still severely impeded. This finding implies that an unknown mechanism regulates cell proliferation depending on the levels of ETC activity. Therefore, in this study, we explored the details of the aforementioned defect in proliferation under mtR/T inhibition, which led us to propose a novel role for ETC activity in cell cycle progression. To the best of our knowledge, this is the first demonstration of a functional linkage between ETC activity and the core regulatory mechanism of cell cycle progression.

Materials and Methods

Full Methods and Materials are available as Supporting Information.

Results

Cell proliferation arrest is induced under electron transport chain-deficient conditions in human breast cancer cells. First, we observed mitochondrial DNA (mtDNA)-less cells, so-called pseudo- $\rho 0$ cells.⁽⁹⁾ The mtDNA exclusively encodes RNA and proteins required for the formation of ETC complex; therefore, the defects in pseudo- $\rho 0$ cells are considered to be associated with ETC functions and limited to their relevant activities. This hypothesis has been supported by extensive studies of $\rho 0$ cells,^(10,12) thereby providing a valuable model for the evaluation of the significance of ETC functions in cells.

In this experiment, we examined pseudo- $\rho 0$ populations obtained from several human breast cancer cell lines, including the MDA-MB-231 (MDA) cell line, after treating them with

ethidium bromide (EtBr), which is an mtR/T inhibitor that is used routinely to selectively deplete mtDNA,⁽¹³⁾ as described previously.⁽¹¹⁾ Figure 1(a–c) shows the effects of EtBr treatment on the condition of mitochondria in MDA cells, which demonstrates that mtDNA and mitochondria-encoded cytochrome b (Cyt.b) mRNA were decreased (Fig. 1a,b). The mitochondrial membrane potential ($\Delta\Psi m$), a direct indicator of ETC functionality, was virtually lost within 5 days (Fig. 1c). However, the amount of ATP remained at a normal level (Fig. 1d), presumably due to the compensation by glycolytic activity. These observations agree with previously described features of $\rho 0$ cells,^(10,11) which support the use of $\rho 0$ or ETC-deficient cells for studying the roles of ETC functions uncoupled from ATP synthesis.

Cell proliferation was markedly inhibited under the ETC-deficient conditions described above (Fig. 1e). The G2 and/or M phases were specifically interrupted in the MDA/ $\rho 0$ cells with concomitant enlargement of the cells (Fig. 1f–h). The short-term treatment of cells with EtBr had no effect, as indicated in the DNA histogram (Fig. 1g, 0 vs 30 min); this excludes the possibility that EtBr treatment interferes with the

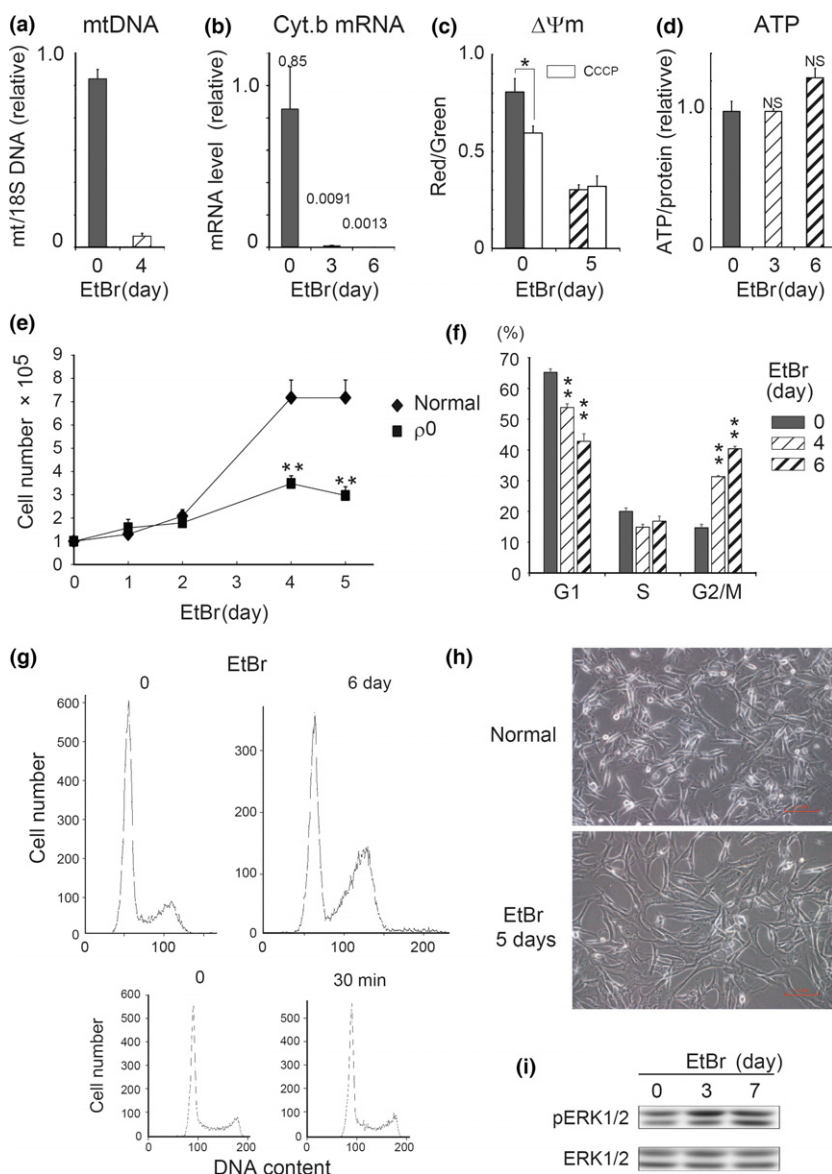


Fig. 1. Cell cycle arrest induced in electron transport chain (ETC)-deficient MDA-MB-231 (MDA) cells. Cells exposed to ethidium bromide (EtBr) (250 ng/mL) on the days indicated (MDA/ $\rho 0$) were analyzed. (a) mitochondrial DNA (mtDNA) relative to genomic DNA (18S) (mt/18S DNA) quantified using qPCR. (b) Levels of cytochrome b (Cyt.b) mRNA as analyzed by qRT-PCR. (c) Mitochondrial membrane potential ($\Delta\Psi m$) monitored with Mito-ID. (d) ATP levels were determined using an ATP determination kit and normalized against the protein levels. (e) Cell proliferation in the presence ($\rho 0$) and absence (normal) of EtBr. (f) Cell cycle distribution determined using DNA histograms obtained by flow cytometry. (g) Representative DNA histograms for normal (0 day) and $\rho 0$ (6 days) cells. Bottom: Histograms did not change with the incubation of cells with EtBr (250 ng/mL) for 30 min. (h) Morphology of cells incubated with or without EtBr (250 ng/mL) for 5 days. Magnification: $\times 100$. (i) Activation-dependent phosphorylation of ERK1/2 as detected by western blot. The pair shown is for the phosphorylated (p) form and for the total protein. * $P < 0.05$ and ** $P < 0.01$.

subsequent staining of cells with PI. According to our results of the dye exclusion test, cell viability was above 90% during the observation of cell proliferation (data not shown) and the sub-G1 population comprised <1% in all of the DNA histograms, which implied that apoptosis was negligible. These observations indicate that the ETC-deficient cells almost completely lost their proliferative capacity even when ATP production was at normal levels, thereby suggesting a previously unknown role for the ETC in cell proliferation. Interestingly, cell-signaling molecules, such as ERK1/2, which are central molecules in controlling cell proliferation, were active at levels comparable to those under normal conditions (Fig. 1i). In addition, the suppression of cell proliferation did not appear to be associated with the DNA damage response (see below), although high doses of EtBr affected nuclear DNA as an intercalator. Collectively, mitotic catastrophe, a mechanism that senses mitotic failure and leads to cell death, such as necrosis, or senescence, might occur under the conditions.

Similar suppression of proliferation was also observed in pseudo- $\rho 0$ cells from other cell lines; namely, T-47D (Fig. 2a) and MCF7 (Fig. S1a). Furthermore, in T-47D/ $\rho 0$ cells, the cell cycle was interrupted at G2 and/or M phases (Fig. 2b), as found in MDA/ $\rho 0$. However, G1/S arrest was dominant in MCF7/ $\rho 0$ cells (Fig. S1b), which was probably attributable to the upregulation of p21CIP1 and p27KIP1 cyclin-dependent kinase inhibitors (CKI) at the mRNA and protein levels, respectively (Fig. S1c,d). These inhibitors were not induced in MDA/ $\rho 0$ cells. In this context, it should be noted that MCF7 retained wild-type p53, whereas T-47D and MDA did not.⁽¹⁴⁾ In a further study, we explored the defects in cell cycle progression under ETC deficiency, especially the CKI-independent mechanisms that resulted in the defects in G2 and/or M phase progression in MDA and T-47D/ $\rho 0$ cells.

Downregulation of a set of cell cycle regulators in electron transport chain-deficient cells. To obtain insight into the mechanisms described above, we studied changes in gene expression

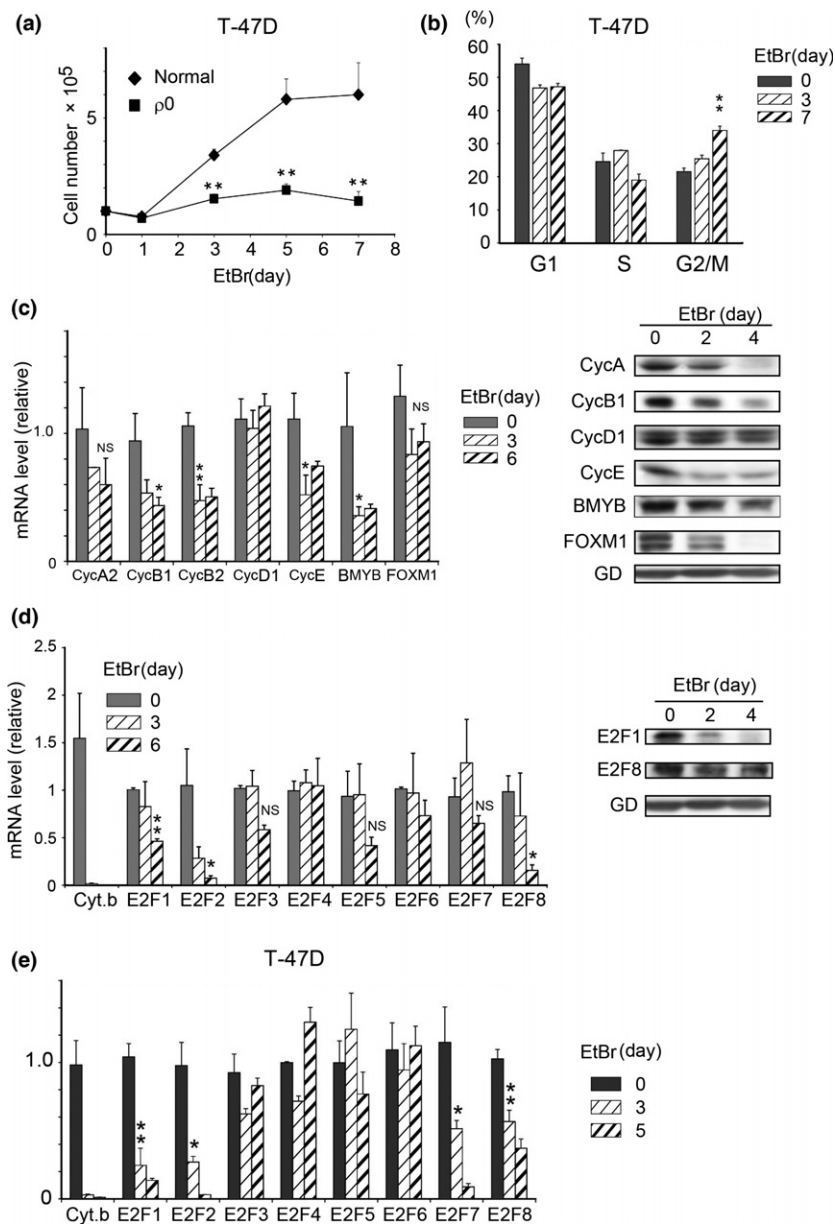


Fig. 2. Downregulation of cell cycle regulators in electron transport chain (ETC)-deficient MDA and T-47D cells. Cell proliferation (a) and cell cycle distribution (b) determined as described in Figure 1(e, f) in ethidium bromide (EtBr)-treated T-47D human breast cancer cells. (c, d) MDA/ $\rho 0$ cells, as described in Figure 1, were analyzed on the days indicated. (c) Left: mRNA levels of cyclins (A2, B1, B2, D1 and E), BMYB and FOXM1 quantified using qRT-PCR. Right: protein levels of the corresponding mRNA detected by western blot. GD was the loading control. (d) Left: mRNA levels of Cyt.b and E2F1–8 evaluated by qRT-PCR. Right: Western blot analysis of E2F1 and 8. GD was the loading control. (e) mRNA levels of Cyt.b and E2F1–8 quantified by qRT-PCR in T-47D/ $\rho 0$ cells. * $P < 0.05$ and ** $P < 0.01$. NS, not significant.

in response to the inhibition of mtR/T. Initially, we analyzed microarray data using murine mammary epithelial cells and found that many proliferation-related genes were downregulated under ETC-deficient conditions. Intriguingly, many of these genes have been previously identified as transcriptional targets of E2F.^(15,16) These genes included cyclins (A2, B1 and E1) and other components involved structurally and/or functionally in cell cycle progression (Table S1).

Downregulation of a similar set of E2F-targeted genes, including cyclins A2, B1, B2 and E, was noted in the MDA/ρ0 cells (Fig. 2c). In addition to these cyclins, *Foxm1* and *Bmyb*, having roles in G2 and M phase regulation as components of the transcriptional regulator complex with MuvB,⁽¹⁷⁾ were downregulated; their expression levels were also attenuated in the MDA/ρ0 cells (Fig. 2c). The expression of cyclin D1, which was absent in the list of downregulated genes, was affected slightly only at the protein level; therefore, it was used as a control due to its relative insensitivity to ETC activity.

Downregulation of E2F1 in electron transport chain-deficient cells. Interestingly, in addition to the aforementioned cell cycle regulators, E2F family members (activator E2F1 and 2) were included in the list of downregulated genes (Table S1). In the MDA/ρ0 cells, E2F1, 2 and 8 (a repressor E2F) exhibited significant sensitivity to ETC deficiency in terms of their mRNA levels (Fig. 2d). At the protein level, the expression of E2F1 was particularly sensitive; it decreased dramatically within 2 days of the treatment (Fig. 2d). The expression level of E2F2 was very low; therefore, its expression was undetectable in MDA cells by immunoblotting. Thus, the E2Fs, particularly E2F1, were found to be ETC-sensitive transcriptional

regulators. Changes in the expression patterns of these E2Fs were also observed in the pseudo-ρ0 cells from T-47D (Fig. 2e) and MCF7 (Fig. S1e, left), thereby suggesting that the phenomenon is independent of CKI induction or defects in cell cycle progression, at G1/S boundary or during G2 and/or M phases, but it is primarily dependent on ETC deficiency.

E2F1 downregulation as a trigger for the downregulation of cell cycle regulators and cell proliferation. Our results mentioned earlier suggest that E2F1 was first downregulated in response to ETC deficiency, followed by its target cell cycle regulators, which eventually suppressed the cell proliferation. As expected, the knockdown of E2F1 with siRNA decreased the expression of the set of cell cycle regulator genes that responded to ETC deficiency, except for cyclin E and the negative control of cyclin D1 (Fig. 3a–c). Therefore, cell proliferation was significantly influenced by E2F1 silencing, whereas little change was observed using siRNA for E2F2 and 8 (Figs 3d, S2a; E2F8).

Significance of BMYB and FOXM1 downregulation for defects in cell cycle progression during the G2 and/or M phases. The expression of the G2 and M phase regulators, BMYB and FOXM1, was also sensitive to ETC deficiency (Fig. 2c); they appear to be under the transcriptional control of E2F1 similar to cyclins A and B (Fig. 3b). However, unlike the two cyclins, the siRNA for E2F1 was ineffective in downregulating the expression of BMYB and FOXM1 at the protein level (Fig. 3c), thereby implying that their expression was subject to an additional layer of regulation at the protein level as well as the transcriptional regulation by E2F1 (Fig. 3e). Therefore, to assess the roles of BMYB and FOXM1, we performed

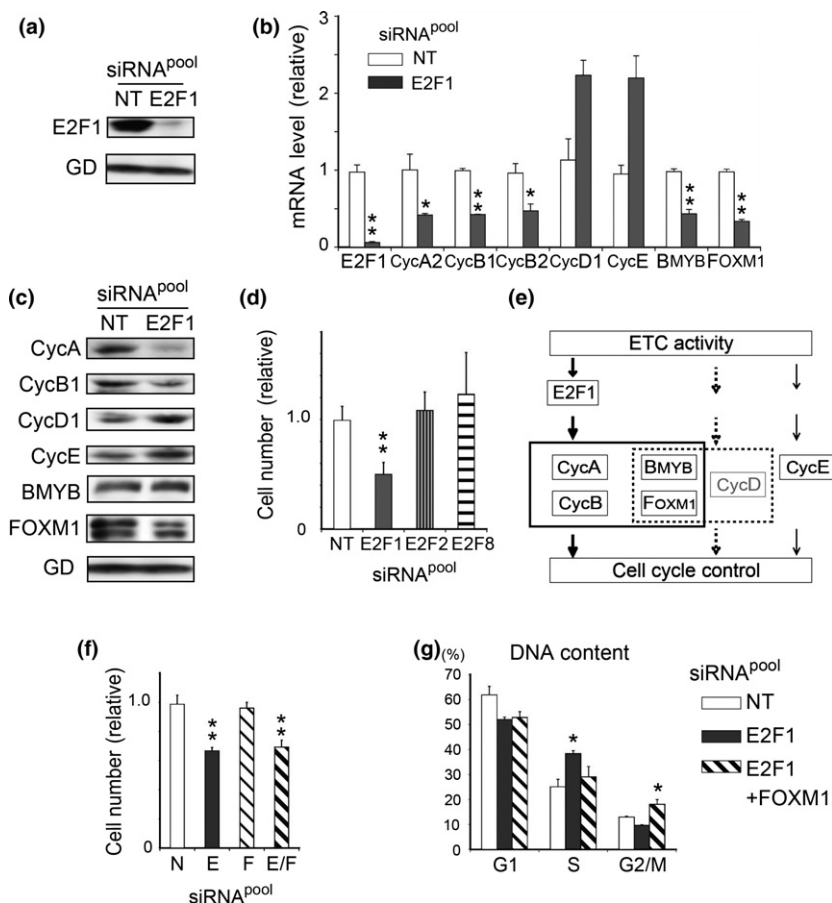


Fig. 3. Downregulation of cell cycle regulators in E2F1-knockdown cells. MDA cells were treated with 50 nM of ON-TARGETplus Human E2F1 siRNA-SMARTpool (E2F1) or non-targeting Pool siRNA (NT). (a) Validation of E2F1 knockdown by western blotting in cells incubated with siRNA for 48 h. (b) mRNA levels of cyclins (A2, B1, B2, D1 and E), BMYB and FOXM1, which were analyzed together with that of E2F1 by qRT-PCR. (c) Western blot analysis of proteins corresponding to the mRNA in (b). GD was the loading control. (d) Effects of E2F1 knockdown (7 days) on cell proliferation compared with those of E2F2 and E2F8. (e) Schematic representation of the electron transport chain (ETC)-dependent cell cycle control mechanisms (see text). (f) Effects of double knockdown of E2F1 and FOXM1 (6 days) with the siRNA on cell proliferation. siRNA: N; NT, E; E2F1, F; FOXM1, E/F; E2F1+ FOXM1. (g) Cell cycle distribution under the knockdown of E2F1 alone or in combination with FOXM1 for 6 days. * $P < 0.05$ and ** $P < 0.01$.

silencing of *FOXM1* and *BMYB* with siRNA for themselves instead of E2F1 (Fig. S2a; FOXM1, BMYB).

Knockdown of FOXM1 (F) or BMYB (M) alone had no obvious effects either on the cell number or on the cell cycle distribution (cell number, Figs 3f, S2b; cell cycle distribution, Fig. S2d). When they were knocked down simultaneously with E2F1, we detected proliferation inhibition (Figs 3f, S2b; E/F and E/M). However, the effect was almost the same as that obtained by the single knockdown of E2F1 (E), which suggests that the proliferation potential of the cells was affected principally by E2F1, rather than by FOXM1 or BMYB.

The cell cycle distribution was influenced by the levels of FOXM1 and BMYB. Thus, silencing of E2F1 alone resulted in the accumulation of cells in the S phase, but the simultaneous silencing of FOXM1 or BMYB together with E2F1 elicited a slight but significant shift in the accumulation of cells from the S phase to the G2 and/or M phases. This suggests that these two proteins have important roles in regulating the progression of G2/M phase (Figs 3g, S2c). Triple knockdown of the three genes suggests that the effects of BMYB and FOXM1 knockdown were redundant (Fig. S2e), which is consistent with a previous demonstration that BMYB and FOXM1 function in a common mechanism that operates at G and M phases.⁽¹⁷⁾ In summary, our results suggest a mechanism for

cell proliferation suppression in ETC-deficient cells, where the downregulation of E2F1 causes defects in cell cycle progression during the G2 and/or M phases when coupled with the downregulation of BMYB and FOXM1.

Altogether, the ETC activity was first coupled with the control of cell proliferation via the regulation of cell cycle-related gene expression. In an emerging mechanism, the ETC activity modulates multiple pathways, including E2F1-mediated transcription (Fig. 3e, box; solid line) and non-transcriptional mechanisms (Fig. 3e, box; broken line), which regulate the expression of components of the core cell cycle machinery.

Recapitulated electron transport chain-deficient phenotypes in mitochondrial transcription factor A-knocked down cells. We further investigated the novel link between the ETC activity and cell cycle regulation using additional ETC-deficient cells, which we generated by the genetic manipulation of mitochondrial transcription factor A (TFAM), a regulator of mitochondrial transcription. This protein has an additional role as an architectural protein, which is essential for the maintenance of mtDNA; therefore, it also serves as a limiting determinant for the mtDNA copy number.^(18,19) Thus, the suppression of TFAM expression (Fig. S3a,b) led to both mtDNA and mtRNA depletion, and a consequent deficiency in ETC function in the same manner as EtBr treatment (Fig. 4a–c), as

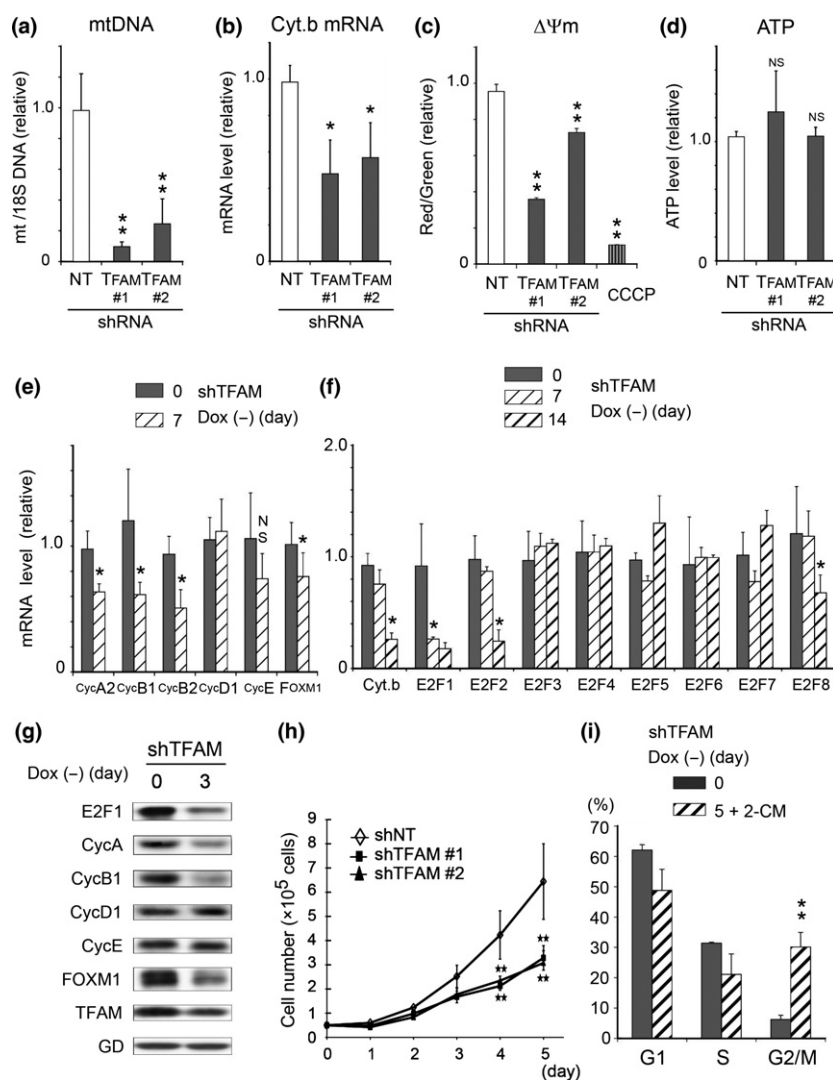


Fig. 4. Downregulation of cell cycle regulators and cell proliferation in mitochondrial transcription factor A (TFAM)-knocked down cells. TFAM-knockdown MDA cells were established as described in Figure S3(a,b). Levels of mtDNA relative to genomic DNA (18S) (mt/18S DNA) (a) and Cyt.b mRNA (b), mitochondrial membrane potential ($\Delta\Psi m$) (c), and ATP levels (d) were determined as described in Figure 1(a–d) after incubating the cells in the absence of Dox for 7 days (a) and 48 h (b–d). (e, f) mRNA levels of cyclins (A2, B1, B2, D1 and E) and FOXM1 (e), as well as those of Cyt.b and E2F1–8 (f) quantified by qRT-PCR in cells where TFAM was knocked down by incubating in the absence of Dox (Dox [–]) for the days indicated. (g) Western blot analysis of representative proteins corresponding to the mRNA in (e) and (f). GD was the loading control. (h) Proliferation of cells with TFAM knockdown by incubating with Dox (–) for the days indicated. (i) Cell cycle distribution of control (0) and TFAM-knockdown cells (Dox [–] 5 days) in the presence of 2-CM (20 μM) (5 + 2-CM), as described in Figure S3(c). * $P < 0.05$ and ** $P < 0.01$. NS, not significant.

described previously.⁽²⁰⁾ In contrast to the pseudo-p0 cells (Fig. 1b), the depletion of mtRNA (Cyt.b) was only partial under TFAM knockdown. Further depletion of mtRNA was achieved by using 2'-C-methyladenosine (2-CM), an inhibitor of mitochondrial RNA polymerase-mediated transcription (Fig. S3c). Similar to the treatment with EtBr (Fig. 1d), the ATP levels in the TFAM-knockdown cells were almost the same as those in the control (Fig. 4d).

Importantly, TFAM knockdown decreased the expression of the set of E2F-target cell cycle regulator genes described above (Fig. 4e–g vs Fig. 2c,d), and it suppressed cell proliferation (Fig. 4h), thereby strongly supporting the involvement of ETC activity in the control of cell proliferation. Enrichment of the G2/M population was observed under decreased mitochondrial activity and it was statistically significant in the presence of 2-CM (Fig. 4i). Moreover, using the genetically ETC-deprived cells, we demonstrate the importance of ETC activity in the long-term growth of cancer cells *in vitro* and *in vivo*. Figure 5(a) indicates that TFAM knockdown impeded anchorage-independent cell growth *in vitro*. More importantly, TFAM knockdown considerably mitigated tumor growth in our *in vivo* orthotopic implantation experiments (Fig. 5b).

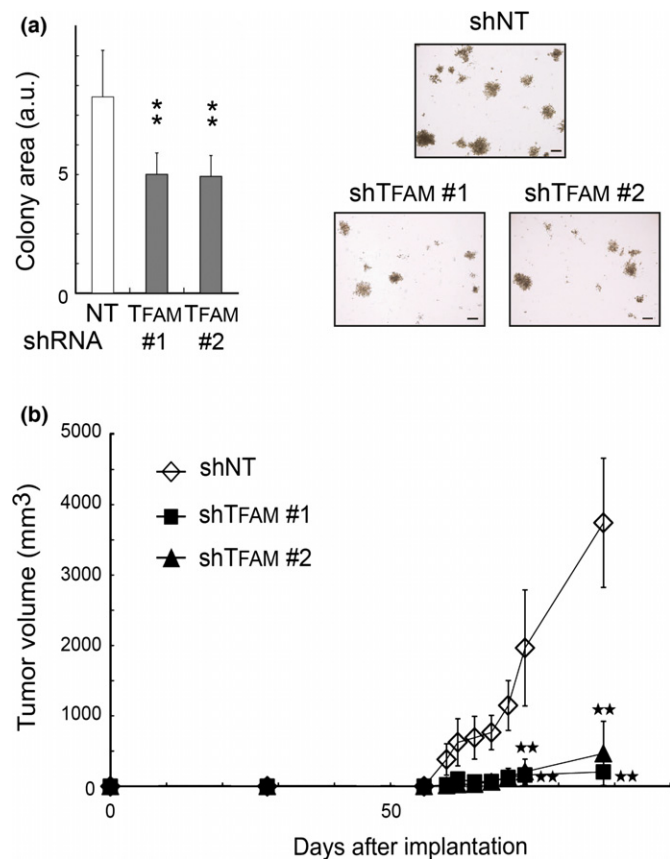


Fig. 5. Suppression of anchorage-independent cell growth and tumor growth *in vivo* by mitochondrial transcription factor A (TFAM) knockdown. (a) Anchorage-independent cell growth of the TFAM short hairpin RNA (shRNA)-expressing MDA cells, as described in Figure S3a,b. Cells grown in methylcellulose under Dox (–) conditions for 4 weeks were photographed (Right; scale bar: 300 μ m) and the areas of colonies in images were quantified using ImageJ software (left). Values represent the mean \pm SD. $**P < 0.01$. (b) TFAM shRNA-expressing cells established from MDA/GFP cells were implanted into the mammary fat pads of SCID mice and the tumor size was monitored. Each data point represents the mean \pm SD based on four or five xenografts. $**P < 0.01$.

Significance of decreased intracellular reactive oxygen species in electron transport chain-deficient cells. Finally, we investigated whether intracellular redox changes derived from mitochondrial sources were involved in the mechanism of ETC-dependent cell proliferation control. The generation of mitochondrial ROS (mtROS) is correlated with levels of $\Delta\Psi_m$ or ETC activity,^(21,22) and ETC-deficient p0 cells are incapable of producing mtROS.^(4,9–11) Our results agree with these previous findings in that the ROS levels measured with H₂DCFDA were significantly lower in the MDA/p0 cells compared with the control cells, where strong fluorescence was observed in the intracellular organelles (Figs 6a, S4a; [–]). The probe detected both cytoplasmic ROS and mtROS,⁽²³⁾ but the majority of the fluorescence appeared to be derived from mtROS under the experimental conditions employed in this study. This is because the fluorescence was largely co-localized with that of a mitochondrial indicator in the cells (Fig. S4a; [–] high magnification). In addition, the fluorescence was sensitive to manipulations of the ETC activity with ETC inhibitors and supplements (Fig. S4b–d). In conclusion, our results suggest that mtROS production was reduced in the MDA/p0 cells similar to the other cell types.^(6,11–13)

To understand the significance of this decrease in mtROS during the suppression of proliferation in ETC-deficient conditions, we attempted to reduce mtROS levels using an antioxidant. We utilized mitoquinol (Mitq), a reduced form of the mitochondria-targeted coenzyme Q (CoQ) analog, which is a well-characterized mitochondria-targeted antioxidant (mt-antioxidant).⁽²⁴⁾ As expected, Mitq, but not CoQ, effectively decreased ROS levels in the MDA cells (Figs 6b, S4a). It was remarkable that the treatment of cells with Mitq but not CoQ consistently recapitulated the changes in gene expression for the cell cycle regulators under ETC-deficient conditions (Fig. 6c [MDA] and Fig. S1e; right [MCF] vs Figs 2c–e, 4e,f) as well as cell proliferation suppression with concomitant defects in cell cycle progression during the G2 and/or M phases (Fig. 6e,f). Therefore, Mitq had almost the same effects on gene expression and cell cycle arrest as EtBr and TFAM knockdown. Gene expression levels decreased significantly at 24 h prior to inhibition of proliferation, which was apparent after several days, thereby indicating that the changes in gene expression were a response to the lower mtROS levels and not because of the inhibition of proliferation. We confirmed that Mitq treatment had no obvious effects on $\Delta\Psi_m$ (Fig. S5a), which excluded the possibility that Mitq affected the functionality of the ETC. Thus, mtROS is the most likely mediator of the effects of ETC activity during the regulation of cell cycle progression. Mechanistically, our results suggest that mtROS levels affected the stability of the E2F1 protein (Fig. 6g).

Finally, we investigated whether the DNA damage response (DDR) and spindle assembly checkpoint (SAC) signaling were involved in the transcriptional response of cells under ETC-deficient (EtBr-treated) or mtROS-decreased (Mitq-treated) conditions. Although treatment with cisplatin (CDDP) clearly increased the immunoreactivity to phospho-histone H2A.X (γ H2AX), a key indicator of DNA damage, treatment of cells with EtBr and Mitq did not increase the activity (Fig. S5b). In addition, treatments with CDDP or paclitaxel (PTX), which induce DDR and SAC, respectively, did not downregulate the E2F transcriptional network (Fig. S5c). Therefore, it is unlikely that these stress response pathways played a role in the transcriptional response of cells to ETC-deficient or mtROS-decreased conditions.

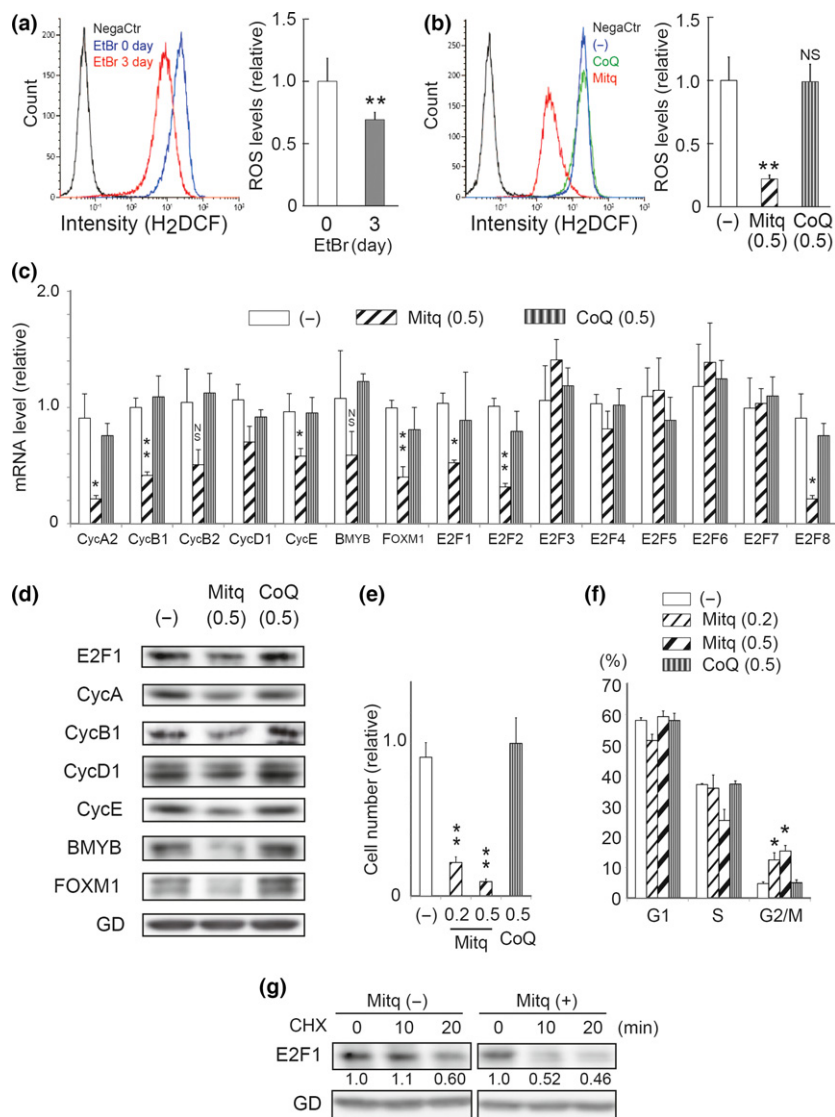


Fig. 6. Decrease in the intracellular reactive oxygen species (ROS) levels in electron transport chain (ETC)-deficient cells and its significance in controlling cell proliferation. (a) ROS levels of normal and pseudo- $\rho 0$ cells determined using H₂DCFDA for flow cytometry. Left: Representative histogram showing the H₂DCFDA fluorescence intensity obtained from calcein-labeled MDA/ $\rho 0$ cells (black [NegaCtr]): ethidium bromide (EtBr) treatment 0 days (unstained), blue: 0 days (stained), red: 3 days (stained). Right: The H₂DCFDA fluorescence intensity normalized against that of calcein blue in an individual cell was determined in at least 10 000 cells and plotted. (b) MDA cells were treated with 0.5 μ M Mitq or CoQ for 24 h, and the ROS levels were determined, as described in (a). Left: Histogram (black [NegaCtr]): unstained control, blue (-): untreated and stained control, red (Mitq): Mitq-treated and stained, green (CoQ): CoQ-treated and stained. (c) mRNA levels of cyclins (A2, B1, B2, D1 and E), BMYB, FOXM1 and E2F1–8 in MDA cells treated with 0.5 μ M of Mitq and CoQ for 24 h, which were quantified by qRT-PCR. (d) Western blot analysis of representative cell cycle regulators with MDA cells treated as described in (c) for 48 h. GD was the loading control. (e) Proliferation of MDA cells treated with 0.2 and 0.5 μ M Mitq, and 0.5 μ M CoQ for 6 days. (f) Cell cycle distribution of MDA cells treated as described in (e) for 48 h. (g) MDA cells treated with 0.5 μ M Mitq for 2 h were incubated with 100 μ g/mL cycloheximide (CHX) for the times indicated. E2F1 expression levels were examined by conducting western blot analysis, quantified using Image J software, and the relative intensities are shown after normalization against GD. * $P < 0.05$ and ** $P < 0.01$. NS, not significant.

Discussion

In this study, we identified a novel role for ETC activity in the control of proliferation of cancer cells. These findings may also be relevant to proliferation control in normal cells under physiological conditions. The principal mechanism that underlies this effect is the sensitivity of E2F1 expression to ETC activity or mtROS, which couples ETC activity with the cell cycle regulatory mechanism via an E2F1-organized transcriptional network. In this context, it is interesting to note that E2F1 also engages in regulating oxidative metabolism by repressing the key genes that regulate mitochondrial functions, including the respiratory chain.⁽²⁵⁾ Thus, according to our results and this previous study, a reciprocal regulatory mechanism may be present between E2F1 and the functions of organelles. In this scenario, when ETC activity declines, E2F1 expression levels decrease (Fig. 2c), which leads to the depression of E2F1-mediated transcriptional repression and the subsequent upregulation of the mitochondrial functions, including ETC activity. This constantly maintains ETC activity above a specific level in cells under physiological conditions. Thus, E2F1 potentially functions as a connector and coordinator between cellular proliferation and metabolic pathways,

which appears to be critically important for cellular homeostasis.

A similar study of cell proliferation under mtR/T inhibition was performed previously using HeLa cells.⁽¹⁰⁾ The results agree with ours in that the slowdown of cell proliferation under mtR/T inhibition was unlikely to be attributable to ATP depletion, but it could be attributable to the downregulation of p21CIP1 due to lower ROS levels in the cells. In $\rho 0$ cells derived from hepatoma cells, lower levels of cyclins A and D1 were observed as well as increased levels of CDK inhibitors, such as p16, p27 and p21,⁽²⁶⁾ which is similar to the case for MCF7/ $\rho 0$ cells. Therefore, the specific mechanisms that underlie the suppression of proliferation through mtR/T inhibition may differ among cell types or genetic backgrounds, particularly the p53 status, although no mention was made regarding the E2F transcriptional network in these previous studies. According to our study, downregulation of the E2F transcriptional network was observed in several different cell types in addition to breast cancer cells irrespective of the p53 status under ETC-deficient conditions (unpublished data); therefore, the regulation appears to be a fundamental response that can be modulated by an additional response such as CKI induction.

At present, the mechanism that allows mtROS to regulate the expression of E2F1 remains largely unknown. However, considering the effect of Mitq (Fig. 5),⁽²⁷⁾ it is probable that a redox change in mitochondria is involved, which is coupled with the stability of the E2F1 protein (Fig. 6g). Given the autoregulatory control of E2F1 expression,⁽²⁸⁾ decreases in E2F1 protein levels are assumed to reduce the activity of the E2F1 promoter, thereby leading to the downregulation of the entire E2F1-mediated transcriptional network.

In addition to elucidating the detailed mechanisms, understanding the negative impact of mtR/T inhibition on cancer cell proliferation may be of practical value, particularly the effects on MDA cells (Fig. 1). MDA is a representative cell line established from triple-negative breast cancer (TNBC), a subtype of the highly malignant cancers that lack specific cell-surface receptors needed for targeted therapeutic treatments and with a poor prognosis. According to the intrinsic impairment of the ETC, which was identified recently in multiple TNBC cell lines,⁽²⁹⁾ it is expected that TNBC will be exceptionally sensitive to mtR/T inhibition, which should further reduce the ETC activity of TNBC cells and effectively suppress their proliferation, thereby providing a promising lead in the fight against the highly malignant cancer.

Gene manipulation is a potential approach for inhibiting mtR/T, as suggested by a previous study where TFAM was knocked down in a Kras-driven mouse model of lung

adenocarcinoma.⁽⁴⁾ Our study extends the possibility of practical applications in human cancers (Figs 4, 5). Methods may be developed to scavenge mtROS as an alternative to gene manipulation that inhibits mtR/T or ETC; in many therapeutic applications, a practical goal of mtR/T inhibition is to decrease mtROS, which act as non-relevant signaling molecules that bring about various adverse conditions. Recently, mt-antioxidants have attracted increasing interest for their potential use in cancer therapy.^(30–33) In this study, we demonstrated the effectiveness of Mitq in inhibiting TNBC cell proliferation based on new mechanistic insights (Fig. 6), which further highlights the potential use of mt-antioxidants in cancer therapy. We are hopeful that our results will contribute to the development of improved cancer therapies.

Acknowledgments

We thank Mr A. Itoh, Mr T. Imai, Ms N. Shioda and Ms A. Nakano for contributing to this study as part of their bachelor's degrees. This study was supported by JSPS KAKENHI Grant Numbers 26460399 and 21570205 and the Private University High Technology Research Center Project matching fund by a subsidy from MEXT.

Disclosure Statement

The authors have no conflict of interest to declare.

References

- DeBerardinis RJ, Lum JJ, Hatzivassiliou G, Thompson CB. The biology of cancer: metabolic reprogramming fuels cell growth and proliferation. *Cell Metab* 2008; **7**: 11–20.
- Frezza C, Gottlieb E. Mitochondria in cancer: not just innocent bystanders. *Semin Cancer Biol* 2009; **19**: 4–11.
- Moreno-Sanchez R, Marin-Hernandez A, Saavedra E, Pardo JP, Ralph SJ, Rodriguez-Enriquez S. Who controls the ATP supply in cancer cells? Biochemistry lessons to understand cancer energy metabolism. *Int J Biochem Cell Biol* 2014; **50**: 10–23.
- Weinberg F, Hamanaka R, Wheaton WW *et al.* Mitochondrial metabolism and ROS generation are essential for Kras-mediated tumorigenicity. *Proc Natl Acad Sci USA* 2010; **107**: 8788–93.
- Sharma LK, Fang H, Liu J, Vartak R, Deng J, Bai Y. Mitochondrial respiratory complex I dysfunction promotes tumorigenesis through ROS alteration and AKT activation. *Hum Mol Genet* 2011; **20**: 4605–16.
- Ishikawa K, Takenaga K, Akimoto M *et al.* ROS-generating mitochondrial DNA mutations can regulate tumor cell metastasis. *Science* 2008; **320**: 661–4.
- Morin A, Letouze E, Gimenez-Roqueplo AP, Favier J. Oncometabolites-driven tumorigenesis: from genetics to targeted therapy. *Int J Cancer* 2014; **135**: 2237–48.
- Singh KK. Mitochondria damage checkpoint, aging, and cancer. *Ann N Y Acad Sci* 2006; **1067**: 182–90.
- Chandel NS, Schumacker PT. Cells depleted of mitochondrial DNA (rho0) yield insight into physiological mechanisms. *FEBS Lett* 1999; **454**: 173–6.
- Schauen M, Spitkovsky D, Schubert J, Fischer JH, Hayashi J, Wiesner RJ. Respiratory chain deficiency slows down cell-cycle progression via reduced ROS generation and is associated with a reduction of p21CIP1/WAF1. *J Cell Physiol* 2006; **209**: 103–12.
- Shibanuma M, Inoue A, Ushida K *et al.* Importance of mitochondrial dysfunction in oxidative stress response: a comparative study of gene expression profiles. *Free Radic Res* 2011; **45**: 672–80.
- Gilkerson RW, Margineantu DH, Capaldi RA, Selker JM. Mitochondrial DNA depletion causes morphological changes in the mitochondrial reticulum of cultured human cells. *FEBS Lett* 2000; **474**: 1–4.
- King MP, Attardi G. Isolation of human cell lines lacking mitochondrial DNA. *Methods Enzymol* 1996; **264**: 304–13.
- Neve RM, Chin K, Fridlyand J *et al.* A collection of breast cancer cell lines for the study of functionally distinct cancer subtypes. *Cancer Cell* 2006; **10**: 515–27.
- Hallstrom TC, Mori S, Nevins JR. An E2F1-dependent gene expression program that determines the balance between proliferation and cell death. *Cancer Cell* 2008; **13**: 11–22.
- Bracken AP, Ciro M, Cocito A, Helin K. E2F target genes: unraveling the biology. *Trends Biochem Sci* 2004; **29**: 409–17.
- Sadasivam S, DeCaprio JA. The DREAM complex: master coordinator of cell cycle-dependent gene expression. *Nat Rev Cancer* 2013; **13**: 585–95.
- Kang D, Kim SH, Hamasaki N. Mitochondrial transcription factor A (TFAM): roles in maintenance of mtDNA and cellular functions. *Mitochondrion* 2007; **7**: 39–44.
- Kanki T, Ohgaki K, Gaspari M *et al.* Architectural role of mitochondrial transcription factor A in maintenance of human mitochondrial DNA. *Mol Cell Biol* 2004; **24**: 9823–34.
- Larsson NG, Wang J, Wilhelmsson H *et al.* Mitochondrial transcription factor A is necessary for mtDNA maintenance and embryogenesis in mice. *Nat Genet* 1998; **18**: 231–6.
- Brand MD, Affourtit C, Esteves TC *et al.* Mitochondrial superoxide: production, biological effects, and activation of uncoupling proteins. *Free Radic Biol Med* 2004; **37**: 755–67.
- Korshunov SS, Skulachev VP, Starkov AA. High protonic potential actuates a mechanism of production of reactive oxygen species in mitochondria. *FEBS Lett* 1997; **416**: 15–8.
- Kuznetsov AV, Kehrer I, Kozlov AV *et al.* Mitochondrial ROS production under cellular stress: comparison of different detection methods. *Anal Bioanal Chem* 2011; **400**: 2383–90.
- Smith RA, Adlam VJ, Blaikie FH *et al.* Mitochondria-targeted antioxidants in the treatment of disease. *Ann N Y Acad Sci* 2008; **1147**: 105–11.
- Blanchet E, Annicotte JS, Lagarrigue S *et al.* E2F transcription factor-1 regulates oxidative metabolism. *Nat Cell Biol* 2011; **13**: 1146–52.
- Park SY, Choi B, Cheon H *et al.* Cellular aging of mitochondrial DNA-depleted cells. *Biochem Biophys Res Commun* 2004; **325**: 1399–405.
- James AM, Smith RA, Murphy MP. Antioxidant and prooxidant properties of mitochondrial Coenzyme Q. *Arch Biochem Biophys* 2004; **423**: 47–56.
- Johnson DG, Ohtani K, Nevins JR. Autoregulatory control of E2F1 expression in response to positive and negative regulators of cell cycle progression. *Genes Dev* 1994; **8**: 1514–25.
- Pelicano H, Zhang W, Liu J *et al.* Mitochondrial dysfunction in some triple-negative breast cancer cell lines: role of mTOR pathway and therapeutic potential. *Breast Cancer Res* 2014; **16**: 434.
- Sullivan LB, Chandel NS. Mitochondrial reactive oxygen species and cancer. *Cancer Metab* 2014; **2**: 17.

- 31 Rao VA, Klein SR, Bonar SJ *et al.* The antioxidant transcription factor Nrf2 negatively regulates autophagy and growth arrest induced by the anticancer redox agent mitoquinone. *J Biol Chem* 2010; **285**: 34447–59.
- 32 Manskikh VN, Krasilshchikova MS, Vygodin VA, Egorov MV. Effect of the mitochondria-targeted antioxidant SkQ1 on development of spontaneous tumors in BALB/c mice. *Biochemistry (Mosc)* 2014; **79**: 1136–9.
- 33 Cheng G, Zielonka J, McAllister DM *et al.* Mitochondria-targeted vitamin E analogs inhibit breast cancer cell energy metabolism and promote cell death. *BMC Cancer* 2013; **13**: 285.

Supporting Information

Additional Supporting Information may be found online in the supporting information tab for this article:

Doc. S1. Materials and Methods, Abbreviations and References.

Fig. S1. Defects in cell cycle progression and downregulation of cell cycle regulators in electron transport chain (ETC)-deficient and Mitq-treated MCF7 cells.

Fig. S2. Effects of BMYB and FOXM1 knockdown on cell proliferation.

Fig. S3. mitochondrial transcription factor A (TFAM) knockdown by expression of shRNA.

Fig. S4. Reactive oxygen species (ROS) detection under treatment with EtBr or Mitq, or with an electron carrier, inhibitors and substrates for electron transport chain (ETC).

Fig. S5. Effects of Mitq on $\Delta\Psi_m$ and effects of signaling activators of DNA damage response and spindle assembly checkpoint on the E2F1 transcriptional network.

Table S1. List of E2F target genes downregulated in pseudo-p0 cells.

A HIC-5- and KLF4-dependent Mechanism Transactivates p21^{Cip1} in Response to Anchorage Loss^{*[5]}

Received for publication, May 8, 2012, and in revised form, August 30, 2012. Published, JBC Papers in Press, September 24, 2012, DOI 10.1074/jbc.M112.377721

Kazunori Mori, Hiroyuki Hamanaka, Yukiko Oshima, Yuri Araki, Fumihiko Ishikawa, Kiyoshi Nose, and Motoko Shibamura¹

From the Department of Molecular Biology, Division of Cancer Cell Biology, Showa University School of Pharmacy, Tokyo 142-8555, Japan

Background: Anchorage dependence of cell growth remains incompletely understood.

Results: A cyclin-dependent kinase inhibitor (p21^{Cip1}) is transcriptionally up-regulated on anchorage loss, depending on Kruppel-like factor 4 (KLF4) and a molecular scaffold of hydrogen peroxide-inducible clone-5 (HIC-5).

Conclusion: On anchorage loss, HIC-5 localizes at the nuclear matrix and promotes KLF4 tethering to DNA.

Significance: A novel mechanism regulating gene expression in a detachment-dependent manner has emerged.

Anchorage loss elicits a set of responses in cells, such as transcriptional changes, in order to prevent inappropriate cell growth in ectopic environments. However, the mechanisms underlying these responses are poorly understood. In this study, we investigated the transcriptional up-regulation of cyclin-dependent kinase inhibitor p21^{Cip1} during anchorage loss, which is important for cell cycle arrest of nonadherent cells in the G1 phase. Up-regulation was mediated by an upstream element, designated as the detachment-responsive element (DRE), that contained Kruppel-like factor 4 (KLF4) and runt-related transcription factor 1 (RUNX1) recognition sites; both of these together were necessary for transactivation, as individually they were insufficient. RNAi experiments revealed that KLF4 and a multidomain adaptor protein, hydrogen peroxide-inducible clone 5 (HIC-5), were critically involved in DRE transactivation. The role of HIC-5 in this mechanism was to tether KLF4 to DNA sites in response to cellular detachment. In addition, further analysis suggested that oligomerization and subsequent nuclear matrix localization of HIC-5, which was accelerated spontaneously in cells during anchorage loss, was assumed to potentiate the scaffolding function of HIC-5 in the nucleus and consequently regulate p21^{Cip1} transcription in a manner responding to anchorage loss. At the RUNX1 site, a LIM-only protein, CRP2, imposed negative regulation on transcription, which appeared to be removed by anchorage loss and contributed to increased transcriptional activity of DRE together with regulation at the KLF4 sites. In conclusion, this study revealed a novel transcriptional mechanism that regulated gene expression in a detachment-dependent manner, thereby contributing to anchorage-dependent cell growth.

Physical and functional cellular adhesion to the extracellular matrix (ECM)² is indispensable to multicellular organisms from embryonic stages throughout maturity (1, 2). In metazoans, cellular adhesion to ECM is mediated by integrins, a class of heterodimeric transmembrane receptors, which on encounter with a ligand, transmit intracellular signals activating numerous downstream classical kinase- and GTPase-mediated pathways (3). Interestingly, the pathways activated by integrin are largely the same as those activated by growth factor and cytokine receptors, and these signals potentiate each other downstream, as observed in the synergistic activation of the extracellular signal-regulated kinase/mitogen-activated protein kinase cascade (4–6).

In numerous cellular activities, cooperation between growth factor receptor kinase and integrin signaling is observed, which is manifested as dependence of activities on cellular adhesion to ECM along with growth factors. A typical example is cell cycle progression where various events from mid- to late-G1 phase culminating in up-regulation of G1-phase cyclin-dependent kinase (CDK) activity require both integrin and growth factor signaling (4–7). In mesenchymal cells, in particular, deprivation of ECM anchorage arrests the cell cycle at the G1-phase, which has led to the concept of anchorage-dependent cell growth and is usually interpreted as a requirement of adhesion for complete activation of G1-phase CDKs, although the detailed mechanisms are not fully understood. For multicellular organisms, the anchorage dependence of cell growth is critical because it prevents promiscuous reattachment and inappropriate proliferation of nonadherent cells in ectopic environments.

Hydrogen peroxide-inducible clone-5 (HIC-5) is a multidomain protein comprising four Leu- and Asp-rich LD and LIM domains (named after the three transcriptional factors Lin-11,

* This work was supported in part by Grant-in-aid for Young Scientists (B) 22790327, the High-Technology Research Center Project from the Ministry for Education, Culture, Sports, Science, and Technology (MEXT) of Japan, and a Private University High Technology Research Center Project matching fund subsidy from MEXT.

[5] This article contains supplemental Figs. S1 and S2.

¹ To whom correspondence should be addressed: Showa University School of Pharmacy, Department of Molecular Biology, Division of Cancer Cell Biology, 1-5-8 Hatanodai, Shinagawa-ku, Tokyo 142-8555, Japan. Tel.: +81-3-3784-8209; Fax: +81-3-3784-6850; E-mail: smotoko@pharm.showa-u.ac.jp.

² The abbreviations used are: ECM, extracellular matrix; Adh, adhesion; BrdU, 5-bromo-2'-deoxyuridine; CDK, cyclin-dependent kinase; CKI, cyclin-dependent kinase inhibitor; CRP, cysteine-rich protein; Dox, doxycycline hyclate; DRE, detachment-responsive element; EGFP, enhanced green fluorescence protein; HIC-5, hydrogen peroxide-inducible clone-5; KLF4, Kruppel-like factor 4; LIM, lin-11, Isl-1, and Mec-3; MEF, mouse embryo fibroblast; NES, nuclear export signal; siRNA, small interfering RNA; shRNA, short hairpin RNA; RUNX1, Runt-related transcription factor 1; Sus, suspension.

Isl-1, and Mec-3) that serve as molecular adaptors in various cellular activities, including integrin signaling at focal adhesions (8, 9) and nuclear transcriptional activities (10). In addition, with a shuttling ability between the two compartments, HIC-5 is capable of coupling cell adhesion with nuclear activities (11). For example, we recently characterized a fail-safe system organized by HIC-5 for anchorage-dependent cell growth (12). The essence of the system was localization of cyclin D1 to the nuclei of only adherent cells and its exclusion from the nucleus on anchorage loss, which is crucial to prevent cell proliferation under nonadherent conditions. This is achieved by adhesion-dependent shuttling of HIC-5, which is regulated by the CRM-dependent nuclear export mechanism (11) and competitively localizes cyclin D1 to the nuclei of adherent cells. On anchorage loss, shuttling is stopped, and cyclin D1 is consequently exported outside the nucleus instead of HIC-5 (12).

In the present study, we addressed another HIC-5-dependent mechanism contributing to growth arrest under nonadherent conditions. The mechanism transcriptionally induced a CDK inhibitor (CKI), p21^{Cip1}, in response to disruption of cell-ECM interactions. In this mechanism, HIC-5 played a crucial role in recruitment and/or retention of Kruppel-like factor 4 (KLF4), a transcription factor essential for transactivation, to DNA sites in a detachment-dependent manner.

EXPERIMENTAL PROCEDURES

Cell Culture—C3H10T1/2 cells, primary mouse embryo fibroblasts (MEFs), and normal human diploid fibroblasts (TIG-7) were grown in Dulbecco's modified Eagle's medium supplemented with 10% fetal calf serum as reported previously (12). TIG-7 cells (JCRB0511) were obtained from the Japanese Collection of Research Bioresources Bank (Osaka, Japan) and used between 33 and 39 passages.

The cells were cultured under adherent (adhesion; Adh) and nonadherent (suspension; Sus) conditions in essentially the same manner as described previously (12). In brief, the cells were detached from a culture dish by trypsinization, divided in half, reseeded onto poly (2-hydroxyethyl methacrylate) (Sigma)-coated (0.8 mg/cm²) (Sus) and noncoated (Adh) dishes, and analyzed simultaneously.

Reagents—Blasticidin was obtained from Kaken Pharmaceutical Co. Ltd. (Tokyo, Japan), and puromycin and doxycycline hyclate (Dox) were purchased from Sigma. Small interfering RNA (siRNA) oligonucleotides used in the present study are listed in the supplemental information.

Expression Vectors—Short hairpin RNA (shRNA) was expressed using CS-RfA-ETBsd (Tet-On), CS-RfA-ErTBsd (Tet-Off), and CS-RfA-EB (constitutive) lentiviral vectors (13). The shRNA target sequence information is provided in the supplemental information.

Retrovirus expression vectors were based on pMXs-IP (14). FLAG-tagged HIC-5 and HA-tagged paxillin constructs were as described previously (15). To generate a pMXs-IP-based series of FLAG-tagged siRNA-resistant HIC-5 mutants (wild type, NLS, ΔLIM4, mLD3, and Cfl/ns), silent mutations were introduced into the siRNA target sequence (ttc aac atc acc gac gaa atc, *Hic-5*; 262–278 nucleotides) at the underlined positions using the PrimeSTAR Mutagenesis Basal Kit (Takara Bio, Inc.,

Otsu, Japan) with a mutated primer according to the manufacturer's instructions.

Real-time Reverse Transcription (RT)-PCR—Total RNA was extracted from the cultured cells, reverse transcribed into cDNA, and analyzed by described previously methods (16).

Antibodies and Immunoblotting—The immunoblotting procedure was essentially the same as that described previously (15). Antibodies to p21^{Cip1} (BD Biosciences, San Jose, CA), glyceraldehyde-3-phosphate dehydrogenase (GAPDH; Chemicon, Temecula, CA), KLF4 (Santa Cruz Biotechnology, Santa Cruz, CA), HIC-5 (BD Biosciences), Lamin B1 (Invitrogen, Carlsbad, CA), and FLAG (Sigma) were used.

Transfection and Infection—siRNA transfection was performed using Lipofectamine RNAiMAX (Invitrogen) according to the manufacturer's instructions. The cells were transfected with siRNA duplexes (100 nM) and processed 48 h after transfection.

Viral infection was performed as described previously (17). In brief, Plat-E (for retrovirus) or HEK293T (for lentivirus) cells were transfected with viral vectors by the calcium phosphate method to obtain culture supernatants containing the virus. The target cells were infected by culturing for 24 h in virus-containing medium. Twenty-four hours after culture in the presence (Tet-Off lentivirus) or absence (Tet-On lentivirus, retrovirus) of Dox (1 μg/ml), the infected cells were selected and maintained in medium supplemented with 10 μg/ml blasticidin (lentivirus) or 5 μg/ml puromycin (retrovirus).

Reporter Constructs and Assay—The WWP reporter containing the 2.4-kbp upstream region of the p21^{Cip1} promoter and the derived deletion reporters (WWP Sac, 2.0, 1.7, 1.4, Hinf, and Pst) were described previously (10, 18).

The pGL4.2/minP vector was generated by inserting the minimal promoter (aga ggg tat ata atg gaa gct cga ctt cca g) immediately upstream of the luciferase reporter gene of pGL4.20 (Promega, Madison, WI). The WWP 2.0-Sac, 2.0–2.1-Sac, and 2.1-Sac reporters were generated by inserting the PCR-amplified fragments (–2243 to –1987 bp, –2243 to –2094 bp, and –2093 to –1987 bp, respectively) upstream of the p21^{Cip1} promoter in the pGL4.2/minP vector. For a mutant series of the WWP 2.0-Sac reporter [KLF, USF, GATA, and Runt-related transcription factor 1 (RUNX1) mt], point mutations were introduced into the wild-type WWP 2.0-Sac reporter as described above. The sequence information on the mutational changes is provided in Fig. 3A.

In the assay, firefly luciferase reporters (1 μg) together with the internal control of the *Renilla* luciferase reporter plasmid (phRL/CMV) (0.02 μg) were transiently introduced into the cells (19). Twenty-four hours after transfection, the cells were transferred to monolayer or suspension cultures and further incubated for 24 h. Luciferase activities were determined using the Dual Luciferase Assay Kit (Promega). Firefly luciferase activities were normalized with those of *Renilla* luciferase.

5-Bromo-2'-deoxyuridine (BrdU) Incorporation—BrdU incorporation was evaluated by immunocytochemistry as described previously (12).

Chromatin Immunoprecipitation (ChIP) Assay—A ChIP assay was performed based on the method described by Nelson *et al.* (20), with slight modifications (19). The antibody used for

p21^{Cip1} Transactivation on Anchorage Loss

this assay was anti-KLF4 (Santa Cruz Biotechnology), and anti-rabbit immunoglobulin (X0903; DAKO Japan, Kyoto, Japan) was used as the control.

Subcellular Fractionation—Subcellular fractionation was performed according to the method described by He *et al.* (21), with minor modifications. The cells were washed with ice-cold PBS and resuspended in CSK buffer (10 mM PIPES (pH 6.8), 100 mM NaCl, 300 mM sucrose, 3 mM MgCl₂, 1 mM EGTA, 0.5% Triton X-100, and protease inhibitor mixture (Sigma)). After 5 min of incubation on ice, nuclear pellets were separated from cytoplasmic supernatants by centrifugation at 3000 × *g* for 10 min and incubated for 45 min at 30 °C in digestion buffer (10 mM PIPES (pH 6.8), 50 mM NaCl, 300 mM sucrose, 3 mM MgCl₂, 1 mM EGTA, 0.025% Triton X-100, 300 units/ml DNase I (RT-grade, Nippon Gene Co., Ltd., Tokyo, Japan), and 4 mM vanadyl ribonucleoside complex (Sigma)). After incubation, ammonium sulfate was added to the digestion buffer to obtain a final concentration of 250 mM. The chromatin fraction (soluble) was removed by centrifugation at 6500 × *g* for 10 min. The nuclear matrix was recovered by centrifugation at 6500 × *g* for 10 min after washing with excess digestion buffer containing 250 mM ammonium sulfate.

Statistical Analysis—Statistical differences were determined using the Student's *t* test.

RESULTS

p21^{Cip1} Transactivation on Anchorage Loss Is Dependent on KLF4 and RUNX1, but Not p53, Binding Sites—It has been previously shown that p21^{Cip1} is up-regulated when anchorage-dependent cells are placed under suspension conditions (22). This leads to inhibition of CDKs such as CDK2 in a complex with cyclin E, which eventually results in growth arrest (23). In the present study, we confirmed p21^{Cip1} up-regulation at the mRNA and protein levels in C3H10T1/2 cells in response to anchorage deprivation (Fig. 1, *A* and *B*). Under the same conditions, the WWP reporter driven by the 2.4-kbp upstream region of p21^{Cip1} increased its activity, suggesting that induction was transcriptionally regulated (Fig. 1*C*). Similar transcriptional responses were observed in primary MEFs and TIG-7 cells (Fig. 1*C*). Another CKI, p27^{Kip1}, was reportedly up-regulated by anchorage loss at the protein level (23), but not at the mRNA level (Fig. 1*A*). BrdU incorporation, which was ~70% in adherent cells, was lowered to less than 10% in nonadherent cells as reported previously (Fig. 1*D*). However, p21^{Cip1} siRNA treatment recovered incorporation to nearly 20% (Fig. 1*D*, *Sus*), suggesting that induced p21^{Cip1} contributed to growth arrest as described previously (24), although the extent was modest, possibly because of p27^{Kip1} compensation (22).

To elucidate the molecular mechanisms underlying the transcriptional response of p21^{Cip1} to anchorage loss, we performed the luciferase assay using a series of WWP deletion mutant reporters (Fig. 2*A*) and defined a regulatory region responsible for the response upstream of the gene. The results were definite as follows. The response of the WWP Sac reporter with the first 0.1 kbp (up to the SacI site at -2.2 kbp) truncated was comparable with that of full-length WWP, indicating that the first 0.1 kbp was dispensable for the response (Fig. 2*B*). In contrast, further deletion to -2.0 kbp (WWP 2.0) completely abolished the

response, suggesting that the response was primarily regulated in the region between -2.2 (the SacI site) and -2.0 kbp. This region, designated as WWP 2.0-Sac, was found to independently exhibit a 2–4-fold response comparable with that of full-length WWP when connected directly to a minimal promoter (Fig. 2*D*), indicating that WWP 2.0-Sac was necessary and sufficient for the response. However, when split into two, neither 2.1-Sac nor 2.1–2.0-Sac could elicit a response (Fig. 2*D*), indicating that multiple (≥two) sites located in either half cooperated to evoke the response. These reporter behaviors were basically recapitulated in primary MEFs (Fig. 2, *B* and *D*).

It should be noted that p53, albeit a well-established p21^{Cip1} transcription activator (25), was not likely involved in this response. Reporter assay results, for example, eliminated the necessity of two p53 binding sites. As shown in Fig. 2, *A* and *B*, the WWP Sac reporter with the first p53 site deleted retained nearly the complete response, whereas the WWP 2.0 reporter lost the response despite retention of the second site. In contrast, WWP 2.0-Sac, which contained no p53 binding sites, responded to detachment conditions comparably well with the intact WWP reporter as noted above (Fig. 2*D*). In addition, p53 siRNA treatment did not affect the p21^{Cip1} response (supplemental Fig. S1), although the basal transcription level was reduced. These results consistently argued against p53 involvement in p21^{Cip1} transactivation on anchorage loss under the experimental conditions in the present study. Rather, the response was considered to be mediated by the WWP 2.0-Sac region, designated as a detachment-responsive (DR) region.

In further study focusing on the DR region, we searched for transcription factor binding sites (Fig. 3*A*) and introduced mutations in WWP 2.0-Sac reporter sequences as indicated in the inset (table). Among the mutations, those disrupting the KLF4 and RUNX1 sites caused distinctive effects. The KLF4 mutations almost completely deprived the reporter of the response (Fig. 3*B*, *KLF4 mt1* and *mt2*), underscoring the importance of the sites for inducing the response. In contrast, the RUNX1 mutation led to a marked increase in the basal transcription level under Adh conditions (Fig. 3*B*, *RUNX mt*), indicating that a negative effect was imposed by this site under normal conditions. Importantly, no further increase in transcriptional activity occurred in this mutation on anchorage loss, suggesting that the RUNX1 site was simultaneously involved in response induction. Thus, the KLF4 and RUNX1 sites emerged as essential elements for the transcriptional response of p21^{Cip1} to anchorage loss. This result was consistent with the above observation, suggesting the requirement of multiple elements in the DR region for the response (Fig. 2, *C* and *D*). KLF4 involvement was also verified at the protein level because a decrease in the protein levels with shRNA expressed under the Tet-Off system (supplemental Fig. S2*A*) resulted in marked deterioration of the p21^{Cip1} response (Fig. 3, *C* and *D*). With regard to RUNX1, we used pooled siRNA because of the unavailability of sequences for shRNA with a sufficient knock-down efficiency. Similar to the disruption of the RUNX1 site (Fig. 3*B*, *RUNXmt*), treatment with siRNA resulted in elevated basal levels of p21^{Cip1} expression (Fig. 3*E*), thus supporting the negative role of RUNX1.

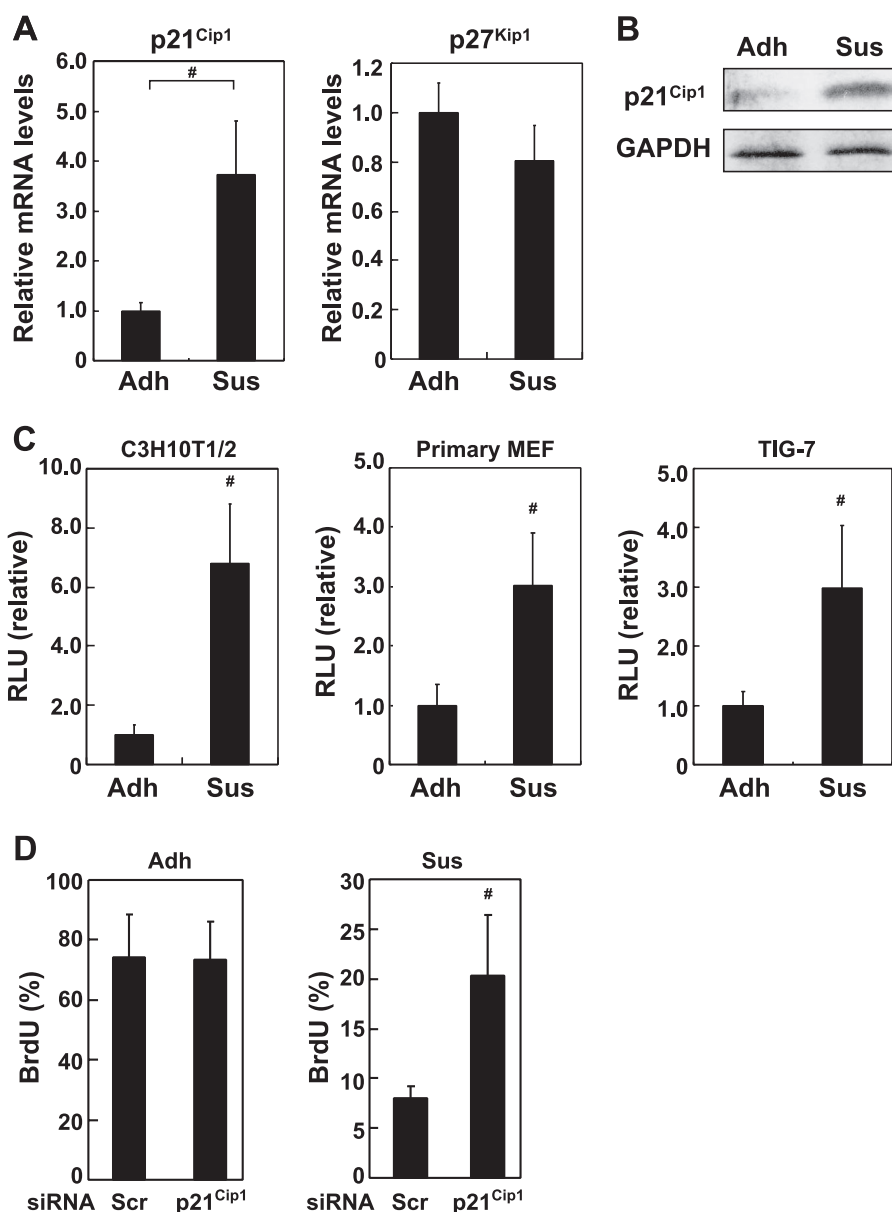


FIGURE 1. *p21^{Cip1} transactivation and growth arrest induced by anchorage loss.* *A*, C3H10T1/2 cells were cultured under adherent (*Adh*) or nonadherent (*Sus*) conditions for 24 h, and total RNA was extracted and quantified by real-time RT-PCR. The *p21^{Cip1}* and *p27^{Kip1}* mRNA levels under *Sus* conditions are shown as a ratio to the control (*Adh*) after normalization with that of GAPDH (mean \pm S.D., #, $p < 0.05$). *B*, cells cultured as in *A* were lysed and subjected to immunoblotting using the indicated antibodies. GAPDH is shown as a loading control. *C*, C3H10T1/2 cells, primary MEFs, and TIG-7 cells were transiently transfected with the WWP reporter plasmid together with the internal control. After 24 h, the cells were transferred and incubated further under culture conditions as in *A*, following which luciferase activities were determined. A ratio to the control (*Adh*) is shown (mean \pm S.D., #, $p < 0.05$). *D*, siRNA for the control (scrambled (Scr)) or for *p21^{Cip1}* (100 nM) was introduced into C3H10T1/2 cells. After 48 h, the cells were transferred and incubated further for 16 h under culture conditions as in *A*, and BrdU incorporation was examined. Data are shown as mean \pm S.D. (#, $p < 0.05$). The experimental conditions are noted under "Experimental Procedures." Each assay was performed in triplicate and repeated at least three times.

HIC-5, a Molecular Scaffold for Transcriptional Complex Assembly, Is Required for the Transcriptional Response of p21^{Cip1}—Our previous result implicated HIC-5 in the control of *p21^{Cip1}* transcription (10) and inferred its involvement in *p21^{Cip1}* transactivation on anchorage loss. In the present study, we examined this possibility and found that HIC-5 depletion by siRNA (supplemental Fig. S2B) significantly reduced *p21^{Cip1}* induction in nonadherent cells (Fig. 4A). Similarly, HIC-5 shRNA expression (Tet-On) (supplemental Fig. S2B) abolished a transcriptional response of the reporter driven by the DR region (WWP 2.0-Sac) (Fig. 4B, *HIC-5; Dox+*). These results

underlined a pivotal role of HIC-5 in *p21^{Cip1}* transcriptional regulation in response to anchorage deprivation. The decrease of BrdU incorporation under anchorage-deprived conditions was alleviated by HIC-5 siRNA (Fig. 4C, *Sus*), which was expected from the inhibitory effect on *p21^{Cip1}* induction and was comparable with the effect of *p21^{Cip1}* siRNA (Fig. 1D, *Sus*).

Given the localization of HIC-5 at multiple cellular compartments and its shuttling ability (11), it was possible that HIC-5 regulated the transcriptional response either directly in the nucleus or indirectly by affecting cytoplasmic cellular events. To discriminate between these cases, we investigated whether

p21^{Cip1} Transactivation on Anchorage Loss

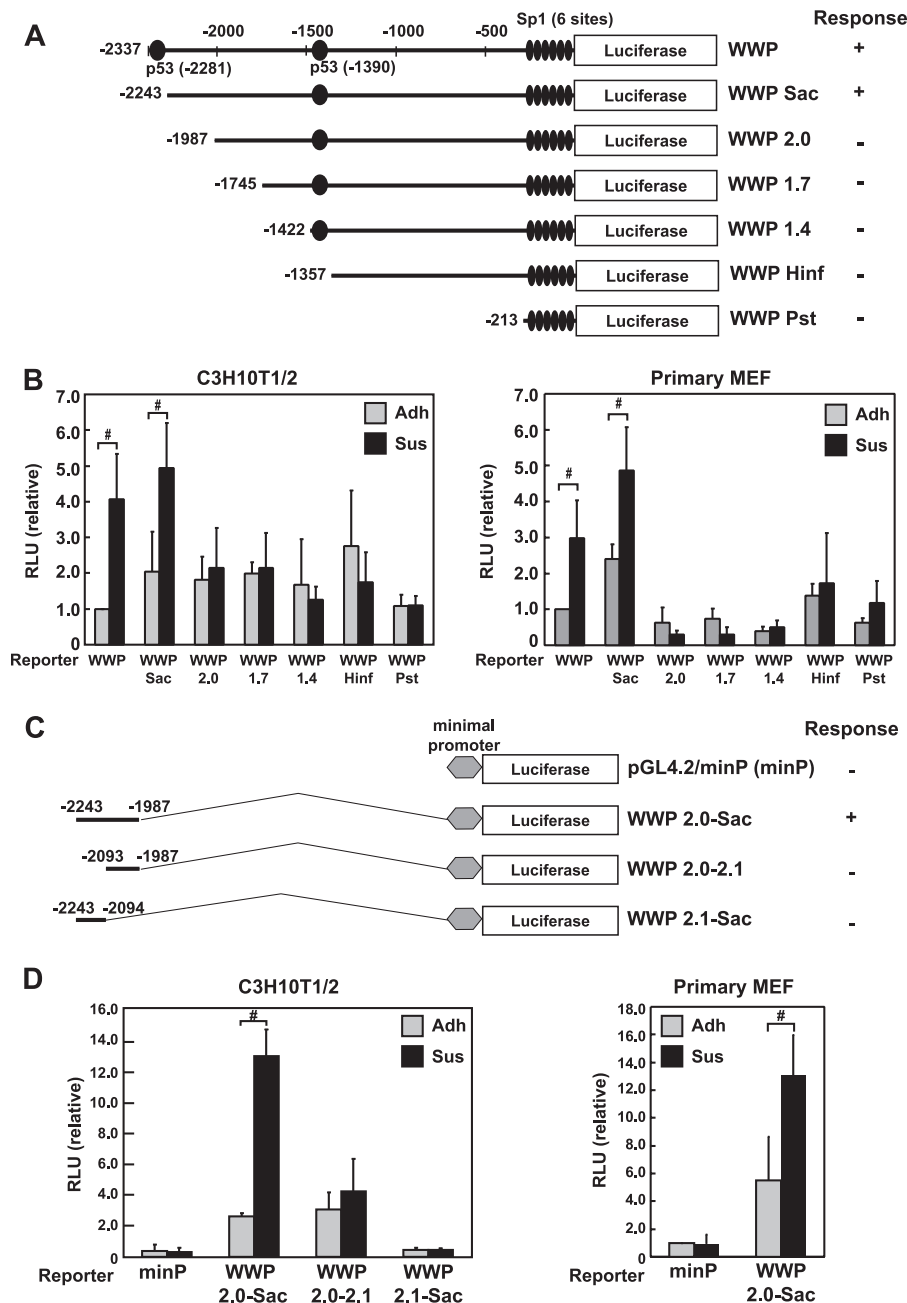


FIGURE 2. Identification of a DR region upstream of p21^{Cip1}. *A*, schematic representation of the WWP deletion series of the p21^{Cip1} promoter reporters (x) along with their responsiveness to detachment. The p53 and Sp1 binding sites are noted. *B*, the reporters as in *A* were transfected into C3H10T1/2 cells and primary MEFs together with the internal control, and reporter activities were evaluated under adherent (*Adh*) and nonadherent (*Sus*) conditions as in Fig. 1C. A ratio to the control (WWP, *Adh*) is shown (mean \pm S.D., #, $p < 0.05$). *C*, schematic representation of the pGL4.2/minP-based WWP p21^{Cip1} promoter reporters along with their responsiveness to detachment. *D*, the reporter assay was performed using the reporters as in *C* under the conditions as in *B*. A ratio to the control [pGL4.2/minP (*minP*), *Adh*] is shown (mean \pm S.D., #, $p < 0.05$). Each assay was performed in triplicate and repeated at least three times.

nuclear localization was a prerequisite for the HIC-5 function in p21^{Cip1} induction. For this purpose, we prepared constructs expressing siRNA-resistant versions of wild- and mutant-types of HIC-5 (supplemental Fig. S2C) whose subcellular localizations were varied and examined their capability to substitute for endogenous HIC-5 depleted by siRNA. As expected, wild-type (WT⁺) HIC-5 expression concomitant with siRNA counteracted the effect of siRNA and restored p21^{Cip1} induction (Fig. 4D). The mLD3 and Cfl/ns mutants, both of which are defective in the nuclear export signal (NES) function and spontaneously accumulate in the nucleus (11), also showed this capability. Of

note, the exclusively nuclear-localized version of HIC-5 (NLS) (10) similarly overcame siRNA effects, providing strong support for the concept that HIC-5 functions to directly promote transcription in the nucleus, but not at focal adhesions or by shuttling. Paxillin exhibited no such capability (Fig. 4D), thereby diminishing the concerns of artifacts because of protein overexpression. Among the HIC-5 mutants, Δ LIM4 was distinctive in that it lost the ability to substitute for endogenous HIC-5 despite retaining the nuclear localizing potential (11), suggesting the importance of this domain in the nuclear HIC-5 function. This is consistent with a previous result identifying

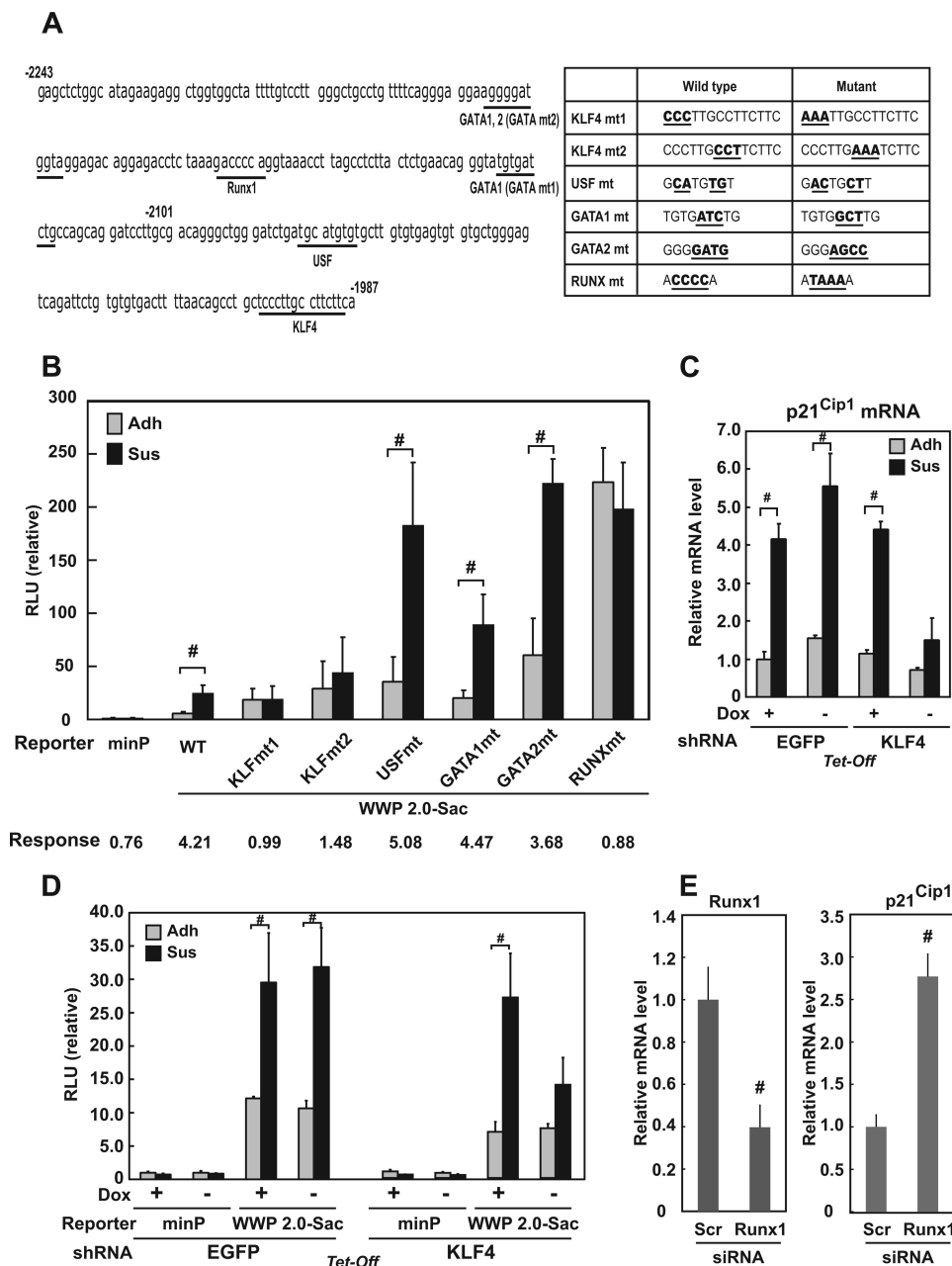


FIGURE 3. Analysis of DRE. *A*, the sequence of the detachment-responsive region in the p21^{Cip1} promoter. Binding sites for the transcriptional factors are underlined. In the table, the wild- and mutant-type binding site sequences are aligned. The underlined bases in *boldface* were changed in the WWP 2.0-Sac reporters (Fig. 2C) to generate the mutant reporters. *B*, C3H10T1/2 cells were transiently transfected with the pGL4.2/minP (minP) vector and the wild-type or mutant WWP 2.0-Sac reporters as described in *A* together with the internal control, and reporter activities were evaluated as above. A ratio to the control [minP; adherent (Adh)] is shown (mean \pm S.D.). The fold response to detachment is shown at the bottom of the graph. *C*, cells were infected with the lentivirus (Tet-Off) encoding shRNA for KLF4 or enhanced green fluorescence protein (EGFP) (control) and selected as described under "Experimental Procedures." The resistant cells were pooled and cultured under Adh or nonadherent (*Sus*) conditions for 24 h in the presence or absence of 1 μ g/ml Dox. The p21^{Cip1} mRNA levels were then quantified by real-time RT-PCR as above. A ratio to the control (EGFP, Dox+; Adh) is shown (mean \pm S.D., #, $p < 0.05$). *D*, the pooled cells in *C* were transfected with the pGL4.2/minP (minP) vector and the wild-type WWP 2.0-Sac reporters together with the internal control in the presence or absence of 1 μ g/ml Dox. After 24 h, the cells were transferred to Adh or *Sus* culture and incubated for another 24 h, and the reporter assay was performed as above. The values are ratios to the control (EGFP, minP; Dox+ /Adh) (mean \pm S.D., #, $p < 0.05$). *E*, cells were transfected with siRNA for RUNX1 or control (Scr), and the p21^{Cip1} mRNA levels were quantified by real-time RT-PCR as above. A ratio to the control is shown (mean \pm S.D., #, $p < 0.05$). Each assay was performed in triplicate and repeated at least three times.

the LIM4 domain as essential for the scaffold function of HIC-5 in the transcriptional complex, although precise roles were unexplored, except for its role as an interface for protein oligomerization (15).

A Role of HIC-5 in Tethering KLF4 to the DNA Sites on Anchorage Loss—Because KLF4 and HIC-5 were found to play important roles in p21^{Cip1} up-regulation, we further investi-

gated whether and how KLF4 and HIC-5 cooperated to achieve this function. Because the HIC-5 function targeted the transcriptional activity of the DR region (WWP 2.0-Sac) harboring the KLF4 sites (Fig. 4B), it was highly possible that HIC-5 regulated the behavior of the KLF4 transcription factor at a certain level. Considering the role of HIC-5 as a molecular scaffold for transcriptional machinery (10), HIC-5 may assist KLF4 recruit-

p21^{Cip1} Transactivation on Anchorage Loss

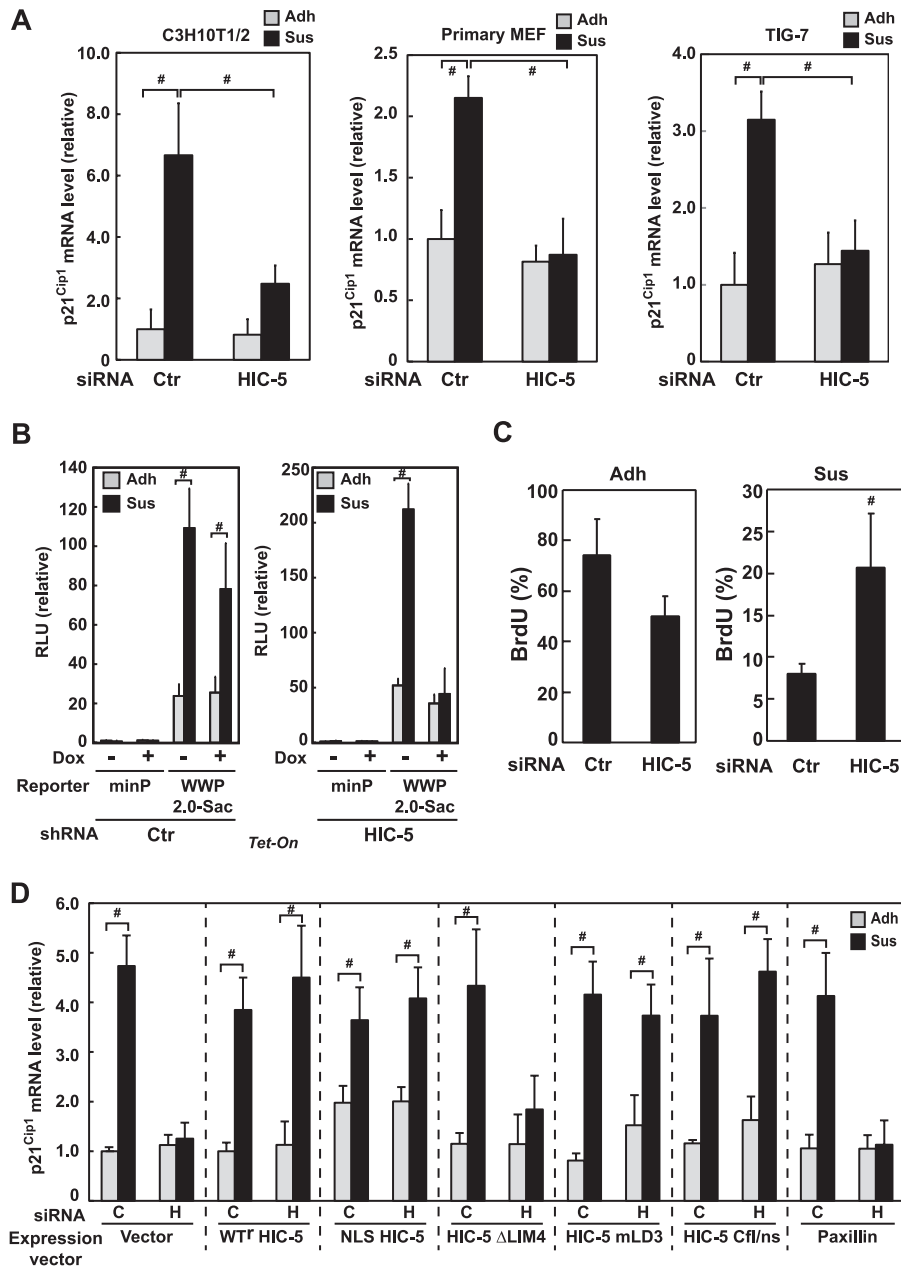


FIGURE 4. Involvement of a molecular scaffold (HIC-5) in p21^{Cip1} transactivation at the DR region. *A*, C3H10T1/2 cells, primary MEFs, and TIG-7 cells were transfected with siRNA for HIC-5 or the negative control (Ctrl) (100 nM) and transferred to culture under adherent (Adh) and nonadherent (Sus) conditions after 48 h. After 24 h of incubation, the p21^{Cip1} mRNA levels were quantified by real-time RT-PCR, and a ratio to the control (Ctrl; Adh) is shown (mean \pm S.D., #, $p < 0.05$). *B*, C3H10T1/2 cells were infected with the lentivirus (Tet-On) encoding HIC-5 shRNA or the negative control (Ctrl), selected, and pooled as described under "Experimental Procedures." Using the resistant pooled cells, reporter activities were assessed in the presence or absence of 1 μ g/ml Dox in the same manner as that shown in Fig. 3*D*. A ratio to the control (Ctrl, minP; Dox-/Adh) is shown (mean \pm S.D., #, $p < 0.05$). *C*, C3H10T1/2 cells transfected with siRNA as in *A* were incubated under Adh or Sus conditions for 16 h, and BrdU incorporation was examined as above. *D*, C3H10T1/2 cells were infected with the retroviral expression vectors; Vector, the empty vector; HIC-5, a siRNA-resistant version of the FLAG-tagged wild-type (WT¹) and that of mutant HIC-5 (NLS, Δ LIM4, mLD3, Cfl/ns); and Paxillin, an HA-tagged paxillin ("Experimental Procedures"). After selection, the pooled cells were transiently transfected with HIC-5 siRNA (H) or the negative control (C). The expression of each exogenous HIC-5 protein under the conditions was examined by immunoblotting as shown in supplemental Fig. S2*C*. Forty-eight hours after siRNA transfection, the cells were cultured under Adh or Sus conditions, and 24 later, the p21^{Cip1} mRNA levels were quantified by real-time RT-PCR. A ratio to the control (Vector, C; Adh) is shown (mean \pm S.D., #, $p < 0.05$). Each assay was performed in triplicate and repeated at least three times.

ment and/or retention in the p21^{Cip1} promoter region of the transcriptional complex. Alternatively, HIC-5 may regulate the KLF4 expression levels by modulating intracellular signaling, thereby affecting p21^{Cip1} expression indirectly.

To examine these possibilities, we first assessed the KLF4 expression levels with or without HIC-5 shRNA expression. As indicated in Fig. 5*A*, KLF4 expression was unaffected by the

HIC-5 levels under these conditions, eliminating the possibility of HIC-5 regulation of the KLF4 expression levels. We next investigated the other possibility. We performed a ChIP assay and evaluated KLF4 binding to the p21^{Cip1} promoter region (Fig. 5*B*), in particular, the DR region, which contained two consensus sequences for KLF4 binding and was crucial for the response (Fig. 3, *A* and *B*). We also assessed binding to the

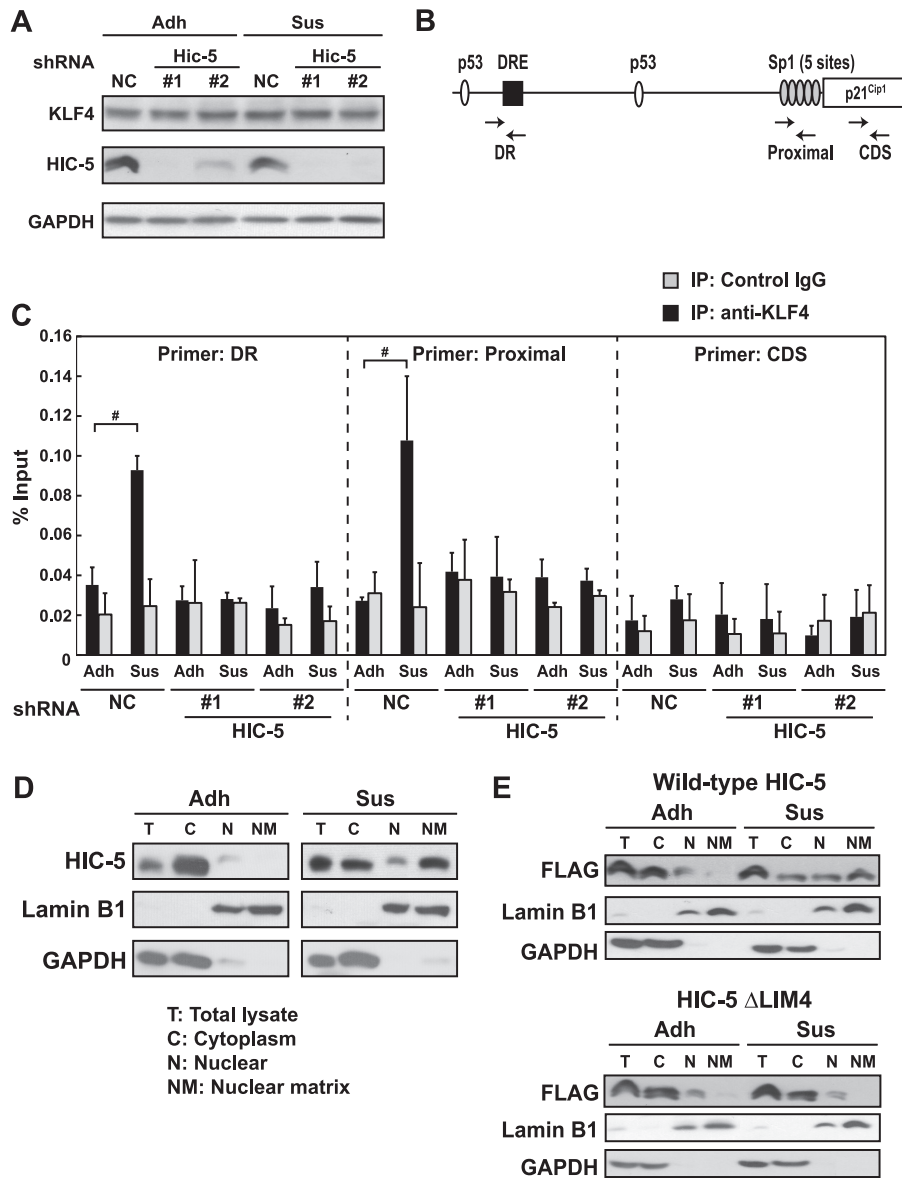


FIGURE 5. Role of HIC-5 in tethering KLF4 to DNA sites. *A*, TIG-7 cells infected with the lentivirus (constitutive) encoding HIC-5 shRNA (#1, #2) or the control (NC) were selected and pooled as described under "Experimental Procedures." After culturing under adherent (*Adh*) or nonadherent (*Sus*) conditions for 24 h, cell lysates were prepared and examined by immunoblotting with the indicated antibodies. GAPDH is shown as a loading control. *B*, the detachment-responsive element (*DRE*) (see text) and Sp1 binding sites in the *p21^{Cip1}* promoter and the primers (*arrows*) used in the ChIP assay are illustrated. *C*, the pooled cells in *A* were cultured under *Adh* and *Sus* conditions for 24 h and lysed after fixation with 1% formaldehyde. The lysates were subjected to ChIP assay as described under "Experimental Procedures" with antiKLF4 antibody or the IgG control. KLF4 binding to the DNA sites was quantified by real-time RT-PCR using specific primers as in *B*. PCR was performed in triplicate, and at least three independent samples were examined. Bars represent averages (%) \pm S.D. normalized to the input. *D*, C3H10T1/2 cells were cultured under *Adh* and *Sus* conditions for 24 h and biochemically fractionated as described under "Experimental Procedures." Fractions were analyzed by immunoblotting with the indicated antibodies. Lamin B1 and GAPDH serve as fractionation monitors as well as loading controls. *E*, C3H10T1/2 cells were infected with the retroviral vectors for the FLAG-tagged wild-type or the LIM4-deleted mutant (Δ LIM4) HIC-5 as described under "Experimental Procedures." After selection, the pooled cells were incubated, fractionated, and analyzed as in *D*.

proximal region encoding a cluster of six GC-rich sequences (Fig. 5*B*, *Proximal*) because the GC-rich sequences, originally identified as Sp1 binding sites (26), were recently shown to serve as KLF4 binding sites (27). The third target was set within the coding region as a negative control (Fig. 5*B*, *CDS*).

Results showed that KLF4 binding to the promoter region was remarkably stimulated by cellular detachment (Fig. 5*C*, NC; *Adh* versus *Sus*). Of note, the response to detachment was completely abolished by HIC-5 shRNA expression, suggesting that HIC-5 played an important role in facilitating KLF4 binding to DNA in nonadherent cells. Binding was increased almost

equally in both DR and proximal regions. Binding enhancement in the proximal region was apparently incompatible with the exclusive dependence of the transcriptional response on the DR region, but not on the proximal region (Fig. 2, *A* and *B*). This inconsistency can be explained by the differences in surrounding sequences of the two regions. The DR region, but not the proximal region, contained the RUNX1 site, another essential element collaborating with the KLF4 sites for the response (Figs. 2, *C* and *D* and 3*B*) in the vicinity of the KLF4 sites. Alternatively, the KLF4 sites in the two regions could be redundant. However, the mutation at the KLF4 site in the DR region sig-

p21^{Cip1} Transactivation on Anchorage Loss

nificantly impaired the WWP full-length reporter response (supplemental Fig. S2E), making the possibility unlikely.

Next, we investigated the mechanism underlying the HIC-5 function of tethering KLF4 to the sites. A clue was obtained when examining cellular HIC-5 localization through biochemical fractionation. In adherent cells, HIC-5 was mostly present in the cytoplasm, as expected from its primary localization at focal adhesions (Fig. 5D, *Adh*). Intriguingly, in nonadherent cells, a significant population changed its localization to the nucleus, specifically to the matrix fraction (Fig. 5D, *Sus*). In case of the functionally defective Δ LIM4 mutant (Fig. 4D), however, the protein largely remained in the cytoplasm even under *Sus* conditions with a little increase in the nuclear matrix (Fig. 5E), indicating that the nuclear matrix localization of HIC-5 in response to detachment was mediated by LIM4. More importantly, it suggests that the HIC-5 function in the nuclei of nonadherent cells is based on its nuclear matrix localization.

Negative Regulation at the RUNX1 Site Is Potentially Mediated by a LIM-only Protein, CRP2—Along with the KLF4 sites, the RUNX1 site also appears to play a role in stimulating p21^{Cip1} transcription on anchorage loss, whereas the site is simultaneously involved in suppressing basal level transcription under *Adh* conditions (Fig. 3B), although the two roles may be closely related to each other (see “Discussion”). With regard to suppression of basal transcription, we found that CRP2, a partner of HIC-5 hetero-oligomerization (28), had a negative effect on p21^{Cip1} basal transcription. As shown in Fig. 6, A and B, a decrease in CRP2 expression by shRNA (Tet-Off) increased the mRNA and reporter activity of p21^{Cip1} in adherent cells, potentially implicating CRP2 in negative regulation at the RUNX1 site. In support of this assumption, we found that increased p21^{Cip1} transcription under CRP2 knockdown (Fig. 6B, shCRP2#1, #2; WT/Dox+ versus –) was compromised when the RUNX1 site was mutated (Fig. 6B, shCRP2#1, #2; mtRUNX1/Dox+ versus –), whereas that at the KLF4 sites did not interfere with CRP2 knockdown effects (Fig. 6C). These results suggest that CRP2 mediates negative regulation of basal transcription at the RUNX1 site under *Adh* conditions and that the KLF4 sites appeared to be unrelated to this regulation as illustrated in Fig. 7A (Adhesion).

DISCUSSION

DR Element (DRE) Identified in the p21^{Cip1} Promoter Region—A line of evidence has shown that cellular detachment from ECM activates transcriptional responses, some of which are engaged in subsequent growth arrest or cell death (29, 30). However, detailed mechanisms underlying the responses remain largely unknown. In the present study, we examined p21^{Cip1} transcriptional up-regulation in cells deprived of ECM attachment and first identified the upstream regulatory region (designated as DR) that mediated the transcriptional response to disruption of cell-ECM interactions. The DR region contains the KLF4 and RUNX1 sites in close proximity, both of which are necessary for the response but are individually insufficient (Fig. 2, C and D) and believed to constitute a “DRE” together. A similar disposition of the RUNX1 and KLF4 sites is found downstream of the p53 binding site in murine p21^{Cip1} genomes (Fig. 7B), suggesting the evolutionary conservation of DRE

across the species. It is also interesting to note that among the tested transcriptional targets of KLF4 (31), half (4/8) responded to loss of anchorage (data not shown).

In our study, p53 involvement was consistently unlikely (supplemental Fig. S1 and Fig. 2) and seemingly contradictory to a previous report (22) in which the authors reached their conclusion largely on the basis of p53-null cell responses. Given the requirement of p53 for the basal transcriptional activity of p21^{Cip1} (32, 33) (supplemental Fig. S1), complete elimination of p53 possibly deprives cells of the fundamental transcriptional potential undermining response induction. Another concern was the possibility that the KLF4 and RUNX1 sites immediately adjacent to the p53 site were deleted together with the p53 site in their mutant reporter that lost the response. A lack of detailed information on the constructs hampered further discussion.

A DR Transcriptional Mechanism Directed by a Molecular Scaffold, HIC-5—The most prominent finding of the present study was a novel mechanism regulating transcription in a detachment-dependent manner with the aid of a molecular scaffold, HIC-5. HIC-5 assists in recruitment and/or retention of transcription factors at a given DNA site in response to cellular detachment. In mechanistic detail, the pivot is the LIM4 domain, a mutant of which lost the potential to stimulate p21^{Cip1} transcription concomitantly with the loss of oligomerization abilities and nuclear matrix localization (10) (Figs. 4D and 5E). Likewise, paxillin, despite high homology to HIC-5, did not stimulate p21^{Cip1} transcription (10) and exhibited neither oligomerization (15) nor nuclear matrix localization (data not shown). This fact provides another instance correlating the HIC-5 function as a scaffold with inherent oligomerization and nuclear matrix localization properties, and along with the case of the LIM4 mutant, strongly supports the hypothesis that HIC-5 oligomerizes and consequently localizes to the nuclear matrix, thereby achieving its function. Accordingly, the primary force driving the system is hypothetically HIC-5 oligomerization in response to anchorage loss. In general, protein oligomerization is promoted by an increase in protein concentration. In case of HIC-5, anchorage loss triggers spontaneous nuclear accumulation of the protein, *i.e.* an increase in concentration in the nucleus, because of NES inactivation (12). Such conditions expectedly accelerate oligomerization and consequently, nuclear matrix localization of HIC-5, which in turn, presumably stabilizes its scaffold architecture and the transcriptional complex including KLF4 on DNA. Because HIC-5 and KLF4 did not appear to make direct contact (data not shown), the transcriptional complex is believed to include additional factors such as nuclear matrix components. Clarification of this transcriptional complex entity is necessary to elucidate this mechanism completely.

In addition, the present study revealed a novel aspect of p21^{Cip1} transcriptional regulation, which operated at the RUNX1 site in the DR region to repress basal transcription under *Adh* conditions (Fig. 3B). CRP2 was identified as a candidate repression regulator (Fig. 6, A and B), although its precise role remains unclear. Because p21^{Cip1} basal level transcription was unaffected by HIC-5 knockdown (Fig. 4, A and B) and similarly by KLF4 knockdown (Fig. 3, C and D) and mutation at

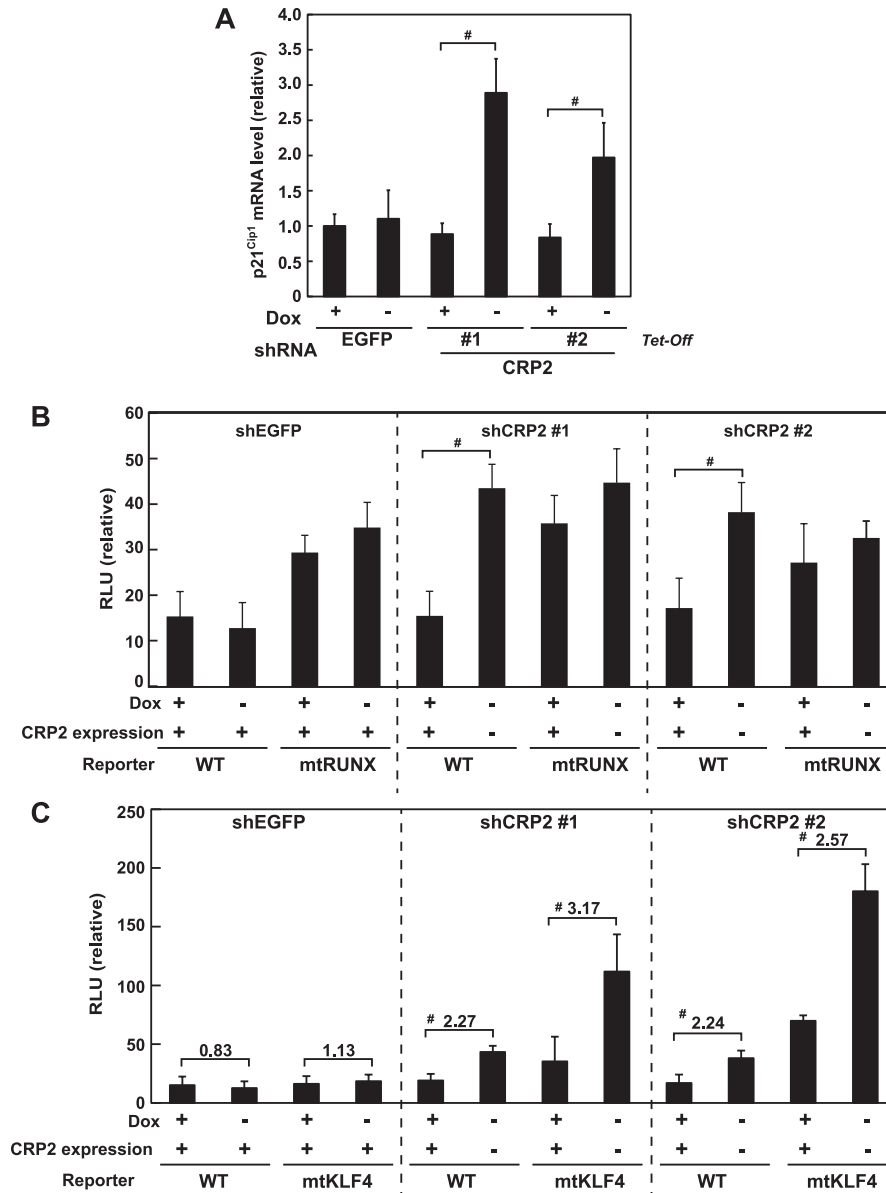


FIGURE 6. Negative regulation at the RUNX1 site by the LIM-only protein CRP2. *A*, primary MEFs were infected with the lentivirus (*Tet-Off*) encoding shRNA against CRP2 (#1, #2) or EGFP (a control). After selection, the cells were pooled and cultured for 48 h in the presence or absence of 1 μ g/ml Dox as above. The p21^{Cip1} mRNA levels were quantified by real-time RT-PCR. The values (mean \pm S.D.) are relative to the control (EGFP, Dox+). *B*, the cells obtained in *A* were transiently transfected with the wild-type (WT) or the RUNX1 mutant (mtRUNX1) WWP 2.0-Sac reporter plasmid (Fig. 3A) together with the internal control in the presence or absence of 1 μ g/ml Dox. After 24 h, reporter activities were measured and graphed as above. The values (mean \pm S.D.) are relative to the control (shEGFP, WT; Dox+) (#, $p < 0.05$). The status of CRP2 expression under Dox \pm conditions is shown below the graph. *C*, the cells obtained in *A* were transiently transfected with WT or the KLF4 mt2 mutant (mtKLF4) WWP 2.0-Sac reporter plasmid (Fig. 3A), and reporter activities were examined as in *B* (#, $p < 0.05$). Each assay was performed in triplicate and repeated at least three times.

the KLF4 sites (Fig. 3B), neither HIC-5 nor KLF4 were likely related to negative regulation at the RUNX1 site under Adh conditions. Rather, in response to detachment, HIC-5 and KLF4 are recruited to the KLF4 sites and may function to eliminate the negative effect on the adjacent RUNX1 site, thereby stimulating DRE transcriptional activity under the conditions (Fig. 7A).

In conclusion, HIC-5 has emerged as a novel molecular adaptor directly coupling the cellular adhesion status to transcription and eventually contributing to anchorage dependence of cell growth. Together with the previous study (12), a molecular function of HIC-5 could be summarized as a bimodal organizer

of a fail-safe system simultaneously targeting two crucial cell-cycle regulators, cyclin D1 and p21^{Cip1}. Such a protective system is pivotal for homeostasis of multicellular organisms. Even under physiological conditions, for instance, when cells move toward a chemoattractant or enter the mitotic phase, cells undergo regional or global provisional loss of ECM contact. Under pathophysiological circumstances such as postinflammatory scarring, cells are inevitably exposed to dynamic changes in surrounding ECM compositions. Therefore, an increased understanding of cellular behaviors upon interference with proper ECM attachment and of underlying mechanisms is not only important in a biological sense but also essen-

p21^{Cip1} Transactivation on Anchorage Loss

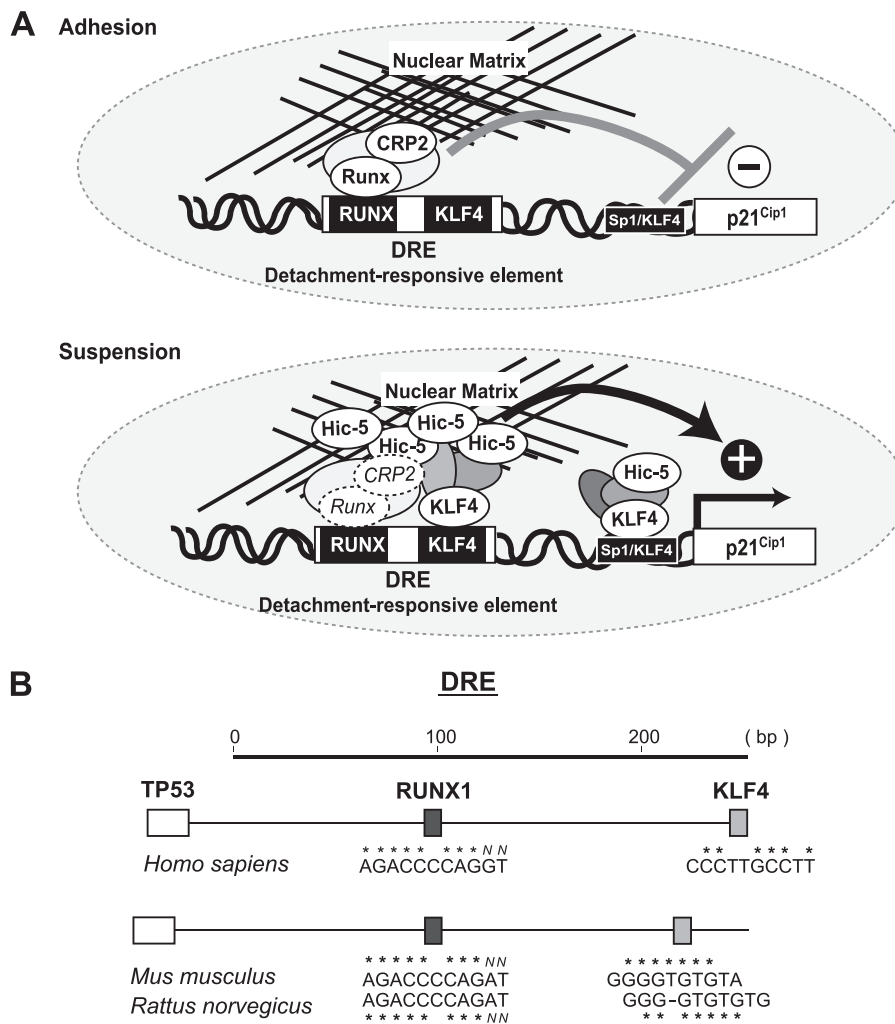


FIGURE 7. Transcriptional mechanism regulating p21^{Cip1} expression in a detachment-dependent manner (hypothesis). *A*, under normal adherent conditions, p21^{Cip1} transcription is suppressed through the RUNX1 site by a mechanism involving CRP2. On anchorage loss, a transcriptional complex is assembled at the KLF4 sites adjacent to the RUNX1 site with the aid of HIC-5, which possibly releases negative regulation at the RUNX1 site, thereby stimulating transcription (see text). *B*, the core elements of the DRE, RUNX1, and KLF4 sites are conserved among humans, mice, and rats, and they are similarly positioned in the corresponding upstream regions of the p21^{Cip1} genes. The nucleotides identical to the consensus (The JASPAR database) are marked with asterisks. N stands for any nucleotide.

tial for therapeutic development for these pathological conditions. HIC-5 could be a key modulator of cellular behavior under such pathophysiological circumstances.

Acknowledgments—We thank Ms. Mizote for construction of the shRNA expression vectors for HIC-5 and Mr. Asakawa for contributing to the study of HIC-5 localization to the nuclear matrix.

REFERENCES

- Chiarugi, P., and Giannoni, E. (2008) Anoikis: a necessary death program for anchorage-dependent cells. *Biochem. Pharmacol.* **76**, 1352–1364
- Reddig, P. J., and Juliano, R. L. (2005) Clinging to life: cell to matrix adhesion and cell survival. *Cancer Metastasis Rev.* **24**, 425–439
- van der Flier, A., and Sonnenberg, A. (2001) Function and interactions of integrins. *Cell Tissue Res.* **305**, 285–298
- Schwartz, M. A. (1997) Integrins, oncogenes, and anchorage independence. *J. Cell Biol.* **139**, 575–578
- Giancotti, F. G. (1997) Integrin signaling: specificity and control of cell survival and cell cycle progression. *Curr. Opin. Cell Biol.* **9**, 691–700
- Kumar, C. C. (1998) Signaling by integrin receptors. *Oncogene* **17**, 1365–1373
- Assoian, R. K. (1997) Anchorage-dependent cell cycle progression. *J. Cell Biol.* **136**, 1–4
- Matsuya, M., Sasaki, H., Aoto, H., Mitaka, T., Nagura, K., Ohba, T., Ishino, M., Takahashi, S., Suzuki, R., and Sasaki, T. (1998) Cell adhesion kinase β forms a complex with a new member, Hic-5, of proteins localized at focal adhesions. *J. Biol. Chem.* **273**, 1003–1014
- Nishiya, N., Tachibana, K., Shibanuma, M., Mashimo, J. I., and Nose, K. (2001) Hic-5-reduced cell spreading on fibronectin: competitive effects between paxillin and Hic-5 through interaction with focal adhesion kinase. *Mol. Cell Biol.* **21**, 5332–5345
- Shibanuma, M., Kim-Kaneyama, J. R., Sato, S., and Nose, K. (2004) A LIM protein, Hic-5, functions as a potential coactivator for Sp1. *J. Cell Biochem.* **91**, 633–645
- Shibanuma, M., Kim-Kaneyama, J. R., Ishino, K., Sakamoto, N., Hishiki, T., Yamaguchi, K., Mori, K., Mashimo, J., and Nose, K. (2003) Hic-5 communicates between focal adhesions and the nucleus through oxidant-sensitive nuclear export signal. *Mol. Biol. Cell* **14**, 1158–1171
- Mori, K., Hirao, E., Toya, Y., Oshima, Y., Ishikawa, F., Nose, K., and Shibanuma, M. (2009) Competitive nuclear export of cyclin D1 and Hic-5 regulates anchorage dependence of cell growth and survival. *Mol. Biol. Cell* **20**, 218–232
- Suga, H., Kadoshima, T., Minaguchi, M., Ohgushi, M., Soen, M., Nakano, T., Takata, N., Wataya, T., Muguruma, K., Miyoshi, H., Yonemura, S.,

- Oiso, Y., and Sasai, Y. (2011) Self-formation of functional adenyphophysis in three-dimensional culture. *Nature* **480**, 57–62
14. Kitamura, T., Koshino, Y., Shibata, F., Oki, T., Nakajima, H., Nosaka, T., and Kumagai, H. (2003) Retrovirus-mediated gene transfer and expression cloning: powerful tools in functional genomics. *Exp. Hematol.* **31**, 1007–1014
 15. Mori, K., Asakawa, M., Hayashi, M., Imura, M., Ohki, T., Hirao, E., Kim-Kaneyama, J. R., Nose, K., and Shibamura, M. (2006) Oligomerizing potential of a focal adhesion LIM protein Hic-5 organizing a nuclear-cytoplasmic shuttling complex. *J. Biol. Chem.* **281**, 22048–22061
 16. Ishikawa, F., Akimoto, T., Yamamoto, H., Araki, Y., Yoshie, T., Mori, K., Hayashi, H., Nose, K., and Shibamura, M. (2009) Gene expression profiling identifies a role for CHOP during inhibition of the mitochondrial respiratory chain. *J. Biochem.* **146**, 123–132
 17. Kanome, T., Itoh, N., Ishikawa, F., Mori, K., Kim-Kaneyama, J. R., Nose, K., and Shibamura, M. (2007) Characterization of Jumping translocation breakpoint (JTB) gene product isolated as a TGF- β 1-inducible clone involved in regulation of mitochondrial function, cell growth and cell death. *Oncogene* **26**, 5991–6001
 18. Egawa, K., Nishigori, H., Kunimoto, S., Takeuchi, T., and Nose, K. (1998) Identification of active substances from *Streptomyces* culture fluids using p53-independent expression of p21/WAF1/Cip1 gene and their mode of action. *Biol. Pharm. Bull.* **21**, 899–904
 19. Ishikawa, F., Miyoshi, H., Nose, K., and Shibamura, M. (2010) Transcriptional induction of MMP-10 by TGF- β , mediated by activation of MEF2A and downregulation of class IIa HDACs. *Oncogene* **29**, 909–919
 20. Nelson, J. D., Denisenko, O., and Bomsztyk, K. (2006) Protocol for the fast chromatin immunoprecipitation (ChIP) method. *Nat. Protoc.* **1**, 179–185
 21. He, D. C., Nickerson, J. A., and Penman, S. (1990) Core filaments of the nuclear matrix. *J. Cell Biol.* **110**, 569–580
 22. Wu, R. C., and Schönthal, A. H. (1997) Activation of p53-p21waf1 pathway in response to disruption of cell-matrix interactions. *J. Biol. Chem.* **272**, 29091–29098
 23. Fang, F., Orend, G., Watanabe, N., Hunter, T., and Ruoslahti, E. (1996) Dependence of cyclin E-CDK2 kinase activity on cell anchorage. *Science* **271**, 499–502
 24. Sherr, C. J., and Roberts, J. M. (1999) CDK inhibitors: positive and negative regulators of G1-phase progression. *Genes Dev.* **13**, 1501–1512
 25. el-Deiry, W. S., Tokino, T., Velculescu, V. E., Levy, D. B., Parsons, R., Trent, J. M., Lin, D., Mercer, W. E., Kinzler, K. W., and Vogelstein, B. (1993) WAF1, a potential mediator of p53 tumor suppression. *Cell* **75**, 817–825
 26. Nakano, K., Mizuno, T., Sowa, Y., Orita, T., Yoshino, T., Okuyama, Y., Fujita, T., Ohtani-Fujita, N., Matsukawa, Y., Tokino, T., Yamagishi, H., Oka, T., Nomura, H., and Sakai, T. (1997) Butyrate activates the WAF1/Cip1 gene promoter through Sp1 sites in a p53-negative human colon cancer cell line. *J. Biol. Chem.* **272**, 22199–22206
 27. Chew, Y. C., Adhikary, G., Wilson, G. M., Reece, E. A., and Eckert, R. L. (2011) Protein kinase C (PKC) delta suppresses keratinocyte proliferation by increasing p21(Cip1) level by a KLF4 transcription factor-dependent mechanism. *J. Biol. Chem.* **286**, 28772–28782
 28. Kim-Kaneyama, J. R., Suzuki, W., Ichikawa, K., Ohki, T., Kohno, Y., Sata, M., Nose, K., and Shibamura, M. (2005) Uni-axial stretching regulates intracellular localization of Hic-5 expressed in smooth-muscle cells in vivo. *J. Cell Sci.* **118**, 937–949
 29. Liu, Z., Li, H., Wu, X., Yoo, B. H., Yan, S. R., Stadnyk, A. W., Sasazuki, T., Shirasawa, S., LaCasse, E. C., Korneluk, R. G., and Rosen, K. V. (2006) Detachment-induced upregulation of XIAP and cIAP2 delays anoikis of intestinal epithelial cells. *Oncogene* **25**, 7680–7690
 30. Yan, S. R., Joseph, R. R., Rosen, K., Reginato, M. J., Jackson, A., Allaire, N., Brugge, J. S., Jobin, C., and Stadnyk, A. W. (2005) Activation of NF- κ B following detachment delays apoptosis in intestinal epithelial cells. *Oncogene* **24**, 6482–6491
 31. Rowland, B. D., and Peeper, D. S. (2006) KLF4, p21 and context-dependent opposing forces in cancer. *Nature Reviews. Cancer* **6**, 11–23
 32. el-Deiry, W. S., Harper, J. W., O'Connor, P. M., Velculescu, V. E., Canman, C. E., Jackman, J., Pietenpol, J. A., Burrell, M., Hill, D. E., and Wang, Y. (1994) WAF1/CIP1 is induced in p53-mediated G1 arrest and apoptosis. *Cancer Res.* **54**, 1169–1174
 33. Weinberg, W. C., Azzoli, C. G., Kadiwar, N., and Yuspa, S. H. (1994) p53 gene dosage modifies growth and malignant progression of keratinocytes expressing the v-rasHa oncogene. *Cancer Res.* **54**, 5584–5592

Critical roles of the cAMP-responsive element-binding protein-mediated pathway in disorganized epithelial phenotypes caused by mitochondrial dysfunction

Motoko Shibamura,^{1,3} Fumihiko Ishikawa,¹ Masayuki Kobayashi,¹ Kazufumi Katayama,² Hiroyuki Miyoshi,² Masami Wakamatsu,¹ Kazunori Mori¹ and Kiyoshi Nose¹

¹Department of Cancer Cell Biology, Showa University School of Pharmacy, Tokyo; ²Subteam for Manipulation of Cell Fate, RIKEN BioResource Center, Tsukuba, Japan

(Received February 1, 2012/Revised June 7, 2012/Accepted June 20, 2012/Accepted manuscript online June 24, 2012/Article first published online August 1, 2012)

In most human cancers, somatic mutations have been identified in the mtDNA; however, their significance remains unclear. We recently discovered that NMuMG mouse mammary epithelial cells, when deprived of mitochondria or following inhibition of respiratory activity, undergo epithelial morphological disruption accompanied with irregular edging of E-cadherin, the appearance of actin stress fibers, and an altered gene expression profile. In this study, using the mtDNA-less pseudo $\rho 0$ cells obtained from NMuMG mouse mammary epithelial cells, we examined the roles of two mitochondrial stress-associated transcription factors, cAMP-responsive element-binding protein (CREB) and C/EBP homologous protein-10 (CHOP), in the disorganization of epithelial phenotypes. We found that the expression of matrix metalloproteinase-13 and that of GADD45A, SNAIL and integrin $\alpha 1$ in the $\rho 0$ cells were regulated by CHOP and CREB, respectively. Of note, knockdown and pharmacological inhibition of CREB ameliorated the disrupted epithelial morphology. It is interesting to note that the expression of high mobility group AT-hook 2 (HMGA2), a non-histone chromatin protein implicated in malignant neoplasms, was increased at the protein level through the CREB pathway. Here, we reveal how the activation of the CREB/HMGA2 pathway is implicated in the repression of integrin $\alpha 1$ expression in HepG2 human cancer cells, highlighting the importance of the CREB/HMGA2 pathway in malignant transformation associated with mitochondrial dysfunction, thereby raising the possibility that the pathway indirectly interferes with the cell-cell adhesion structure by influencing the cell-extracellular matrix adhesion status. Overall, the data suggest that mitochondrial dysfunction potentially contributes to neoplastic transformation of epithelial cells through the activation of these transcriptional pathways. (*Cancer Sci* 2012; 103: 1803–1810)

Over the past decades, a range of somatic mutations and depletions have been identified in the mtDNA in most primary human cancers.^(1–3) However, the relationship between mtDNA instability and neoplastic cell development remains unclear. Recent studies with regard to mtDNA heteroplasmy in cancers have suggested that somatic mutations in mtDNA are enriched during tumorigenic processes, implying that they confer a selective advantage for the survival and growth of pre-neoplastic cells.^(4–6) In other studies, several mutations in the mtDNA regions encoding polypeptides for the respiration and oxidative phosphorylation chain have been suggested to actively contribute to tumor progression and metastasis.^(7,8) It is noteworthy that all such mutations are associated with increased levels of reactive oxygen species (ROS), suggesting

the involvement of ROS in the development of malignant phenotypes.

Somatic mutations in mtDNA are found not only in the protein-coding regions but also in the non-coding regions. In human tumors, point mutations are frequently observed (39.7% of the cancerous tissues examined) in the D-loop (non-coding) region.⁽³⁾ Mutations in this region, which contains the important regulatory sequences for transcription and replication initiation, hypothetically affect the copy number and/or gene expression of the mitochondrial genome. One study supporting this assumption reports a decrease in mtDNA copy number in 17 hepatocellular carcinoma (HCC) cases out of 24 cases with somatic mutation(s) in the D-loop region.⁽⁹⁾ Of note, instability in the mtDNA D-loop region leading to decreased copy number has been suggested to be involved in human carcinogenesis.⁽³⁾ In most cases of HCC and gastric cancers, carcinogenesis is accompanied with an alteration in mitochondrial biogenesis and a repression of mtDNA replication.^(3,10,11) However, the effects of repression of mitochondrial biogenesis on tumorigenesis are poorly understood. The involvement of ROS in these processes remains an open question.

The present study examines the impact of decreased mitochondrial function on epithelial phenotypes associated with malignant transformations. We used the mtDNA-less pseudo $\rho 0$ cells with decreased mitochondrial function. The $\rho 0$ state was attained by inhibiting mtDNA replication and transcription using ethidium bromide (EtBr) rather than by D-loop mutations interfering with mtDNA replication and transcription.⁽¹²⁾ We obtained the $\rho 0$ cells from NMuMG mouse mammary epithelial cells (NMuMG cells) and assessed their morphology and gene expression. In the $\rho 0$ state, the typical cobblestone-like epithelial morphology was disrupted, resulting in irregular cell-cell junctions. We also observed some alterations in gene expression, including alterations in integrin $\alpha 1$ (ITGA1) expression. In conclusion, we demonstrated the importance of the two mitochondrial stress-associated transcription factors, particularly that of cAMP-responsive element-binding protein (CREB), in the disorganization of epithelial morphology.

Materials and Methods

Cell culture, $\rho 0$ cell preparation and chemicals. NMuMG mouse mammary epithelial cells were obtained and maintained as described previously.⁽¹³⁾ $\rho 0$ cells were obtained by culturing

³To whom correspondence should be addressed.
E-mail: smotoko@pharm.showa-u.ac.jp

in a normal medium containing 250 ng/mL EtBr and 50 μ g/mL uridine for 4–6 days.⁽¹²⁾

A panel of human cancer cell lines was maintained in DMEM (MCF-7, A549, MDA-MB-231, HepG2, HOS, MIA-Paca-2, Colo205 and EJ-1), F-12 (Hela S3) and RPMI1640 (Lu65) supplemented with 10% FCS. A set of HCC cell lines was obtained from the Japanese Collection of Research Bioresources Bank (Osaka, Japan), and cultured in accordance with the accompanying instructions.

CREB–CREB binding protein (CBP) interaction inhibitor [N-(4-chlorophenyl)-3-hydroxy-2-naphthamide] was purchased from Merck KGaA (Darmstadt, Germany). Protein kinase inhibitors were obtained from Merck KGaA, except for H-89 and LY294002, which were purchased from Sigma (St Louis, MO, USA) and LC Laboratories (Woburn, MA, USA), respectively.

Expression of shRNA. shRNA was expressed using a lentivirus vector, CS-RfA-ErTbsd, based on the CS-RfA-ETBsd plasmid and modified to include the Tet-Off system.⁽¹⁴⁾ HEK293T cells were transfected with lentivirus vectors by the calcium phosphate method to obtain culture supernatants containing the lentivirus. Target cells were infected with the virus by culturing these in virus-containing medium for 24 h. After another 24-h incubation in the presence of doxycycline (Dox, 500 ng/mL), infected cells were selected and maintained in medium containing 10 μ g/mL blasticidin for 2 days.

Antibodies and western blotting. Western blotting was performed as described previously.⁽¹⁵⁾ We used monoclonal antibodies to E-cadherin, β -catenin, p120 (BD Transduction Laboratories, Lexington, KY, USA), GAPDH (Chemicon, Temecula, CA, USA), C/EBP homologous protein-10 or CHOP-10 (GADD 153; Santa Cruz Biotechnology, Santa Cruz, CA, USA), and CREB (48H2; Cell Signaling, Beverly, MA,

USA). Polyclonal antibodies included ZO-1 (Zymed Laboratories, San Francisco, CA, USA), phosphor-CREB (Ser133; Cell Signaling), high mobility group AT-hook 2 (HMGA2) (R&D Systems, Minneapolis, MN, USA) and HMGA1 (Santa Cruz Biotechnology).

Real-time RT-PCR. Total RNA was extracted, and cDNA was synthesized and analyzed using methods described previously.⁽¹⁶⁾ The assay was performed in triplicate, and at least three independent samples were analyzed.

Attachment assay. Cells were washed, dissociated with trypsin, resuspended in the assay buffer (DMEM supplemented with 0.1% BSA), plated onto ECM-coated wells and incubated for 20 min at 37°C. After 20–90 min, the cells were washed, fixed with 3.7% formalin, and stained with 0.5% crystal violet. An image of each well was acquired, and the number of cells was counted. The experiments were performed in triplicate and were repeated five times.

Results

Disorganized epithelial morphology in ρ 0 cells. We treated NMuMG cells with EtBr for 4–6 days to obtain the ρ 0 cells, as described previously.⁽¹²⁾ Interestingly, the cells were slowly flattened, and this was accompanied with obscure and disarranged cell–cell junctions concomitant with deterioration in mitochondrial activity (Fig. 1a). In particular, the cells exhibited irregular edging of E-cadherin, and actin stress fibers were present in their cytoplasm (Fig. 1b,c). Pharmacological inhibition of respiratory activity caused a similar morphological change (Fig. S1), suggesting that interference with respiratory chain activity was the primary cause of disorganization at the cell–cell junctions. Expression levels of the cell–cell junction proteins, such as E-cadherin and ZO-1, were only marginally

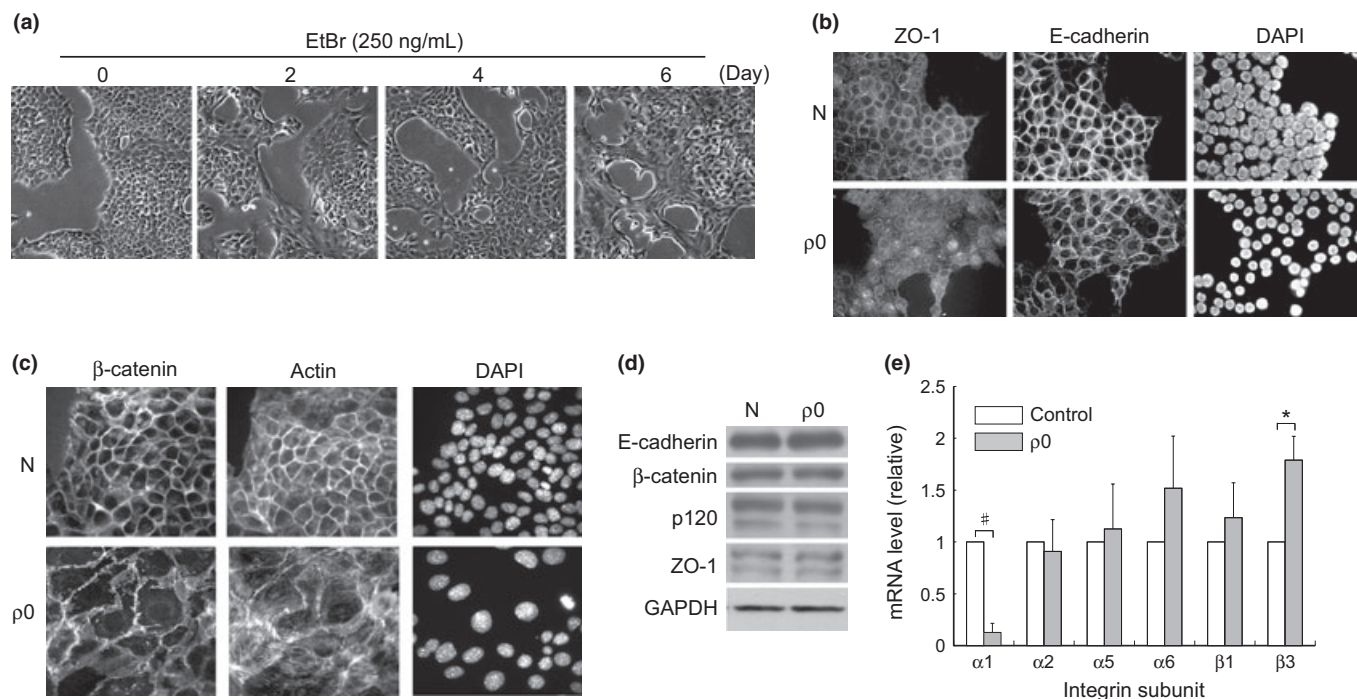


Fig. 1. Disorganized epithelial morphology in the ρ 0 cells. (a) NMuMG cells were treated with EtBr (250 ng/mL) for the indicated periods and observed by phase contrast microscopy. (b),(c) Treated cells were examined by indirect immunofluorescence labeling using specific antibodies. Actin fibers were stained with fluorescence-labeled phalloidin and the nuclei with DAPI. N: Control. ρ 0: 6-day treatment with EtBr. (d) Cell lysate was examined by immunoblotting with the antibodies as indicated. GAPDH was used as the loading control. (e) Total RNA was extracted and analyzed by real-time RT-PCR, as described in the Materials and Methods section. The PCR products derived from each mRNA were normalized to that derived from GAPDH in the same sample and are shown as a ratio relative to the control. The difference in ITGA1 expression in control and ρ 0 samples was assessed by *t*-test. # $P < 2 \times 10^{-6}$, * $P < 0.05$.

affected (Fig. 1d), whereas expression patterns of integrins (a group of cell-ECM receptors) were changed (Fig. 1e). In particular, ITGA1 mRNA expression was significantly repressed in the $\rho 0$ cells (Fig. 1e). As described previously,⁽¹²⁾ levels of intracellular ROS were reduced along with the membrane potential in the $\rho 0$ cells, suggesting that the involvement of ROS in the above changes was unlikely.

Upregulation of C/EBP homologous protein-10 and cAMP-responsive element-binding protein and their roles in the phenotypic disruption of $\rho 0$ cells. We recently found a stress-inducible transcription factor, CHOP, induced in murine myofibroblasts under conditions of mitochondrial dysfunction.⁽¹⁶⁾ Similarly, we found that CHOP expression was induced at the mRNA and protein levels in the NMuMG $\rho 0$ cells (Figs S2,2a). Under the same conditions, CREB, which has been identified as a mitochondrial stress mediator in sarcoma cell lines,⁽¹⁷⁾ was either activated or heavily phosphorylated at Ser133 (Fig. 2b). In the current study, we assessed the roles of two transcription factors, CREB and CHOP, in epithelial cells under mitochondrial stress, focusing on their roles associated with morphological disruption.

We established a cell line in which the expression of each transcription factor was inhibited by shRNA (using the Tet-Off system) and observed the cellular responses following mitochondrial dysfunction. The knockdown effects of shRNA are shown in Supplementary Figure S2 (mRNA) and in Figure 2(a,c) (protein). We first studied the involvement of CREB and CHOP in gene expression in the $\rho 0$ state, and found that induction of matrix metalloproteinase-13 and GADD45A under mitochondrial stress was attenuated by the shRNA for CHOP and CREB, respectively (Fig. 2d).⁽¹⁶⁾ Of note, we observed a recovery of clear cell-cell junctions in the $\rho 0$ cells after the knockdown of CREB (Fig. 3a). In parallel, the delocalization of E-cadherin and ZO-1 was alleviated under the same conditions (Fig. 3b). A low molecular weight

chemical, designated CCI, interfered with the CREB-CBP interactions and was also effective in repressing the morphological disruption (Fig. 3c), thereby supporting the important role of CREB in this process. CREB was also implicated in regulating the expression of ITGA1 and zinc finger transcription factors, SNAIL and ZEB2, under conditions of mitochondrial dysfunction. In the CREB-knockdown $\rho 0$ cells, the originally downregulated ITGA1 expression was increased, whereas upregulated SNAIL and ZEB2 expression was decreased (Fig. 3d). These results suggest that CHOP and CREB have important functions in stress response signaling under mitochondrial dysfunction. In particular, CREB is likely to be implicated in the disruption of epithelial morphology.

High mobility group AT-hook 2 as a downstream mediator in the cAMP-responsive element-binding pathway. To obtain insight into the mechanisms underlying the diverse effects of the CREB pathway ranging from gene expression to cellular morphology, we focused on HMGA2. HMGA2, a non-histone nuclear protein with DNA binding ability, alters chromatin structure and/or interacts with several transcription factors, thereby regulating a wide range of transcriptions.^(18,19) Our previous microarray analysis results (data not included) suggested that this protein is activated in the $\rho 0$ cells. Indeed, as indicated in Figure 4(a), the protein level of HMGA2 in the $\rho 0$ cells was elevated to the same extent as in the cells treated with transforming growth factor (TGF)- β , a well-known inducer of HMGA2. Of note, HMGA2 expression was mitigated by the shRNA for CREB, suggesting that HMGA2 was upregulated downstream in the CREB pathway. The effect of the shRNA was specific to the $\rho 0$ state as the induction by TGF- β was unaffected (Fig. 4a). CCI treatment also alleviated the induction of HMGA2 protein expression in the $\rho 0$ cells (Fig. 4b), further supporting the important role of CREB in this process. Given that only marginal changes were observed in the mRNA levels (Fig. S3), we suggest that CREB may

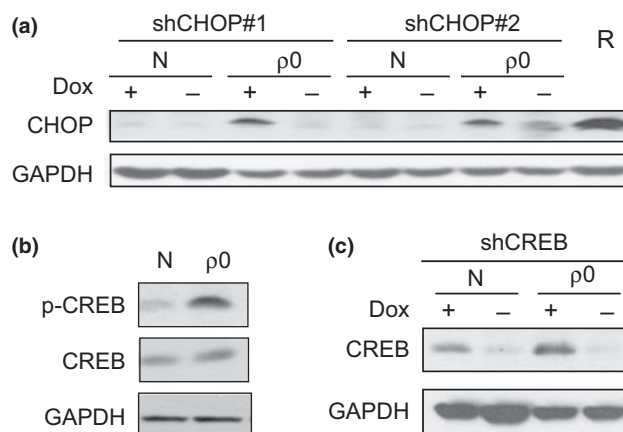
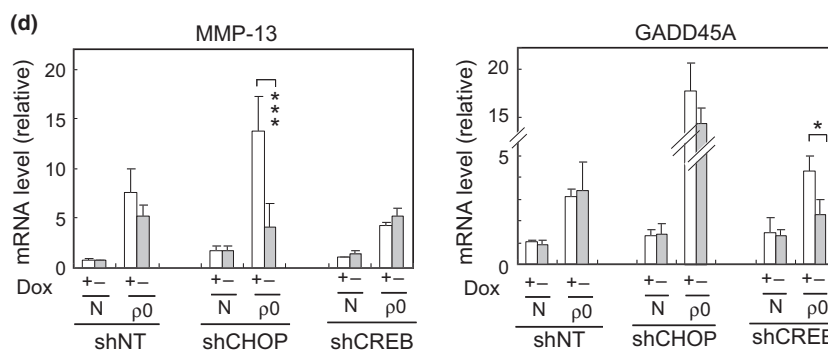


Fig. 2. Upregulation of cAMP-responsive element-binding protein (CREB) and C/EBP homologous protein-10 (CHOP) and their roles in gene expression. (a-d) Cell lysates from control (N) and EtBr-treated cells ($\rho 0$) (as shown in Fig. 1) with (Dox-) or without (Dox+) expression of shRNA for CHOP and CREB were subjected to immunoblotting using specific antibodies. shRNA was expressed by removal of Dox (0.5 μ g/mL) from the culture medium for 48 h. R is a positive control for CHOP induction, exposed to rotenone (1 μ M). In (d), total RNA extracted under the same conditions was analyzed by real-time RT-PCR. A ratio relative to the control (Dox+ sample of the control) is shown. shNT: negative control for shRNA (sequence was not found in mammals). * $P < 0.05$, *** $P < 0.0005$.



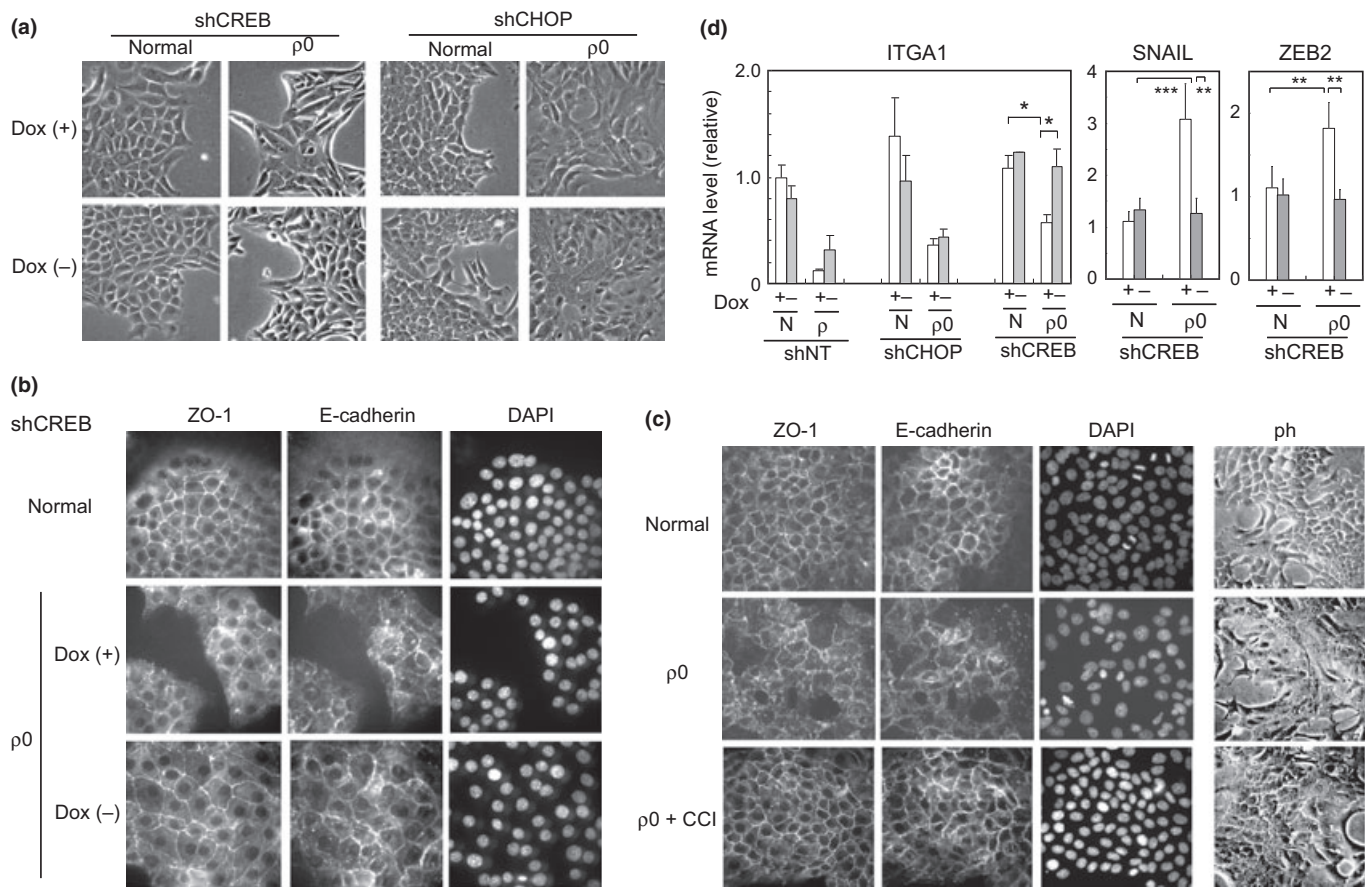


Fig. 3. The involvement of cAMP-responsive element-binding protein (CREB) in the disruption of epithelial morphology. (a–c) Normal and $\rho 0$ cells were examined by phase contrast microscopy (a) and (c) and by indirect immunofluorescence labeling (as described above) (b),(c). In (b), shRNA for CREB were expressed under Dox– conditions. DAPI stained nuclei. In (c; $\rho 0$ + CCI), the $\rho 0$ cells were treated with CCI [N-(4-chlorophenyl)-3-hydroxy-2-naphthamide] (10 μ M), a CREB-CBP interaction inhibitor, for 48 h. (d) Total RNA from normal (N) and the $\rho 0$ cells expressing conditional shRNA as in Figure 2 was examined by real-time RT-PCR, as above. A ratio relative to the control (Dox+ sample of the control) is shown. * $P < 0.05$, ** $P < 0.005$, *** $P < 0.0005$.

indirectly regulate HMGA2 expression at a post-translational level. Supporting this view, the rate of degradation of the HMGA2 protein in the presence of cycloheximide (CHX) was lower in the $\rho 0$ cells compared with the normal cells (Fig. 4c).

Activation of the cAMP-responsive element-binding protein/high mobility group AT-hook 2 pathway in a human cancer cell line. To determine whether the CREB/HMGA2 pathway was activated in human cancer cells, 10 human cancer cell lines were examined in this study. As shown in Figure 5(a), in HepG2 cells, HMGA2 was highly expressed, and CREB appeared to be phosphorylated to a substantial level (taking the relatively low amount of the total CREB protein into account). Moreover, HMGA2 expression in HepG2 cells was sensitive to treatment with CCI, whereas the EJ-1 line, which had no sign of CREB activation, was unaffected (Fig. 5a,c). HMGA1 was hardly detected in any of the cell lines tested in this study. Thus, we suggest that similar to the $\rho 0$ cell model, CREB is activated, which, in turn, upregulates HMGA2 expression in HepG2 cells. Of interest, HMGA2 expression was observed along with CREB phosphorylation in five of the six HCC cell lines (Fig. 5b), suggesting that activation of the CREB/HMGA2 cascade is a prevalent trait in HCC.

The similarity between the results for the $\rho 0$ and HepG2 cells suggests a mitochondrial dysfunction underlying the activation of the CREB/HMGA2 pathway in HepG2 cells. In support of this notion, a recent study identified a pathogenic mtDNA mutation in HepG2 cells that resulted in reduced

activity of respiratory complex I.⁽²⁰⁾ We reinforce the involvement of mitochondrial stress signaling in the activation of CREB by demonstrating the involvement of calcium/calmodulin (CaM) kinase. In an earlier study, this kinase was identified as an activator of CREB under conditions of mitochondrial dysfunction.⁽¹⁷⁾ As shown in Figure 5(d), when HepG2 cells were treated with a panel of kinase inhibitors, only KN-93, an inhibitor of CaM kinase, significantly decreased the level of CREB phosphorylation. This inhibitor also decreased HMGA2 expression in HepG2 cells (Fig. 5d). It should be noted that mutations were also found in the mtDNA of the other HCC, particularly in the D-loop region, which is a mutational hotspot (Motoko Shibamura, unpublished data, 2012).

We also attempted to define the biological roles of the CREB/HMGA2 pathway in HepG2 cells. Unlike in the $\rho 0$ cells derived from NMuMG cells, CREB was unlikely to play a role in the gene expression of GADD45A, SNAIL and ZEB2, as well as in the subcellular distribution of E-cadherin and ZO-1 in this fully malignant human cancer cell line (data not shown). Only the expression of ITGA1 was dependent on the CREB/HMGA2 pathway. Treatment with both CCI and siRNA for HMGA2 (Fig. S4) caused an increase in ITGA1 expression (Fig. 6a). This suggests that in HepG2 cells, the activated CREB pathway mediates the downregulation of ITGA1 through the upregulation of HMGA2. In EJ-1 cells, the level of ITGA1 was also increased by inhibiting HMGA2, but no such effect was observed with CCI (Fig. 6a). This

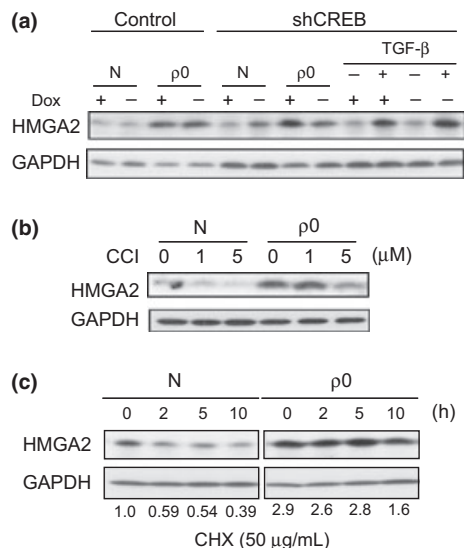


Fig. 4. High mobility group AT-hook 2 (HMGA2) upregulated downstream in the cAMP-responsive element-binding protein (CREB) pathway. (a–c) Cell lysates from control (N) and the p0 cells were subjected to immunoblotting using an antibody specific for HMGA2, as above. In (a), shRNA for CREB or the control was expressed under Dox– conditions. Cells were treated with TGF- β 1 (2 ng/mL) for 24 h (a; TGF- β +), CCI at the indicated doses for 48 h (b) and cycloheximide at 50 μ g/mL for the indicated times (c). Intensities of HMGA2 bands normalized to those of GAPDH are shown as ratios relative to the control (N, 0 h) at the bottom in the lower panel.

observation is consistent with the above results suggesting that the expression of HMGA2 in EJ-1 cells was regulated by mechanisms unrelated to CREB (Fig. 5b).

Finally, we studied the effect of CREB/HMGA2 pathway activation on the cellular phenotypes of HepG2 cells. Keeping in mind the important role of the pathway in the expression of ITGA1, a subunit of cell adhesion receptors specific to collagen, we examined the attachment phenotype of HepG2 cells. We compared cell attachment to collagen and fibronectin with and without CCI. We found that the attachment preference of HepG2 cells was shifted in favor of collagen following CCI interference in CREB function (Fig. 6b); this is consistent with the observed recovery of ITGA1 expression (Fig. 6a).

Discussion

In general, lesions in the mtDNA coding or non-coding regions result in deficiencies in the respiratory chain. In a defective respiratory chain, aberrant ROS production often occurs as a result of leakage of electrons to oxygen, and, consequently, a catastrophic cycle of respiratory function dysregulation is created because of additional mutations caused by ROS.⁽²¹⁾ During such a cycle, the cells are continuously exposed to ROS and are either at a risk of developing oncogenic somatic mutations, thereby activating the oncogenic pathways, or are at risk of increased genome instability. Thus, the aberrant production of ROS possibly accounts for some of the effects of mtDNA mutations on tumorigenesis, especially in the initial stages.

In the final phase of respiratory chain deficiency, however, mitochondria are assumed to be completely deprived of their ROS-producing capability, regardless of the formation of the catastrophic cycle.⁽¹²⁾ In this phase, the impact of ROS and their signals presumably subsides. Instead, stress signals are likely to be elicited due to the sensing of the loss of normal mitochondrial functions. A recent study described such a stress

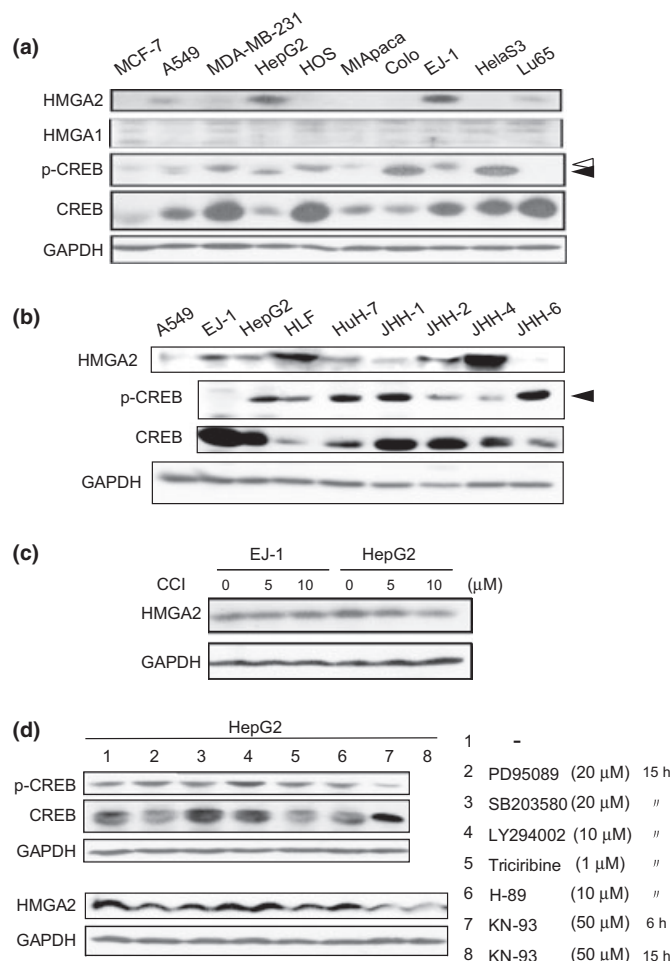


Fig. 5. The cAMP-responsive element-binding protein (CREB)/high mobility group AT-hook 2 (HMGA2) pathway activated in a human cancer cell line. (a) Cell lysates prepared from the human cancer cell lines (Materials and Methods) were studied to determine the expression levels of HMGA2, HMGA1, CREB (total) and p-CREB (phosphorylated form) by immunoblotting with the specific antibodies. A solid arrowhead indicates ser-133 phosphorylated CREB, and an empty arrowhead indicates nonspecific bands. (b) Cell lysates from HCC cell lines were processed as in (a). (c) HepG2 and EJ-1 cells were treated with CCI at the indicated doses for 48 h, and the cell lysates were then subjected to immunoblotting. (d) HepG2 cells treated with a panel of protein kinase inhibitors (PD95089: MEK1/2, SB203580: p38MAPK, LY294002: PI3K, Triciribine: Akt1/2/3, H-89: PKA, and KN-93: CaMKII), as indicated, were lysed and examined by immunoblotting. Consistent with the decrease in phosphorylated CREB, double bands of CREB become single after treatment with KN-93.

response to mitochondrial dysfunction that was mediated by stress-inducible transcription factors, including CHOP⁽¹⁶⁾ and CREB.⁽¹⁷⁾ Hypoxia-inducible factor-1 α signaling, which requires mitochondria-derived ROS, appears to be dormant in the p0 cells.⁽²²⁾

In the present study, we explored the potential contribution of mitochondrial dysfunction in tumorigenesis as a stress modulating intracellular signaling during the later stages of the process. It is noteworthy that the incidence of somatic mutations in the D-loop of mtDNA is increased in late stage rather than early stage cancers.⁽³⁾ At the onset of neoplastic transformation in cells harboring mtDNA mutation(s), ROS are expected to be the dominant mutagens. However, we reasoned that in the resulting pre-neoplastic cells, stress signaling activated by decreased mitochondrial function would play an

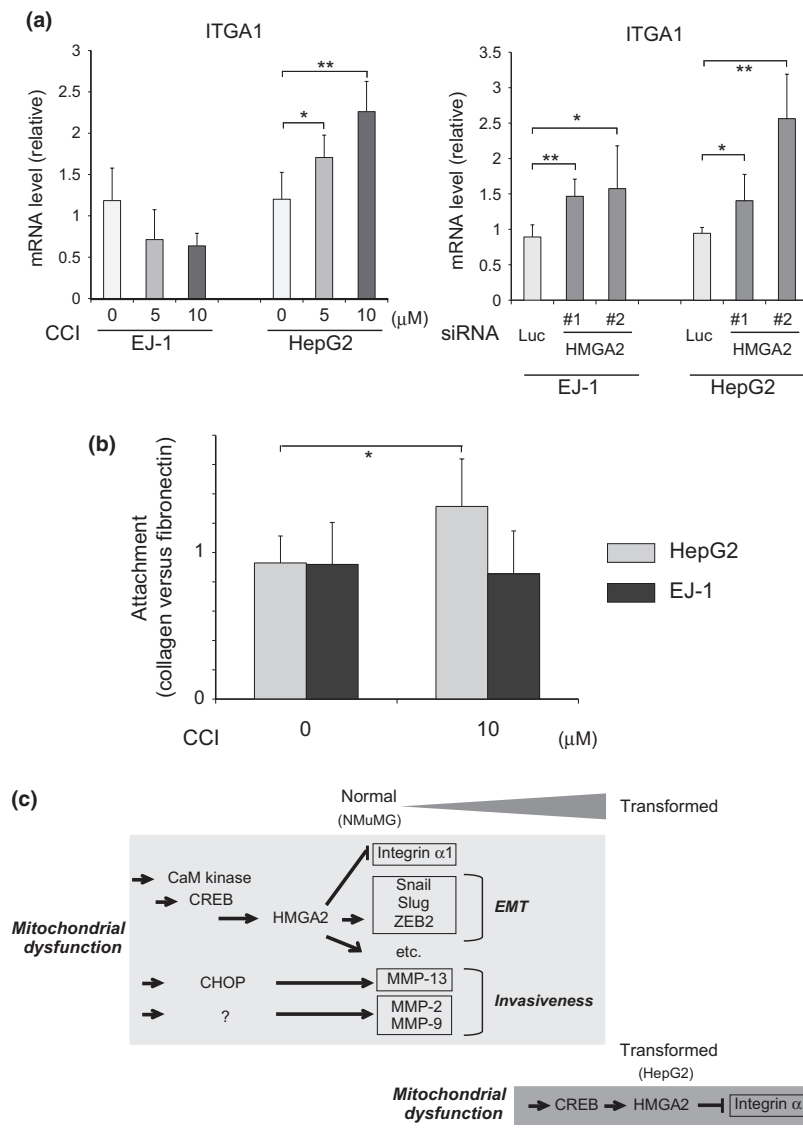


Fig. 6. The cAMP-responsive element-binding protein (CREB)/high mobility group AT-hook 2 (HMGA2) pathway decreases ITGA1 expression in HepG2 cells. (a) HepG2 and EJ-1 cells were treated with CCI at the indicated doses for 20 h or with siRNA for HMGA2 (50 nM for 48 h) and examined by real-time RT-PCR to determine ITGA1 expression. The knockdown effects of the HMGA2 siRNA are shown in Figure S1c. A ratio relative to the control is shown. * $P < 0.05$, ** $P < 0.005$. (b) Cells pretreated with CCI for 48 h were dissociated, plated onto collagen-coated and fibronectin-coated wells, and processed for the attachment assay, as described in the Materials and Methods section. A ratio of the cell number in the collagen-coated wells to that in fibronectin-coated wells is shown. * $P < 0.05$. (c) Contribution of mitochondrial dysfunction to malignant transformation of epithelial cells. Mitochondrial dysfunction propagated stress signaling by activating CREB-mediated and C/EBP homologous protein-10 (CHOP)-mediated transcriptional networks. HMGA2 played an intermediary role in the CREB pathway and regulated a variety of transcriptional activities downstream. In non-transformed NMuMG mouse mammary epithelial cells, the epithelial-mesenchymal transition (EMT) regulators and ITGA1 were regulated downstream of HMGA2. Together with previous findings,⁽¹²⁾ the cascades and their targets that potentially contribute to neoplastic transformation are shown. In the HepG2-transformed cancer cell line, the CREB/HMGA2 axis is suggested to be active in regulating the expression of ITGA1, but not the EMT (see text). ** $P < 0.005$, *** $P < 0.00005$.

increased role in tumorigenic progression. In the present study, we observed changes in cell-cell junction structures as well as altered gene expression in the $\rho 0$ cells, and characterized the roles of the CHOP and CREB mitochondrial stress mediators in altering the cellular phenotypes. This is the first report to evaluate the impact of mitochondrial dysfunction on epithelial morphology; cells of mesenchymal origin and fully transformed cancer cells have been studied previously.^(16,17,23)

The mechanisms by which CREB and CHOP are upregulated under $\rho 0$ conditions remain an open question. Based on our previous study, ROS are unlikely to be involved in signaling.⁽¹²⁾ Indeed, the phosphorylation of CREB was insensitive to an antioxidant, N-acetylcysteine (Motoko Shibamura, unpublished data, 2012). The involvement of an unfolded protein response, which is a major stress inducing CHOP, is also unlikely.⁽¹⁶⁾ Instead, perturbed intracellular calcium distribution is the most likely mechanism.⁽²⁴⁾ Mitochondria are implicated in intracellular calcium storage and homeostasis together with the endoplasmic reticulum (ER). In addition, they are physically associated, and the transport of calcium from one organelle to the other is highly efficient. In a previous report, ER calcium depletion and the consequent increase in the cytosolic fraction were shown to, respectively, induce CHOP and

activate CREB.⁽²⁵⁾ The inhibition of CREB phosphorylation by a CaM kinase inhibitor supports a similar involvement of calcium signaling in $\rho 0$ cells (Fig. 5d).

Our findings revealed the critical role of CREB in the disorganization of epithelial phenotypes because of decreased mitochondrial functioning. The detailed mechanisms whereby the architecture of the cell-cell junctions of the $\rho 0$ cells was disorganized downstream in the CREB pathway remain unclear. ATP depletion has been associated with disordered cell-cell adhesion.⁽²⁶⁾ The upregulation of the SNAIL family members SNAIL, ZEB2 and SLUG⁽¹⁶⁾ may have contributed to this process through the induction of the epithelial-mesenchymal transition (EMT), as has been reported in some cases of adenocarcinoma.⁽²⁷⁾ However, E-cadherin, an EMT regulator target, remained highly expressed, and so activation of EMT was unlikely in the $\rho 0$ state. In other studies, depletion of mtDNA has also been associated with tumorigenic phenotypes, although, again, the detailed mechanisms remain unclear.⁽²⁷⁻³²⁾

Unexpectedly and interestingly, our study revealed a close relationship between CREB and HMGA2, namely, CREB regulation of HMGA2 expression, implying the existence of a novel transcriptional network organized by CREB and downstream HMGA2. HMGA2 is an oncofetal protein that is

frequently amplified, rearranged and overexpressed in multiple human cancers,^(18,19) and it is causally related to neoplastic cell transformation.^(33,34) In this study, we originally identified ITGA1 as a potential transcriptional target of HMGA2. Given the possible interplay between cell–cell and cell–ECM adhesions, it is likely that the disorganized epithelial morphology that arises following mitochondrial dysfunction stems from a change in ITGA1 expression downstream in the CREB/HMGA2 cascade, which indirectly interferes with cell–cell adhesion structures by influencing cell–ECM adhesion status. Chen *et al.*⁽³⁵⁾ report that ITGA1 serves as a negative regulator of epidermal growth factor receptor (EGFR) activity. This observation raises another interesting possibility that EGFR signaling, augmented by the repression of ITGA1 expression, is a primary cause of the disorganized epithelial structures in the $\rho 0$ cells. Future studies should address the roles of the CREB/HMGA2 pathway in neoplastic transformation in more detail. The hypothetical contribution of mitochondrial dysfunction to malignant transformation in epithelial cells is illustrated in Figure 6(c), highlighting the roles of the CREB/HMGA2 pathway and the CHOP-mediated transcriptional cascade.

We suggest that the CREB/HMGA2 pathway operates not only in the $\rho 0$ model but also in HepG2 human cancer cells. However, we also noticed a difference between HepG2 and NMuMG $\rho 0$ model cells. For example, activation of the CHOP pathway was not detected in the human cancer cell lines studied (data not shown). Moreover, SNAIL and ZEB2 were

not regulated by the CREB/HMGA2 pathway in HepG2 cells. Given that HMGA2 is an architectural nuclear factor modulating transcription through interaction with DNA and/or canonical transcription factors, the difference may be ascribed to the profiles of the transcription factors present in cells.

Interestingly, among cancerous tissues, HCC is characterized by a high number of mutations in the D-loop (42.6% of HCC carry the mutations) and a decreased mtDNA copy number (57.4%).⁽³⁾ Accordingly, the CREB/HMGA2 pathway deserves further research as a potential therapeutic target against HCC and other cancers that feature activated mitochondrial stress signaling.

Acknowledgments

We thank Ms A. Kanno, Ms R. Miura, and Ms K. Mogi for contributing to this study as part of their bachelor degrees. This study was supported in part by a Grant-in-Aid for Scientific Research (C) (21570205), a grant from the High-Technology Research Center Project from the Ministry for Education, Culture, Sports, Science and Technology (MEXT) of Japan, and also by MEXT-Supported Program for the Strategic Research Foundation at Private Universities, 2010–2012.

Disclosure Statement

The authors have no conflict of interest to declare.

References

- Chatterjee A, Dasgupta S, Sidransky D. Mitochondrial subversion in cancer. *Cancer Prev Res (Phila)* 2011; **4**: 638–54.
- Chatterjee A, Mambo E, Sidransky D. Mitochondrial DNA mutations in human cancer. *Oncogene* 2006; **25**: 4663–74.
- Lee HC, Yin PH, Lin JC *et al.* Mitochondrial genome instability and mtDNA depletion in human cancers. *Ann N Y Acad Sci* 2005; **1042**: 109–22.
- He Y, Wu J, Dressman DC *et al.* Heteroplasmic mitochondrial DNA mutations in normal and tumour cells. *Nature* 2010; **464**: 610–4.
- Mambo E, Gao X, Cohen Y, Guo Z, Talalay P, Sidransky D. Electrophile and oxidant damage of mitochondrial DNA leading to rapid evolution of homoplasmic mutations. *Proc Natl Acad Sci U S A* 2003; **100**: 1838–43.
- Polyak K, Li Y, Zhu H *et al.* Somatic mutations of the mitochondrial genome in human colorectal tumours. *Nat Genet* 1998; **20**: 291–3.
- Petros JA, Baumann AK, Ruiz-Pesini EJ *et al.* mtDNA mutations increase tumorigenicity in prostate cancer. *Proc Natl Acad Sci U S A* 2005; **102**: 719–24.
- Zhou S, Kachhap S, Sun W *et al.* Frequency and phenotypic implications of mitochondrial DNA mutations in human squamous cell cancers of the head and neck. *Proc Natl Acad Sci U S A* 2007; **104**: 7540–5.
- Lee HC, Li SH, Lin JC, Wu CC, Yeh DC, Wei YH. Somatic mutations in the D-loop and decrease in the copy number of mitochondrial DNA in human hepatocellular carcinoma. *Mutat Res* 2004; **547**: 71–8.
- Nomoto S, Sanchez-Céspedes M, Sidransky D. Identification of mtDNA mutations in human cancer. *Methods Mol Biol* 2002; **197**: 107–17.
- Nomoto S, Yamashita K, Koshikawa K, Nakao A, Sidransky D. Mitochondrial D-loop mutations as clonal markers in multicentric hepatocellular carcinoma and plasma. *Clin Cancer Res* 2002; **8**: 481–7.
- Shibanuma M, Inoue A, Ushida K *et al.* Importance of mitochondrial dysfunction in oxidative stress response: a comparative study of gene expression profiles. *Free Radic Res* 2011; **45**: 672–80.
- Kanome T, Itoh N, Ishikawa F *et al.* Characterization of Jumping translocation breakpoint (JTB) gene product isolated as a TGF- β 1-inducible clone involved in regulation of mitochondrial function, cell growth and cell death. *Oncogene* 2007; **26**: 5991–6001.
- Suga H, Kadoshima T, Minaguchi M *et al.* Self-formation of functional adenohypophysis in three-dimensional culture. *Nature* 2011; **480**: 57–62.
- Ishikawa F, Nose K, Shibanuma M. Downregulation of hepatocyte nuclear factor-4 α and its role in regulation of gene expression by TGF- β 1 in mammary epithelial cells. *Exp Cell Res* 2008; **314**: 2131–40.
- Ishikawa F, Akimoto T, Yamamoto H *et al.* Gene expression profiling identifies a role for CHOP during inhibition of the mitochondrial respiratory chain. *J Biochem* 2009; **146**: 123–32.
- Arnould T, Vankoningsloo S, Renard P *et al.* CREB activation induced by mitochondrial dysfunction is a new signaling pathway that impairs cell proliferation. *EMBO J* 2002; **21**: 53–63.
- Fusco A, Fedele M. Roles of HMGA proteins in cancer. *Nat Rev Cancer* 2007; **7**: 899–910.
- Cleynen I, Van de Ven WJ. The HMGA proteins: a myriad of functions (Review). *Int J Oncol* 2008; **32**: 289–305.
- Gao W, Xu K, Li P, Tang B. Functional roles of superoxide and hydrogen peroxide generated by mitochondrial DNA mutation in regulating tumorigenicity of HepG2 cells. *Cell Biochem Funct* 2011; **29**: 400–7.
- Ralph SJ, Rodriguez-Enriquez S, Neuzil J, Saavedra E, Moreno-Sanchez R. The causes of cancer revisited: “Mitochondrial malignancy” and ROS-induced oncogenic transformation – Why mitochondria are targets for cancer therapy. *Mol Aspects Med* 2010; **31**: 145–70.
- Chandel NS, McClintock DS, Feliciano CE *et al.* Reactive oxygen species generated at mitochondrial complex III stabilize hypoxia-inducible factor-1 α during hypoxia: a mechanism of O₂ sensing. *J Biol Chem* 2000; **275**: 25130–8.
- Amuthan G, Biswas G, Ananadtheerthavarada HK, Vijayasathy C, Shephard HM, Avadhani NG. Mitochondrial stress-induced calcium signaling, phenotypic changes and invasive behavior in human lung carcinoma A549 cells. *Oncogene* 2002; **21**: 7839–49.
- Biswas G, Adebajo OA, Freedman BD *et al.* Retrograde Ca²⁺ signaling in C2C12 skeletal myocytes in response to mitochondrial genetic and metabolic stress: a novel mode of inter-organelle crosstalk. *EMBO J* 1999; **18**: 522–33.
- Copanaki E, Schurmann T, Eckert A *et al.* The amyloid precursor protein potentiates CHOP induction and cell death in response to ER Ca²⁺ depletion. *Biochim Biophys Acta* 2007; **1773**: 157–65.
- Tsukamoto T, Nigam SK. Tight junction proteins form large complexes and associate with the cytoskeleton in an ATP depletion model for reversible junction assembly. *J Biol Chem* 1997; **272**: 16133–9.
- Naito A, Cook CC, Mizumachi T *et al.* Progressive tumor features accompany epithelial-mesenchymal transition induced in mitochondrial DNA-depleted cells. *Cancer Sci* 2008; **99**: 1584–8.
- Kulawiec M, Arnouk H, Desouki MM, Kazim L, Still I, Singh KK. Proteomic analysis of mitochondria-to-nucleus retrograde response in human cancer. *Cancer Biol Ther* 2006; **5**: 967–75.
- Kulawiec M, Safina A, Desouki MM *et al.* Tumorigenic transformation of human breast epithelial cells induced by mitochondrial DNA depletion. *Cancer Biol Ther* 2008; **7**: 1732–43.
- van Waveren C, Sun Y, Cheung HS, Moraes CT. Oxidative phosphorylation dysfunction modulates expression of extracellular matrix-remodeling genes and invasion. *Carcinogenesis* 2006; **27**: 409–18.

- 31 Mambo E, Chatterjee A, Xing M *et al.* Tumor-specific changes in mtDNA content in human cancer. *Int J Cancer* 2005; **116**: 920–4.
- 32 Xing J, Chen M, Wood CG *et al.* Mitochondrial DNA content: its genetic heritability and association with renal cell carcinoma. *J Natl Cancer Inst* 2008; **100**: 1104–12.
- 33 Wood LJ, Maher JF, Bunton TE, Resar LM. The oncogenic properties of the HMG-I gene family. *Cancer Res* 2000; **60**: 4256–61.
- 34 Di Cello F, Hillion J, Hristov A *et al.* HMGA2 participates in transformation in human lung cancer. *Mol Cancer Res* 2008; **6**: 743–50.
- 35 Chen X, Abair TD, Ibanez MR *et al.* Integrin alpha1beta1 controls reactive oxygen species synthesis by negatively regulating epidermal growth factor receptor-mediated Rac activation. *Mol Cell Biol* 2007; **27**: 3313–26.

Supporting Information

Additional Supporting Information may be found in the online version of this article:

Fig. S1. Disorganization of epithelial morphology caused by respiratory chain interference.

Fig. S2. Knockdown of C/EBP homologous protein-10 (CHOP) and cAMP-responsive element-binding protein (CREB) with shRNA.

Fig. S3. mRNA levels of HMGA2 in normal and $\rho 0$ cells.

Fig. S4. Knockdown of HMGA2 with siRNA. EJ-1 and HegG2 cells were treated with siRNA (50 nM) for two kinds of HMGA2 (#1, #2) and luciferase (control) for 48 h, and mRNA levels were examined by real-time RT-PCR.

Please note: Wiley-Blackwell are not responsible for the content or functionality of any supporting materials supplied by the authors. Any queries (other than missing material) should be directed to the corresponding author for the article.

Loss of anchorage primarily induces non-apoptotic cell death in a human mammary epithelial cell line under atypical focal adhesion kinase signaling

F Ishikawa¹, K Ushida¹, K Mori¹ and M Shibamura¹

Anchorage dependence of cellular growth and survival prevents inappropriate cell growth or survival in ectopic environments, and serves as a potential barrier to metastasis of cancer cells. Therefore, obtaining a better understanding of anchorage-dependent responses in normal cells is the first step to understand and impede anchorage independence of growth and survival in cancer cells and finally to eradicate cancer cells during metastasis. Anoikis, a type of apoptosis specifically induced by lack of appropriate cell-extracellular matrix adhesion, has been established as the dominant response of normal epithelial cells to anchorage loss. For example, under detached conditions, the untransformed mammary epithelial cell (MEC) line MCF-10 A, which exhibits myoepithelial characteristics, underwent anoikis dependent on classical ERK signaling. On the other hand, recent studies have revealed a variety of phenotypes resulting in cell death modalities distinct from anoikis, such as autophagy, necrosis, and cornification, in detached epithelial cells. In the present study, we characterized detachment-induced cell death (DICD) in primary human MECs immortalized with hTERT (^{Tert}HMECs), which are bipotent progenitor-like cells with a differentiating phenotype to luminal cells. In contrast to MCF-10 A cells, apoptosis was not observed in detached ^{Tert}HMECs; instead, non-apoptotic cell death marked by features of entosis, cornification, and necrosis was observed along with downregulation of focal adhesion kinase (FAK) signaling. Cell death was overcome by anchorage-independent activities of FAK but not PI3K/AKT, SRC, and MEK/ERK, suggesting critical roles of atypical FAK signaling pathways in the regulation of non-apoptotic cell death. Further analysis revealed an important role of TRAIL (tumor necrosis factor (TNF)-related apoptosis-inducing ligand) as a mediator of FAK signaling in regulation of entosis and necrosis and a role of p38 MAPK in the induction of necrosis. Overall, the present study highlighted outstanding cell subtype or differentiation stage specificity in cell death phenotypes induced upon anchorage loss in human MECs.

Cell Death and Disease (2015) 6, e1619; doi:10.1038/cddis.2014.583; published online 22 January 2015

Normal cells undergo cell death and/or growth arrest in the absence of attachment to extracellular matrix (ECM) or upon contact with abnormal or ectopic ECM, which constitutes a physiologically important defense mechanism in multicellular organisms for preventing re-adhesion of detached cells to foreign matrices and their dysplastic growth in inappropriate sites.^{1,2} On the other hand, the process of cancer metastasis demands that cancer cells circumvent such cell death/growth arrest. This is true even for incipient tumors, where outgrowth and displacement of cells from their original location in a mass result in loss of adequate contact of cells with innate ECM. Cells that disseminate through foreign stroma experience more deviant conditions, and upon reaching the parenchyma of distant organs need to adapt to the non-permissive matrix in the foreign tissue. To survive through this process, cancer cells acquire resistance to cell death/growth arrest induced in the

absence of appropriate adhesion to ECM. Therefore, the eradication of cancer cells in ectopic environments requires an understanding of their resistance to anchorage dependence for growth and survival based on responsiveness of their normal counterparts.

Anoikis is a particular type of apoptosis that is induced by inadequate or inappropriate cell–ECM interactions, and is the best-characterized phenotype induced by loss of anchorage in anchorage-dependent epithelial cells.^{2,3} On the other hand, detachment of cells from ECM has been observed to induce a variety of cell death phenotypes that are distinct from the typical anoikis; these include entosis, autophagy, and squamous transdifferentiation.^{4–8} The emerging diversity of cell death phenotypes necessitates extension of the study of adhesion-dependent cell death beyond classical anoikis.

¹Division of Cancer Cell Biology, Department of Molecular Biology, Showa University School of Pharmacy, Tokyo 142-8555, Japan

*Corresponding author: M Shibamura, Division of Cancer Cell Biology, Department of Molecular Biology, Showa University School of Pharmacy, 1-5-8 Hatanodai, Shinagawa-ku, Tokyo 142-8555, Japan. Tel: +81 3 3784 8209; Fax: +81 3 3784 6850; E-mail: smotoko@pharm.showa-u.ac.jp

Abbreviations: DICD, detachment-induced cell death; DR, death receptor; ECM, extracellular matrix; ERK, extracellular signal-regulated kinase; FAK, focal adhesion kinase; GRB2, growth factor receptor-bound protein 2; ^{Tert}HMEC, human mammary epithelial cell immortalized with hTERT; ILK, integrin-linked kinase; LDH, lactate dehydrogenase; MAPK, mitogen-activated protein kinase; MEC, mammary epithelial cell; PARP, poly(ADP-ribose) polymerase; PI, propidium iodide; PI3K, phosphatidylinositol-4,5-bisphosphate 3-kinase; polyHEMA, poly(2-hydroxyethyl methacrylate); shRNA, short hairpin RNA; STS, staurosporine; TEM, transmission electron microscopy; TRAIL, tumor necrosis factor (TNF)-related apoptosis-inducing ligand; Z-VAD (Z-VAD-fmk, *N*-benzyloxycarbonyl-Val-Ala-Asp(O-Me) fluoromethylketone

Received 07.8.14; revised 05.12.14; accepted 10.12.14; Edited by M Leverkus

A considerable number of studies have suggested that anoikis is the predominant cell death phenotype induced in mammary epithelial cells (MECs) upon anchorage loss,^{9–13} however, many of these studies employed rodent cells or the human cell line MCF-10 A, which has been characterized as being predominantly myoepithelial or classified into basal B subtype.^{14–16} Given that the majority of malignant breast cancers exhibit the luminal characteristics, a phenotype based on a normal counterpart or a correspondent luminal subtype of human MECs needs to be defined, particularly given the current limited knowledge in this respect.

In the present study, we characterized anchorage loss-induced cell death in MECs using primary human MECs immortalized with hTERT (^{Tert}HMEC).^{17,18} The established cells are potential stem/progenitors of mammary epithelial cells¹⁸ and show a partial differentiation toward to the luminal phenotype in the culture system developed by Stampfer *et al* (<http://hmec.lbl.gov/mreview.htm>). Unlike previous observations based on MCF-10 A cells, the detached ^{Tert}HMECs were found to have an apparent defect in the execution of apoptosis and instead, underwent non-apoptotic cell death through simultaneous entosis, cornification, and necrotic processes. The roles of focal adhesion kinase (FAK) and its atypical signaling mediated by TRAIL (tumor necrosis factor (TNF)-related apoptosis-inducing ligand) in this process have been highlighted.

Results

Anchorage loss-dependent cell death is induced in ^{Tert}HMECs through downregulation of focal adhesion signaling. Induction of cell death (hereafter designated as detachment-induced cell death or DICD) was observed in ^{Tert}HMECs that were incubated in suspension or in a culture dish coated with the non-adhesive material poly(2-hydroxyethyl methacrylate) or polyHEMA. Approximately 20% of the cells were observed to show positive propidium iodide (PI) staining 48 h after the loss of anchorage (Figure 1a; Supplementary Figure S1a), indicating that a fraction of cells died with concomitant loss of plasma membrane integrity. Supplementation of the suspension culture with exogenous ECM (matrigel) resulted in almost complete abrogation of the increase in PI staining (Supplementary Figure S1b), suggesting that cell death was triggered *per se* by loss of adhesion to ECM and not by an unintentional side effect of the detachment process. In contrast to PI staining, staining with Annexin V resulted in a marginal increase in the fraction of positively stained cells (Figure 1a; Supplementary Figure S1a). Annexin V stains phosphatidylserine exposed in the outer leaflet of plasma membrane, which is an early hallmark of apoptosis. Accordingly, treatment with staurosporine (STS), a typical inducer of apoptosis, increased Annexin V rather than PI-positive cell populations at an early time point (Figure 1a; Supplementary Figure S1a).

The effects of loss of cell-ECM adhesion on intracellular signaling were investigated, with primary focus on FAK and its downstream signaling, which have a central role in cell adhesion-mediated signal transduction.^{19,20} The survival signals generated upon cell-ECM adhesion are transmitted

by FAK and its downstream effectors SRC, phosphatidylinositol-4,5-bisphosphate 3-kinase (PI3K)/AKT, and growth factor receptor-bound protein 2 (GRB2)-MEK/extracellular signal-regulated kinase (ERK) axes.^{3,20,21} The initial event in this cascade is a conformational change in FAK that is elicited upon its binding to the cytoplasmic domain of integrin β , which leads to autophosphorylation of FAK at Y397 and its concomitant activation. Activated FAK activates SRC, which in turn phosphorylates additional sites in FAK; this leads to the complete activation of FAK, and therefore that of its downstream effectors. However, in detached cells, these signal transduction events are usually downregulated. Figure 1b shows the attenuation of FAK autophosphorylation and activation-dependent phosphorylation of the downstream kinases SRC, AKT, and ERK with a concomitant decrease in expression levels of SRC and AKT in detached ^{Tert}HMECs. In marked contrast to other kinases, p38 mitogen-activated protein kinase (MAPK) appeared to be upregulated, as previously reported.^{8,22}

FAK and its downstream atypical signaling pathway function as a determinant of survival in detached ^{Tert}HMECs. To show the causal association between downregulation of FAK signaling and DICD, overriding the signaling downregulation in detached cells was attempted under the assumption that sustained or adhesion-independent activation of survival signaling could counteract DICD. For this purpose, a series of constitutively active forms of kinases associated with the signaling pathway was utilized. Myristoylated FAK (myrFAK), which is known to exhibit adhesion-independent activity,²³ was first tested. As expected, robust phosphorylation of FAK at Y397 was detected in cells expressing myrFAK (Figure 1c), which was mostly located in the cytoplasm (Supplementary Figure S2a), and phosphorylation became resistant to detachment (Figure 1c). Similar results were obtained for phosphorylation at Y925 and S910 (Supplementary Figure S2b). Consistent with this, paxillin and SRC, which are representative effectors of FAK, were found to be phosphorylated in these cells under detached conditions at levels comparable to an attached cell control (Figure 1c), indicating that FAK transduced signals to the downstream effectors even under conditions of cell detachment. Notably, the cells with such adhesion-independent FAK activity almost completely overcame DICD (Figure 1d; Supplementary Figure S2c), underscoring the important role of FAK signaling in DICD.

Furthermore, constitutively active forms of PI3K (myristoylated PI3K or myrPI3K)²⁴ and Src (Y527F mutant or Src (Y527F))²⁵ were employed for examining whether DICD could be similarly overcome by these kinases. However, despite expression in cells at detectable levels (Figure 1c), neither myrPI3K nor Src(Y527F) rescued cells from DICD (Figure 1d). Moreover, the expression of myrPI3K failed to have any impact on the phosphorylation of AKT, a downstream effector of PI3K under the condition (unpublished data). Therefore, constitutively active forms of AKT isoforms (myrHA-AKT1, 2, and 3)²⁶ were used instead of PI3K. Although myristoylated AKTs were expressed and phosphorylated in cells in an anchorage-independent manner (Supplementary Figure S3a), they failed

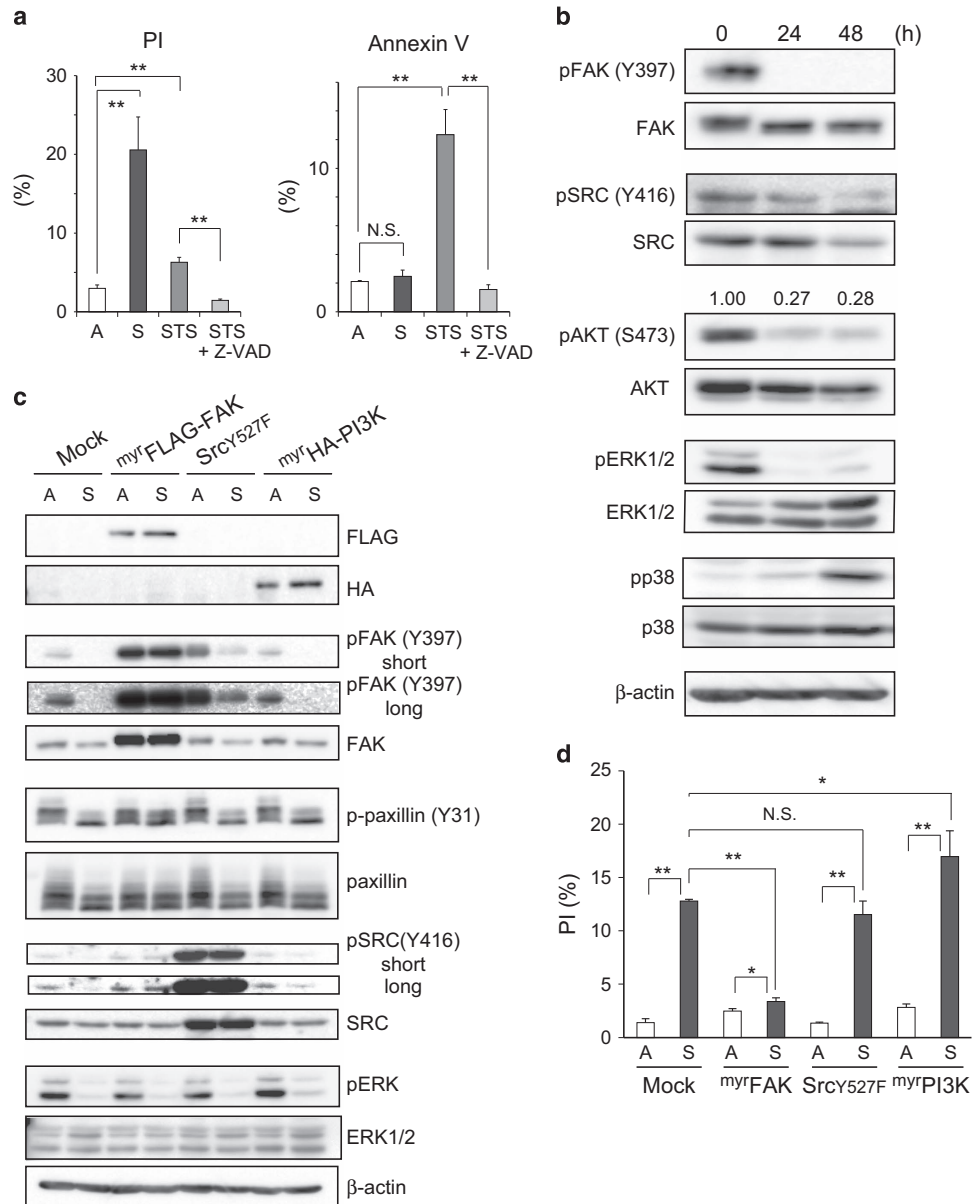


Figure 1 Cell death is induced in suspension cultures of ^{Tert}HMECs accompanying downregulation of adhesion signaling. (a) ^{Tert}HMECs were cultured as monolayers (A) or suspension (S) for 48 h, stained with PI and Annexin V, and subjected to flow cytometry. The percentages of PI- and Annexin V-positive subpopulations are depicted as a graph (means ± S.D. from at least three independent experiments). For experimental control, monolayer cultures were treated with 0.5 μM staurosporine (STS) in the presence or absence of 50 μM Z-VAD for 6 h. (b) Cells were cultured in suspension for the indicated time periods, and examined by immunoblot analysis using the indicated antibodies. β-Actin was used as a loading control. Quantification of band densities was performed using Image J software, and the ratio of the phosphorylated form of AKT to total proteins is shown. (c and d) Cells were infected with lentivirus constructs expressing control (Mock), FLAG-tagged myrFAK, Src(Y527F), or HA-tagged myrPI3K, and blasticidin selection was performed to obtain cells that stably expressed these proteins. The cells were cultured for 24 h as in (a) and examined using immunoblot (c). For flow cytometry analysis (d), cells were cultured for 48 h, stained with PI and Annexin V, and analyzed as in (a). *P < 0.05; **P < 0.01; NS, not significant

to reduce DICD (Supplementary Figure S3b), arguing against a major role of the PI3K/AKT pathway in DICD. Similarly, dominant active MEK (MEK2DD) exerted no inhibitory effect on DICD (Supplementary Figure S3c and d). Thus, it was likely that the MEK/ERK pathway was also uncoupled from DICD, which was supported by the observation that myrFAK alleviated DICD with ERK activity remaining downregulated in detached cells (Figures 1c and d). This is in contrast to anoikis in MCF-10A cells, which was dependent on ERK signaling.¹² Thus, DICD in ^{Tert}HMECs was shown to be

dependent on FAK activity but not on any of its downstream effectors SRC, PI3K, or GRB2/MEK. Because the ratio of activated β1 integrins was rather decreased in detached cells by myrFAK, involvement of inside-out signaling was also unlikely (Supplementary Figure S2d). Although the possibility exists that FAK simultaneously engages multiple downstream pathways for counteracting DICD, with individual downstream pathways being insufficient for cell survival, DICD in ^{Tert}HMECs is possibly regulated by atypical and not classical pathways of FAK signaling.

Other signaling molecules, such as ILK, EGFR, ERBB2, p21 protein (Cdc42/Rac)-activated kinase, and Rho family of small G proteins (Rho, Cdc42, Rac), that potentially have a role in DICD regulation, were also investigated. Among these, EGFR overexpression had a modest effect on DICD, while the overexpression or expression of constitutively active forms of the other molecules, including ERBB2, had essentially no effect (unpublished data).

Typical apoptosis or anoikis is not detectable in detached $Tert^+$ HMECs. The lack of dependence of DICD on classical survival signaling and the observation that DICD was not accompanied by an overt increase in Annexin V staining (Figure 1a; Supplementary Figure S1a) suggested that classical apoptosis or anoikis was unlikely to be responsible for DICD in $Tert^+$ HMECs. In fact, this assumption was corroborated by further experiments. In particular, increase in the typical indices of apoptosis such as DNA fragmentation and activation of caspases, including caspase 3, were not detected in detached $Tert^+$ HMECs (Figures 2a and b). An active (cleaved) form of caspase 3 or its activity, manifested through cleavage of poly(ADP-ribose) polymerase (PARP), was also not detectable (Figure 2c). Furthermore, the effect of BCL2L1 (Bcl-xL) on DICD was incompatible with the occurrence of apoptosis. As an anti-apoptotic protein of the Bcl-2 family, the expression of BCL2L1 was found to antagonize apoptosis induced by STS (Supplementary Figure S3e and f) but exerted no effect on DICD (Figure 2d). Taken together, these observations supported the conclusion that DICD in $Tert^+$ HMECs was primarily caspase independent or non-apoptotic, at least under the culture conditions adopted in the present study.

To obtain further information on DICD in $Tert^+$ HMECs, a pharmacological survey using a set of enzyme inhibitors for a particular type of cell death was conducted. Consistent with the aforementioned results (Figures 2a–d), Z-VAD-fmk (Z-VAD), a broad-spectrum caspase inhibitor,²⁷ caused little effect on DICD (Figure 2e). Other inhibitors, such as pepstatin A (PepA), E64d, and bafilomycin for autophagy⁷ and necrostatin for necroptosis,²⁸ also exerted only marginal effects (Figure 2e).

Entosis is observed in detached $Tert^+$ HMECs. With respect to cell death modality responsible for DICD, a morphological study provided clues. As shown in Figure 3a, transmission electron microscopy (TEM) revealed unique ultrastructural changes in the detached population of $Tert^+$ HMECs; cell internalization within another cell was observed, which closely resembled what has been referred to as cell-in-cell structure,²⁹ characterized as the complete inclusion of one cell within another. Such inclusion of cells within other cells was confirmed in detached population of $Tert^+$ HMECs using red- or green-labeled cell populations which were mixed, incubated in suspension, and visualized by confocal microscopy (Figure 3b). The structure appeared within 12 h, and further incubation resulted in its growth into a large cellular aggregate due to reiterative internalization, which hampered the accurate enumeration of internalization ratio after 24 h (Figure 3c). Nuclear staining with DAPI or TUNEL suggested that cell death was induced in cells inside the structure

(Figures 3d and e). Internalized cells have been shown to be degraded by lysosomal activity.⁶ These observations suggest that a cell death modality, which is typified by cell internalization termed entosis, occurs in $Tert^+$ HMECs upon loss of attachment to ECM. Cell internalization was the only morphological phenotype discernible by TEM in detached $Tert^+$ HMECs, and this process was suppressed by the expression of myrFAK but not myrPI3K and Src(Y527F), as shown in Figure 3f.

DICD in $Tert^+$ HMECs is mediated by at least three types of non-apoptotic cell death modalities. Gene expression profiling and biochemical analysis were performed for more precise characterization of DICD. Gene expression profiling suggested that caspase 14, a non-canonical caspase specifically associated with terminal differentiation in keratinocytes,³⁰ was upregulated in detached $Tert^+$ HMECs (unpublished data). Its upregulation was confirmed by quantitative RT-PCR and immunoblotting along with the induction of cornification markers, such as keratin 10 and filaggrin (Figure 4a). This finding is in good agreement with previous observations of epidermis-like cornification in MECs.^{8,31} Similar to entosis, the expression of these cornification markers was remarkably inhibited by myrFAK expression (Figure 4b). The expression of SrcY527F and myrPI3K also reduced the expression, but their effects were modest and not significant in some cases.

On the other hand, biochemical analysis suggested that DICD assumed features of necrosis, as manifested by the release of lactate dehydrogenase (LDH), which was increased 72 h postincubation under detached conditions (Figure 4c); this increase was also suppressed by expression of myrFAK (Figure 4d). Before LDH release, a decrease in ATP/ADP ratio accompanying the deterioration of mitochondrial membrane potential ($\Delta\Psi_m$) was observed (Supplementary Figure S4a and b). According to a recent report,^{4,32} MECs suffered metabolic defects under detached conditions, which resulted in necrotic cell death.

Collectively, three simultaneous types of cell death, entosis, cornification, and necrosis, were possibly implicated in DICD of $Tert^+$ HMECs, and all three types of cell death were mitigated by the expression of myrFAK. In conclusion, DICD in $Tert^+$ HMECs is mediated by at least three types of non-apoptotic cell death modalities that were presumably primed by downregulation of FAK activity upon loss of anchorage.

Role of TRAIL in DICD of $Tert^+$ HMECs. Compared with apoptosis, non-apoptotic cell death and its modalities, regulatory signaling, and mechanisms are poorly understood. In the present study, an important cue was obtained for regulatory signaling in DICD from the results of the aforementioned DNA microarray-based genome-wide screening; TRAIL was found to be upregulated during DICD along with caspase 14. As shown in Figures 5a and b, quantitative reverse transcription (RT)-PCR and immunoblot analyses verified the induction of TRAIL; the induction was detected at the mRNA level as early as 3 h following detachment (Supplementary Figure S5a) and persisted for 72 h (Figure 5b). The expression of myrFAK but not Src (Y527F) or myrPI3K resulted in significantly impaired

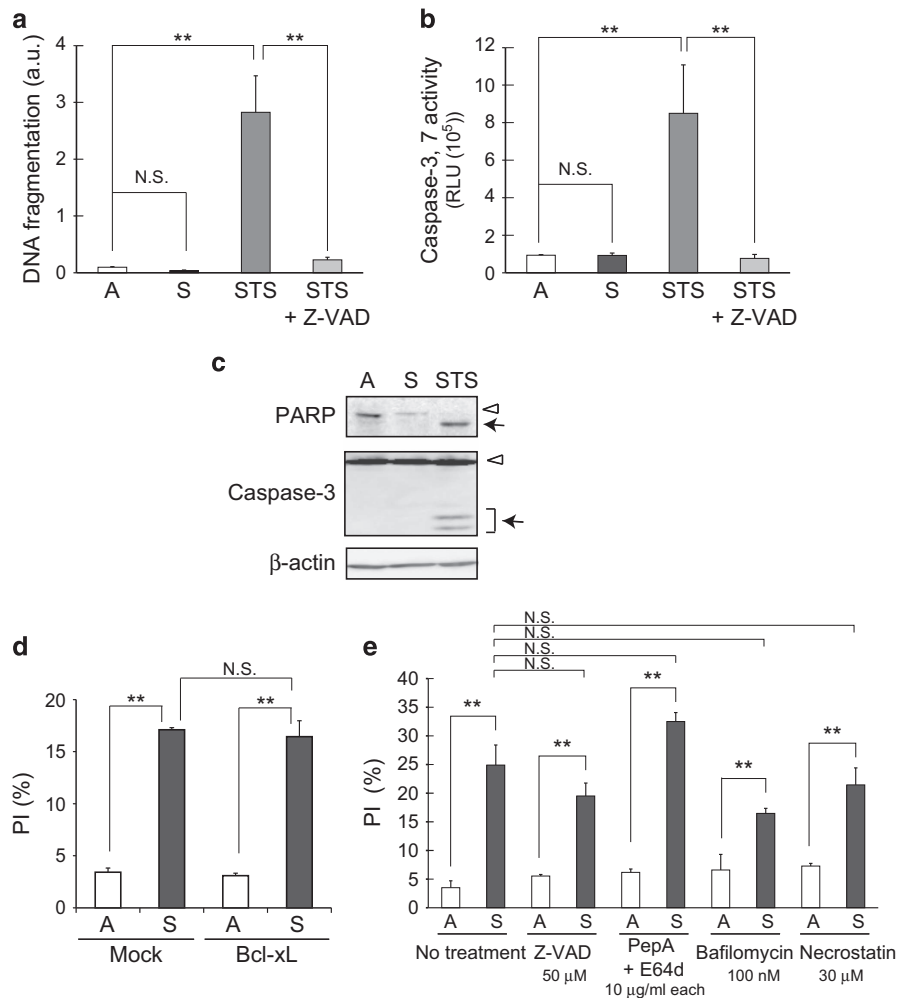


Figure 2 Apoptosis indices are undetectable in detached $TertHMECs$. (a) DNA fragmentation was quantified in $TertHMECs$ incubated as monolayers (A) or suspension (S) for 72 h, using the DNA Fragmentation Cell Death ELISA PLUS kit. Values represent means \pm S.D. from at least three independent experiments, with measurements in triplicate in each experiment. Monolayer cultures treated with $0.5 \mu M$ STS in the presence or absence of $50 \mu M$ Z-VAD for 24 h were employed as experimental controls. (b) Caspase 3/7 activity was assessed in cells cultured for 48 h as in (a) using a Caspase-Glo 3/7 assay kit. Representative results from three independent experiments are shown (means \pm S.D. of triplicate samples). Monolayer cultures treated with $0.5 \mu M$ STS in the presence or absence of $50 \mu M$ Z-VAD for 17 h were employed as experimental controls. (c) Cells cultured for 48 h as in (a) were subjected to immunoblot analysis with the indicated antibodies. The arrowhead and arrow indicate intact and cleaved PARP and caspase-3, respectively. Cells treated with STS ($0.5 \mu M$) for 17 h were employed as the positive control. (d) Cells expressing Bcl-xL were cultured for 48 h as in (a), stained with PI and Annexin V, and analyzed by flow cytometry as detailed in Figure 1a. (e) Cells cultured in the presence or absence of the indicated inhibitors for 48 h as in (a) were stained with PI and Annexin V, and analyzed by flow cytometry as described above. Z-VAD ($50 \mu M$), a caspase inhibitor; pepstatin A (PepA) and E64d ($10 \mu g/ml$), lysosomal cathepsin inhibitors; bafilomycin ($100 nM$), a vacuolar H^+ ATPase (V-ATPase) inhibitor; necrostatin ($30 \mu M$), a necroptosis inhibitor. Representative results from three independent experiments are shown (means \pm S.D. of triplicate samples). $**P < 0.01$; NS, not significant

induction of TRAIL (Figure 5c). shRNA-mediated knockdown of TRAIL expression interfered with cell internalization and LDH release (Figures 5d–f), while the expression of cornification markers was not significantly affected (Figure 5g). DR4 was inferred to function as a receptor for TRAIL (Supplementary Figure S5b–d). These results suggest that in detached $TertHMECs$, TRAIL is induced upon down-regulation of FAK signaling, and in turn contributes to entosis and necrosis but not cornification mechanisms. Thus, an important role of TRAIL as a mediator of FAK signaling that regulates DICD in $TertHMECs$ has emerged.

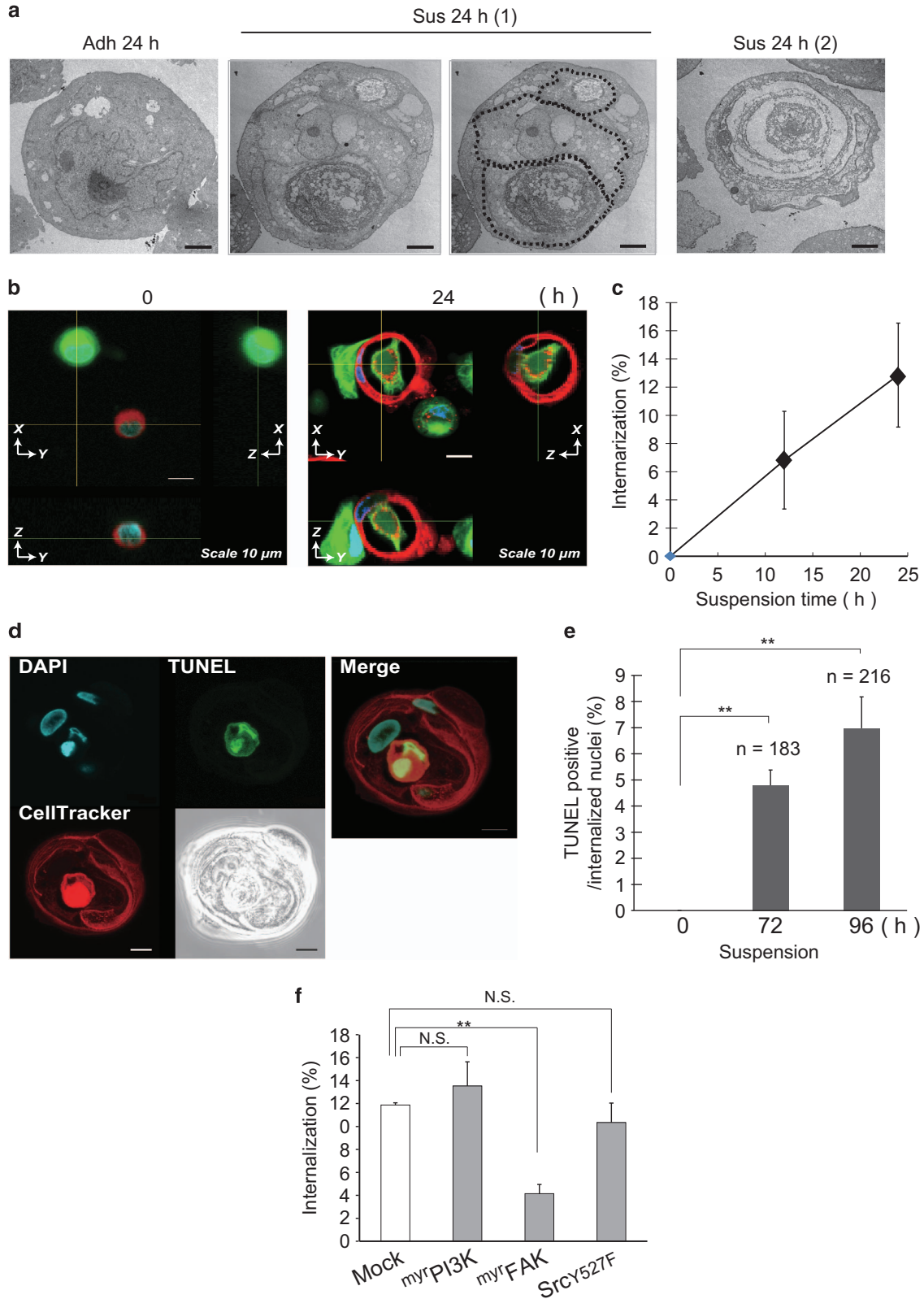
Role of p38 MAPK in DICD of $TertHMECs$. The possible involvement of p38 MAPK in the regulation of DICD was

investigated. As noted above, p38 MAPK was distinct from other adhesion-related signaling molecules, including JNK, in that it was evidently activated in response to loss of anchorage (Figures 1b and 6f). In addition, a previous study using an inhibitor, SB203580, of p38 MAPK suggested a role for this kinase in activation of cornification program in detached MECs.⁸

In fact, the induction of the cornification markers was similarly inhibited with the inhibitor in detached $TertHMECs$ in the present study (Supplementary Figure S6). However, the results were different when the activity of the kinase was attenuated with shRNA (Figures 6a and b). The inconsistency between the results of the two approaches is possibly attributed to the limitations of pharmacological inhibition with

respect to the specificity of targets. As shown in Figure 6b, shRNAs for p38 MAPK failed to inhibit the expression of the cornification markers, arguing against a role of the kinase in activation of cornification program in detached $Tert^+$ HMECs.

Likewise, the ratio of PI-positive cells and the frequency of cell internalization (Figures 6c and d); only LDH release was suppressed (Figure 6e), suggesting a role for this kinase in necrosis but



not entosis and cornification processes. When the association of p38 MAPK activation with FAK and TRAIL signaling was examined, the activation was observed to be significantly impeded by myrFAK expression and shRNA for TRAIL (Figures 6f and g); this observation together with that in Figure 5c suggested that the activation of p38 MAPK was mediated by TRAIL under the downregulation of FAK activity.

Discussion

Diversity of DICD in epithelial cells. The diversity of phenotypes assumed by cells upon loss of ECM attachment has been perceived from the seminal study on anoikis, which mentioned different phenotypes in the epithelial cells of gut versus ureters.³³ In the two decades that have elapsed since this study, our knowledge of detachment-responsive phenotypes in cells, particularly in MECs, has been enormously expanded by a series of studies on lumen formation in mammary glands during morphogenesis.^{8,11,34–36} Experiments in mice that were genetically deficient for caspase-dependent cell death mechanisms revealed the requirement of caspase-dependent cell death for efficient luminal clearing but not the eventual formation of a lumen, suggesting that caspase-independent or non-apoptotic cell death programs function as an alternative mechanism for luminal clearing in the absence of apoptosis.⁸ Subsequent studies led to the discovery of autophagy, necrosis, and cornification as such alternatives.^{4,34}

A salient observation of the present study is that immortalized human MECs, bipotent progenitor-like cells with a differentiating phenotype to luminal cells (TertHMECs)¹⁸ (<http://hmec.lbl.gov/mreview.htm>), primarily underwent non-apoptotic instead of apoptotic cell death under detached conditions, at least in forced suspension cultures *in vitro*. This mechanism is in striking contrast to MCF-10A cells, another immortalized, non-tumorigenic MEC cell line, which has been established to execute anoikis in response to loss of anchorage.^{11,12} In this cell line, the apoptosis program is tightly coupled with growth factor signaling; EGFR expression is downregulated upon loss of adhesion, resulting in upregulation of the Bcl-2 protein Bim.¹² If this is the case, then it is hypothesized that EGFR expression and signaling is sustained under conditions of detachment in TertHMECs so that apoptosis is not executed. However, this is unlikely because downregulation of EGFR expression in response to detachment has also been observed in TertHMECs similar to that in MCF-10A cells (unpublished data). Therefore, the difference

between the two cell lines is possibly attributed to the difference in their cell subtypes,^{14–16} basal/myoepithelial- or luminal-like, although details remain unclear.

Non-apoptotic cell death in detached TertHMECs. The identified cell death modalities in detached TertHMECs include entosis and necrosis along with the activation of the transdifferentiation program resulting in cornification. Given that the majority of malignant breast cancers assume luminal traits, this finding is potentially of great significance as it suggests that metastatic mammary tumors, if not all, acquire resistance to non-apoptotic cell death mechanisms rather than to classical apoptosis and that non-apoptotic cell death mechanisms have the potential to function as an important barrier to the development of breast carcinoma. The tumorigenic role of ERBB2 is also open to alternate interpretations. Although anoikis in MCF-10A cells was suppressed by the activation of ERBB2,¹² non-apoptotic cell death mechanisms in detached TertHMECs were apparently unaffected as mentioned above (unpublished data). ERBB2 signaling potentially contributes to tumorigenesis through the regulation of cellular metabolism rather than of cell death.³²

A critical role of FAK, which engages atypical survival signaling that is tightly coupled with TRAIL expression, emerged in the regulation of non-apoptotic cell death. In contrast to myrFAK, FAK(397E), which is another constitutively active form of the kinase, was unable to suppress DICD (unpublished data); this observation implied that kinase activity alone is insufficient for protecting cells from DICD, and that subcellular localization of the kinase or its anchoring to the plasma membrane, which was achieved by myristoylation, was critical for the regulation of DICD by FAK. On the other hand, recent studies have revealed highly context- and cell type-dependent aspects of FAK signaling.²³ The present study revealed a novel role of TRAIL in FAK signaling regulating non-apoptotic cell death mechanisms, particularly in entosis (Figure 5), albeit it has been generally accepted as an apoptosis inducer.³⁷ A previous study showed that the Rho-dependent actomyosin-mediated contractile system played a role in entosis.⁶ The results obtained in the present study suggest that TRAIL mediates the adhesion-dependent activation of Rho-actomyosin system, although details are yet to be defined. In conclusion, a schematic representation of the key players and their roles in DICD of TertHMECs is shown in Figure 6h.

The overall phenotype of detached TertHMECs resembles that of differentiating keratinocytes, which appears natural given that both skin and mammary glands are derived from the ectoderm of the embryo. More specifically, instead of apoptosis,

Figure 3 Detached TertHMECs undergo cell internalization, followed by cell death. (a) TertHMECs cultured for 24 h under adherent (Adh) or non-adherent (Sus) conditions were fixed with 2.5% glutaraldehyde and processed for TEM analysis. Dashed lines outline engulfed cells. Scale bar: 2 μm. (b and c) Single-cell suspensions of cells labeled with CellTracker Green or Red were mixed in 1 : 1 ratio and plated onto polyHEMA-coated plates. At the indicated time points, cells were stained with Hoechst 33342 (10 μM) and fixed. Confocal images were acquired as z-stacks, processed, and shown as orthogonal views of z-stacks (b). Lines on images indicate corresponding points in the orthogonal planes. Three dimensional axes and scale bar (10 μm) are indicated. Percentages of internalization were calculated from 200 cells viewed under a confocal microscope in three independent experiments, and depicted as graph (means ± S.D.) (c). (d and e) Cells in suspension culture as in (b) were fixed after 96 h (d) or 72 h and 96 h (e), and TUNEL staining was performed. Confocal images of internalized cells stained with TUNEL (green), CellTracker Red (red), and DAPI (blue) are shown (d). Scale bar: 10 μm. Percentages of TUNEL-positive population among the internalized cells were calculated by counting under a confocal microscope, and depicted as a graph (total numbers of cells counted in three independent experiments are shown) (e). (f) Cells expressing constitutively active forms of various kinases (myrFAK, Src(Y527F), and myrPI3K) were cultured under non-adherent conditions for 48 h as in (b). Cell internalization was evaluated as in (c), and percentages of internalization were depicted as graphs (means ± S.D.). **P < 0.01; NS, not significant

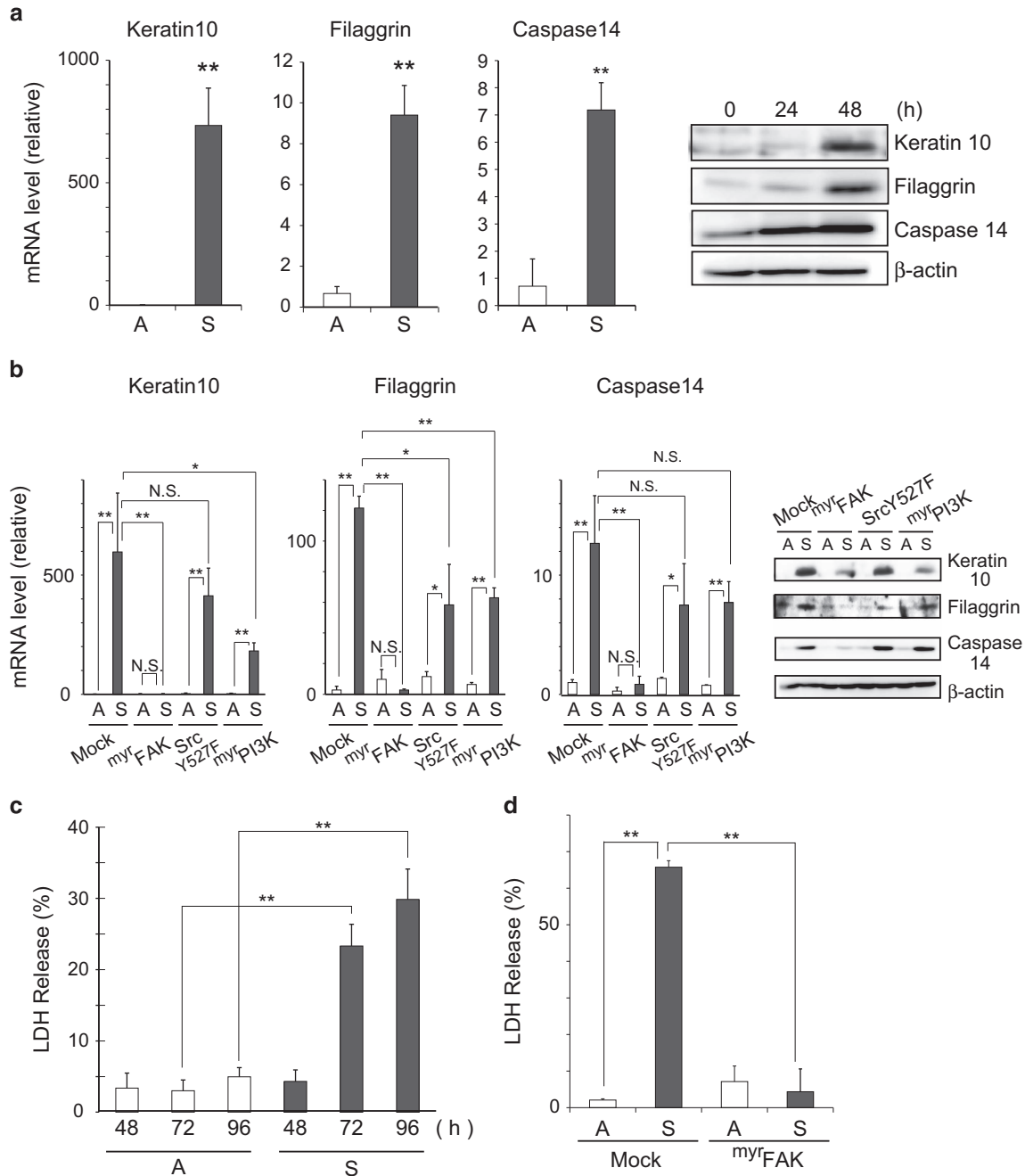


Figure 4 Cornification and necrosis programs are activated in detached $Tert^+$ HMECs. (a) $Tert^+$ HMECs were cultured as monolayers (A) or suspension (S) for 24 h, following which total RNA was extracted. The levels of various mRNAs were examined by quantitative RT-PCR using the indicated primers (Supplementary Information), and normalized with respect to GAPDH control. Ratio of mRNA levels in suspension (S) cultures to monolayer (A) cultures is shown. Cell lysates from the indicated periods were analyzed by immunoblotting using the indicated antibodies. β -Actin was used as a loading control. (b) Cells expressing constitutively active forms of various kinases were cultured as in (a), and mRNA and protein levels were examined as above. The ratios of mRNA levels with respect to those in monolayer cultures of Mock-infected cells are graphed. (c) Cells were cultured as above for the indicated time periods, and LDH activities were measured as described in the Materials and Methods. LDH release (%) represents the ratio of LDH activity in media to total (media and cells) activity. (d) Cells expressing myrFAK were cultured as above for 72 h and LDH release (%) was examined as in (c). Values represent means \pm S.D. from at least three independent experiments, with measurements in triplicate in each experiment. * $P < 0.05$; ** $P < 0.01$; NS, not significant

both the cell types activate non-apoptotic cell death mechanisms along with metabolic inactivation upon anchorage loss (Figure 4a, Supplementary Figures S4a and b).^{38–41} In differentiating keratinocytes, apoptosis is naturally prevented to ensure completion of the differentiation process resulting in non-apoptotic cell death by cornification.^{40,42,43} Likewise, under

conditions where apoptosis is inhibited, MECs undergo non-apoptotic cell death.^{8,11,34} The same regulatory mechanisms that counterbalance apoptosis and non-apoptotic cell death are likely shared between keratinocytes and MECs.

Metastasis is a formidable challenge not only for cancer patients to survive but also for cancer cells to achieve.

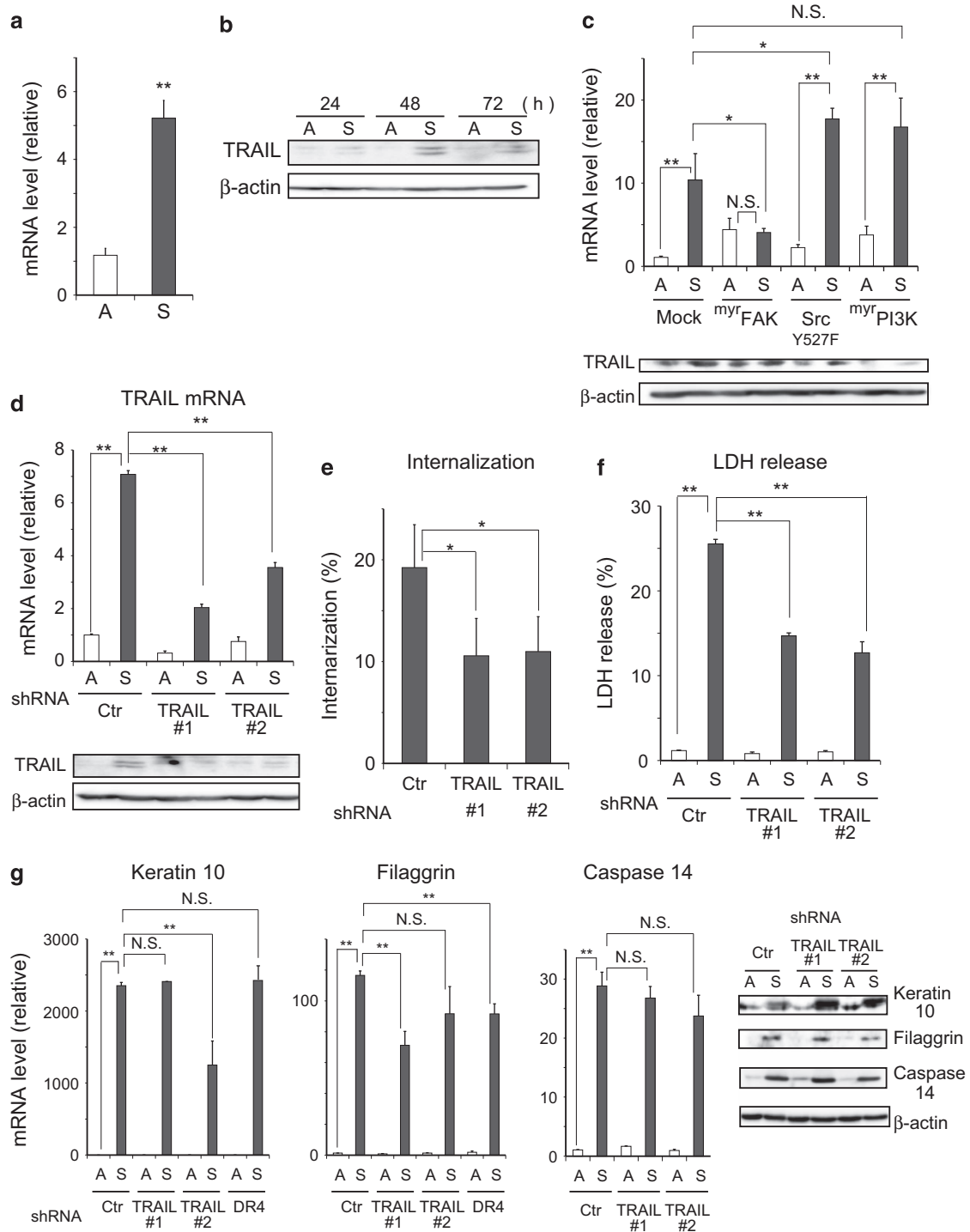


Figure 5 TRAIL upregulation in detached $TERT$ HMECs contributes to cell internalization and necrosis. (a) $TERT$ HMECs were cultured as monolayers (A) or suspension (S) for 24 h, and TRAIL mRNA levels were evaluated as in Figure 4a. (b) Cells cultured as in (a) for the indicated time periods were examined by immunoblot analysis using TRAIL-specific antibody. β -Actin was employed as a loading control. (c) Cells expressing constitutively active forms of various kinases were cultured as above and TRAIL mRNA and protein levels were examined. The ratio with respect to mRNA levels in monolayer cultures of Mock-infected cells is shown. (d) Cells infected with lentiviral expression constructs of shRNAs (Ctr: control, TRAIL #1, #2: two shRNAs with unrelated sequences specific for TRAIL (Materials and Methods)) were cultured as in (a) and TRAIL mRNA levels were analyzed as above. Cell lysates from 48h cultures were analyzed by immunoblot using TRAIL-specific antibody as mentioned in (b). (e) shRNA-expressing cells were stained with 10 μ M CellTracker Red or Green, mixed, and cultured in suspension for 20 h, followed by counting of internalized cells by confocal microscopy, as mentioned in Figures 3b and c. (f) shRNA-expressing cells were cultured as in (a) for 72 h, and LDH release (%) was examined as mentioned in Figure 4c. (g) shRNA-expressing cells were cultured as in (a) for 24 h, and mRNA and protein levels were analyzed as described in Figure 4a. Values represent means \pm S.D. from at least three independent experiments, with measurements made in triplicate for each experiment. * $P < 0.05$; ** $P < 0.01$; NS, not significant

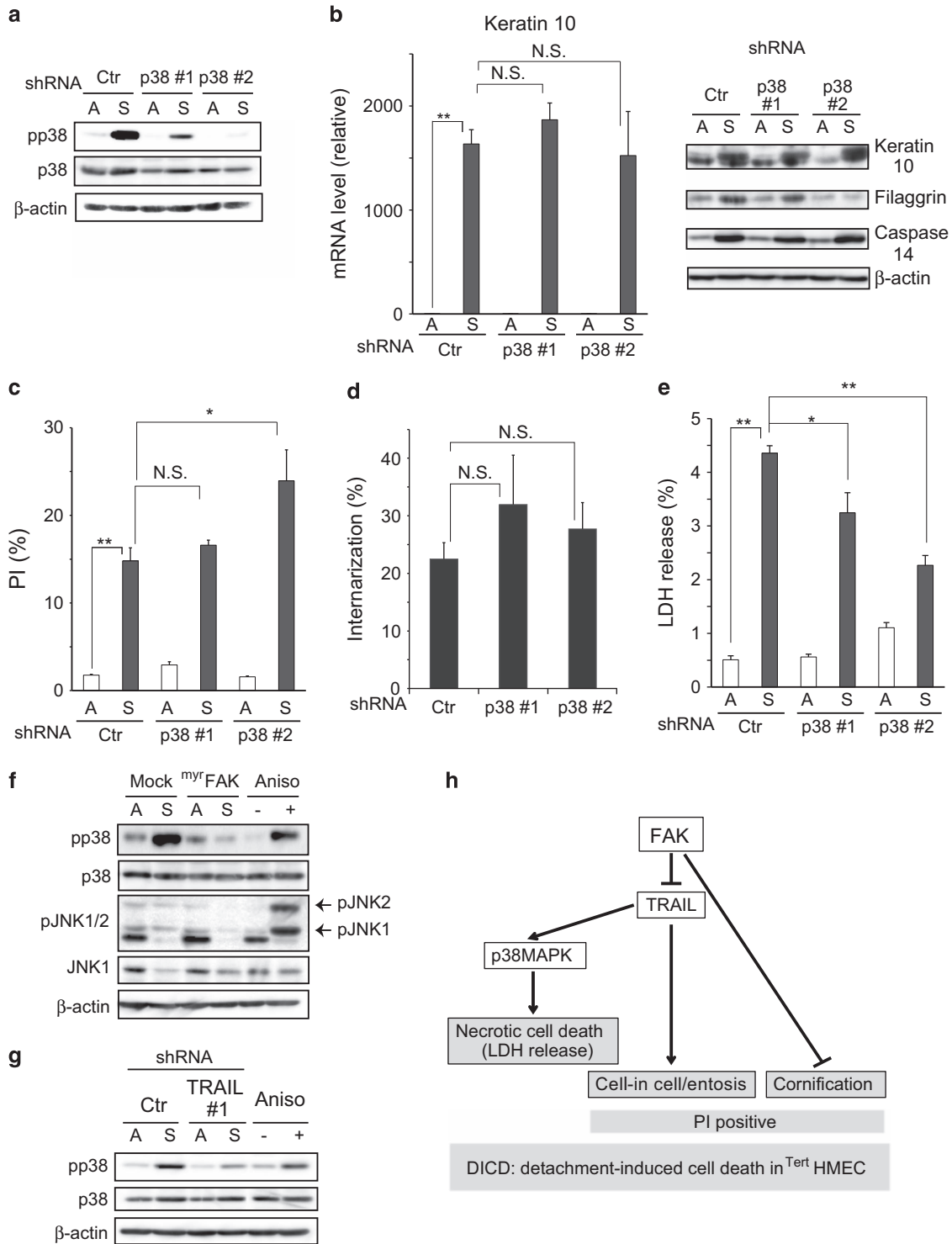


Figure 6 p38 MAPK has a role in inducing necrosis in detached $TertHMECs$. (a) $TertHMECs$ expressing shRNAs (Ctr: control, p38 MAPK # 1, # 2: two shRNAs with unrelated sequences specific for p38 MAPK; Materials and Methods) were cultured as monolayers (A) or suspension (S) for 48 h, and examined as described above by immunoblot analysis using the indicated antibodies. β -Actin was employed as a loading control. (b) Total RNA was extracted from cells cultured for 24 h as in (a), and keratin 10 mRNA levels were analyzed as described above. Cell lysates were analyzed by immunoblotting using the indicated antibodies. β -Actin was used as a loading control. (c) shRNA-expressing cells were cultured as in (a), followed by staining with PI and annexin V, and subjected to flow-cytometry analysis, as described in Figure 1a. (d) shRNA-expressing cells were stained with 10 μ M CellTracker Red or Green, mixed, and cultured for 20 h in suspension. Internalized cells were counted using confocal microscope as described in Figures 3b and c. (e) shRNA-expressing cells were cultured as in (a) for 72 h, and LDH release (%) was examined as mentioned in Figure 4c. (f and g) Cells expressing myrFAK (f) or shRNA (Ctr: Control, TRAIL # 1) (g) were cultured as in (a) for 48 h, and examined by immunoblot analysis using the indicated antibodies. Anisomycin (50 μ g/ml, 30 min) was used as a positive control for the phosphorylation of p38 MAPK and JNKs. β -Actin loading control was used. Values represent means \pm S.D. from at least three independent experiments, with measurements made in triplicate for each experiment. * P <0.05; ** P <0.01; NS, not significant. (h) Schematic illustration of FAK-dependent detachment-induced cell death (DICD) in $TertHMECs$

Millions of cells are possibly released from a primary tumor every day, but only a small minority colonizes a distant organ. Thus, the process of metastasis could be exploited as an opportunity for eradicating cancer cells, particularly during their dormant period, which is probably underpinned by resistance to DICD or anchorage-independent cell growth and survival. This study is expected to set the stage for the identification of relevant molecular targets for interfering with anchorage-independent growth, thereby inducing death in metastasizing breast cancer cells.

Materials and Methods

Cell culture and chemicals. HMECs were purchased from Lonza (Walkersville, MD, USA) and cultured in MCDB170 (US Biological, Salem, MA, USA) supplemented with 0.1 mM ethanolamine (Sigma-Aldrich, St Louis, MO, USA), 0.1 mM ortho-phosphoethanolamine (Sigma), 0.25% bovine pituitary extract (Hammond Cell Tech, Windsor, CA, USA), 5 ng/ml EGF (Peprotech, Rocky Hill, NJ, USA), 0.5 μ g/ml hydrocortisone (Sigma), 5 μ g/ml insulin (Sigma), 5 μ g/ml transferrin (Sigma), and 5 μ M isoproterenol (Sigma).⁴⁴ For immortalization, HMECs were transduced with hTERT-expressing retrovirus as described previously.¹⁷

For suspension culture, cells were detached by treatment with 0.025% trypsin, followed by resuspension in the growth medium supplemented with 0.5% methylcellulose and plated on polyHEMA-coated dishes. Anisomycin, pepstatin A, and polyHEMA were obtained from Sigma-Aldrich. E64d and Z-VAD-fmk (Z-VAD) were purchased from Peptide Institute, Inc. (Osaka, Japan), staurosporine (STS) and bafilomycin from Wako Pure Chemical Industries, Ltd. (Osaka, Japan), and necrostatin-1 from Enzo Life Sciences, Inc. (Farmingdale, NY, USA). BD Matrigel Matrix Growth Factor Reduced (GFR) was obtained from BD Biosciences (Franklin Lakes, NJ, USA).

Expression vectors. The cDNAs for human FAK, catalytic subunit (p110) of PI3K, Bcl-xL, AKT1, AKT2, AKT3, and MEK2 were amplified from HMEC cDNA library and cloned into CSII-CMV-MCS-IRES2-Bsd vector⁴⁵ (CSII vector) with FLAG or HA tag sequences. cDNA for Src was amplified from pcDNA3 chick c-Src⁴⁶ (a generous gift from Dr T Akagi, Osaka Bioscience Institute, Osaka, Japan) and cloned into the CSII vector. The constitutively active Src(Y527F) and MEK2DD were generated using PrimeSTAR Mutagenesis Basal Kit (Takara Bio, Inc., Otsu, Japan). Constitutively active forms of FAK, PI3K, and AKT isoforms were generated by amplification of respective cDNAs using 5' primers that included c-Src myristoylation signal sequences, followed by cloning into CSII vector. The lentiviral destination vector, CS-RfA-EP, was generated by replacing the gene encoding blasticidin S deaminase in CS-RfA-EB with the gene for puromycin N-acetyltransferase from pGL4.2 vector (Promega, Madison, WI, USA).

For construction of shRNA expression vectors, target sequences for control (SHC002), TRAIL (# 1: TRCN0000005924; # 2: TRCN0000005925), DR4 (TRCN0000005934), DR5 (TRCN0000005933), and p38 (# 1: TRCN0000000510; # 2: TRCN0000000511) shRNAs were obtained from Mission shRNA (Sigma-Aldrich). Oligonucleotides encoding the target sequences were subcloned into pENTR4-H1, and the shRNA expression cassettes were recombined into CS-RfA-EB (for TRAIL, DR4, and DR5) or CS-RfA-EP (for p38) using LR Clonase II (Invitrogen, Carlsbad, CA, USA).

Infection. Lentivirus production and infection have been previously described.⁴⁷ The selection and maintenance of infected cells was accomplished using 10 μ g/ml blasticidin for CSII and CS-RfA-EB vectors and using 1 μ g/ml puromycin for CS-RfA-EP constructs.

Flow cytometry. Cells were washed with PBS/EDTA, digested with 0.25% trypsin, and centrifuged (800 \times g, 5 min, 4 °C). Following washes with PBS containing 0.2% serum, the cells were resuspended in incubation buffer (10 mM HEPES (pH 7.4), 140 mM NaCl, 5 mM CaCl₂) containing Annexin V (Annexin-V-FLUOS; Roche Applied Science, Penzberg, Upper Bavaria, Germany) and 1 μ g/ml PI (Sigma-Aldrich), incubated for 30 min at room temperature under dark conditions, filtered using 0.4- μ m filter, and analyzed using Epics XL (Beckman Coulter, Inc., Fullerton, CA, USA).

Immunoblot analysis. Immunoblot analysis was conducted as previously described.⁴⁵ The primary antibodies employed in the study are listed in Supplementary Information.

DNA fragmentation and caspase 3/7 activity assays. DNA fragmentation and activities of caspase 3/7 were assessed using DNA Fragmentation Cell Death ELISA PLUS Kit (Roche Applied Science) and Caspase-Glo 3/7 assay kit (Promega), respectively, according to the manufacturers' instructions.

Transmission electron microscopy. Cell pellet was fixed with 2.5% (v/v) phosphate-buffered glutaraldehyde for 2 h, washed with phosphate buffer, postfixed in 1% (w/v) phosphate-buffered osmium tetroxide for 1 h at 4 °C, and subjected to TEM as previously described.⁴⁸

Cell internalization assay. Monolayer cultures of cells were stained with 1 μ M solutions of CellTracker Green CMFDA or Red CMTPX (Invitrogen) for 30 min in a CO₂ incubator. Equal volumes of single-cell suspensions of red and green-labeled cells at densities of 1.0 \times 10⁵ cells/ml were mixed in growth media containing 0.5% methylcellulose, and placed on polyHEMA-coated plates. Aliquots of suspended cells were withdrawn at regular intervals and stained with Hoechst 33342 (10 μ M; Sigma-Aldrich) for 15 min at room temperature, washed with PBS, and fixed with 3.7% formaldehyde for 10 min at room temperature. Fixed cells were washed with PBS and placed in glass bottom dishes.

Laser scanning confocal microscopy was performed using FV10i-LIV confocal microscope (Olympus Corporation, Shinjuku, Tokyo, Japan). Three-dimensional images were acquired through z-stacking of sequential optical x-y sections taken at 0.5–1.0 μ m z-intervals. Orthogonal slice views from z-stack images were processed with the FLUOview software (Olympus).

TUNEL assay. Cells were fixed with freshly prepared 2% paraformaldehyde for 60 min at room temperature, washed with PBS, and permeabilized with 0.2% Triton X-100 for 2 min at 4 °C. The cells were then incubated with TUNEL reaction mixture containing TUNEL Enzyme and TUNEL label mix (Roche) according to the manufacturer's instructions. Positive staining in the nucleus was identified using FV10i-LIV confocal microscope (Olympus).

RNA extraction and quantitative RT-PCR. RNA extraction and quantitative RT-PCR were performed as previously described,⁴⁷ with minor modifications. The cDNA samples were mixed with specific primers (Supplementary Information) and GoTaq qPCR Master Mix (Promega), and amplified using MyiQ Real-time PCR detection system (Bio-Rad Laboratories Inc., Hercules, CA, USA) according to the manufacturer's instructions. The mRNA levels were normalized with respect to the control, glyceraldehyde-3-phosphate dehydrogenase (GAPDH).

LDH release assay. LDH activities were measured using LDH-Cytotoxic Test Wako (Wako Pure Chemical Industries, Ltd.). In brief, cells were cultured in polyHEMA-coated 12-well plates containing 1 ml of medium with 0.5% methylcellulose, and precipitated by centrifugation (800 \times g, 5 min, 4 °C). An aliquot of the supernatant (i.e., medium) was diluted with equivalent volume of PBS containing 0.2% Tween-20 for the quantification of LDH in media. The cell pellet was resuspended in growth medium, and an aliquot of the suspension was similarly mixed with equivalent volume of PBS/0.2% Tween-20, followed by overnight incubation at 4 °C to obtain total LDH levels (media and cells). The mixtures were cleared by centrifugation, incubated with coloring solution, and absorbance at 570 nm was obtained using Appliskan (Thermo Electron Corp., Madison, WI, USA). PBS/0.1% Tween-20 was employed for measuring background. LDH release was evaluated as a ratio of LDH activity in media to total LDH activity (media and cells).

Statistics. Data are expressed as mean \pm S.D. unless otherwise indicated. Differences between experimental samples were all analyzed by two-tailed Student's *t*-test. *P*-values less than 0.05 and 0.01 are shown as * and **, respectively. A *P*-value of less than 0.05 was considered as statistically significant.

Conflict of Interest

The authors declare no conflict of interest.

Acknowledgements. We thank Ms Y Chiba, Ms Y Hirose, Mr A Itoh, Ms A Matsushima, Ms N Mochida, Ms Y Nomoto, Mr Y Ohmachi, Mr K Sato, Ms S Tamura, Ms I Yamane, and Ms S Watanabe for contribution to this study as part of their bachelor's degree. This work was supported by a Grant-in-Aid for Young Scientist (B) (23790378), in part by a Grant-in-Aid for Science Research (C) (21570205), and also by a Private University High Technology Research Center Project matching fund by subsidy from MEXT.

1. Assoian RK. Anchorage-dependent cell cycle progression. *J Cell Biol* 1997; **136**: 1–4.
2. Chiarugi P, Giannoni E. Anoikis: a necessary death program for anchorage-dependent cells. *Biochem Pharmacol* 2008; **76**: 1352–1364.
3. Paoli P, Giannoni E, Chiarugi P. Anoikis molecular pathways and its role in cancer progression. *Biochim Biophys Acta* 2013; **1833**: 3481–3498.
4. Grassian AR, Coloff JL, Brugge JS. Extracellular matrix regulation of metabolism and implications for tumorigenesis. *Cold Spring Harb Symp Quant Biol* 2011; **76**: 313–324.
5. Buchheit CL, Rayavarapu RR, Schafer ZT. The regulation of cancer cell death and metabolism by extracellular matrix attachment. *Semin Cell Dev Biol* 2012; **23**: 402–411.
6. Overholzer M, Mailloux AA, Mouneim G, Normand G, Schnitt SJ, King RW et al. A nonapoptotic cell death process, entosis, that occurs by cell-in-cell invasion. *Cell* 2007; **131**: 966–979.
7. Fung C, Lock R, Gao S, Salas E, Debnath J. Induction of autophagy during extracellular matrix detachment promotes cell survival. *Mol Biol Cell* 2008; **19**: 797–806.
8. Mailloux AA, Overholzer M, Schmelzle T, Bouillet P, Strasser A, Brugge JS. BIM regulates apoptosis during mammary ductal morphogenesis, and its absence reveals alternative cell death mechanisms. *Dev Cell* 2007; **12**: 221–234.
9. Boudreau N, Simpson CJ, Werb Z, Bissell MJ. Suppression of ICE and apoptosis in mammary epithelial cells by extracellular matrix. *Science* 1995; **267**: 891–893.
10. Farrelly N, Lee YJ, Oliver J, Dive C, Streuli CH. Extracellular matrix regulates apoptosis in mammary epithelium through a control on insulin signaling. *J Cell Biol* 1999; **144**: 1337–1348.
11. Debnath J, Mills KR, Collins NL, Reginato MJ, Muthuswamy SK, Brugge JS. The role of apoptosis in creating and maintaining luminal space within normal and oncogene-expressing mammary acini. *Cell* 2002; **111**: 29–40.
12. Reginato MJ, Mills KR, Paulus JK, Lynch DK, Sgroi DC, Debnath J et al. Integrins and EGFR coordinately regulate the pro-apoptotic protein Bim to prevent anoikis. *Nat Cell Biol* 2003; **5**: 733–740.
13. Pullan S, Wilson J, Metcalfe A, Edwards GM, Goberdhan N, Tilly J et al. Requirement of basement membrane for the suppression of programmed cell death in mammary epithelium. *J Cell Sci* 1996; **109**: 631–642.
14. Gordon LA, Mulligan KT, Maxwell-Jones H, Adams M, Walker RA, Jones JL. Breast cell invasive potential relates to the myoepithelial phenotype. *Int J Cancer* 2003; **106**: 8–16.
15. Neve RM, Chin K, Fridlyand J, Yeh J, Baehner FL, Fevr T et al. A collection of breast cancer cell lines for the study of functionally distinct cancer subtypes. *Cancer Cell* 2006; **10**: 515–527.
16. Kao J, Salari K, Bocanegra M, Choi YL, Girard L, Gandhi J et al. Molecular profiling of breast cancer cell lines defines relevant tumor models and provides a resource for cancer gene discovery. *PLoS One* 2009; **4**: e6146.
17. Elenbaas B, Spirio L, Koerner F, Fleming MD, Zimonjic DB, Donaher JL et al. Human breast cancer cells generated by oncogenic transformation of primary mammary epithelial cells. *Genes Dev* 2001; **15**: 50–65.
18. Zhao X, Malhotra GK, Lele SM, Lele MS, West WW, Eudy JD et al. Telomerase-immortalized human mammary stem/progenitor cells with ability to self-renew and differentiate. *Proc Natl Acad Sci USA* 2010; **107**: 14146–14151.
19. Schatzmann F, Marlow R, Streuli CH. Integrin signaling and mammary cell function. *J Mammary Gland Biol Neoplasia* 2003; **8**: 395–408.
20. Zhao J, Guan JL. Signal transduction by focal adhesion kinase in cancer. *Cancer Metastasis Rev* 2009; **28**: 35–49.
21. Zhong X, Rescorla FJ. Cell surface adhesion molecules and adhesion-initiated signaling: understanding of anoikis resistance mechanisms and therapeutic opportunities. *Cell Signal* 2012; **24**: 393–401.
22. Wen HC, Avivar-Valderas A, Sosa MS, Girmis N, Farias EF, Davis RJ et al. p38alpha Signaling Induces Anoikis and Lumen Formation During Mammary Morphogenesis. *Sci Signal* 2011; **4**: ra34.
23. Zouq NK, Keeble JA, Lindsay J, Valentijn AJ, Zhang L, Mills D et al. FAK engages multiple pathways to maintain survival of fibroblasts and epithelia: differential roles for paxillin and p130Cas. *J Cell Sci* 2009; **122**: 357–367.
24. Klippel A, Reinhard C, Kavanaugh WM, Apell G, Escobedo MA, Williams LT. Membrane localization of phosphatidylinositol 3-kinase is sufficient to activate multiple signal-transducing kinase pathways. *Mol Cell Biol* 1996; **16**: 4117–4127.
25. Cartwright CA, Eckhart W, Simon S, Kaplan PL. Cell transformation by pp60c-src mutated in the carboxy-terminal regulatory domain. *Cell* 1987; **49**: 83–91.
26. Kohn AD, Takeuchi F, Akt Roth RA. A pleckstrin homology domain containing kinase, is activated primarily by phosphorylation. *J Biol Chem* 1996; **271**: 21920–21926.
27. Dolle RE, Hoyer D, Prasad CV, Schmidt SJ, Helaszek CT, Miller RE et al. P1 aspartate-based peptide alpha-((2,6-dichlorobenzoyl)oxy)methyl ketones as potent time-dependent inhibitors of interleukin-1 beta-converting enzyme. *J Med Chem* 1994; **37**: 563–564.
28. Degterev A, Huang Z, Boyce M, Li Y, Jagtap P, Mizushima N et al. Chemical inhibitor of nonapoptotic cell death with therapeutic potential for ischemic brain injury. *Nat Chem Biol* 2005; **1**: 112–119.
29. Overholzer M, Brugge JS. The cell biology of cell-in-cell structures. *Nat Rev Mol Cell Biol* 2008; **9**: 796–809.
30. Denecker G, Ovaere P, Vandenabeele P, Declercq W. Caspase-14 reveals its secrets. *J Cell Biol* 2008; **180**: 451–458.
31. Schaefer FV, Custer RP, Sorof S. Induction of abnormal development and differentiation in cultured mammary glands by cyclic adenosine nucleotide and prostaglandins. *Nature* 1980; **286**: 807–810.
32. Schafer ZT, Grassian AR, Song L, Jiang Z, Gerhart-Hines Z, Irie HY et al. Antioxidant and oncogene rescue of metabolic defects caused by loss of matrix attachment. *Nature* 2009; **461**: 109–113.
33. Meredith JE Jr, Fazeli B, Schwartz MA. The extracellular matrix as a cell survival factor. *Mol Biol Cell* 1993; **4**: 953–961.
34. Mailloux AA, Overholzer M, Brugge JS. Lumen formation during mammary epithelial morphogenesis: insights from in vitro and in vivo models. *Cell Cycle* 2008; **7**: 57–62.
35. Humphreys RC, Krajewska M, Krnacik S, Jaeger R, Weiher H, Krajewski S et al. Apoptosis in the terminal endbud of the murine mammary gland: a mechanism of ductal morphogenesis. *Development* 1996; **122**: 4013–4022.
36. Reginato MJ, Mills KR, Becker EB, Lynch DK, Bonni A, Muthuswamy SK et al. Bim regulation of lumen formation in cultured mammary epithelial acini is targeted by oncogenes. *Mol Cell Biol* 2005; **25**: 4591–4601.
37. MacFarlane M. TRAIL-induced signalling and apoptosis. *Toxicol Lett* 2003; **139**: 89–97.
38. Green H. Terminal differentiation of cultured human epidermal cells. *Cell* 1977; **11**: 405–416.
39. Watto FM. Role of integrins in regulating epidermal adhesion, growth and differentiation. *EMBO J* 2002; **21**: 3919–3926.
40. Allombert-Blaise C, Tamiji S, Mortier L, Fauvel H, Tual M, Delaporte E et al. Terminal differentiation of human epidermal keratinocytes involves mitochondria- and caspase-dependent cell death pathway. *Cell Death Differ* 2003; **10**: 850–852.
41. Lippens S, Denecker G, Ovaere P, Vandenabeele P, Declercq W. Death penalty for keratinocytes: apoptosis versus cornification. *Cell Death Differ* 2005; **12**: 1497–1508.
42. Raj D, Brash DE, Grossman D. Keratinocyte apoptosis in epidermal development and disease. *J Invest Dermatol* 2006; **126**: 243–257.
43. Eckhart L, Lippens S, Tschachler E, Declercq W. Cell death by cornification. *Biochim Biophys Acta* 2013; **1833**: 3471–3480.
44. Hammond SL, Ham RG, Stampfer MR. Serum-free growth of human mammary epithelial cells: rapid clonal growth in defined medium and extended serial passage with pituitary extract. *Proc Natl Acad Sci USA* 1984; **81**: 5435–5439.
45. Ishikawa F, Kaneko E, Sugimoto T, Ishijima T, Wakamatsu M, Yuasa A et al. A mitochondrial thioredoxin-sensitive mechanism regulates TGF-beta-mediated gene expression associated with epithelial-mesenchymal transition. *Biochem Biophys Res Commun* 2014; **443**: 821–827.
46. Akagi T, Shishido T, Murata K, Hanafusa H. v-Crk activates the phosphoinositide 3-kinase/AKT pathway in transformation. *Proc Natl Acad Sci USA* 2000; **97**: 7290–7295.
47. Ishikawa F, Miyoshi H, Nose K, Shibamura M. Transcriptional induction of MMP-10 by TGF-beta, mediated by activation of MEF2A and downregulation of class IIa HDACs. *Oncogene* 2010; **29**: 909–919.
48. Uchio-Yamada K, Sawada K, Tamura K, Katayama S, Monobe Y, Yamamoto Y et al. Tenc1-deficient mice develop glomerular disease in a strain-specific manner. *Nephron Exp Nephrol* 2013; **123**: 22–33.



Cell Death and Disease is an open-access journal published by Nature Publishing Group. This work is

licensed under a Creative Commons Attribution 4.0 International Licence. The images or other third party material in this article are included in the article's Creative Commons licence, unless indicated otherwise in the credit line; if the material is not included under the Creative Commons licence, users will need to obtain permission from the licence holder to reproduce the material. To view a copy of this licence, visit <http://creativecommons.org/licenses/by/4.0>

Supplementary Information accompanies this paper on Cell Death and Disease website (<http://www.nature.com/cddis>)

ORIGINAL ARTICLE

Identification of Hic-5 as a novel regulatory factor for integrin α IIB β 3 activation and platelet aggregation in mice

J.-R. KIM-KANEYAMA,*¹ A. MIYAUCHI,*^{†1} X.-F. LEI,* S. ARITA,* T. MINO,* N. TAKEDA,‡
K. KOU,§ K. ETO,¶ T. YOSHIDA,† T. MIYAZAKI,* S. SHIODA** and A. MIYAZAKI*

*Department of Biochemistry, Showa University School of Medicine, Tokyo; †Department of Clinical Toxicology, Showa University School of Pharmacy, Tokyo; ‡Center for Animal Resources and Development, Kumamoto University, Kumamoto; §Laboratory of Electronic Microscopy, Showa University, Tokyo; ¶Center for iPS Cell Research and Application (CiRA), Kyoto University, Kyoto; and **Department of Anatomy, Showa University School of Medicine, Tokyo, Japan

To cite this article: Kim-Kaneyama Jr, Miyauchi A, Lei X-F, Arita S, Mino T, Takeda N, Kou K, Eto K, Yoshida T, Miyazaki T, Shioda S, Miyazaki A. Identification of Hic-5 as a novel regulatory factor for integrin α IIB β 3 activation and platelet aggregation in mice. *J Thromb Haemost* 2012; **10**: 1867–74.

Summary. *Background:* Integrin α IIB β 3 plays key roles in platelet aggregation and subsequent thrombus formation. Hydrogen peroxide-inducible clone-5 (Hic-5), a member of the paxillin family, serves as a focal adhesion adaptor protein associated with α IIB β 3 at its cytoplasmic strand. *Objectives:* Hic-5 function in α IIB β 3 activation and subsequent platelet aggregation remains unknown. To address this question, platelets from Hic-5^{-/-} mice were analyzed. *Methods and Results:* Hic-5^{-/-} mice displayed a significant hemostatic defect and resistance to thromboembolism, which were explained in part by weaker thrombin-induced aggregation in Hic-5^{-/-} platelets. Mechanistically, Hic-5^{-/-} platelets showed limited activation of α IIB β 3 upon thrombin treatment. Morphological alteration in Hic-5^{-/-} platelets after thrombin stimulation on fibrinogen plates was also limited. As a direct consequence, the quantity of actin co-immunoprecipitating with the activated α IIB β 3 was smaller in Hic-5^{-/-} platelets than in wild-type platelets. *Conclusion:* We identified Hic-5 as a novel and specific regulatory factor for thrombin-induced α IIB β 3 activation and subsequent platelet aggregation in mice.

Keywords: focal adhesion protein, Hic-5, integrin, platelet.

Introduction

Circulating platelets are activated by vascular endothelial dysfunction, which induces morphological changes and

discharge of intracellular granules, leading to platelet aggregation. Platelet aggregation, a key step in thrombus formation, is caused by the activation of integrin α IIB β 3, which was clearly demonstrated in integrin β 3-deficient mice [1]. Integrin α IIB β 3 displays low affinity for its ligands (e.g. fibrinogen and von Willebrand factor), under unstimulated conditions. However, following three-dimensional conformational change due to inside-out signaling, integrin α IIB β 3 shifts to an activated form characterized by higher affinity for its ligands [2–4]. Integrin itself possesses no kinase domain, no enzymatic activity and no actin-binding activity [5]. Rather, integrin activation is controlled by a series of molecules forming a complex with integrin at its cytoplasmic short strand through inside-out signaling, which results in the formation of a signaling platform [5]. More than 30 types of proteins (e.g. talin, kindlin and RIAM) are known to be integrin-associated proteins; [6–11] moreover, these proteins appear to play key roles in inside-out signaling. However, the precise mechanisms governing α IIB β 3 activation and the signaling pathway involving integrin and platelet membrane receptors remain unknown.

Hic-5 (hydrogen peroxide-inducible clone-5), the molecule in question in the current study, was isolated as a gene induced by TGF- β or hydrogen peroxide [12]. The Hic-5 gene codes for a protein localized in focal adhesion, which serves as a cellular attachment point to extracellular matrix [13]. Talin is also localized in focal adhesion and binds to Hic-5 in platelets [14]. It is notable that Hic-5 is an adaptor molecule sharing high homology with paxillin, a member of the four LIM domain family [15]. The paxillin family includes three members, paxillin, Hic-5 and leupaxin. These three molecules are expressed in murine platelets; however, only Hic-5 is expressed in human platelets [16].

Recently, we succeeded in terms of the generation of Hic-5^{-/-} mice; subsequently, our data revealed that the recovery of arterial media following vascular injury is delayed significantly in Hic-5^{-/-} mice [17]. Moreover, our prelimi-

Correspondence: Joo-ri Kim-Kaneyama, Department of Biochemistry, Showa University School of Medicine, 1-5-8 Hatanodai, Shinagawa-ku, Tokyo 142-8555, Japan.

Tel.: +81 3 3784 8116; fax: +81 3 3784 2346.

E-mail: shuri@pharm.showa-u.ac.jp

¹Both authors contributed equally to this study.

Received 13 October 2011, accepted 1 July 2012

ary observations regarding vascular lesions in *Hic-5^{-/-}* mice suggested that morphological changes are suppressed in those platelets attached to a damaged vascular wall immediately after vascular injury. Therefore, we hypothesized that *Hic-5* might play an important role in controlling inside-out and/or outside-in signal(s) in platelet aggregation. Consequently, we examined the role of *Hic-5* in platelet aggregation as well as its molecular mechanism in thrombosis and hemostasis.

Materials and methods

Determination of bleeding times

Adult C57BL/6N mice were anesthetized via intraperitoneal injection of pentobarbital (50 mg kg⁻¹ body weight) and intramuscular injection of xylazine (3 mg kg⁻¹). The tail was cut 1 mm from the tip and immersed in saline at 37 °C. Bleeding time was defined as the time at which all visible signs of bleeding from the incision had abated. The experiment was terminated 10 min after the tail was cut. All animal studies were conducted in accordance with the protocols approved by the institutional committee for animal research of Showa University.

Thromboembolism model

To induce thromboembolism, a mixture of collagen (0.5 mg kg⁻¹, equine collagen; NYCOMED, Munich, Germany) and epinephrine (60 µg kg⁻¹, Sigma) was injected into tail veins of wild-type (*n* = 5) and *Hic-5^{-/-}* mice (*n* = 5). Blood and lungs were collected 15 min after the injection and platelet counts were determined. Three mice from each group were histologically analyzed.

Platelet preparation and aggregation

Whole blood was collected from the heart (100 µL mL⁻¹ blood) of anesthetized mice in acidic citrate dextrose, after which it was centrifuged at 220 × *g* for 10 min. To the supernatant transferred to a new tube, 1 µM prostaglandin E₁ and 1 U mL⁻¹ apyrase were added to prevent platelet activation. The mixture was centrifuged at 400 × *g* for 10 min to sediment a platelet pellet. The pellet was then resuspended in an appropriate volume of modified Tyrode-HEPES buffer at pH 7.4 (10 mM HEPES, 12 mM NaHCO₃, 138 mM NaCl, 5.5 mM glucose, 2.9 mM KCl and 1 mM MgCl₂) and used for the following assay after addition of 1 mM CaCl₂. Platelet aggregation was measured with a platelet aggregometer (PA-200, KOWA, Nagoya, Japan) following stimulation with thrombin (Sigma-Aldrich, St. Louis, MO, USA). The degree of platelet aggregation was expressed as %light transmission and the maximal aggregation (Tmax) was expressed as % light transmission determined 10 min after addition of the stimulus.

Flow cytometry

To examine αIIbβ3 activation, whole blood was incubated for 10 min at room temperature with PE-conjugated JON/A (emfret, Eibelstadt, Germany) in the presence of ADP (0.1 or 1 µM), Convulxin (10 or 100 ng mL⁻¹) or human thrombin (0.01 or 0.5 U mL⁻¹). JON/A binding to platelets was quantified with a flow cytometer (BD Biosciences, San Jose, CA, USA). Platelets were gated by forward and side scatters. P-selectin surface expression was analyzed via detecting FITC-conjugated CD62 (emfret, Eibelstadt, Germany) binding to platelets using the flow cytometer.

Immunoblotting

Platelet lysates, which were treated with RIPA buffer (20 mM Tris-HCl, pH 8.0, 0.5% Triton-X 100 and 5 mM EDTA) supplemented with proteinase inhibitor cocktail (Sigma-Aldrich, St. Louis, MO, USA), were separated by electrophoresis on 10% SDS-polyacrylamide gel and transferred to a polyvinylidene difluoride membrane (Millipore, Bedford, MA, USA). Immunodetection was performed utilizing the primary antibodies against *Hic-5* (BD Biosciences, San Jose, CA, USA), paxillin, vinculin, GAPDH, β-actin (these antibodies were purchased from Sigma-Aldrich), integrin β3 (Santa Cruz Biotechnology), kindlin-3 (abcam, Cambridge, UK), ILK (BD Biosciences), followed by the appropriate secondary antibodies conjugated with horseradish peroxidase.

Electron microscopic observation

Immunoelectron microscopy was performed as previously described [18]. Briefly, the sections were stained first with the primary antibodies (anti-*Hic-5*, BD Biosciences; anti-αIIbβ3 (Leo), emfret; anti-β3, Santa Cruz, Santa Cruz, CA, USA), followed by incubation with their appropriate secondary antibodies (BBI International, Cardiff, UK) conjugated with smaller sized (5 nm) and larger sized (10 or 15 nm) colloidal golds, respectively; subsequently, sections were evaluated with a JEM-1200 EXII electron microscope (JEOL, Tokyo, Japan) at an accelerating voltage of 80 kV. For scanning electron microscopy analysis, cover slips were coated overnight with 1 mg mL⁻¹ human fibrinogen and then blocked for 1 h with 1% BSA in PBS. Platelets were activated with 0.01 U mL⁻¹ thrombin shortly before plating on fibrinogen-, fibronectin- or collagen-coated cover slips. Platelets were allowed to spread for 30 min, after which they were fixed in 2.5% glutaraldehyde in Tyrode's-HEPES buffer and processed for scanning electron microscopy. Numbers of platelets displaying filopodia longer than 3.5 µm as well as total platelets were counted in 10 separate fields and totaled for each sample (Fig. 1B). The ratios of platelets exhibiting longer filopodia to total platelets were calculated and compared between wild-type and *Hic-5^{-/-}* platelets. In another set of experiments, platelets were seeded on fibrinogen-coated cover slips in the presence of

MnCl₂ (3 mM of Mn²⁺) for analysis of spreading filopodia as above.

Immunoprecipitation MALDI-TOF-MS

Platelets were treated with thrombin for 10 min at room temperature; platelets were then lysed upon the addition of 2 × IP buffer (1% Triton X-100, 150 mM NaCl, 20 mM Hepes, pH 7.4, 1 mM Na₃V0₄, 1 mM NAF) containing a mixture of proteinase inhibitors (Sigma-Aldrich). Dynabeads conjugated with an antibody against αIIbβ₃ (Leo) or control IgG were added to lysates (5 μg per sample) and rotated at room temperature for 60 min. Samples were washed with 1 × IP buffer three times and soaked in elution buffer for 10 min. Immunoprecipitated proteins were subjected to 10% SDS-PAGE for immunoblotting or MALDI-TOF. The MALDI-TOF analysis was performed as previously described [19]. Briefly, the excised polyacrylamide gel pieces were incubated

with wash solution (50% acetonitrile plus 50 mM ammonium bicarbonate) for 10 min. Disulfide bond cleavage was effected with 10 mM dithiothreitol and 100 mM carbamidomethylation in the presence of 55 mM iodine acetamide. The dried gel pieces were soaked in 5 μL of trypsin solution (12.5 ng μL⁻¹ trypsin and 10 mM ammonium bicarbonate) and incubated overnight. On the following day, sonicated samples were spotted on a stainless steel MALDI carrier tray with matrix. MALDI-time-of-flight (TOF)-MS was conducted on an AXIMA Performance (Shimadzu, Kyoto, Japan). The tryptically-digested proteins were identified using the MASCOT database search engine with National Center for Biotechnology Information and the Swissprot database with a mass tolerance below 0.1 Da of the monoisotopic peaks.

Statistical analysis

All data are expressed as means ± SD. The two-unpaired *t*-test (Figs 2B, 3B-F and 1B), the Mann-Whitney *U*-test (Fig. 2A) and the chi-square test (Fig. 4A) were used to detect differences. A value of *P* < 0.05 was considered to be significant.

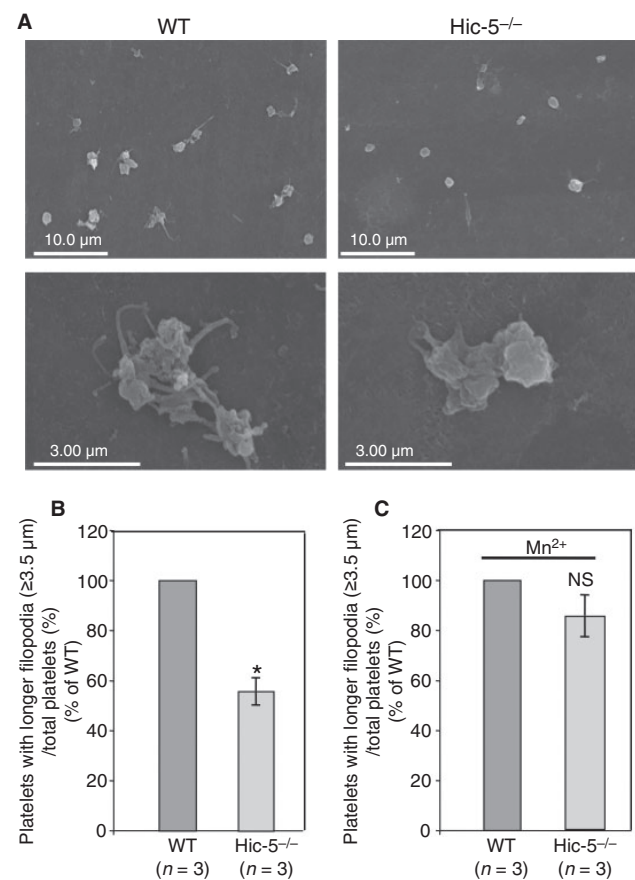


Fig. 1. Limited platelet morphological changes due to Hic-5 deficiency. (A) Scanning electron micrograph of wild-type or Hic-5^{-/-} platelets. Washed wild-type and Hic-5^{-/-} platelets were stimulated with 0.1 U mL⁻¹ thrombin; subsequently, platelets were allowed to adhere to immobilized fibrinogen for 30 min. Scale bars represent 10 μm (upper) and 3 μm (lower). (B) The ratios of platelets displaying filopodia longer than 3.5 μm to total platelets are presented as % of wild type (see 'Methods' for details). (C) Wild-type and Hic-5^{-/-} platelets were plated on fibrinogen-coated cover slips for 30 min in the presence of 3 mM MnCl₂ (Mn²⁺) followed by analysis of platelet spreading as (B). Values are means ± SEM from three independent experiments. **P* < 0.05; NS, no significant difference.

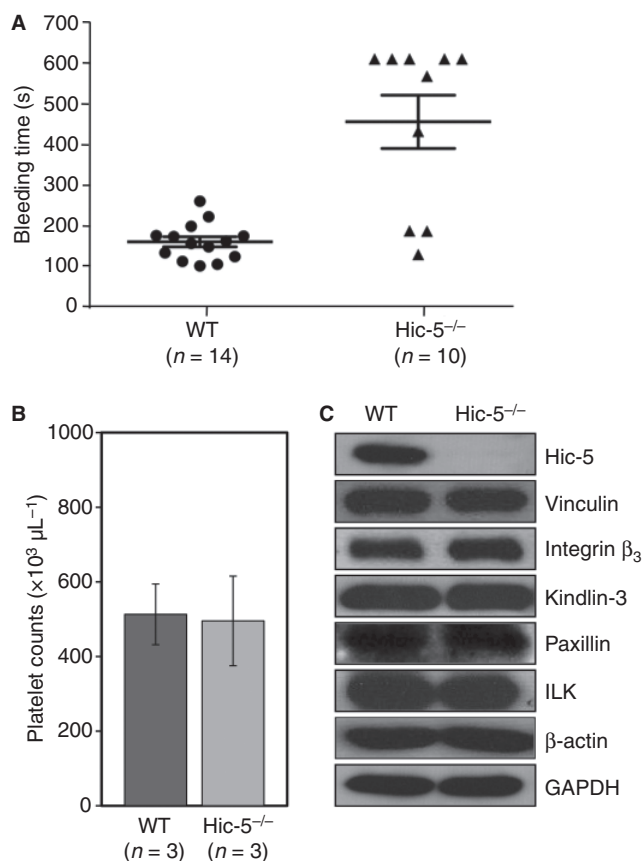


Fig. 2. Prolonged bleeding times in Hic-5^{-/-} mice. (A) Tail bleeding time in wild-type (circle) and Hic-5^{-/-} mice (triangle). The tails of wild-type and Hic-5^{-/-} mice were cut and the duration of bleeding was measured. Statistical significance was determined with Mann-Whitney *U*-tests (*P* = 0.0016). (B) Peripheral platelet counts in wild-type and Hic-5^{-/-} mice. (C) Western blot analyses of platelet lysates from wild-type and Hic-5^{-/-} mice demonstrating Hic-5, vincullin, integrin β₃, kindlin-3, paxillin, ILK, β-actin and GAPDH expression. GAPDH served as a loading control.

Result

To address the function of *Hic-5* in platelets, the hemostatic abilities of wild-type and *Hic-5*^{-/-} mice were tested via tail bleeding in 8–10-week-old offspring of *Hic-5*^{+/-} and *Hic-5*^{+/-} mating under conditions with genotype blind until study completion. *Hic-5*^{-/-} mice exhibited a pronounced hemostatic defect in comparison to the wild-type background (KO, 7.60 ± 3.40 min vs. wt, 2.72 ± 0.75 min) (Fig. 1A). To determine whether the hemostatic disorder was due to defective thrombopoiesis, platelet counts were compared between wild-type and *Hic-5*^{-/-} mice. However, *Hic-5*^{-/-} mice demonstrated platelet counts similar to those of wild-type mice (Fig. 2B). Additionally, expression levels of the proteins, namely, integrin

β3, kindlin-3, vinculin, paxillin, integrin-linked kinase and β-actin, were unaltered (Fig. 2C).

To further evaluate the *in vivo* consequence of *Hic-5* deficiency, we examined a model of thromboembolism challenged by collagen and epinephrine. The numbers of platelets in challenged *Hic-5*^{-/-} mice were significantly larger than those in *Hic-5*^{+/-} mice (Fig. 4A). Furthermore, histological analysis of three *Hic-5*^{+/-} mice revealed multiple pulmonary thromboembolism in every mouse (Fig. 4B, upper panel). In a sharp contrast, three *Hic-5*^{-/-} mice did not show any pulmonary thromboembolism (Fig. 4B, lower panel). These data indicate that *Hic-5*^{-/-} mice are more resistant to thromboembolism than *Hic-5*^{+/-} mice.

To determine whether the hemostatic defect and resistance to thromboembolism in *Hic-5*^{-/-} mice are attributable to the

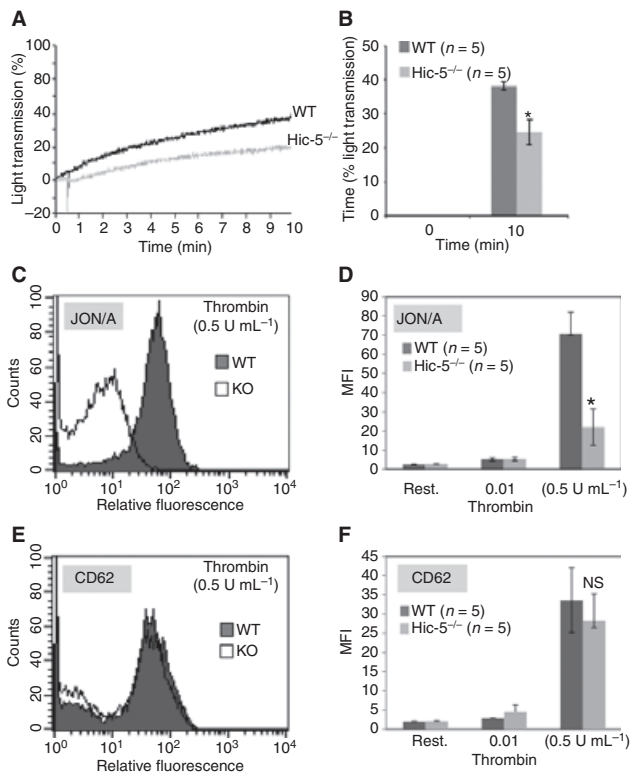


Fig. 3. Limited platelet aggregation and integrin αIIbβ3 activation in *Hic-5*^{-/-} platelets in response to thrombin. (A) Washed platelets were stimulated with thrombin; subsequently, platelet aggregation was monitored employing an aggregometer at 37 °C for 10 min. The aggregation was assessed by measuring %light transmission. In contrast to wild-type platelets, thrombin-induced aggregation was significantly limited in *Hic-5*^{-/-} platelets. (B) Statistical analysis showing significantly different T_{max} between wild-type mice and *Hic-5*^{-/-} platelets after addition of thrombin. (C) Integrin αIIbβ3 activation was assessed by flow cytometry of wild-type or *Hic-5*^{-/-} platelets following stimulation with thrombin. Platelets were incubated with PE-labeled anti-mouse αIIbβ3 monoclonal antibody (JON/A) specific for the activated conformation of mouse αIIbβ3. (D) *Hic-5*^{-/-} platelets showed limited activation of integrin αIIbβ3 after stimulation with 0.5 U mL⁻¹ thrombin. (E, F) Thrombin-induced platelet degranulation measured by the surface expression of CD62 (P-selection) was not affected in *Hic-5*^{-/-} platelets. (F) Resting (Rest.) platelets were used as control. MFI, mean fluorescence intensity. (**P* < 0.05; NS, no significant difference).

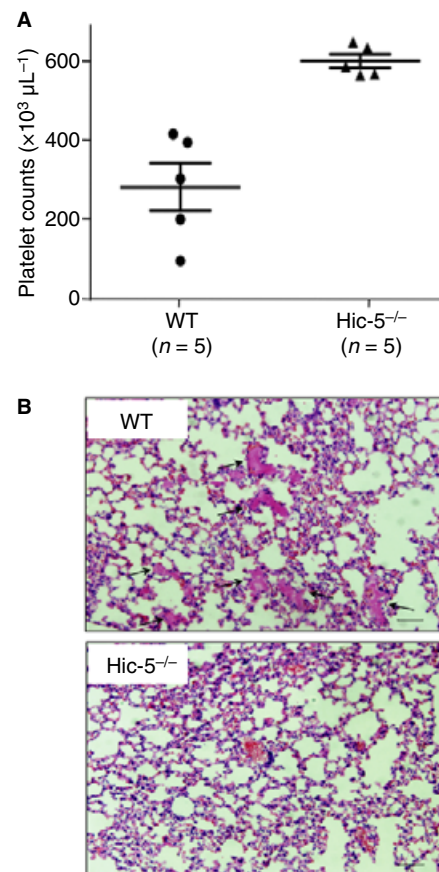


Fig. 4. Deficiency of *Hic-5* protects mice against thromboembolism. (A) Mice were treated with 600 ng g⁻¹ collagen plus 60 ng g⁻¹ epinephrine by intravenous injection via tail veins and platelets were counted 15 min after injection. Each symbol represents the platelet count of a single mouse. Bars represent the mean values of the two groups. The numbers of platelets after the challenge were significantly smaller in wild-type mice (285 ± 108 × 10³ μL⁻¹, circle, *n* = 5) than in *Hic-5*^{-/-} mice (606 ± 33 × 10³ μL⁻¹, triangle, *n* = 5) (mean ± SEM; *P* < 0.001). (B) Light microscopy (H&E staining) of the lungs after collagen/epinephrine injection, revealing extensive platelet thromboembolism (arrows) in wild-type mice (*n* = 3) but no thrombosis in *Hic-5*^{-/-} mice (*n* = 3). Scale bars, 100 μm.

impairment of platelet function, platelet aggregation induced by thrombin was assessed. Representative aggregometric tracing of platelets demonstrated weaker aggregation (lower %light transmission) of *Hic-5*^{-/-} platelets after thrombin stimulation compared with *Hic-5*^{+/+} platelets (Fig. 3A). As a result, T_{\max} following the addition of thrombin was limited to 27% in *Hic-5*^{-/-} platelets relative to wild-type platelets (36%) (Fig. 3B). This result was suggestive of a possible dysfunction of platelets in *Hic-5*^{-/-} mice. Interestingly, T_{\max} values following the addition of ADP or collagen were not statistically different between *Hic-5*^{+/+} and *Hic-5*^{-/-} platelets (data not shown).

Platelet aggregation occurs consequent to the activation of α IIb β 3. To test whether activation of α IIb β 3 is actually limited in *Hic-5*^{-/-} platelets, we measured agonist-induced binding of JON/A-PE antibody, which selectively binds to activated α IIb β 3 of mouse platelets [20]. Integrin α IIb β 3 in wild-type platelets was activated in response to thrombin (Fig. 3C,D). In addition, the amount of activated α IIb β 3 in *Hic-5*^{-/-} platelets was much smaller than that in wild-type platelets (Fig. 3C,D). Thus, *Hic-5* deficiency led to limited thrombin activation of α IIb β 3. *Hic-5*^{-/-} platelets also showed limited activation of integrin α IIb β 3 after stimulation with a PAR4 agonist (Fig. S1D). Notably, other agonists such as ADP, the GPVI receptor agonist Convulxin, the TxA2 analog U46619 and MnCl₂ induced α IIb β 3 activation in *Hic-5*^{+/+} and *Hic-5*^{-/-} platelets to the same extents (Fig. 2A). Furthermore, there was no significant difference in the surface expression of integrin α IIb β 3 between *Hic-5*^{+/+} and *Hic-5*^{-/-} platelets (Fig. 2C). P-selectin surface translocation by thrombin or Convulxin in *Hic-5*^{-/-} platelets was similar to that in *Hic-5*^{+/+} platelets (Fig. 3E,F and Fig. S1B). This suggests a selective defect in α IIb β 3-dependent aggregation in response to thrombin rather than an impairment of general signaling pathways in *Hic-5*^{-/-} platelets.

Hic-5 is a focal adhesion scaffolding protein that binds to integrin $\alpha_4\beta_1$ [21]. Activation of α IIb β 3 was limited in *Hic-5*^{-/-} platelets (Fig. 3); consequently, we hypothesized that *Hic-5* might bind to α IIb β 3 other than integrin $\alpha_4\beta_1$. In order to test this possibility, the association between *Hic-5* and α IIb β 3 was evaluated via immunoprecipitation. As shown in Fig. 5(A), *Hic-5* co-precipitated with α IIb β 3 in the presence or absence of thrombin involving anti- α IIb β 3 antibody. Moreover, the colocalization of α IIb β 3 and *Hic-5* was examined utilizing an immunoelectron microscopic method in platelets from mice (Fig. 5B) and humans (Fig. 5C). *Hic-5* and α IIb β 3 were detected by their primary antibodies followed by the secondary antibodies conjugated with smaller sized (5 nm) and larger sized (10 and 15 nm) gold colloids, respectively. The colocalization of α IIb β 3 and *Hic-5* was demonstrated by the proximity of these different sized colloids. Association of α IIb β 3 and *Hic-5* in both mouse and human platelets suggested the possibility that *Hic-5* may modulate the function of α IIb β 3 in platelets. It is also noteworthy that there was no difference in the numbers of gold colloids in resting and activated *Hic-5*^{-/-} platelet surfaces (data not shown).

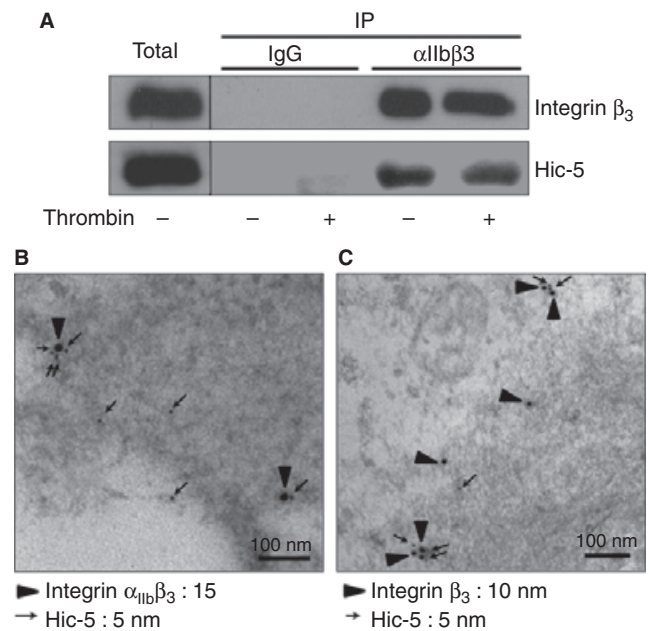


Fig. 5. Association of *Hic-5* with integrin α IIb β 3 in mouse and human platelets. (A) Co-immunoprecipitation of *Hic-5* with α IIb β 3 in mouse platelets treated with or without 1 U mL⁻¹ thrombin for 10 min. Total platelet extract and its immunoprecipitates prepared with normal IgG and anti- α IIb β 3 antibody were subjected to western blot. Integrin β 3 and *Hic-5* were detected in the platelet extract and immunoprecipitates. (B, C) Co-localization of *Hic-5* and α IIb β 3 in mouse platelets (B) and human platelets (C). Immunogold electron microscopy of wild-type platelets was performed. Platelets were treated with 1 U mL⁻¹ thrombin; subsequently, endogenous α IIb β 3 and *Hic-5* were detected utilizing the secondary antibodies conjugated with larger sized (10 or 15 nm) and smaller sized (5 nm) gold colloids, respectively. Arrows indicate *Hic-5* (5 nm gold colloids). Arrowheads indicate α IIb β 3 (10 or 15 nm gold colloids).

An α IIb β 3-associated protein in platelets, *Hic-5* probably acts as an adaptor molecule and a scaffold for various functionally interacting molecules. In order to analyze the changes in the components of α IIb β 3 complexes due to *Hic-5* deficiency, we compared the α IIb β 3 interacting molecules between wild-type and *Hic-5*^{-/-} platelets. Platelets were immunoprecipitated with beads conjugated to the anti- α IIb β 3 antibody; subsequently, molecules exhibiting different levels of co-precipitation between wild-type and *Hic-5*^{-/-} platelets were analyzed by MALDI-TOF-MS. As a result, we found that the amount of actin co-precipitating with activated α IIb β 3 was smaller in *Hic-5*^{-/-} platelets than that in wild-type platelets (Fig. 6, arrow).

Platelets demonstrate dynamic morphological changes such as the extension of lamellipodia and filopodia due to agonist stimulation. These morphological changes are caused by remodeling of actin cytoskeleton. Thus, actin plays key roles in cytoskeletal construction of platelets. *Hic-5* depletion from the α IIb β 3 complex led to limited integrin anchorage to the actin cytoskeletal matrix (Fig. 6). Therefore, we hypothesized that platelet morphological changes might be affected in *Hic-5*^{-/-} platelets. Wild-type and *Hic-5*^{-/-} platelets were stimulated with thrombin and placed on a fibrinogen-coated

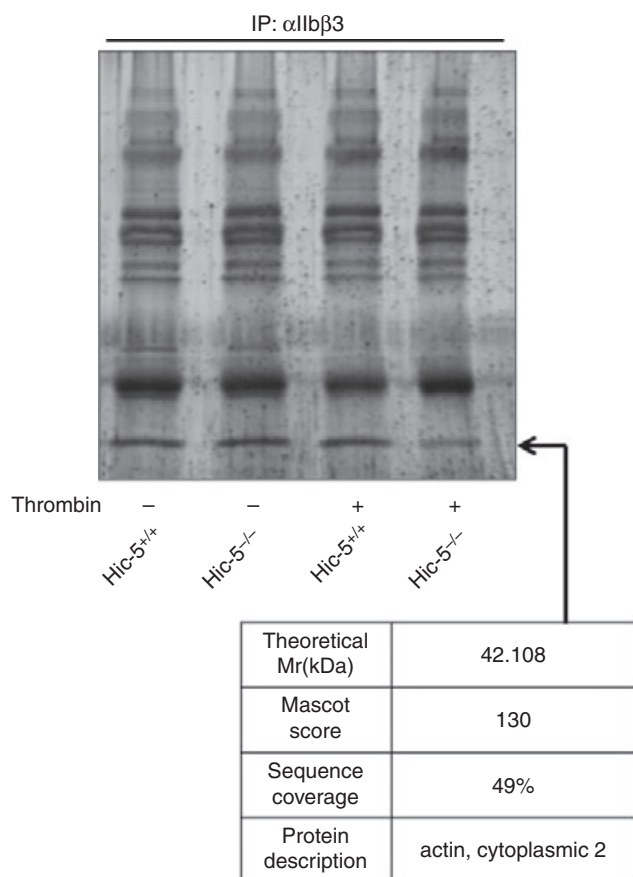


Fig. 6. Co-immunoprecipitated actin with activated integrin α IIB β 3 decreased in *Hic-5*^{-/-} platelets. Flamingo-stained SDS-polyacrylamide gel following electrophoresis of immunoprecipitated proteins. Immunoprecipitation was conducted employing wild-type and *Hic-5*^{-/-} platelet lysates and antibody to α IIB β 3 in the presence or the absence of 1 U mL⁻¹ thrombin for 10 min. The band indicated by the arrow was identified by MALDI-TOF MS analysis.

glass slide for analysis with a scanning electron microscope. The findings revealed that the numbers of platelets displaying filopodia longer than 3.5 μ m were smaller in *Hic-5*^{-/-} platelets than in wild-type platelets (Fig. 1A,B), which indicated that *Hic-5* deficiency affects platelet morphological changes consequent to actin cytoskeleton remodeling. Moreover, this change was canceled when platelets were placed on a fibrinogen-coated glass slide in the presence of Mn²⁺ (Fig. 1C). Thus, *Hic-5* is not essential for α IIB β 3-dependent outside-in signaling. Finally, the extension of filopodia in *Hic-5*^{-/-} platelets was not affected by extracellular matrices themselves such as collagen and fibronectin (Fig. S2).

Discussion

Hic-5^{-/-} mice grew normally, as did wild-type mice with no apparent abnormality [17]. These results suggested that *Hic-5* is functionally replaceable with paxillin, another member of the paxillin family, which includes *Hic-5*, under physiological conditions in mice. Although no difference in paxillin protein

expression level was evident between *Hic-5*^{-/-} and *Hic-5*^{+/+} platelets (Fig. 2C), this level of paxillin may be sufficient to compensate for *Hic-5* deficiency. Moreover, no difference was observed in the number of platelets between *Hic-5*^{-/-} and *Hic-5*^{+/+} mice; thus, it is unlikely that *Hic-5* deficiency in megakaryocytes might affect the platelet production process (Fig. 2B).

During electron microscopic evaluation of arterial restenosis after wire injury in mice,¹⁴ we noted as a preliminary result that *Hic-5*^{-/-} platelets, unlike *Hic-5*^{+/+} platelets, formed unstable platelet morphology in thrombosis. This finding led us to examine hemostatic function in *Hic-5*^{-/-} mice. Indeed, we observed elongation of bleeding time (Fig. 2A) and limited platelet aggregation in *Hic-5*^{-/-} mice (Fig. 4). Platelet aggregation is a key step in thrombus formation. Moreover, *Hic-5* is the sole member of the paxillin family expressed in human platelets, which is indicative of the indispensable roles of *Hic-5* in human platelets. Therefore, identification of *Hic-5* function in platelet aggregation is essential in order to advance the understanding of platelet dysfunction and subsequent hemorrhagic diseases in human.

Platelet aggregation is caused by the eventual activation of α IIB β 3, the focal adhesion receptor crucial for aggregation [22]. The activation of α IIB β 3 is controlled by the two types of intracellular molecular mechanisms, namely, inside-out and outside-in signaling. Dysfunctions of these mechanisms play a role in Glanzmann's thrombasthenia and other platelet disorders consequent to quantitative or qualitative abnormality of α IIB β 3. Identification of a novel molecule involved in the regulation of α IIB β 3 activation may lead to a novel therapeutic target.

In this study, we proposed that *Hic-5* may be a novel α IIB β 3 regulatory factor based on the findings that *Hic-5* demonstrated interaction and co-localization with α IIB β 3 (Fig. 5) and that thrombin-induced α IIB β 3 activation was limited in *Hic-5*^{-/-} platelets (Fig. 3). *Hic-5* is a well-known adaptor protein, which functions as a scaffold for various interacting molecules and participates in integrin signal transduction [13,16,23,24]. In order to identify the changes attributable to *Hic-5* deficiency in the α IIB β 3-interacting proteins in platelets, we conducted immunoprecipitation followed by MALDI-TOF-MS (Fig. 6). As a result, we determined that the amount of actin co-precipitating with activated α IIB β 3 decreased in *Hic-5*^{-/-} platelets. Thus, *Hic-5* is likely to act as a scaffold that stabilizes the association between α IIB β 3 and actin. When the scaffold is destabilized consequent to *Hic-5* deficiency, the binding between α IIB β 3 and actin may weaken. Integrin α IIB β 3 is known to interact indirectly with actin in the presence of vinculin and talin mediation [25–28]. Vinculin and talin binding to *Hic-5* was examined via GST pull-down assay. These data indicated that *Hic-5* behaves as an intermedialator in conjunction with vinculin and talin in the association between α IIB β 3 and actin [15].

Complex formation of *Hic-5* and CrKL was also noted in studies regarding actin cytoskeleton regulation [29]. CrKL, Wiskott-Aldrich syndrome protein (WASP) and syk play key

roles in adhesion and migration of leukocytes. During platelet aggregation, the majority of Hic-5, CrKL, syk and WASP localized in cytoplasm migrates to actin cytoskeleton; moreover, Hic-5 is thought to serve as an essential scaffold for CrKL during the migration process [29]. Moreover, when platelets were stimulated and stretched on fibrinogen, Hic-5 was phosphorylated by protein-rich tyrosine kinase 2 (Pyk2); eventually, Hic-5 localization shifted to the terminal region of actin filaments [30]. These findings were suggestive of a cooperative relationship between Hic-5 and actin in terms of morphological change in platelets due to reassembly of actin cytoskeleton.

In addition, the number of Hic-5^{-/-} platelets characterized by longer filopodia decreased in comparison with wild-type platelets (Fig. 1B). Platelet adhesion and aggregation occur as a result of the tangling of stretched filopodia; this process leads to the formation of clumps of deformed platelets in which each platelet is indistinguishable from adjacent cells. Thus, Hic-5 is believed to play an important role in platelet morphological change and aggregation, which are mediated by actin cytoskeleton reassembly. The aforementioned results suggested that Hic-5 regulates α IIB β 3 activation by thrombin and participates in the process of thrombus formation, including platelet aggregation.

In summary, the current study demonstrated essential roles of Hic-5 in α IIB β 3 activation and platelet aggregation in mice. Paxillin, a molecule belonging to the family that includes Hic-5, is not expressed in human platelets; consequently, Hic-5 deficiency is expected to exert more serious effects on human platelet function relative to mouse platelet function. Therefore, it is possible that the Hic-5 gene could be responsible for platelet disorders in humans with unknown molecular basis. Furthermore, because platelets are involved in both thrombosis and hemostasis, elucidation of pathophysiological implications of Hic-5 in human platelets may provide novel mechanistic insights into more common and fatal human diseases such as stroke and acute coronary syndrome, the leading causes of death in western countries.

Addendum

Contribution: A. Miyauchi, Jr Kim-Kaneyama, N. Takeda, K. Kou, S. Arita, X.-F. Lei, K. Kou, T. Mino and T. Miyazaki performed experiments; Jr Kim-Kaneyama and A. Miyauchi analyzed results and prepared the figures; Jr Kim-Kaneyama, K. Eto, T. Yoshida, S. Shioda and A. Miyazaki designed the research and wrote the paper; all authors approved the final manuscript.

Acknowledgements

We gratefully acknowledge A. Sasai for her contribution to basic data collection as the theme for her master's degree. This work was supported by Grants-in-Aid for Young Scientists (B) (20790076 and 23791090 to K.-K. J.), Scientific Research (C) (23591341 to A. M.) from the Japan Society

for the Promotion of Science and MEXT-Supported Program for the Strategic Research Foundation at Private Universities, 2012-2016.

Disclosure of Conflict of Interests

The authors state that they have no conflict of interests.

Supporting Information

Additional Supporting Information may be found in the online version of this article:

Figure S1. Analyses of integrin α IIB β 3 activation and P-selectin surface expression after agonist stimulation in wild-type and Hic-5^{-/-} platelets.

Figure S2. Platelet spreading on immobilized fibronectin or collagen.

Please note: Wiley-Blackwell is not responsible for the content or functionality of any supporting materials supplied by the authors. Any queries (other than missing material) should be directed to the corresponding author for the article.

References

- 1 Denis CV, Wagner DD. Platelet adhesion receptors and their ligands in mouse models of thrombosis. *Arterioscler Thromb Vasc Biol* 2007; **27**: 728–39.
- 2 Barczyk M, Carracedo S, Gullberg D. Integrins. *Cell Tissue Res* 2010; **339**: 269–80.
- 3 Hughes PE, Diaz-Gonzalez F, Leong L, Wu C, McDonald JA, Shattil SJ, Ginsberg MH. Breaking the integrin hinge. A defined structural constraint regulates integrin signaling. *J Biol Chem* 1996; **271**: 6571–4.
- 4 Sakai T, Zhang Q, Fassler R, Mosher DF. Modulation of beta1A integrin functions by tyrosine residues in the beta1 cytoplasmic domain. *J Cell Biol* 1998; **141**: 527–38.
- 5 Legate KR, Fassler R. Mechanisms that regulate adaptor binding to beta-integrin cytoplasmic tails. *J Cell Sci* 2009; **122**: 187–98.
- 6 Moser M, Nieswandt B, Ussar S, Pozgajova M, Fassler R. Kindlin-3 is essential for integrin activation and platelet aggregation. *Nat Med* 2008; **14**: 325–30.
- 7 Petrich BG, Marchese P, Ruggeri ZM, Spiess S, Weichert RA, Ye F, Tiedt R, Skoda RC, Monkley SJ, Critchley DR, Ginsberg MH. Talin is required for integrin-mediated platelet function in hemostasis and thrombosis. *J Exp Med* 2007; **204**: 3103–11.
- 8 Nieswandt B, Moser M, Pleines I, Varga-Szabo D, Monkley S, Critchley D, Fassler R. Loss of talin1 in platelets abrogates integrin activation, platelet aggregation, and thrombus formation in vitro and in vivo. *J Exp Med* 2007; **204**: 3113–8.
- 9 Tadokoro S, Shattil SJ, Eto K, Tai V, Liddington RC, de Pereda JM, Ginsberg MH, Calderwood DA. Talin binding to integrin beta tails: a final common step in integrin activation. *Science* 2003; **302**: 103–6.
- 10 Ma YQ, Qin J, Wu C, Plow EF. Kindlin-2 (Mig-2): a co-activator of beta3 integrins. *J Cell Biol* 2008; **181**: 439–46.
- 11 Schaller MD, Otey CA, Hildebrand JD, Parsons JT. Focal adhesion kinase and paxillin bind to peptides mimicking beta integrin cytoplasmic domains. *J Cell Biol* 1995; **130**: 1181–7.

- 12 Shibamura M, Mashimo J, Kuroki T, Nose K. Characterization of the TGF beta 1-inducible hic-5 gene that encodes a putative novel zinc finger protein and its possible involvement in cellular senescence. *J Biol Chem* 1994; **269**: 26767–74.
- 13 Tumbarello DA, Turner CE. Hic-5 contributes to epithelial-mesenchymal transformation through a RhoA/ROCK-dependent pathway. *J Cell Physiol* 2007; **211**: 736–47.
- 14 Hagmann J, Grob M, Welman A, van Willigen G, Burger MM. Recruitment of the LIM protein hic-5 to focal contacts of human platelets. *J Cell Sci* 1998; **111**: 2181–8.
- 15 Thomas SM, Hagel M, Turner CE. Characterization of a focal adhesion protein, Hic-5, that shares extensive homology with paxillin. *J Cell Sci* 1999; **112**: 181–90.
- 16 Rathore VB, Okada M, Newman PJ, Newman DK. Paxillin family members function as Csk-binding proteins that regulate Lyn activity in human and murine platelets. *Biochem J* 2007; **403**: 275–81.
- 17 Kim-Kaneyama JR, Takeda N, Sasai A, Miyazaki A, Sata M, Hirabayashi T, Shibamura M, Yamada G, Nose K. Hic-5 deficiency enhances mechanosensitive apoptosis and modulates vascular remodeling. *J Mol Cell Cardiol* 2011; **50**: 77–86.
- 18 Kim-Kaneyama JR, Suzuki W, Ichikawa K, Ohki T, Kohno Y, Sata M, Nose K, Shibamura M. Uni-axial stretching regulates intracellular localization of Hic-5 expressed in smooth-muscle cells in vivo. *J Cell Sci* 2005; **118**: 937–49.
- 19 Cid C, Garcia-Bonilla L, Camafeita E, Burda J, Salinas M, Alcazar A. Proteomic characterization of protein phosphatase 1 complexes in ischemia-reperfusion and ischemic tolerance. *Proteomics* 2007; **7**: 3207–18.
- 20 Bergmeier W, Schulte V, Brockhoff G, Bier U, Zirngibl H, Nieswandt B. Flow cytometric detection of activated mouse integrin alphaIIb beta3 with a novel monoclonal antibody. *Cytometry* 2002; **48**: 80–6.
- 21 Liu S, Thomas SM, Woodside DG, Rose DM, Kiosses WB, Pfaff M, Ginsberg MH. Binding of paxillin to alpha4 integrins modifies integrin-dependent biological responses. *Nature* 1999; **402**: 676–81.
- 22 Hodivala-Dilke KM, McHugh KP, Tsakiris DA, Rayburn H, Crowley D, Ullman-Cullere M, Ross FP, Collier BS, Teitelbaum S, Hynes RO. Beta3-integrin-deficient mice are a model for Glanzmann thrombasthenia showing placental defects and reduced survival. *J Clin Invest* 1999; **103**: 229–38.
- 23 Fujita H, Kamiguchi K, Cho D, Shibamura M, Morimoto C, Tachibana K. Interaction of Hic-5, A senescence-related protein, with focal adhesion kinase. *J Biol Chem* 1998; **273**: 26516–21.
- 24 Arthur JF, Shen Y, Gardiner EE, Coleman L, Kenny D, Andrews RK, Berndt MC. TNF receptor-associated factor 4 (TRAF4) is a novel binding partner of glycoprotein Ib and glycoprotein VI in human platelets. *J Thromb Haemost* 2011; **9**: 163–72.
- 25 Bass MD, Smith BJ, Prigent SA, Critchley DR. Talin contains three similar vinculin-binding sites predicted to form an amphipathic helix. *Biochem J* 1999; **341**: 257–63.
- 26 Gingras AR, Bate N, Goult BT, Hazelwood L, Canestrelli I, Grossmann JG, Liu H, Putz NS, Roberts GC, Volkman N, Hanein D, Barsukov IL, Critchley DR. The structure of the C-terminal actin-binding domain of talin. *EMBO J* 2008; **27**: 458–69.
- 27 Gingras AR, Ziegler WH, Frank R, Barsukov IL, Roberts GC, Critchley DR, Emsley J. Mapping and consensus sequence identification for multiple vinculin binding sites within the talin rod. *J Biol Chem* 2005; **280**: 37217–24.
- 28 Hemmings L, Rees DJ, Ohanian V, Bolton SJ, Gilmore AP, Patel B, Priddle H, Trevithick JE, Hynes RO, Critchley DR. Talin contains three actin-binding sites each of which is adjacent to a vinculin-binding site. *J Cell Sci* 1996; **109**: 2715–26.
- 29 Oda A, Ochs HD, Lasky LA, Spencer S, Ozaki K, Fujihara M, Handa M, Ikebuchi K, Ikeda H. CrkL is an adapter for Wiskott-Aldrich syndrome protein and Syk. *Blood* 2001; **97**: 2633–9.
- 30 Osada M, Ohmori T, Yatomi Y, Satoh K, Hosogaya S, Ozaki Y. Involvement of Hic-5 in platelet activation: integrin alphaIIb beta3-dependent tyrosine phosphorylation and association with proline-rich tyrosine kinase 2. *Biochem J* 2001; **355**: 691–7.

Identification of Hic-5 as a Novel Scaffold for the MKK4/p54 JNK Pathway in the Development of Abdominal Aortic Aneurysms

Xiao-Feng Lei, PhD; Joo-ri Kim-Kaneyama, PhD; Shigeko Arita-Okubo, BSc; Stefan Offermanns, MD, PhD; Hiroyuki Itabe, PhD; Takuro Miyazaki, PhD; Akira Miyazaki, MD, PhD

Background—Although increased amounts of reactive oxygen species in the pathogenesis of abdominal aortic aneurysm (AAA) are well documented, the precise molecular mechanisms by which reactive oxygen species induce AAAs have not been fully elucidated. This study focused on the role of hydrogen peroxide-inducible clone 5 (Hic-5), which is induced by hydrogen peroxide and transforming growth factor- β , in the cellular signaling of AAA pathogenesis.

Methods and Results—Using the angiotensin II-induced AAA model in *Apoe*^{-/-} mice, we showed that *Apoe*^{-/-}*Hic-5*^{-/-} mice were completely protected from AAA formation and aortic rupture, whereas *Apoe*^{-/-} mice were not. These features were similarly observed in smooth muscle cell-specific Hic-5-deficient mice. Furthermore, angiotensin II treatment induced Hic-5 expression in a reactive oxygen species-dependent manner in aortic smooth muscle cells in the early stage of AAA development. Mechanistic studies revealed that Hic-5 interacted specifically with c-Jun N-terminal kinase p54 and its upstream regulatory molecule mitogen-activated protein kinase kinase 4 as a novel scaffold protein, resulting in the expression of membrane type 1 matrix metalloproteinase and matrix metalloproteinase 2 activation in aortic smooth muscle cells.

Conclusion—Hic-5 serves as a novel scaffold protein that specifically activates the mitogen-activated protein kinase kinase 4/p54 c-Jun N-terminal kinase pathway, thereby leading to the induction and activation of matrix metalloproteinases in smooth muscle cells and subsequent AAA formation. Our study provided a novel therapeutic option aimed at inhibiting the mitogen-activated protein kinase kinase 4–Hic-5–p54 c-Jun N-terminal kinase pathway in the vessel wall, particularly through Hic-5 inhibition, which may be used to produce more precise and effective therapies. (*J Am Heart Assoc.* 2014;3:e000747 doi: 10.1161/JAHA.113.000747)

Key Words: aneurysm • Hic-5 • JNK-signaling scaffold protein • smooth muscle

Abdominal aortic aneurysm (AAA) is an age-associated disease that affects approximately 5% of elderly individuals and is responsible for a significant number of deaths in Western countries.¹ Oxidative stress, generated by excessive reactive oxygen species (ROS), has been shown to play causal roles in AAAs.^{2,3} Animal models deficient in ROS-generating

enzymes, such as inducible nitric oxide synthase, NADPH oxidase-1, and p47phox, clearly demonstrated preserved aortic wall morphology and attenuated AAA development.^{4–6} Increased activities of matrix metalloproteinases (MMPs) play a key mechanical role in the formation of AAAs.^{7,8} A strong mechanistic link exists between increased ROS production and MMP activity. As has been reported recently, angiotensin II (Ang II) induces the generation of ROS in vascular smooth muscle cells (VSMCs), which triggers the activation of MMPs and vascular inflammatory responses, thereby promoting the formation of AAAs in an animal model.^{2,9} However, little is known about the detailed signaling pathways that regulate these processes.

Hydrogen peroxide-inducible clone 5 (Hic-5), originally identified as a gene induced by H₂O₂ as well as transforming growth factor- β 1 (TGF- β 1), has been shown to serve as a focal adhesion protein that belongs to the paxillin family.¹⁰ We recently successfully generated Hic-5-deficient mice, which were viable and fertile and had no obvious abnormalities.¹¹

From the Department of Biochemistry, Showa University School of Medicine, Tokyo, Japan (X.-F.L., J.K.-K., S.A., T.M., A.M.); Division of Biological Chemistry, Departments of Molecular Biology, Showa University School of Pharmacy, Tokyo, Japan (H.I.); Department of Pharmacology, Max-Planck-Institute for Heart and Lung Research, Bad Nauheim, Germany (S.O.).

Correspondence to: Joo-ri Kim-Kaneyama, PhD, Department of Biochemistry, Showa University School of Medicine, 1-5-8 Hatanodai, Shinagawa-ku, Tokyo 142-8555, Japan. E-mail: shuri@pharm.showa-u.ac.jp

Received January 5, 2014; accepted March 5, 2014.

© 2014 The Authors. Published on behalf of the American Heart Association, Inc., by Wiley Blackwell. This is an open access article under the terms of the Creative Commons Attribution-NonCommercial License, which permits use, distribution and reproduction in any medium, provided the original work is properly cited and is not used for commercial purposes.

The molecular basis of Hic-5 and its implications in various pathophysiological conditions including vascular remodeling have already been described.^{11,12} However, whether Hic-5 is involved in AAA formation is unknown. In this study, we analyzed the potential role of Hic-5 in AAA formation. We found that AAA formation and rupture were almost completely prevented in Hic-5-deficient mice. Mechanistic studies showed that Hic-5 served as a novel scaffold protein to regulate c-Jun N-terminal kinase (JNK) pathway activation, which resulted in MMP expression and activation in VSMCs and the subsequent formation of AAAs.

Methods

Generation of Mice

All experiments were conducted in accordance with the protocols approved by the Institutional Committee for Animal Research of Showa University. All of the mice were bred in C56BL/6 background genotype. *Apoe*^{-/-}*Hic-5*^{-/-} mice were generated by crossing *Hic-5*^{-/-} mice with *Apoe*^{-/-} mice. For the generation of smooth muscle (SM)-specific knockout mice for Hic-5 (SM-Hic-5KO), we used our previously produced mouse strain in which all exons of Hic-5 were floxed (*Hic-5*^{F/F}).¹¹ *Hic-5*^{F/F} mice were intercrossed with a transgenic mouse line expressing inducible SM-specific Cre recombinase with a modified estrogen receptor binding domain (CreER^{T2}) under the control of the SM-specific SM myosin heavy chain promoter (SMMHC).¹³ The SMMHC-Cre gene is located on the Y chromosome in this mouse line, and only male offspring carried the SMMHC-Cre gene. The *Hic-5*^{F/F}/*SMMHC-Cre*^{Y+} (*Hic-5*^{F/F}/*sCre*^{Y+}) mice strain was used. *Apoe*^{-/-} *Hic-5*^{F/F}/*sCre*^{Y+} mice were generated by crossing *Hic-5*^{F/F}/*sCre*^{Y+} mice with *Apoe*^{-/-} mice. Male *Hic-5*^{F/F}/*sCre*^{Y+} mice (5 to 6 weeks old) were injected with tamoxifen (1 mg/day IP) on 5 consecutive days. The day of the last tamoxifen injection was defined as day 0. The Ang II treatment was performed for 4 weeks from day 55 after the tamoxifen injection. All animals were housed under a 12-hour light/12-hour dark regimen and consumed on a normal chow diet.

The Mouse Model of Ang II-Induced Aortic Aneurysm

The mouse model of Ang II-induced aneurysm formation has been previously described.¹⁴ Ang II was infused via the use of ALZET model 2004 osmotic pumps (ALZA Corp) at 1000 ng/kg per minute. After 4 weeks of infusion, aneurysm size was evaluated by measuring maximal abdominal aortic diameters with a digital caliper. Systolic blood pressure was measured in conscious mice by using the tail-cuff method (MK-2000;

Muromachi Kikai Co). Serum total cholesterol concentrations were determined by using a cholesterol determination kit (Wako Chemicals).

Histological Analysis

After the animals were killed, their aortas were perfused with 10% phosphate-buffered formalin for 5 minutes. Whole aortas were harvested and fixed with 10% formalin for 24 hours. The aortas were cut and embedded in paraffin or OCT compound for the preparation of cross sections (5 μm). Paraffin sections were stained with hematoxylin and eosin (H&E) staining and Victoria Blue H&E staining or used for immunostaining. Frozen sections were used for immunofluorescence.

Immunohistochemistry

Formaldehyde-fixed paraffin sections and frozen sections were incubated with primary antibodies overnight at 4°C. The primary antibodies used were Hic-5 monoclonal (BD Biosciences), α-SM actin monoclonal (Sigma-Aldrich), and rat anti-mouse macrophage-monocyte specific monoclonal (AbD Serotec). As a negative control, isotype-matched antibodies were used in place of the primary antibodies. Slides were viewed with use of a microscope (IX70; Olympus) and digital camera (DP72; Olympus). Immunofluorescence images were captured and analyzed with Lumina vision software (Mitani Visual System).

Harvest of Mouse Aortic VSMCs

The preparation of mouse aortic VSMCs was performed as previously described.¹¹ In brief, aortas were isolated from *Hic-5*^{+/+} and *Hic-5*^{-/-} mice, followed by separation of tunica media from the adventitia and endothelium. The cells were dispersed in collagenase and elastase and maintained in Dulbecco's modified Eagle's medium. Passage 2 to 8 VSMCs were used for experiments.

Western Blotting

VSMCs were harvested on ice-cold lysis buffer. In some experiments, VSMCs were infected with adenovirus encoding *Hic-5* (Ad-hic-5/flag) or β-galactosidase (Ad-β-gal) as a control. Aortic tissue samples were crushed with a biomasher (Nippi) and lysed in lysis buffer. Equal amounts of protein were separated by 10% SDS-PAGE. Immunodetection was performed using the following primary antibodies: Hic-5; GAPDH and MMP2 (Santa Cruz Biotechnology), membrane type 1 (MT1)-MMP (Sigma-Aldrich); extracellular signal-regulated kinase (ERK), p38, mitogen-activated protein kinase kinase (MAPKK; also known as MKK) 4, MKK7, and their

phosphorylated (P) forms (P-ERK, P-p38, P-MKK4, P-MKK7, and P-JNK1/2) (Cell Signaling); and JNK1/2 (Santa Cruz Biotechnology). The densities of the bands were measured using Light-Capture and Densitograph software (AE-6962FC, CS Analyzer version 2.0; ATTO).

Gelatin Zymography and In Situ Zymography

The evaluation of MMP activities in response to Ang II was performed as described previously.^{9,15} To analyze the role of Hic-5 in Ang II–induced MMP activation, VSMCs were treated with Ang II (1 $\mu\text{mol/L}$) for 24 hours. Aortas from *ApoE*^{-/-} and *ApoE*^{-/-}*Hic-5*^{-/-} mice infused with Ang II for 7 days were incubated in culture medium for 20 hours. The medium was then collected and centrifuged to remove cell debris. The conditioned medium was concentrated and electrophoresed in SDS-PAGE gels containing gelatin (Sigma-Aldrich). Gels were washed in 2.5% Triton X-100 and incubated overnight in zymography buffer (50 mmol/L Tris, pH 7.4, 10 mmol/L CaCl₂) at 37°C. Gels were subsequently stained with Coomassie brilliant blue. For in situ zymography, freshly cut frozen aortic sections (10 μm) were incubated with a fluorogenic gelatin substrate (DQ gelatin; Invitrogen) dissolved to 25 mg/mL in zymographic buffer. Proteolytic activity was detected as green fluorescence with microscopy (IX70; Olympus, Japan). Negative control zymograms were incubated in the presence of 5 mmol/L EDTA.

Immunoprecipitation

Aortic media were lysed in RIPA buffer containing a mixture of proteinase inhibitors and 1 mmol/L sodium vanadate for immunoprecipitation studies. Dynabeads (Invitrogen) conjugated with an antibody against Hic-5 or control mouse IgG (Santa Cruz Biotechnology) were added to the lysates (5 μg per sample) and rotated at room temperature for 60 minutes. Samples were washed with RIPA buffer 3 times and soaked in elution buffer for 10 minutes. Immunoprecipitated proteins were then processed for SDS-PAGE and Western blot analysis.

In Situ Proximity Ligation Assay

The in situ proximity ligation assay (PLA) method allows the subcellular colocalization of protein–protein interactions to be determined.^{16,17} Mouse VSMCs were cultured in cover glasses. After culture in serum-free medium for 24 hours, VSMCs were treated with or without Ang II for 10 minutes. VSMCs were then washed in PBS and fixed with 4% paraformaldehyde for 15 minutes. PLA assays were performed as recommended by the manufacturer (OLink Biosciences). Red fluorescent spots were then visualized with

microscopy (IX70; Olympus). The negative control was performed without primary antibodies.

Electron Microscopic Observations

Immunoelectron microscopy was performed as previously described.¹¹ Briefly, sections of mouse aortas were incubated overnight with primary antibodies at 4°C. After the sections were washed with PBS, 10-nm gold-labeled sheep anti-mouse IgG and 15-nm gold-labeled goat anti-rabbit IgG secondary antibodies (BBI International) were used; subsequently, sections were evaluated with Hitachi H-7600 transmission electron microscope.

Statistical Analyses

The data are presented as mean \pm SEM. Statistical tests including the Mann–Whitney test (for comparisons of parameters among 2 groups), Gehan–Breslow–Wilcoxon test (for survival curves), Fisher's exact test (for aneurysm incidence), and 2-way ANOVA using the Bonferroni posttests (for comparisons of different parameters between 2 genotypes) were performed using GraphPad Prism (version 5.0 for Mac) software. $P < 0.05$ was considered statistically significant.

Results

Hic-5 Deficiency Suppressed Ang II–Induced AAA Formation and AAA Rupture

Ang II infusion for 4 weeks induced AAA formation in *ApoE*^{-/-} mice.¹⁴ Here, we used *ApoE*^{-/-} mice and *ApoE*^{-/-}*Hic-5*^{-/-} mice to investigate the role of Hic-5 in the pathogenesis of Ang II–induced AAAs. Ang II infusion increased systolic blood pressure in both groups to the same extent (Table). No significant difference in cholesterol levels was observed between these 2 groups after Ang II infusion (Table).

No aneurysm was detected in either group after saline infusion (Figure 1A). Ang II infusion markedly induced AAAs in 87% (13/15) of *ApoE*^{-/-} mice (Figure 1A and 1C), while only 11% (1/9) of *ApoE*^{-/-}*Hic-5*^{-/-} mice developed small AAAs. We also noted that maximal aortic diameter (Figure 1B and 1D) was significantly smaller in *ApoE*^{-/-}*Hic-5*^{-/-} mice than in *ApoE*^{-/-} mice. Interestingly, over the 4 weeks of the experiment, 40% (6/15) of the *ApoE*^{-/-} mice infused with Ang II died in the first week, whereas none of the *ApoE*^{-/-}*Hic-5*^{-/-} mice died during the entire experiment (Figure 1E). *ApoE*^{-/-} mice showed arterial rupture and massive bleeding in the abdominal cavities (Figure 1F and 1G). In Victoria Blue H&E staining, which specifically demonstrates elastic fibers in the background of H&E-stained tissues, the elastic lamina was

Table. Systolic Blood Pressure and Total Cholesterol Levels of *Apoe*^{-/-}, *Apoe*^{-/-}*Hic-5*^{-/-} and *Apoe*^{-/-}*Hic-5*^{F/F}/*sCre*^{Y+} Mice

Mice	Systolic Blood Pressure, mm Hg		Total Cholesterol, mg/dL (Ang II Infusion)
	Before Treatment	Ang II Infusion	
<i>Apoe</i> ^{-/-}	109.5±5.7	140.2±9.7*	651.2±81.8
<i>Apoe</i> ^{-/-} <i>Hic-5</i> ^{-/-}	104.4±7.9	136.8±12.3* [†]	615.4±104.4 [†]
<i>Apoe</i> ^{-/-} (tamoxifen)	108±8.5	141.4±9.6*	524.1±106.7
<i>Apoe</i> ^{-/-} <i>Hic-5</i> ^{F/F} / <i>sCre</i> ^{Y+} (tamoxifen)	109±10.7	135.9±10.6* [†]	518.7±73.7 [†]

**P*<0.01 versus before Ang II treatment.

[†]No significant difference between *Apoe*^{-/-} and *Apoe*^{-/-}*Hic-5*^{-/-} or *Apoe*^{-/-}*Hic-5*^{F/F}/*sCre*^{Y+} mice.

extensively disrupted and degraded in *Apoe*^{-/-} mice. In contrast, Hic-5 deficiency completely prevented the elastic lamina from degradation (Figure 1G). These results suggest that protection from elastin degradation is a key mechanism for the inhibition of Ang II–induced AAA formation in *Apoe*^{-/-}*Hic-5*^{-/-} mice.

VSMC-Derived Hic-5 Was Required for AAA Formation

We first investigated the expression of Hic-5 in aortic tissues from normal and Ang II–infused *Apoe*^{-/-} mice. Consistent with our previous report,^{12,18} Hic-5 was highly expressed in SM cells (SMCs) in addition to endothelium (Figure 2A) but not in macrophages in the aortas of *Apoe*^{-/-} mice after the Ang II treatment for 7 days or 4 weeks (Figure 2B and 2C). The expression pattern of Hic-5 was similar to that of α -SM actin in both normal aorta and AAA lesions, which was consistent with our previous report.¹⁸ Although macrophages have been reported to have a crucial role in the development of Ang II–induced AAAs,¹⁹ Hic-5 was not detected by immunostaining in the macrophages of AAA lesions (Figure 2B) or by Western blotting analyses in cultured macrophages (data not shown).

To obtain direct evidence for the key role of VSMC-derived Hic-5 in AAA formation, we created SM-specific Hic-5 knockout mice (SM-Hic-5 KO). We used a transgenic mouse line, which expressed in an SMC-specific manner a tamoxifen-inducible Cre recombinase under the control of the SMMHC promoter,¹³ bred to the well-established *Hic-5*^{flxed} mouse line.¹¹ *Hic-5*^{fllox/fllox}/*SMMHC-Cre*^{Y+} (*Hic-5*^{F/F}/*sCre*^{Y+}) mice (see “Methods” for details) were treated with tamoxifen as shown in Figure 3A. As a control, we used *Hic-5*^{F/F}/*sCre*^{Y+} mice to which tamoxifen was not administered. The successful SMC-specific deletion of Hic-5 in the aortic media was

shown by Western blotting after the tamoxifen treatment (Figure 3B). Cre expression in this mouse line has previously been shown to be specific for vascular and visceral SMCs.¹³ We also noted that tamoxifen treatment suppressed Hic-5 expression in the colon (Figure 3B) but not in the lung. Hic-5 was expressed mainly in the endothelium and pneumocytes rather than SMCs in the mouse lung (data not shown).

By crossing male *Hic-5*^{F/F}/*sCre*^{Y+} mice with female *Apoe*^{-/-} mice, *Apoe*^{-/-}*Hic-5*^{F/F}/*sCre*^{Y+} mice were generated. The Ang II treatment was performed from day 55 after the tamoxifen injection (Figure 3A) using tamoxifen-injected *Apoe*^{-/-} mice as a control. The successful SMC-specific deletion of Hic-5 in tamoxifen-injected *Apoe*^{-/-}*Hic-5*^{F/F}/*sCre*^{Y+} mice was confirmed with use of Western blotting assay of the aortic media after the Ang II treatment, which showed a 98% reduction in Hic-5 protein levels after the tamoxifen treatment (Figure 3D). In contrast, Hic-5 expression in the aortic media from *Apoe*^{-/-} mice was not affected by tamoxifen. Systolic blood pressure and total cholesterol levels were not significantly different between the 2 groups (Table). Although total cholesterol levels were decreased after the tamoxifen treatment in *Apoe*^{-/-} mice, as previously reported,²⁰ treatment of *Apoe*^{-/-} mice and tamoxifen-injected *Apoe*^{-/-} mice with Ang II for 4 weeks induced AAA formation (13/15 and 5/7, respectively) and AAA rupture (6/15 and 3/7, respectively) to the same extent. However, in contrast to tamoxifen-injected *Apoe*^{-/-}, a marked reduction in AAA rupture (0/8), AAA formation (1/8), and maximal aortic diameter was observed in tamoxifen-injected *Apoe*^{-/-}*Hic-5*^{F/F}/*sCre*^{Y+} mice (Figure 3C, 3E through 3G). These results suggest that the loss of Hic-5 expression in aortic VSMCs, but not other aortic wall cells, is crucial for Ang II–induced AAA formation.

We next examined the effects of Ang II on Hic-5 expression in the aorta from *Apoe*^{-/-} mice and cultured aortic VSMCs. Hic-5 levels in aortic tissues were significantly enhanced in *Apoe*^{-/-} mice in the early stage of Ang II infusion (Figure 4A). Hic-5 expression was also increased by Ang II in a concentration-dependent manner in cultured mouse aortic VSMCs (Figure 4B). As was previously reported, Ang II increased the amount of NADPH oxidase–derived ROS in aortic VSMCs.^{21,22} Pretreatment with ROS scavenger *N*-acetyl-L-cysteine markedly reduced Ang II–induced Hic-5 expression (Figure 4B).

Hic-5 Deficiency Prevented Ang II–Induced MMP Expression and Activation in VSMCs

Among the MMPs, VSMC-derived MMP-2, which is cleaved by MT1-MMP into active MMP2, and macrophage-derived MMP9 were shown to work in concert to degrade extracellular matrix, thereby promoting AAA formation and rupture.^{7,23} Ang II has been shown to stimulate the secretion and activation of MMP2 in VSMCs during AAA formation.^{9,24,25} Ang II infusion

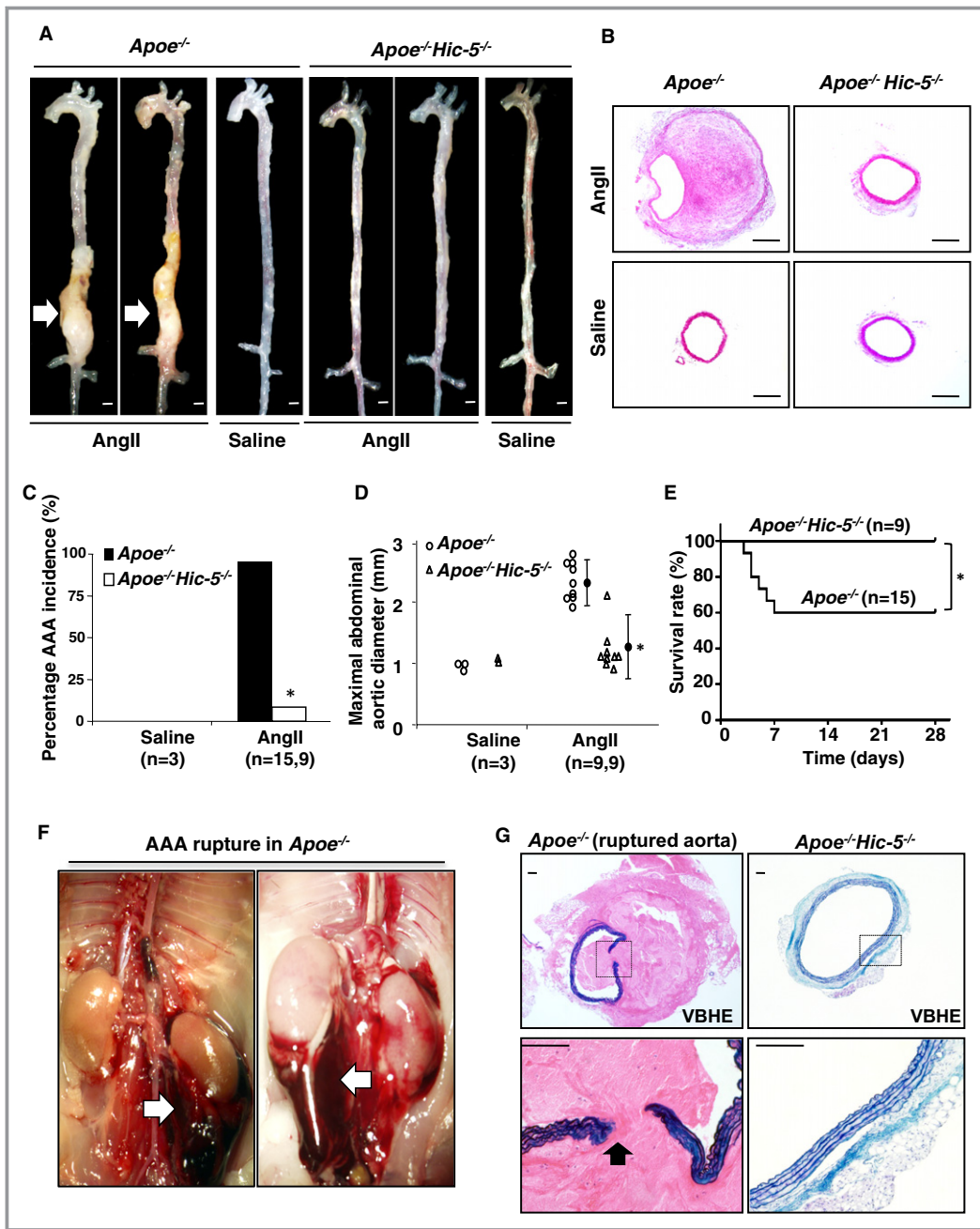


Figure 1. Hic-5 deficiency blocked Ang II-induced AAA formation and AAA rupture in vivo. *Apoe*^{-/-} and *Apoe*^{-/-}*Hic-5*^{-/-} mice were treated with Ang II or saline for 4 weeks. **A**, Representative aortas from mice treated with saline or Ang II. The arrows point to typical AAAs in *Apoe*^{-/-} mice. Scale bars, 1 mm. **B**, Hematoxylin and eosin (H&E [HE]) stains of aortic cross sections from *Apoe*^{-/-} and *Apoe*^{-/-}*Hic-5*^{-/-} mice after saline or Ang II infusion for 4 weeks. Scale bars, 500 μm. **C**, The incidence of Ang II-induced AAAs in *Apoe*^{-/-} (n=15) and *Apoe*^{-/-}*Hic-5*^{-/-} mice (n=9). No AAA formation was observed in the control groups (saline treatment) in both *Apoe*^{-/-} (n=3) and *Apoe*^{-/-}*Hic-5*^{-/-} mice (n=3). **P*<0.05, significantly different from Ang II-infused *Apoe*^{-/-} mice. **D**, Maximal diameters of the abdominal aortas of *Apoe*^{-/-} and *Apoe*^{-/-}*Hic-5*^{-/-} mice after the Ang II treatment for 4 weeks (n=9). Closed circles represent the means, and error bars denote SEM. **P*<0.01, significantly different from Ang II-infused *Apoe*^{-/-} mice. **E**, Survival curves of *Apoe*^{-/-} and *Apoe*^{-/-}*Hic-5*^{-/-} mice during the Ang II treatment. **P*<0.05 significantly different from *Apoe*^{-/-} mice. **F**, Typical AAA rupture in Ang II-infused *Apoe*^{-/-} mice. The arrows point to a hematoma in the abdominal cavity. **G**, Victoria Blue H&E (VBHE) stains of aortic cross sections from *Apoe*^{-/-} and *Apoe*^{-/-}*Hic-5*^{-/-} mice after Ang II infusion. The arrows indicate ruptured elastic lamina in *Apoe*^{-/-} mice. Scale bars, 100 μm. AAA indicates abdominal aortic aneurysm; Ang II, angiotensin II; Hic-5, hydrogen peroxide-inducible clone 5.

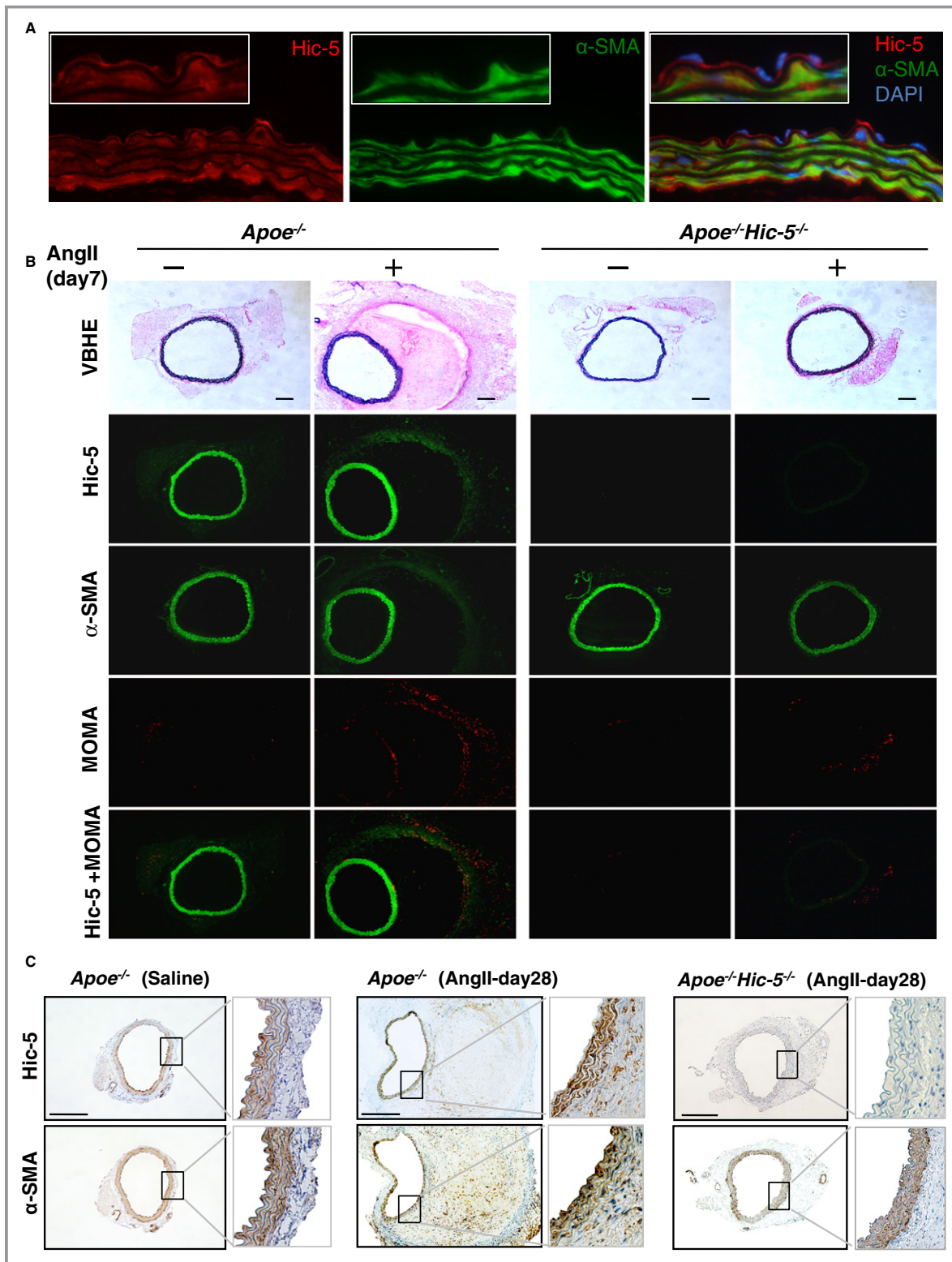


Figure 2. The expression of Hic-5 in the mouse aorta. A, Representative fluorescent immunostaining for Hic-5 (red), α -smooth muscle actin (α -SMA) (green), and DAPI for nucleus in aortic serial sections from *Apoe*^{-/-}. B, Representative VBHE staining elastin and fluorescent immunostaining for Hic-5 (green), α -SMA (green), and monocyte/macrophage (MOMA) (red) in aortic serial sections from *Apoe*^{-/-} and *Apoe*^{-/-Hic-5}^{-/-} mice after saline or Ang II infusion for 7 days. Scale bars, 200 μ m. C, Representative immunostaining for Hic-5 and α -SMA in aortic cross sections from *Apoe*^{-/-} and *Apoe*^{-/-Hic-5}^{-/-} mice after saline or Ang II infusion for 4 weeks. AAA indicates abdominal aortic aneurysm; Ang II, angiotensin II; Hic-5, hydrogen peroxide-inducible clone 5; VBHE, Victoria Blue hematoxylin & eosin.

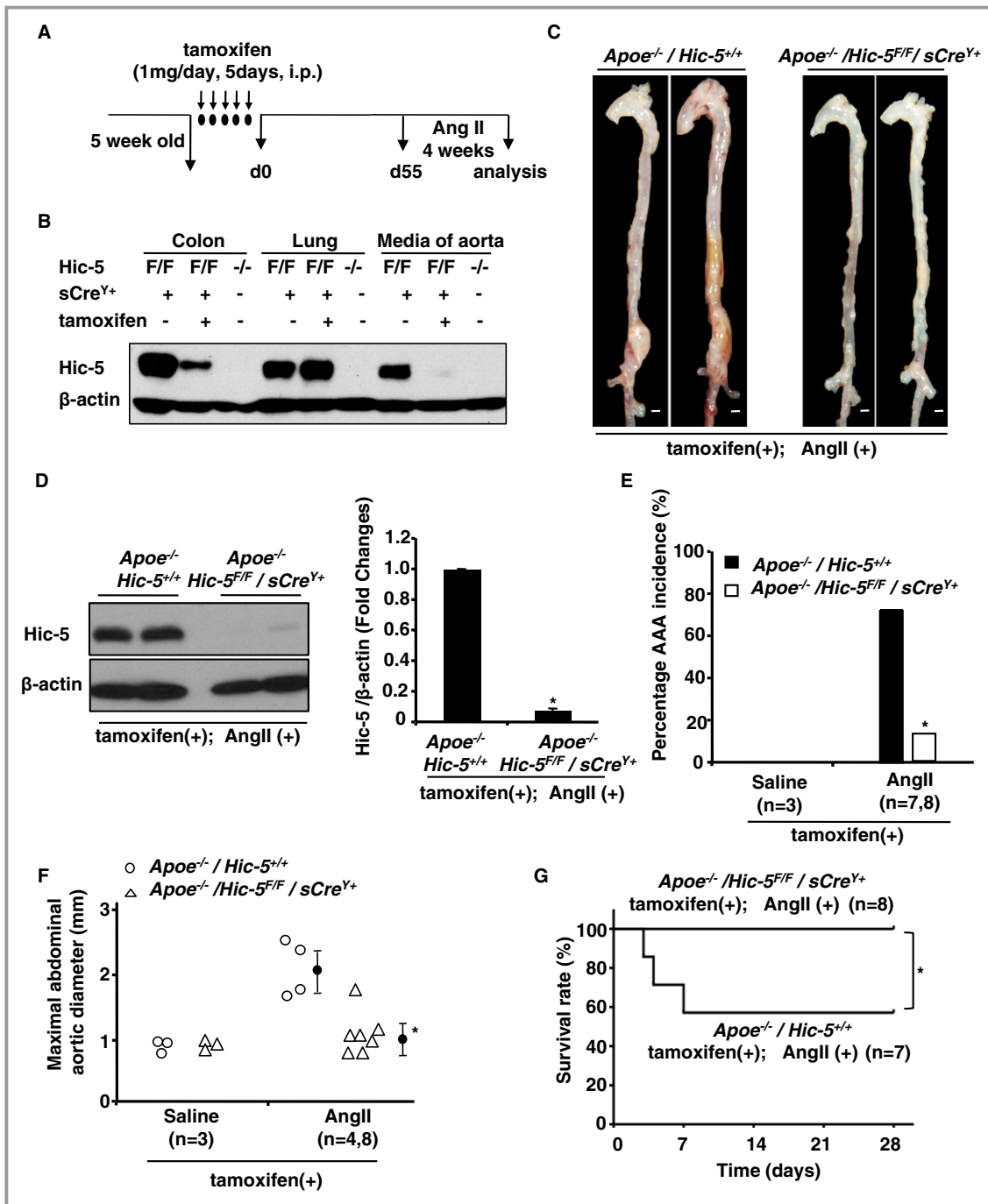


Figure 3. Smooth muscle–specific deletion of Hic-5 inhibited Ang II–infused AAA formation in vivo. **A**, Time scheme for the generation of smooth muscle–specific knockout mice for Hic-5 (*SM-Hic-5KO*). **B**, Immunoblots to assess the expression of Hic-5 in the colon, lung, and aortic media from *Hic-5*^{-/-} and *Hic-5*^{F/F}/*sCre*^{Y+} with or without the tamoxifen treatment. **C**, Representative aortas from *Apoe*^{-/-}/*Hic-5*^{+/+} and *Apoe*^{-/-}/*Hic-5*^{F/F}/*sCre*^{Y+} mice treated with Ang II after the tamoxifen injection. Scale bars, 1 mm. **D**, Immunoblots to analyze the expression of Hic-5 in the aortic media. Quantitative analyses of Hic-5 are shown in the right panel. **P*<0.01 significantly different from *Apoe*^{-/-}/*Hic-5*^{+/+} mice. **E**, The incidence of Ang II–induced AAAs in *Apoe*^{-/-}/*Hic-5*^{+/+} (n=7) and *Apoe*^{-/-}/*Hic-5*^{F/F}/*sCre*^{Y+} (n=8) after the tamoxifen injection. **P*<0.05 significantly different from *Apoe*^{-/-}/*Hic-5*^{+/+} mice. Saline infusion did not induce AAA formation in either group. **F**, Maximal diameters of abdominal aortas in both groups. Open circles represent *Apoe*^{-/-}/*Hic-5*^{+/+} mice; triangles represent *Apoe*^{-/-}/*Hic-5*^{F/F}/*sCre*^{Y+} mice. Closed circles represent the means, and error bars denote SEM. **P*<0.01 significantly different from Ang II–infused *Apoe*^{-/-} mice. **G**, Survival curve of both groups during the Ang II treatment after the tamoxifen injection. **P*<0.05 significantly different from *Apoe*^{-/-}/*Hic-5*^{+/+} mice. AAA indicates abdominal aortic aneurysm; Ang II, angiotensin II; Hic-5, hydrogen peroxide–inducible clone 5.

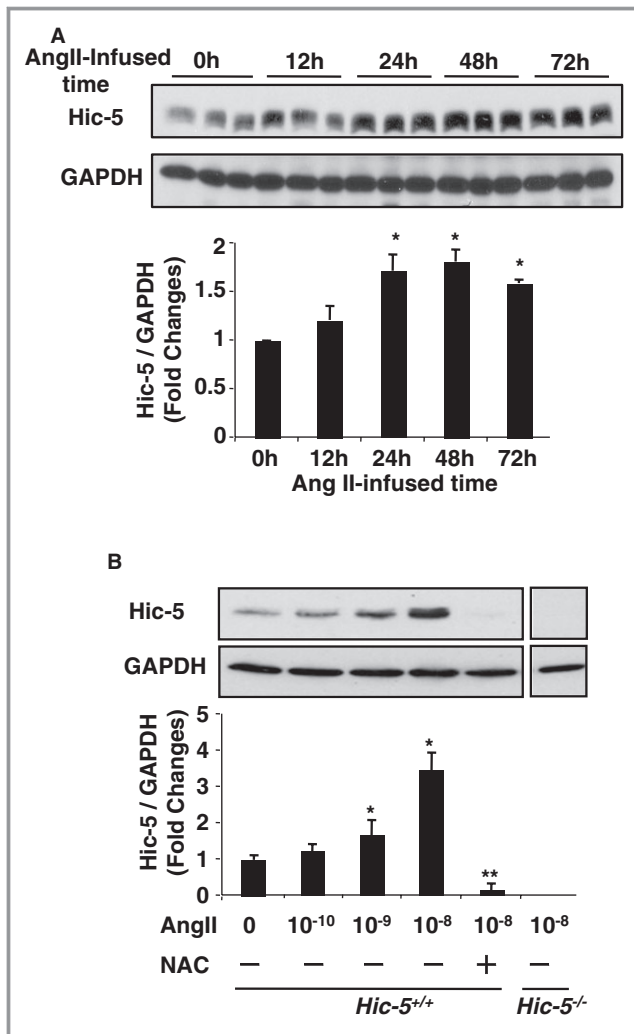


Figure 4. Ang II upregulated the expression of Hic-5 in the mouse aorta and cultured VSMCs. A, Immunoblot analysis of Hic-5 expression in the aortic media from Ang II-infused *ApoE*^{-/-} mice at the indicated times. The lower panel shows quantitative analyses of Hic-5 expression after normalization with glyceraldehyde 3-phosphate dehydrogenase (GAPDH). B, Immunoblots to analyze the expression of Hic-5 in cultured *Hic-5*^{+/+} VSMCs in response to Ang II with or without an ROS scavenger, 10 mmol/L *N*-acetyl L-cysteine (NAC). The lower panel shows the results of the densitometric analysis of immunoblots after normalization with GAPDH. Data are expressed as means±SEM of 3 independent experiments. **P*<0.01 significantly different from untreated controls; ***P*<0.01 significantly different from the Ang II 10⁻⁸ mol/L treatment without ROS scavengers. AAA indicates abdominal aortic aneurysm; Ang II, angiotensin II; Hic-5, hydrogen peroxide-inducible clone 5; ROS, reactive oxygen species; VSMCs, vascular smooth muscle cells.

for 7 days in *ApoE*^{-/-} mice markedly increased the expression of proMMP2 and activated MMP2 in the aortic media (Figure 5A). The induction of these 2 MMP2 proteins by Ang II infusion was significantly weaker in *ApoE*^{-/-}*Hic-5*^{-/-} mice than in *ApoE*^{-/-} mice (Figure 5A and 5B). We next focused on

MT1-MMP, a major activator of proMMP2. Basal expression of MT1-MMP was negligible in the aortic media from both *ApoE*^{-/-} and *ApoE*^{-/-}*Hic-5*^{-/-} mice. The Ang II treatment increased MT1-MMP protein expression in both groups; however, the induction of MT1-MMP was significantly attenuated in *ApoE*^{-/-}*Hic-5*^{-/-} mice (Figure 5A and 5C). Gelatin zymography of the aortas from *ApoE*^{-/-} showed an increase in proMMP2 and activated MMP2. In contrast, Ang II-treated aortas from *ApoE*^{-/-}*Hic-5*^{-/-} mice showed markedly reduced MMP2 expression and activation (Figure 5D). We obtained a similar result by in situ zymography, which showed that Ang II infusion markedly increased MMP activity in the medial layers of *ApoE*^{-/-} mice but not in *ApoE*^{-/-}*Hic-5*^{-/-} mice (Figure 5E). MMP activity was negligible in both *ApoE*^{-/-} and *ApoE*^{-/-}*Hic-5*^{-/-} mice after saline infusion (Figure 5E). We also observed that the Ang II treatment induced the expression of MT1-MMP and MMP2 in cultured VSMCs isolated from *Hic-5*^{+/+} mice, whereas VSMCs from *Hic-5*^{-/-} mice did not exhibit such an upregulation (Figure 5F and 5G). As shown with gelatin zymography, the secretion and activation of MMP2 in the culture media were lower in *Hic-5*^{-/-} VSMCs than in *Hic-5*^{+/+} VSMCs (Figure 5F, lower panel). In contrast to VSMCs, macrophages did not express Hic-5. As expected, no significant difference in MMP9 production was observed for macrophages from *Hic-5*^{+/+} and *Hic-5*^{-/-} mice (data not shown).

Hic-5 Regulated Phosphorylation of the JNK Pathway in VSMCs

We next analyzed the mechanism for decreases in MMP secretion and activation by Hic-5 deficiency. Although the enhanced production of ROS and associated vascular inflammation are known to accelerate Ang II-induced MMP induction and subsequent AAA development and progression,^{2,5,26} we found that Hic-5 deficiency in *ApoE*^{-/-} mice did not affect Ang II-induced ROS production or the secretion of proinflammatory cytokines and chemokines in cultured VSMCs and isolated aortas (data not shown).

The JNK pathway was previously shown to upregulate the expression of MMPs including MMP2 and MT1-MMP.^{17,27} We next investigated whether Hic-5 was required for JNK activation by phosphorylation. VSMCs from *Hic-5*^{+/+} and *Hic-5*^{-/-} mice were treated with Ang II at the indicated times, and the phosphorylation of JNK was analyzed (Figure 6A). We used anisomycin, a potent stimulator of JNK, as a positive control.²⁸ Figure 5A showed no significant differences between *Hic-5*^{+/+} and *Hic-5*^{-/-} VSMCs in the phosphorylation of ERK1/2 and p38 after the Ang II treatment. However, Ang II-induced phosphorylation of JNK was markedly lower in *Hic-5*^{-/-} VSMCs than in *Hic-5*^{+/+} VSMCs, particularly in phosphorylation of p54 JNK, in which

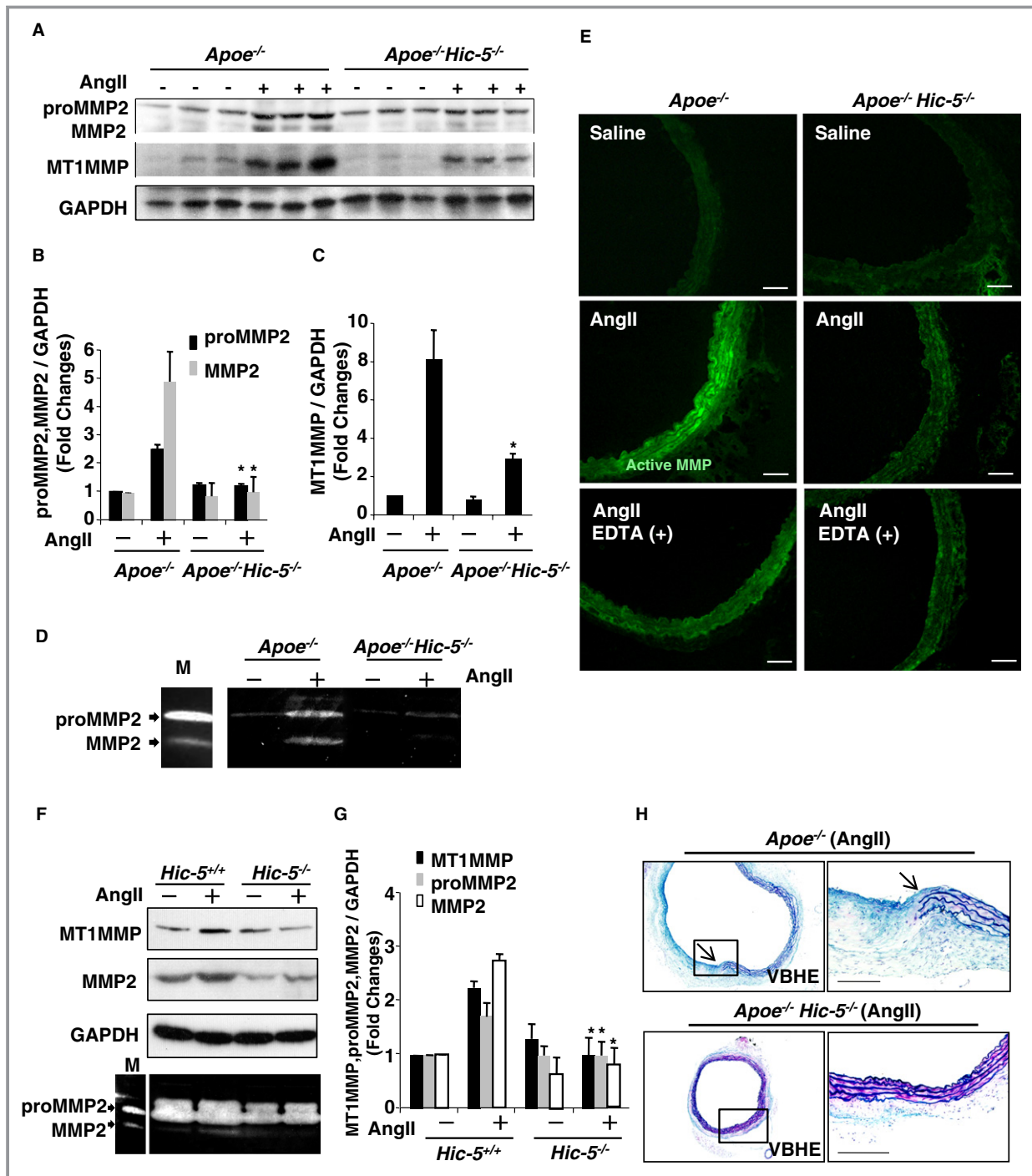


Figure 5. Ang II-induced MMP expression and activation were inhibited in the *Hic-5*^{-/-} mouse aorta and cultured VSMCs. Representative immunoblots for proMMP2, MMP2, and MT1-MMP in the aortic media after Ang II infusion for 7 days (A) and immunoblots for MMP2 and MT1-MMP in cultured VSMCs after the Ang II treatment for 48 hours (F, upper 2 panels) in the indicated genotypes. (B, C, and G) Densitometric analyses of immunoblots for proMMP2, MMP2, and MT1-MMP after normalization with GAPDH. Data are expressed as means±SEM of 3 independent experiments. **P*<0.01 significantly different from *ApoE*^{-/-} mice (B and C) or *Hic-5*^{+/+} VSMCs (G). Gelatin zymography of conditioned medium from the whole aorta organ culture (D) or cultured VSMCs (F, lowest panel) in the indicated genotypes. E, Aortas from *ApoE*^{-/-} and *ApoE*^{-/-}*Hic-5*^{-/-} mice infused with saline or Ang II for 7 days were analyzed by in situ zymography for gelatinase activity. Active MMPs are indicated by the green color. Scale bars, 50 μm. H, VBHE staining of aortas from *ApoE*^{-/-} and *ApoE*^{-/-}*Hic-5*^{-/-} mice 4 weeks after Ang II infusion. The arrows indicate degradation of the elastic lamina in *ApoE*^{-/-} mice. AAA indicates abdominal aortic aneurysm; Ang II, angiotensin II; *Hic-5*, hydrogen peroxide-inducible clone 5; MMPs indicates matrix metalloproteinases; VBHE, Victoria Blue hematoxylin & eosin; VSMCs, vascular smooth muscle cells.

phosphorylation was almost completely suppressed even under anisomycin stimulation (Figure 6A and 6B). In vivo, the Ang II treatment of *ApoE*^{-/-} mice for 7 days significantly induced the phosphorylation of JNK, as shown by Western blotting assay of the aortic media. In contrast, a marked reduction in the phosphorylation of JNK after Ang II infusion was observed in *ApoE*^{-/-} *Hic-5*^{-/-} mice (Figure 6C). We next restored Hic-5 expression in *Hic-5*^{-/-} VSMCs through adenovirus-mediated gene transfer (Ad-hic-5/flag), using the β -galactosidase gene (Ad- β -gal) as a control. Compared with control gene, exogenous *Hic-5* (flag-tagged) expression in *Hic-5*^{-/-} VSMCs efficiently restored basal and Ang II-induced phosphorylation of JNK, especially p54 JNK (Figure 6D). We next examined whether Hic-5 served as a component of the JNK pathway. JNK protein kinases are activated by phosphorylation by MKK4 and MKK7, which are well known as adjacent upstream kinases of JNK.^{29,30} We found that Hic-5 deficiency hardly affected the phosphorylation of MKK7 (data not shown). However, the phosphorylation of MKK4 was significantly higher in *Hic-5*^{-/-} VSMCs than in *Hic-5*^{+/+} VSMCs, even at basal levels (Figure 6E).

Hic-5 Is Associated Directly With MKK4 and JNK

The specificity of signal transduction depends on specific protein-protein interactions. Scaffold proteins, including the JNK interacting protein group bind to MKK4 and/or MKK7, in addition to JNK, and coordinate signal transduction in the JNK pathway.^{30,31} As described previously, Hic-5 serves as a scaffold of integrin signaling through interactions with multiple signaling molecules.¹² Because Hic-5 deficiency led to the decreased phosphorylation of p54 JNK and increased phosphorylation of MKK4, we reasoned that Hic-5 may serve as a scaffold protein between MKK4 and p54 JNK. To test this possibility, we performed immunoprecipitation experiments using an Hic-5-specific antibody and aortic tissue lysate from *Hic-5*^{+/+} mice. The results showed that the Hic-5 antibody pulled down JNK, especially p54 JNK and MKK4, but not MKK7, p38, or ERK together with Hic-5 (Figure 7A). Using the specific antibody of JNK1 and JNK2, we found that JNK2 is primarily composed of the p54 JNK isoform in cultured mouse VSMCs (data not shown).

To further validate the association of Hic-5 with p54 JNK or MKK4 in *Hic-5*^{+/+} VSMCs, we performed in situ proximity ligation assays, which identify the subcellular localization of interacting endogenous proteins within approximately 40 nm at single molecule resolution.³² A fluorescent signal by this method (red dots) indicated the association of Hic-5 with p54 JNK or MKK4. Clear red spots were detected with the Hic-5 antibody in combination with the JNK2 antibody or MKK4 antibody in *Hic-5*^{+/+} VSMCs, whereas only background staining was obtained with the Hic-5 antibody in combination

with control IgG (Figure 7B). These results indicate that Hic-5 colocalized with p54 JNK and MKK4 within 40 nm in VSMCs. The colocalization of these molecules was further demonstrated by using an immunoelectron microscopic method in aortas from *Hic-5*^{+/+} mice (Figure 7C). We next analyzed the interaction of Hic-5 with P-JNK or P-MKK4 in cultured *Hic-5*^{+/+} VSMCs using PLA assays. More red fluorescent dots were detected with the Hic-5 antibody in combination with the P-JNK antibody or P-MKK4 antibody in VSMCs after Ang II treatment than in those detected with the control (untreated with Ang II) (Figure 7D), suggesting that Hic-5 also contributes to the association of P-JNK and P-MKK4 in VSMCs. Together, these results suggest that Hic-5 serves as a scaffold selective for p54 JNK and MKK4 in VSMCs and contributes to the activation of p54 JNK by binding to both MKK4 and p54 JNK (Figure 7E).

Discussion

We showed that Ang II-induced ROS promoted the expression of Hic-5 in VSMCs, which subsequently accelerated the phosphorylation of JNK, especially p54 JNK. Mechanistically, Hic-5 can bind to both p54 JNK and its upstream regulatory molecule, MKK4. Suppression of the p54 JNK pathway by Hic-5 loss resulted in the limited secretion of proMMP2 and MMP2 and expression of MT1-MMP, which led to protection from elastin degradation and subsequent AAA formation and rupture (Figure 8). This study not only identified Hic-5 as a downstream molecule of ROS, which promotes AAA formation, but also suggested that Hic-5 can serve as a specific scaffold between MKK4 and p54 JNK in VSMCs.

Although numerous studies have clearly demonstrated that ROS play an important role in the development of aneurysms, no strong therapeutic strategy currently exists for the clinical benefits of antioxidant administration. One potential reason for this could be the crucial role of ROS in mediating the transduction of intracellular signals that are also important for regulating both VSMC and vascular functions.^{33,34} Our findings not only demonstrated that Hic-5, as a downstream molecule of ROS in the transduction of intracellular signals, regulates AAA development but also that its absence did not affect ROS production or normal function in mice. In addition, Hic-5 specifically binds to p54 JNK and its upstream molecule, MKK4, and plays an essential role in the phosphorylation of p54 JNK in VSMCs. Although the inhibition of JNKs has been considered as a potential therapeutic target for aneurysms,¹⁷ JNKs have been shown to play critical roles in adult tissue homeostasis. In fact, the knockout of both *Jnk1* and *Jnk2* genes in mice was shown to be an embryonic lethal mutation.³⁵ Thus, targeting JNKs themselves may be limited to be used as a mainstream treatment approach. Therefore, the exact JNK isoform (JNK1

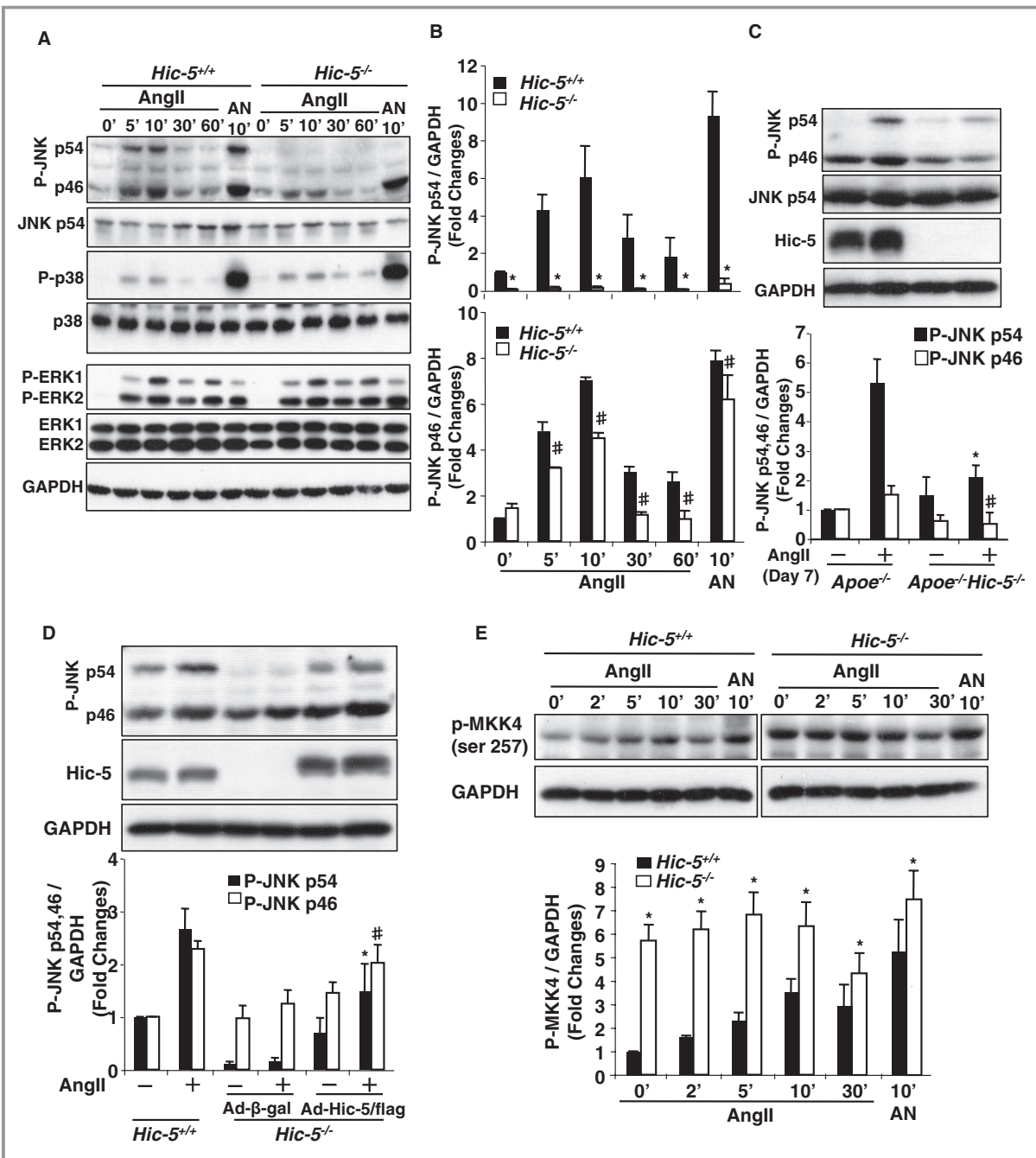


Figure 6. Hic-5 deficiency inhibited the phosphorylation of c-Jun N-terminal kinase (JNK) in VSMCs. A, Representative immunoblots of VSMCs are shown for MAP kinases (ERK, p38, and JNK) and for their phosphorylated forms (P-ERK, P-p38, and P-p54/p46 JNK, respectively) in the indicated genotypes after the Ang II (10^{-7} mol/L) or anisomycin (AN; 20 μ g/mL) treatment. B, Quantitative analyses of P-p54/p46 JNK are shown after normalization with GAPDH. C, Phosphorylation of p54/p46 JNK was detected using mouse aortas from Ang II-infused *Apoe*^{-/-} and *Apoe*^{-/-}*Hic-5*^{-/-} mice for 7 days. Quantitative analyses of P-p54/p46 JNK are shown in the lower panel. D, Adenovirus-mediated expression of flag-tagged *Hic-5* (Ad-Hic-5/flag) in *Hic-5*^{-/-} VSMCs induced the phosphorylation of p54/p46 JNK. *Hic-5*^{-/-} VSMCs were infected with Ad-Hic-5/flag or the adenovirus-mediated β -galactosidase gene (Ad- β -gal) as a control. After 12 hours of infection, the expression of P-JNK and Hic-5 with or without the Ang II treatment was analyzed by immunoblots. E, Enhanced phosphorylation of MKK4 in *Hic-5*^{-/-} VSMCs. The levels of MKK4 phosphorylation induced by Ang II were detected at each of the indicated times. AN was used as a positive control. All results are means \pm SEM of 3 independent experiments. **P*<0.01, #*P*<0.05 significantly different from *Hic-5*^{+/+} VSMCs (B and E) or *Apoe*^{-/-}*Hic-5*^{+/+} mice (C) or infected with Ad- β -gal gene (D). AAA indicates abdominal aortic aneurysm; Ang II, angiotensin II; Hic-5, hydrogen peroxide-inducible clone 5; JNK, Jun N-terminal kinase; MKK, mitogen-activated protein kinase; VSMCs, vascular smooth muscle cells.

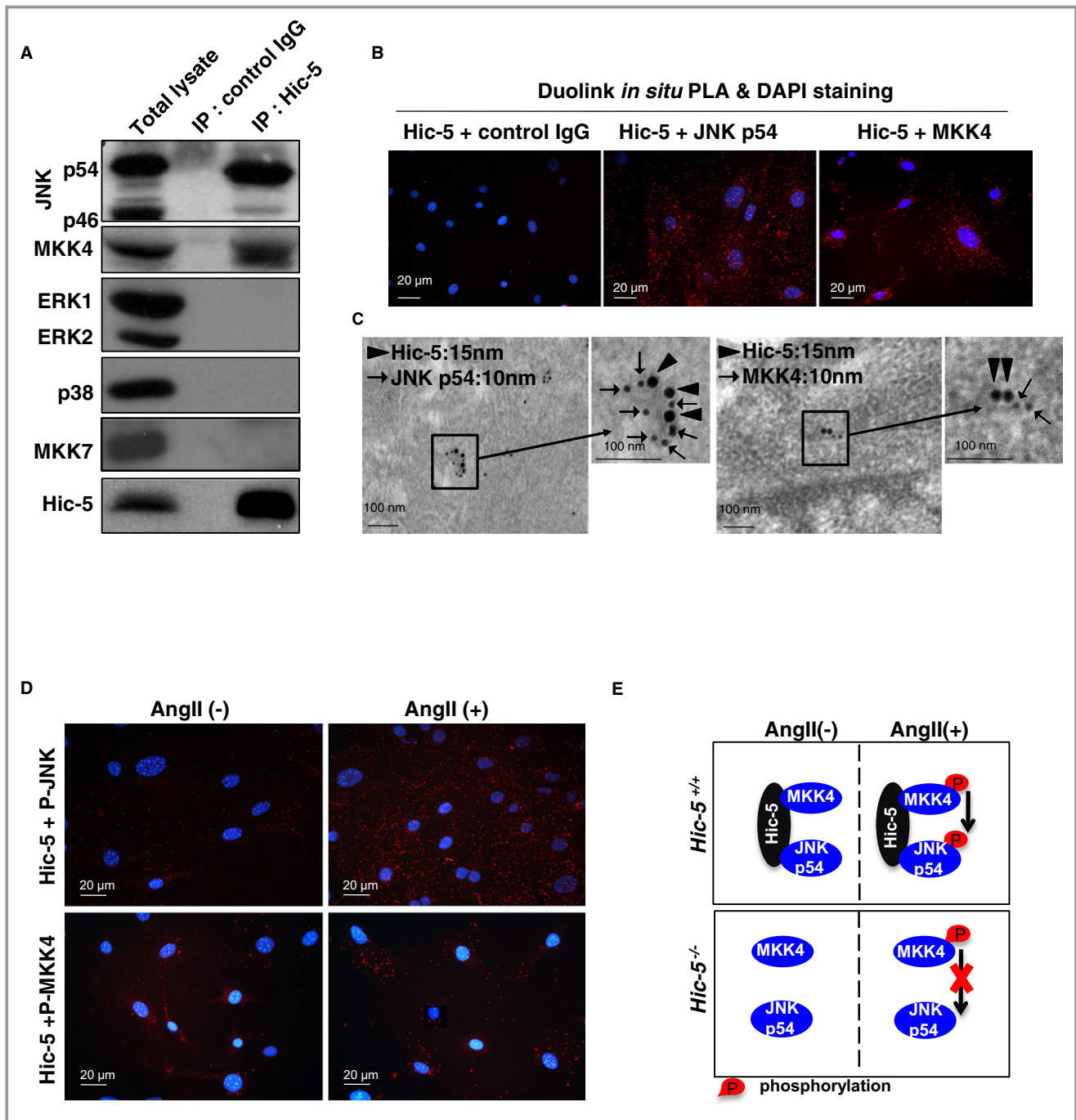


Figure 7. Hic-5 interacted with p54 JNK and MKK4 in VSMCs. Coimmunoprecipitation of p54 JNK and MKK4 with the Hic-5 antibody in the mouse aorta. Immunoblots for p54/p46 JNK, MKK4, ERK1/2, p38, MKK7, and Hic-5 in the total lysates of the mouse aorta or that after immunoprecipitation with the Hic-5–specific antibody or nonimmune mouse IgG as a negative control. IP, immunoprecipitation. B, Interaction of endogenous Hic-5 and p54 JNK or MKK4 in cultured *Hic-5*^{+/+} VSMCs. PLA was carried out to detect the proximal location of Hic-5 and p54 JNK or that of Hic-5 and MKK4 (shown as red dots) as described in “Methods.” All samples were stained with DAPI (blue) to visualize nuclei. C, Immunogold electron microscopy of *Hic-5*^{+/+} mouse aortas was performed. Co-localization of Hic-5 with p54 JNK or that with MKK4 in mouse aortic SMCs was detected using secondary antibodies conjugated with larger (15-nm) gold colloids for Hic-5 (arrowheads) and smaller (10-nm) gold colloids for p54 JNK or MKK4 (arrows), respectively. D, Interaction of Hic-5 with P-JNK or that with P-MKK4 in cultured *Hic-5*^{+/+} VSMCs with or without the Ang II treatment as demonstrated by the PLA method. E, Schematic diagram summarizing the interaction of Hic-5 and p54 JNK or MKK4 in VSMCs. Red circles represent phosphorylation. Arrows indicate signal transduction for p54 JNK phosphorylation after the Ang II treatment. The red X-mark represents inhibited signal transduction by Hic-5 deficiency. AAA indicates abdominal aortic aneurysm; Ang II, angiotensin II; Hic-5, hydrogen peroxide–inducible clone 5; JNK, Jun *N*-terminal kinase; MKK, mitogen-activated protein kinase; PLA, proximity ligation assay.

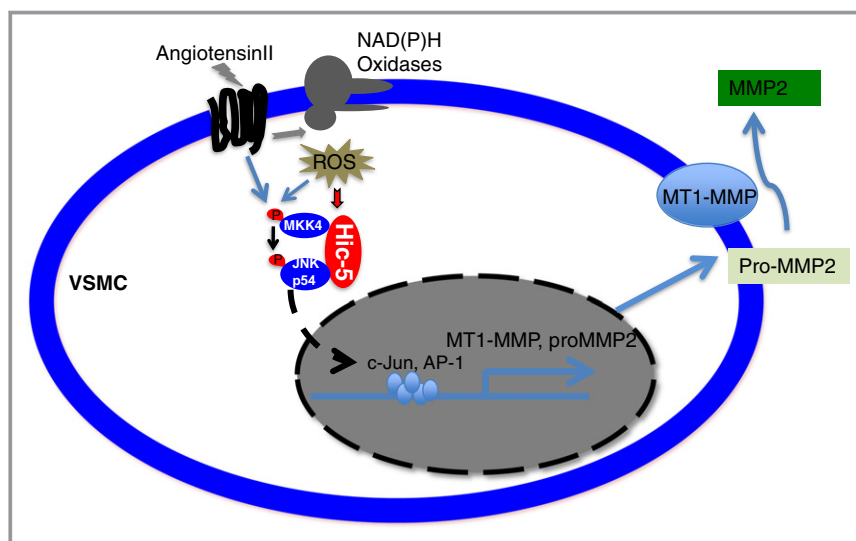


Figure 8. Ang II-induced AAA formation via Hic-5 in mice. Ang II binds to its receptors and induces the production of ROS in VSMCs. Ang II-induced ROS promote the expression of Hic-5 in VSMCs and Hic-5 serves as a specific scaffold between JNK p54 and its upstream molecule, MKK4, which contributes to the transmission of the activated signal from MKK4 to JNK p54. The loss of Hic-5 suppresses the JNK p54 pathway and results in the limited expression of proMMP2 and MT1-MMP and activation of MMP2. AAA indicates abdominal aortic aneurysm; Ang II, angiotensin II; Hic-5, hydrogen peroxide-inducible clone 5; JNK, Jun N-terminal kinase; MMP, matrix metalloproteinase; MKK, mitogen-activated protein kinase; ROS, reactive oxygen species.

or JNK2) is required to be identified in aneurysm formation. We found that JNK2 is primarily composed of the p54 JNK isoform in cultured mouse VSMCs. In addition, *Jnk2* deficiency in mouse VSMCs markedly inhibited the secretion of MMP2.¹⁷ All these suggest that Hic-5-targeted therapy may be more specific for the treatment of aneurysms with minimum side effects.

Paxillin, a member of paxillin family proteins together with Hic-5, has extensive homology with Hic-5 and is known to provide an efficient scaffold for the ERK module.³⁶ In the present study, we demonstrated that Hic-5 served as a scaffold for the p54 JNK module. These results raise the possibility that each paxillin family protein may behave as a respective scaffold for one of the MAPK modules.

We also found that Hic-5 expressed in VSMCs, rather than other types of cells, was essential for the development of AAAs. A couple of molecules expressed in VSMCs have been proposed to initiate AAA development by promoting the secretion of MMP2 and inflammatory cell recruitment in aneurysm formation in mice and humans.^{9,25,37} These studies strongly support our findings that VSMC-derived Hic-5 played a key role in the initiation of AAAs by promoting the secretion and activation of MMP2. Moreover, our results showed that Hic-5 was induced in the aorta in the early stage of Ang II-induced AAA formation. Although the Ang II-induced vascular inflammatory response contributes to AAA progression, Hic-5 deficiency did not affect

the secretion of proinflammatory cytokines in VSMCs, and Hic-5 was also not expressed in mouse macrophages. In light of these findings, Hic-5 may not play a major role in inflammatory responses in AAA development.

It has been previously reported that there are differences between human AAAs and Ang II-induced mouse AAAs including their location in the infrarenal versus suprarenal region, respectively; and aortic dissection is an early event in Ang II-induced mouse AAAs but not in human AAAs.¹⁹ Previous studies have shown that an Ang II receptor blocker prevented aortic aneurysm dilatation in mouse and human Marfan syndrome (MFS).^{38,39} One of the major clinical manifestations of MFS is aortic aneurysm. Fibrillin-1 has been identified as the gene responsible for MFS.⁴⁰ Recently, elevated circulating TGF- β 1 concentrations and the critical role of TGF- β -activated MAPK signaling were reported in human and mouse MFS, respectively.^{41,42} Hic-5 was originally identified as a TGF- β 1-inducible gene; moreover, the Gene Coexpression Database, which is a database of comparative gene coexpression networks in mammals (<http://www.coxpresdb.jp/>),⁴³ revealed that fibrillin-1 and Hic-5 were spatiotemporally coexpressed in mice and humans. Therefore, it is reasonable to speculate that Hic-5 may play a key role in the development of MFS together with fibrillin-1. Future studies should focus on the role of Hic-5 in MFS using an appropriate animal model.

The current study demonstrated that Hic-5 deficiency resulted in the effective suppression of AAAs in an animal model. Hic-5-targeted therapy may provide a novel therapeutic option for the treatment of AAAs in the future.

Sources of Funding

This work was supported by Grants-in-Aid for Young Scientists (B) (24791396 to X.-F. Lei and 23791090 to J.-r. Kim-Kaneyama), Scientific Research (C) (23591341 to T. Miyazaki) from The Ministry of Education, Culture, Sports, Science and Technology of Japan, Showa University Medical Foundation, Japan-China Medical Association, and Japan Heart Foundation Dr Hiroshi Irisawa & Aya Irisawa Memorial Research Grant (to J.-r. Kim-Kaneyama). This work was also supported in part by the MEXT (Ministry of Education, Culture, Sports, Science and Technology)-Supported Program for the Strategic Research Foundation at Private Universities, 2012–2016.

Disclosures

None.

References

- Stanley JC, Barnes RW, Ernst CB, Hertzner NR, Mannick JA, Moore WS. Vascular surgery in the united states: workforce issues. Report of the society for vascular surgery and the international society for cardiovascular surgery, north american chapter, committee on workforce issues. *J Vasc Surg.* 1996;23:172–181.
- McCormick ML, Gavrila D, Weintraub NL. Role of oxidative stress in the pathogenesis of abdominal aortic aneurysms. *Arterioscler Thromb Vasc Biol.* 2002;22:461–469.
- Miller FJ Jr, Sharp WJ, Fang X, Oberley LW, Oberley TD, Weintraub NL. Oxidative stress in human abdominal aortic aneurysms: a potential mediator of aneurysmal remodeling. *Arterioscler Thromb Vasc Biol.* 2002;22:560–565.
- Gavazzi G, Deffert C, Trocme C, Schappi M, Herrmann FR, Krause KH. NOX1 deficiency protects from aortic dissection in response to angiotensin II. *Hypertension.* 2007;50:189–196.
- Thomas M, Gavrila D, McCormick ML, Miller FJ Jr, Daugherty A, Cassis LA, Dellsperger KC, Weintraub NL. Deletion of p47phox attenuates angiotensin II-induced abdominal aortic aneurysm formation in apolipoprotein E-deficient mice. *Circulation.* 2006;114:404–413.
- Xiong W, Mactaggart J, Knispel R, Worth J, Zhu Z, Li Y, Sun Y, Baxter BT, Johanning J. Inhibition of reactive oxygen species attenuates aneurysm formation in a murine model. *Atherosclerosis.* 2009;202:128–134.
- Longo GM, Xiong W, Greiner TC, Zhao Y, Fiotti N, Baxter BT. Matrix metalloproteinases 2 and 9 work in concert to produce aortic aneurysms. *J Clin Invest.* 2002;110:625–632.
- Hellenthal FA, Buurman WA, Wodzig WK, Schurink GW. Biomarkers of AAA progression. Part 1: extracellular matrix degeneration. *Nat Rev Cardiol.* 2009;6:464–474.
- Satoh K, Nigro P, Matoba T, O'Dell MR, Cui Z, Shi X, Mohan A, Yan C, Abe J, Iliig KA, Berk BC. Cyclophilin A enhances vascular oxidative stress and the development of angiotensin II-induced aortic aneurysms. *Nat Med.* 2009;15:649–656.
- Shibanuma M, Mashimo J, Kuroki T, Nose K. Characterization of the TGF beta 1-inducible hic-5 gene that encodes a putative novel zinc finger protein and its possible involvement in cellular senescence. *J Biol Chem.* 1994;269:26767–26774.
- Kim-Kaneyama JR, Takeda N, Sasai A, Miyazaki A, Sata M, Hirabayashi T, Shibanuma M, Yamada G, Nose K. Hic-5 deficiency enhances mechanosensitive apoptosis and modulates vascular remodeling. *J Mol Cell Cardiol.* 2011;50:77–86.
- Kim-Kaneyama JR, Lei XF, Arita S, Miyauchi A, Miyazaki T, Miyazaki A. Hydrogen peroxide-inducible clone 5 (hic-5) as a potential therapeutic target for vascular and other disorders. *J Atheroscler Thromb.* 2012;19:601–607.
- Wirth A, Benyo Z, Lukasova M, Leutgeb B, Wettschureck N, Gorbey S, Orsy P, Horvath B, Maser-Gluth C, Greiner E, Lemmer B, Schutz G, Gutkind JS, Offermann S. G12-g13-larg-mediated signaling in vascular smooth muscle is required for salt-induced hypertension. *Nat Med.* 2008;14:64–68.
- Daugherty A, Manning MW, Cassis LA. Angiotensin II promotes atherosclerotic lesions and aneurysms in apolipoprotein E-deficient mice. *J Clin Invest.* 2000;105:1605–1612.
- Sun J, Sukhova GK, Yang M, Wolters PJ, MacFarlane LA, Libby P, Sun C, Zhang Y, Liu J, Ennis TL, Knispel R, Xiong W, Thompson RW, Baxter BT, Shi GP. Mast cells modulate the pathogenesis of elastase-induced abdominal aortic aneurysms in mice. *J Clin Invest.* 2007;117:3359–3368.
- Soderberg O, Gullberg M, Jarvius M, Ridderstrale K, Leuchowius KJ, Jarvius J, Wester K, Hydbring P, Bahram F, Larsson LG, Landegren U. Direct observation of individual endogenous protein complexes in situ by proximity ligation. *Nat Methods.* 2006;3:995–1000.
- Yoshimura K, Aoki H, Ikeda Y, Fujii K, Akiyama N, Furutani A, Hoshii Y, Tanaka N, Ricci R, Ishihara T, Esato K, Hamano K, Matsuzaki M. Regression of abdominal aortic aneurysm by inhibition of c-Jun N-terminal kinase. *Nat Med.* 2005;11:1330–1338.
- Kim-Kaneyama JR, Wachi N, Sata M, Enomoto S, Fukabori K, Koh K, Shibanuma M, Nose K. Hic-5, an adaptor protein expressed in vascular smooth muscle cells, modulates the arterial response to injury in vivo. *Biochem Biophys Res Commun.* 2008;376:682–687.
- Saraff K, Babamusta F, Cassis LA, Daugherty A. Aortic dissection precedes formation of aneurysms and atherosclerosis in angiotensin II-infused, apolipoprotein E-deficient mice. *Arterioscler Thromb Vasc Biol.* 2003;23:1621–1626.
- Bourassa PA, Milos PM, Gaynor BJ, Breslow JL, Aiello RJ. Estrogen reduces atherosclerotic lesion development in apolipoprotein E-deficient mice. *Proc Natl Acad Sci USA.* 1996;93:10022–10027.
- Griendling KK, Minieri CA, Ollerenshaw JD, Alexander RW. Angiotensin II stimulates nadh and nadph oxidase activity in cultured vascular smooth muscle cells. *Circ Res.* 1994;74:1141–1148.
- Zafari AM, Ushio-Fukai M, Akers M, Yin Q, Shah A, Harrison DG, Taylor WR, Griendling KK. Role of NADH/NADPH oxidase-derived H₂O₂ in angiotensin II-induced vascular hypertrophy. *Hypertension.* 1998;32:488–495.
- Visse R, Nagase H. Matrix metalloproteinases and tissue inhibitors of metalloproteinases: structure, function, and biochemistry. *Circ Res.* 2003;92:827–839.
- Luchtefeld M, Grote K, Grothusen C, Bley S, Bandlow N, Selle T, Struber M, Haverich A, Bavendiek U, Drexler H, Schieffer B. Angiotensin II induces MMP-2 in a p47phox-dependent manner. *Biochem Biophys Res Commun.* 2005;328:183–188.
- Wang S, Zhang C, Zhang M, Liang B, Zhu H, Lee J, Viollet B, Xia L, Zhang Y, Zou MH. Activation of AMP-activated protein kinase alpha2 by nicotine instigates formation of abdominal aortic aneurysms in mice in vivo. *Nat Med.* 2012;18:902–910.
- Tieu BC, Lee C, Sun H, Lejeune W, Recinos A III, Ju X, Spratt H, Guo DC, Milewicz D, Tilton RG, Brasier AR. An adventitial IL-6/MCP1 amplification loop accelerates macrophage-mediated vascular inflammation leading to aortic dissection in mice. *J Clin Invest.* 2009;119:3637–3651.
- Ispanovic E, Haas TL. JNK and PI3k differentially regulate MMP-2 and MT1-MMP mRNA and protein in response to actin cytoskeleton reorganization in endothelial cells. *Am J Physiol Cell Physiol.* 2006;291:C579–C588.
- Schmitz U, Ishida T, Ishida M, Surapisitchat J, Hasham MI, Pelech S, Berk BC. Angiotensin II stimulates p21-activated kinase in vascular smooth muscle cells: role in activation of JNK. *Circ Res.* 1998;82:1272–1278.
- Haeusgen W, Herdegen T, Waetzig V. The bottleneck of JNK signaling: molecular and functional characteristics of MKK4 and MKK7. *Eur J Cell Biol.* 2011;90:536–544.
- Davis RJ. Signal transduction by the JNK group of map kinases. *Cell.* 2000;103:239–252.
- Dhanasekaran DN, Kashef K, Lee CM, Xu H, Reddy EP. Scaffold proteins of map-kinase modules. *Oncogene.* 2007;26:3185–3202.
- Fredriksson S, Gullberg M, Jarvius J, Olsson C, Pietras K, Gustafsdottir SM, Ostman A, Landegren U. Protein detection using proximity-dependent DNA ligation assays. *Nat Biotechnol.* 2002;20:473–477.
- Martin-Garrido A, Gonzalez-Ramos M, Griera M, Guijarro B, Cannata-Andia J, Rodriguez-Puyol D, Rodriguez-Puyol M, Saura M. H₂O₂ regulation of vascular function through sGC mRNA stabilization by HuR. *Arterioscler Thromb Vasc Biol.* 2011;31:567–573.

34. Sundaresan M, Yu ZX, Ferrans VJ, Irani K, Finkel T. Requirement for generation of H₂O₂ for platelet-derived growth factor signal transduction. *Science*. 1995;270:296–299.
35. Kuan CY, Yang DD, Samanta Roy DR, Davis RJ, Rakic P, Flavell RA. The JNK1 and JNK2 protein kinases are required for regional specific apoptosis during early brain development. *Neuron*. 1999;22:667–676
36. Ishibe S, Joly D, Zhu X, Cantley LG. Phosphorylation-dependent paxillin-ERK association mediates hepatocyte growth factor-stimulated epithelial morphogenesis. *Mol Cell*. 2003;12:1275–1285.
37. Hofmann Bowman M, Wilk J, Heydemann A, Kim G, Rehman J, Lodato JA, Raman J, McNally EM. S100A12 mediates aortic wall remodeling and aortic aneurysm. *Circ Res*. 2010;106:145–154
38. Groenink M, den Hartog AW, Franken R, Radonic T, de Waard V, Timmermans J, Scholte AJ, van den Berg MP, Spijkerboer AM, Marquering HA, Zwinderman AH, Mulder BJ. Losartan reduces aortic dilatation rate in adults with marfan syndrome: a randomized controlled trial. *Eur Heart J*. 2013;34:3491–3500.
39. Habashi JP, Judge DP, Holm TM, Cohn RD, Loeys BL, Cooper TK, Myers L, Klein EC, Liu G, Calvi C, Podowski M, Neptune ER, Halushka MK, Bedja D, Gabrielson K, Rifkin DB, Carta L, Ramirez F, Huso DL, Dietz HC. Losartan, an AT1 antagonist, prevents aortic aneurysm in a mouse model of marfan syndrome. *Science*. 2006;312:117–121.
40. Pearson GD, Devereux R, Loeys B, Maslen C, Milewicz D, Pyeritz R, Ramirez F, Rifkin D, Sakai L, Svensson L, Wessels A, Van Eyk J, Dietz HC. Report of the national heart, lung, and blood institute and national marfan foundation working group on research in marfan syndrome and related disorders. *Circulation*. 2008;118:785–791.
41. Matt P, Schoenhoff F, Habashi J, Holm T, Van Erp C, Loch D, Carlson OD, Griswold BF, Fu Q, De Backer J, Loeys B, Huso DL, McDonnell NB, Van Eyk JE, Dietz HC. Circulating transforming growth factor-beta in marfan syndrome. *Circulation*. 2009;120:526–532.
42. Holm TM, Habashi JP, Doyle JJ, Bedja D, Chen Y, van Erp C, Lindsay ME, Kim D, Schoenhoff F, Cohn RD, Loeys BL, Thomas CJ, Patnaik S, Marugan JJ, Judge DP, Dietz HC. Noncanonical TGFbeta signaling contributes to aortic aneurysm progression in marfan syndrome mice. *Science*. 2011;332:358–361.
43. Obayashi T, Hayashi S, Shibaoka M, Saeki M, Ohta H, Kinoshita K. Coexpressdb: a database of coexpressed gene networks in mammals. *Nucleic Acids Res*. 2008;36:D77–D82.

Hic-5 deficiency attenuates the activation of hepatic stellate cells and liver fibrosis through upregulation of Smad7 in mice

Xiao-Feng Lei^{1,†}, Wenguang Fu^{1,2,†}, Joo-ri Kim-Kaneyama^{1,*}, Tomokatsu Omoto¹, Takuro Miyazaki¹, Bo Li², Akira Miyazaki¹

¹Department of Biochemistry, Showa University School of Medicine, Tokyo, Japan; ²Department of Hepatobiliary Surgery, The First Affiliated Hospital of Sichuan Medical University, Luzhou, China

Background & Aim: Hydrogen peroxide-inducible clone-5 (Hic-5), also named as transforming growth factor beta-1-induced transcript 1 protein (Tgfb1i1), was found to be induced by TGF- β . Previous studies have shown that TGF- β is a principal mediator of hepatic stellate cell (HSC) activation in liver fibrosis. However, this process remains elusive. In this study, we aimed to define the role of Hic-5 in HSC activation and liver fibrosis.

Methods: We examined the expression levels of Hic-5 during HSCs activation and in fibrotic liver tissues by quantitative real-time reverse transcriptase polymerase chain reaction, Western blot and immunohistochemistry. Hic-5 knockout (KO) and wild-type (WT) mice were subjected to bile duct ligation (BDL) or carbon tetrachloride (CCl₄) injection to induce liver fibrosis.

Results: Hic-5 expression was strongly upregulated in activated HSCs of the human fibrotic liver tissue and BDL or CCl₄-induced mouse liver fibrosis. Hic-5 deficiency significantly attenuated mouse liver fibrosis and HSC activation. Furthermore, Hic-5 knockdown by siRNA *in vivo* repressed CCl₄-induced liver fibrosis in mice. Mechanistically, the absence of Hic-5 significantly inhibited the TGF- β /Smad2 signaling pathway, proved by increasing Smad7 expression, resulting in reduced collagen production and α -smooth muscle actin expression in the activated HSCs.

Conclusion: Hic-5 deficiency attenuates the activation of HSCs and liver fibrosis though reducing the TGF- β /Smad2 signaling

by upregulation of Smad7. Thus, Hic-5 can be regarded as a potential therapeutic target for liver fibrosis.

© 2015 European Association for the Study of the Liver. Published by Elsevier B.V. All rights reserved.

Introduction

Liver fibrosis represents a wound healing process in response to chronic liver damage from a variety of causes and is characterized by the deposition of extracellular matrix (ECM) proteins, which can impair the normal liver function [1]. Following liver injury, quiescent hepatic stellate cells (HSCs) are activated and believed to be the major source of myofibroblasts, which are the main ECM-producing cells during liver fibrosis [2,3]. Increasing evidence has shown that transforming growth factor- β (TGF- β)/Smad signaling pathway plays a critical role in the activation of HSCs [4–6], Smad7, a TGF- β inducible antagonist for TGF- β signaling [7], has been shown to inhibit the activation of HSCs and prevent liver fibrosis [8,9], as well as other fibrotic diseases such as renal and pulmonary fibrosis [10,11]. From these findings, we are aware of the importance of the cellular expression of Smad7 in the regulation of TGF- β /Smad signaling during progression of organ fibrosis. However, the intracellular Smad7 regulatory mechanism in this pathogenic process remains elusive.

Hydrogen peroxide-inducible clone 5 (Hic-5), also known as transforming growth factor beta-1-induced transcript 1 (Tgfb1i1), is originally identified as a gene induced by H₂O₂ as well as TGF- β 1 and is a focal adhesion scaffold LIM-containing protein with homology to paxillin [12]. Hic-5 is highly expressed in the vascular smooth muscle cells of different organs [13]. This molecule can shuttle between focal adhesions and the nucleus in response to oxidants [14]. Furthermore, Hic-5 participates in the transcriptional regulation of several genes [15–17]. It was reported that Hic-5 upregulates TGF- β signaling through its ability to directly interact with and neutralize Smad7 in a myofibroblast cell line [18]. In a recent study, we successfully generated mice lacking Hic-5, which developed with no obvious abnormalities [19]. However, in the various types of vascular disorder models, we found that Hic-5 contributes to vascular repair and remodeling [19,20]. Interestingly, Hic-5 also plays an important role in some fibrotic disorders, including scar formation and glomerulosclerosis [21–23]. Currently, no studies have examined

Keywords: Hic-5; Tgfb1i1; Smad2; Smad7; Hepatic stellate cells; Liver fibrosis.
Received 9 February 2015; received in revised form 25 July 2015; accepted 17 August 2015; available online 31 August 2015

* Corresponding author. Address: Department of Biochemistry, Showa University School of Medicine, 1-5-8 Hatanodai, Shinagawa-ku, Tokyo 142-8555, Japan. Tel.: +81 3 3784 8116; fax: +81 3 3784 2346.

E-mail address: shuri@pharm.showa-u.ac.jp (J.-r. Kim-Kaneyama).

[†] These authors contributed equally to the work.

Abbreviations: Ad-Hic-5/flag, adenovirus-mediated flag-tagged Hic-5; Ad- β -gal, adenovirus-mediated β -galactosidase; α -SMA, alpha smooth muscle actin; BDL, bile duct ligation; CCl₄, carbon tetrachloride; COL, collagen; ECM, extracellular matrix; GAPDH, glyceraldehyde 3-phosphate dehydrogenase; Hep, hepatocytes; Hic-5, Hydrogen peroxide-inducible clone-5; Hic-5 KO, Hic-5 knockout; HSCs, hepatic stellate cells; LSECs, liver sinusoid endothelial cells; P-Smad2, phosphorylated Smad2; siRNA, small interfering RNA; TGF- β , transforming growth factor- β ; Tgfb1i1, Transforming growth factor beta-1-induced transcript 1; WT, Wild-type.



the role of *Hic-5* in the liver. Here we hypothesized that *Hic-5* may be involved in liver fibrosis. Thus, we first examined *Hic-5* expression in normal and fibrotic human and mouse livers. Second, we determined whether *Hic-5* is involved in liver fibrosis using the *Hic-5* knockout mice. Third, we investigated the mechanisms by which *Hic-5* contributes to liver fibrosis.

Materials and methods

Please refer to the [Supplementary materials and methods](#) for more detailed descriptions.

Human liver samples

Human liver samples were obtained from patients undergoing surgical hepatectomy. The study protocol was approved by the local ethics committee (The first affiliated Hospital of Sichuan Medical University, Luzhou city, China), and all samples collected were from subjects who provided informed consent for their tissues to be used for research purposes. Patient characteristics were summarized in [Supplementary Table 1](#).

Animal studies

Wild-type (WT) and systemic *Hic-5* knockout (*Hic-5* KO) mice (C57BL/6 background) [19] were maintained under specific pathogen-free conditions in the animal care facility of Showa University School of Medicine. Experiments were performed with age- and sex-matched mice at 8–12 weeks of age. Liver fibrosis was induced by bile duct ligation (BDL) for 2 weeks or injection with carbon tetrachloride (CCl₄) for 12 times (twice a week for six weeks). All experiments were approved by the regional Animal Study Committees and performed according to the institutional guidelines stipulated by Showa University School of Medicine.

Cell isolation and culture

Major cell types in the liver include hepatocytes, Kupffer cells, liver sinusoid endothelial cells (LSECs), and HSCs.

Mouse HSCs were isolated by *in situ* perfusion of livers with pronase/collagenase perfusion digestion followed by subsequent density gradient centrifugation as reported [24]. HSCs were maintained in Dulbecco's modified Eagle medium (WAKO Chemicals, Japan) supplemented with 10% fetal bovine serum, 1% penicillin/streptomycin, and 10 mM HEPES; cells were counted and cell suspensions were incubated in collagen I-coated dishes (IWAKI, Japan) and maintained at 37 °C in a humidified atmosphere of containing 5% CO₂ and 95% air. After culturing for 2 h, the purity of isolated HSCs was checked by identifying the blue fluorescence of vitamin A when excited by ultraviolet light ([Supplementary Fig. 1](#)). The culture medium was replaced every 48 h unless otherwise described.

Human primary HSCs were purchased from ScienCell Research Laboratories (San Diego, CA, USA; Catalog #5300) and cultured in stellate cell medium (Catalog #5301) according to the manufacturer's instructions.

Refer to the [Supplementary materials and methods](#) section for isolation of other cell types.

Statistical analysis

Animals were randomly allocated to control and treatment groups. At least three samples were tested in each assay. All data were expressed as means ± the standard error of the mean. Statistical analyses were performed using Mann-Whitney test (GraphPad Prism, version 5.0 for MAC) for comparisons of parameters between the two groups and differences were considered statistically significant at *p* value <0.05.

Results

Hic-5 expression is enhanced in activated HSCs and fibrotic liver

We first assessed *Hic-5* expression in normal and fibrotic human livers. Real-time reverse transcriptase polymerase chain reaction

(RT-PCR) and Western blot analyses confirmed that the mRNA or protein expression of *Hic-5*, α -smooth muscle actin (*ACTA2*) and collagen I (*COL1A1*) was markedly increased in human fibrotic livers vs. normal livers ([Fig. 1A, B](#); [Supplementary Fig. 2A](#)). Using immunostaining, *Hic-5* expression was only found in vascular smooth muscle cells of Glisson's sheath in normal livers, whereas the enhanced expression of *Hic-5* was found in human fibrotic livers ([Fig. 1C](#); [Supplementary Fig. 2B](#)). Furthermore, we analyzed colocalization of *Hic-5* with each of α -SMA, LYVE1, and Iba1, the cell type marker for activated HSCs, LSECs, and Kupffer cells, respectively. *Hic-5* expression overlapped with α -SMA-positive HSCs as seen by the yellow fluorescence in human fibrotic liver ([Fig. 1C](#), enlarged), but neither LSECs, including endothelial cells of liver central vein, nor Kupffer cells expressed *Hic-5* ([Supplementary Fig. 3A–C](#)). In addition, immunofluorescence staining of commercially available primary human HSCs showed significant *Hic-5* expression ([Supplementary Fig. 4A](#)). We then analyzed *Hic-5* levels in mouse fibrotic livers that were generated by two different methods, BDL and intraperitoneal CCl₄ injection. Similar to the human results, both mouse models of liver fibrosis showed a significant increase in *Hic-5* protein expression: a 5.5-fold increase with BDL and a 4.7-fold increase with CCl₄ injection compared with controls ([Fig. 1D](#)). Immunofluorescent microscopy revealed the colocalization of *Hic-5* and α -SMA in both the BDL and the CCl₄ fibrosis models evidenced by yellow fluorescence ([Fig. 1E](#)). We next examined *Hic-5* expression in isolated mouse primary liver cells such as HSCs, LSECs, Kupffer cells, and hepatocytes. After culturing for 2 h, *Hic-5* expression was detected only in HSCs, but not in other cell types ([Fig. 1F](#)). We comparatively analyzed the expression of *Hic-5* and α -SMA in cultured primary mouse HSCs undergoing differentiation from quiescent to activated HSCs at different times (from 2 h to 15 days) by Western blot analysis. Both of these proteins gradually increased during differentiation. Meanwhile, we detected *Hic-5* at an earlier stage of differentiation compared with α -SMA ([Fig. 2H](#)). Similarly, immunofluorescence analysis confirmed that *Hic-5* and α -SMA were increased during differentiation. *Hic-5* was detected at focal adhesions of cells from 2 h of culture, while α -SMA was observed at day 3 of culture ([Fig. 2G](#), [Supplementary Fig. 4B](#)). Of note, vitamin A lipid droplets were depleted during HSC differentiation as previously reported.

Hic-5 deficiency reduces BDL- and CCl4-induced liver fibrosis

To investigate the contributing roles of *Hic-5* in liver fibrogenesis, we induced liver fibrosis using two different ways, BDL or CCl₄ injection, in WT and *Hic-5* KO mice. Sirius Red and Masson's trichrome stainings were used for morphometric analysis of liver fibrosis. After treatment of mice with BDL or CCl₄, we found significant reduction in both kinds of staining in *Hic-5* KO mice compared with WT mice ([Fig. 2A, B](#) and [Fig. 2C, D](#) left panels). Histological examination of hematoxylin and eosin-stained liver sections indicated that necrotic area was significantly decreased in *Hic-5* KO mice compared with WT mice after BDL ([Supplementary Fig. 5](#)). Moreover, the liver from *Hic-5* KO mice displayed a marked decrease in hydroxyproline, a specific amino acid component of collagen ([Fig. 2C, D](#) right panels). In addition, RT-PCR analysis confirmed significantly lower expression of fibrosis-related genes, including collagen I (*Col1a1*, *Col1a2*) and collagen III (*Col3a1*) in *Hic-5* KO mouse livers compared with WT mouse livers after BDL ([Fig. 2E](#)) or treatment with CCl₄ ([Fig. 2F](#)). We also

Research Article

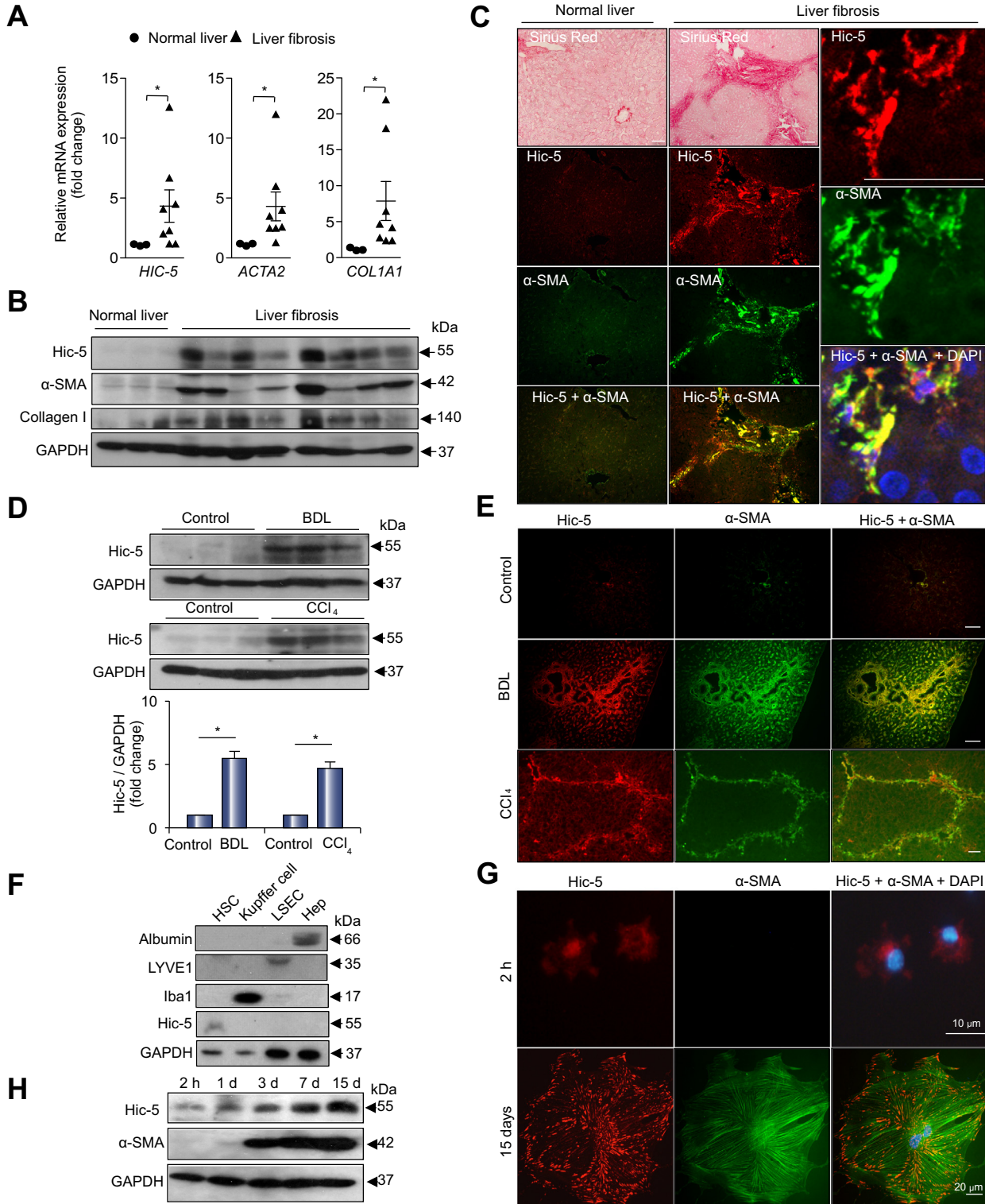


Fig. 1. Expression of Hic-5 is upregulated in activated HSCs and in human and mouse liver fibrosis. (A) mRNA and (B) protein expression of Hic-5, α -SMA (*ACTA2*) and collagen I (*COL1A1*) in three normal and eight fibrotic human livers. $^*p < 0.01$ (C) Sirius Red staining and double immunofluorescence staining for Hic-5 (red) and α -SMA (green) in normal and fibrotic human livers. Scale bars = 50 μ m. (D) Representative Western blot analysis of Hic-5 expression in mouse livers from WT mice with or without BDL or injections of CCl₄. Quantitative analyses of Hic-5 is shown in the lower panel. (E) Double immunofluorescence staining for Hic-5 (red) and α -SMA (green) in the livers from WT mice with or without BDL or injections of CCl₄. Scale bars = 50 μ m. (F) Western blot analysis of Hic-5, lymphatic vessel endothelial receptor (LYVE-1), and Iba1 expression in isolated HSCs, liver sinusoid endothelial cells (LSEC), Kupffer cells and hepatocytes (Hep) from WT mice after 2 h incubation. (G) Representative double immunofluorescence staining for Hic-5 (red) and α -SMA (green) in cultured HSCs from WT mice at the indicated time points. (H) Western blot analysis of Hic-5 and α -SMA expression in cultured HSCs from WT mice at the indicated times.

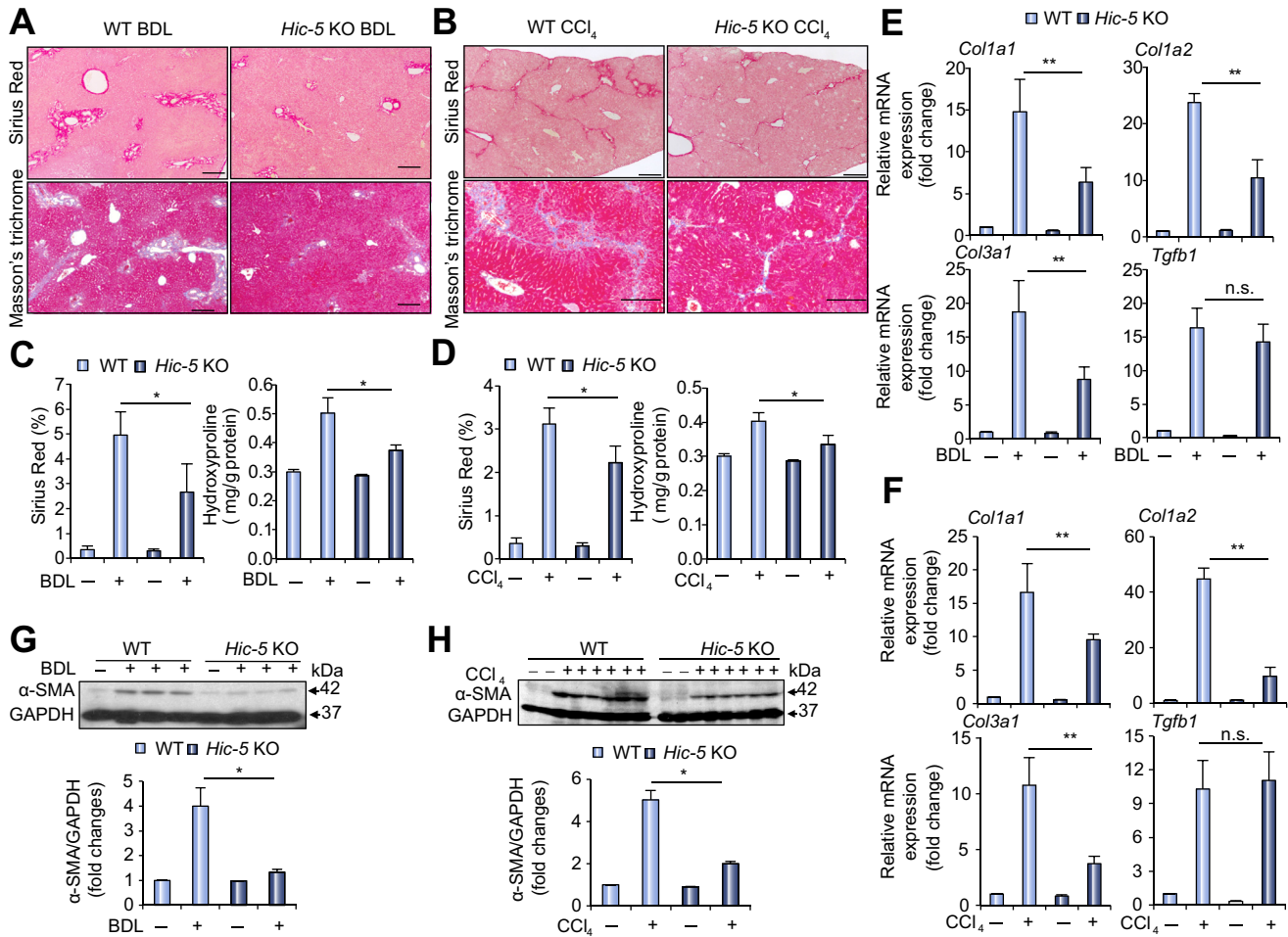


Fig. 2. *Hic-5* KO attenuates mouse liver fibrosis following BDL or CCl_4 -treatment. (A, C, E, G) WT (n = 10) and *Hic-5* KO (n = 9) mice underwent BDL for two weeks and (B, D, F, H) WT (n = 13) and *Hic-5* KO (n = 11) mice underwent CCl_4 injection for 12 times. Liver fibrosis was evaluated by Sirius Red and Masson's trichrome staining (Scale bars = 50 μ m) (A, B and C, D left panels) and hydroxyproline content (C, D right panels). (E, F) mRNA expression of collagen I (*Col1a1*, *Col1a2*), collagen III (*Col3a1*) and TGF- β 1 (*Tgfb1*) in the livers of WT and *Hic-5* KO mice. (G, H) Representative Western blot analysis of α -SMA expressions in the livers from WT and *Hic-5* KO mice. The lower panels show quantitative analyses of α -SMA expression after normalization with glyceraldehyde 3-phosphate dehydrogenase (GAPDH). * p < 0.05. ** p < 0.01.

assessed the protein levels of α -SMA, a marker of activated HSCs [3], in the liver by Western blot analysis. The fibrotic livers of WT mice showed high levels of α -SMA expression, but the expression was markedly reduced in *Hic-5* KO after BDL (Fig. 2G) or treatment with CCl_4 (Fig. 2H). These results suggest that *Hic-5* contributes to liver fibrosis induced by BDL or CCl_4 treatment in mice. Interestingly, there was no difference in mRNA expression of inflammatory cytokines including TGF- β 1 between WT mice and *Hic-5* KO mice (Fig. 2E, F and Supplementary Fig. 6). In addition, we did not observe the differences in the proliferation of cholangiocytes and hepatocytes between WT mice and *Hic-5* KO mice in both models of liver fibrosis (Supplementary Figs. 7 and 8).

Hic-5 deficiency attenuates activation of cultured HSCs

Activation and proliferation of HSCs is well known to play a crucial role in promoting ECM production and liver fibrosis [2,3]. Cultured WT HSCs at day 7 showed phenotypic change to myofibroblast-like cells characterized by a loss of vitamin A and upregulated α -SMA, an activation marker of HSCs (Supplementary Fig. 4B). To assess if *Hic-5* is required for the activation of

HSCs *in vitro*, we isolated HSCs from the livers of WT and *Hic-5* KO mice and cultured HSCs on collagen I-coated plastic dishes for seven days. Quantitative mRNA analysis showed a marked decrease in the expression of multiple genes associated with activated HSCs, including α -SMA (*Acta2*), collagen I (*Col1a1*), collagen III (*Col3a1*), in *Hic-5* KO HSCs compared with WT mice (Fig. 3A). Furthermore, Western blot analysis showed that α -SMA protein levels were reduced in culture-activated *Hic-5* KO HSCs (Fig. 3B). Consistent with the mRNA levels in mouse livers, HSCs activated in culture from WT and *Hic-5* KO mice had similar TGF- β 1 mRNA expression (data not shown). In addition, cell proliferation was detected by MTT assay. During the differentiation of cultured mouse HSCs at different times (from 1 day to 7 days), we found no significant difference in the proliferation rates between WT HSCs and *Hic-5* KO HSCs (Supplementary Fig. 9A). We also knocked down *Hic-5* in cultured human HSCs using *Hic-5* siRNA. Western blot analysis showed that the expression of both α -SMA and collagen I was suppressed in addition to *Hic-5* (Fig. 3C). These results indicate that the activation of HSCs is mediated through *Hic-5* expression and imply that *Hic-5* serves as a potential novel marker for activated HSCs.

Research Article

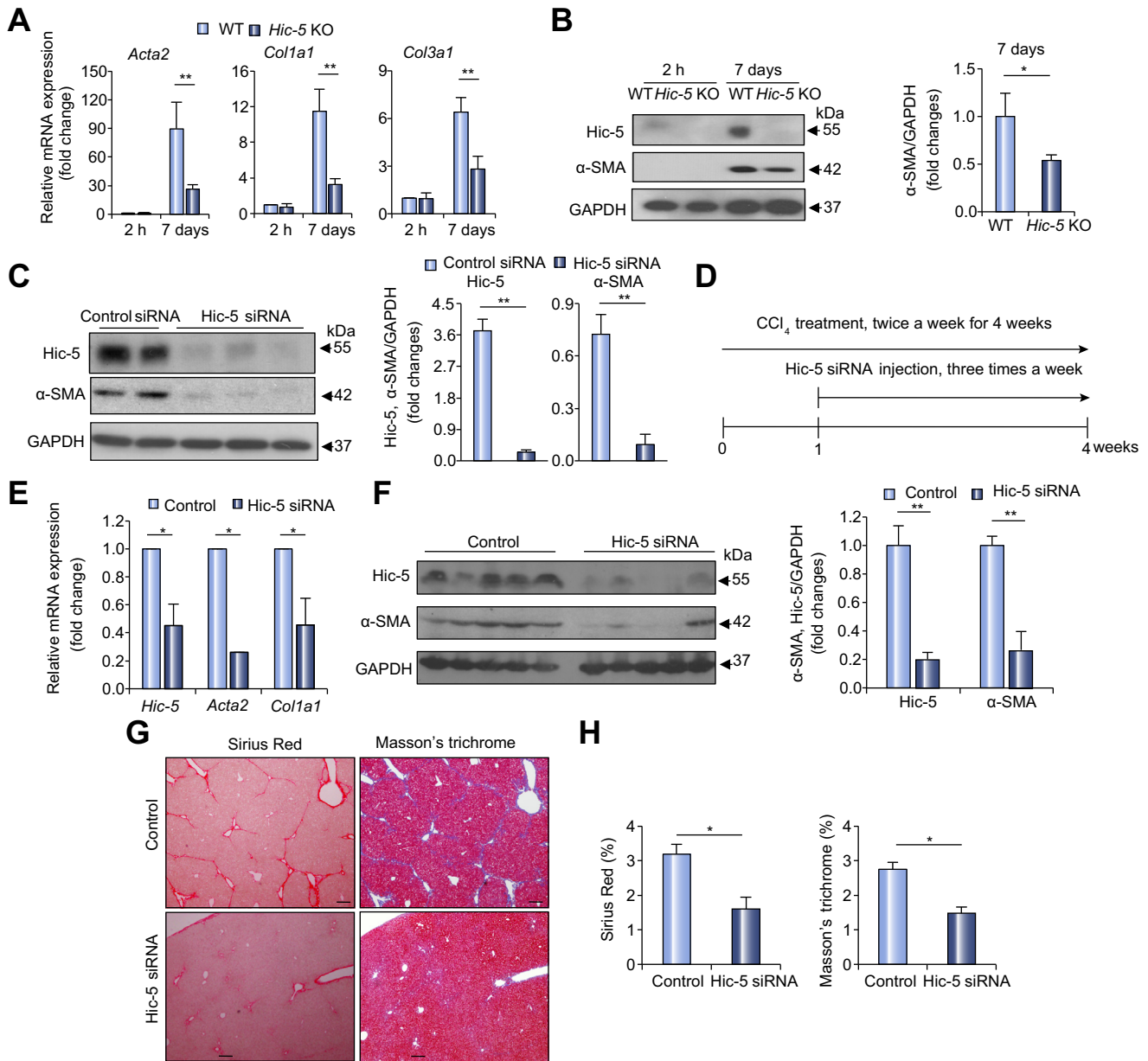


Fig. 3. Hic-5 deficiency reduces the activation of HSCs and *in vivo* knockdown of Hic-5 causes a decrease of CCl₄-induced liver fibrosis. (A) mRNA expression of α -SMA (*Acta2*), collagen I (*Col1a1*) and collagen III (*Col3a1*) in cultured HSCs from the livers of WT and *Hic-5* KO mice at the indicated time points. (B) Representative Western blot analysis of Hic-5 and α -SMA expressions in cultured HSCs from WT and *Hic-5* KO mice at the indicated time points. The right panel shows quantitative analyses of α -SMA expression after normalization with GAPDH. (C) Representative Western blot analysis of Hic-5 and α -SMA expression in cultured human HSCs after transfection with control siRNA or Hic-5 siRNA for 24 h. The right panel shows quantitative analyses of Hic-5 and α -SMA expression after normalization with GAPDH. (D) Timeline of the experimental procedure. The siRNA against Hic-5 was intravenously injected with an amount of 3 mg/g (weight) through the tail vein thrice a week for three weeks. PBS was injected for control (n = 5 per group). (E) mRNA expression of *Hic-5*, α -SMA (*Acta2*), and collagen I (*Col1a1*) in control and Hic-5 siRNA-injected mouse liver after CCl₄ treatment. (F) Western blot analysis of Hic-5 and α -SMA expression in control and Hic-5 siRNA-injected mouse liver after CCl₄ treatment. The right panel shows quantitative analyses of Hic-5 and α -SMA expression after normalization with GAPDH. (G, H) Representative images of Sirius Red staining and Masson's trichrome staining for the detection of collagens in control and Hic-5 siRNA-injected mouse liver after CCl₄ treatment. Scale bars = 50 μ m. Representative data from 3 to 5 independent experiments. *p < 0.05. **p < 0.01.

In vivo knockdown of Hic-5 attenuates CCl₄-induced liver fibrosis

To evaluate the therapeutic potential of Hic-5 in CCl₄-induced liver fibrosis, Hic-5 siRNA was intravenously injected through the tail vein of the mice from the second week to the fourth week

after CCl₄ treatment (Fig. 3D). Efficiency of Hic-5 *in vivo* knockdown was assessed by RT-PCR (Fig. 3E) and Western blot (Fig. 3F). Hic-5 siRNA treatment caused a significant decrease in *Hic-5* mRNA and protein expression (Fig. 3E, F). To analyze the antifibrotic effects of Hic-5 siRNA on the liver fibrogenesis,

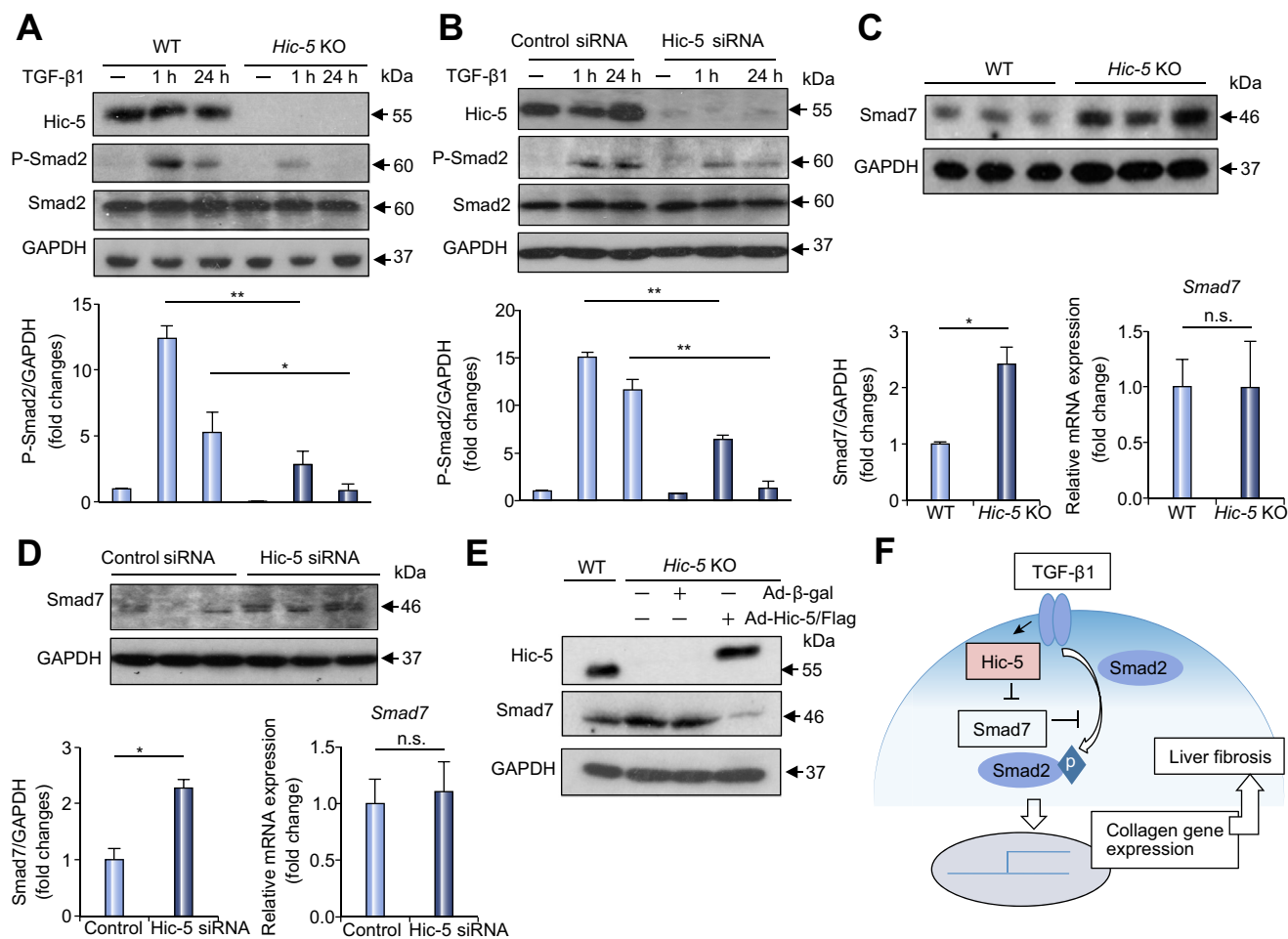


Fig. 4. Hic-5 depletion impairs Smad2 phosphorylation by upregulating Smad7 expression in both cultured murine and human HSCs. Representative Western blot analysis of phosphorylated Smad2 (P-Smad2) in cultured HSCs from WT and *Hic-5* KO mice livers (A) or in cultured human HSCs transfected with Hic-5/control siRNA (B). These cells were treated with TGF-β1 (5 ng/ml) for 1 h and 24 h. Quantitative analyses of P-Smad2 are shown in the lower panels. Representative Western blot analysis of Smad7 in cultured HSCs from WT and *Hic-5* KO mice livers (C) or in cultured human HSCs transfected with Hic-5/control siRNA (D). The lower left panel shows quantitative analyses of Smad7 protein expression after normalization with GAPDH. The lower right panel shows quantitative analyses of Smad7 mRNA expression after normalization with GAPDH. (E) Western blot analysis of Smad7 and Hic-5 in cultured *Hic-5* KO HSCs. Cells were infected with adenovirus-mediated flag-tagged Hic-5 (Ad-Hic-5/flag) or adenovirus-mediated β-galactosidase (Ad-β-gal) as a control for 12 h. Representative data from 3 to 5 independent experiments. **p* < 0.05. ***p* < 0.01. (F) A signal transduction diagram showing that Hic-5 enhances TGF-β signaling in liver fibrosis.

α-SMA, and collagen I contents were measured. A significant reduction in α-SMA (*Acta2*) and collagen I (*Col1a1*) mRNA expression was observed in Hic-5 siRNA-treated mice relative to controls (Fig. 3E). Furthermore, the level of α-SMA proteins was significantly lower in Hic-5 siRNA-treated mice than controls (Fig. 3F). Sirius Red staining as well as Masson's trichrome staining also showed that CCl₄-induced liver fibrosis was inhibited in the Hic-5 siRNA-treated group compared with controls (Fig. 3G, H). These results demonstrate that Hic-5 siRNA can inhibit CCl₄-induced liver fibrosis *in vivo*, proposing Hic-5 as a potential therapeutic target for liver fibrosis.

Hic-5 depletion impairs Smad2 phosphorylation by upregulating Smad7 expression in both cultured murine and human HSCs

The TGF-β/Smad pathway was previously shown to contribute to HSC activation and production of ECM. We next investigated whether Hic-5 is required for the activation of the TGF-β/Smad

pathway. Using HSCs isolated from WT and *Hic-5* KO mice, we found that the phosphorylated Smad2 levels were significantly increased after TGF-β treatment in WT HSCs, but not in *Hic-5* KO HSCs (Fig. 4A). Furthermore, RNAi depletion of endogenous Hic-5 in cultured human HSCs showed a similar effect (Fig. 4B). These data strongly indicate a requirement for Hic-5 in the TGF-β/Smad2 signaling pathway in murine and human. For the detailed mechanism, we analyzed the effect of Hic-5 depletion on the expression of Smad7, which is a well-known antagonist of TGF-β signaling. Consistent with a previous report [18], Hic-5 deficiency enhanced Smad7 protein level but not mRNA expression level in murine and human HSCs (Fig. 4C, D). We also restored Hic-5 expression in *Hic-5* KO HSCs through adenovirus-mediated gene transfer, and compared with the control gene. Exogenous Hic-5 depressed the expression of Smad7 in *Hic-5* KO HSCs (Fig. 4E). Together, these results suggest that Hic-5 deficiency reduces the phosphorylation of Smad2 by upregulation of Smad7 expression (Fig. 4F), thereby inhibiting the HSC activation.

Research Article

Discussion

The major finding of this study is the identification of a pathological role of *Hic-5* in the activation of HSCs and liver fibrosis. First, *Hic-5* expression was significantly upregulated in both mouse liver fibrosis models (BDL and CCl₄) and human fibrotic livers (Fig. 1). Second, *Hic-5* deficiency markedly lessened the development of mouse liver fibrosis caused by BDL or CCl₄ treatment (Fig. 2). Third, *Hic-5* was highly expressed in activated HSCs (Fig. 1) and promoted liver fibrosis by upregulating the activation of HSCs (Fig. 3). Fourth, siRNA knockdown of *Hic-5* *in vivo* reduced liver fibrogenesis in the CCl₄-induced liver fibrosis model (Fig. 3). Finally, *Hic-5* promoted the TGF- β -induced phosphorylation of Smad2 by reducing Smad7 protein levels in mouse and human HSCs (Fig. 4). Therefore, *Hic-5* is considered a potential marker of activated HSCs and therapeutic target in the treatment of liver fibrosis.

Little is known about the function of *Hic-5* in the liver. A transcriptome analysis of mRNA expression from quiescent to culture-activated human HSCs and a proteomic analysis of cultured rat HSCs showed that *Hic-5* was not detected in quiescent HSCs, while *Hic-5* was markedly enhanced during the activation process [25,26]. We previously demonstrated in mice that the expression pattern of *Hic-5* was similar to that of α -SMA in both normal and lesion tissues in balloon injury and abdominal aortic aneurysms [19,20]. α -SMA is a well-known marker of activated HSCs and is highly expressed in liver fibrosis [3]. In normal liver tissue, *Hic-5* expression was detected only in vascular smooth muscle cells of Glisson's sheath, whereas in fibrotic livers expression of *Hic-5* was markedly enhanced together with colocalized α -SMA (Fig. 1). It is noteworthy that *Hic-5* expression was detected at an earlier stage (cultured for 2 h) than α -SMA expression (cultured for three days) (Fig. 1). In culture-activated HSCs at day 7, *Hic-5* gene deletion significantly decreased the activated marker, α -SMA expression (Fig. 3A, B). This result was consistent with the recent reports that α -SMA expression was upregulated through a *Hic-5*-dependent pathway [27,28]. Together, these results strongly suggest that *Hic-5* serves as a potential novel marker for activated HSCs, as well as a more sensitive diagnostic marker than α -SMA for early stage liver fibrosis.

Substantial evidence has clearly demonstrated that intracellular TGF- β signaling pathways mediate the progression of liver fibrosis following injury in experimental and human fibrotic liver [6,29–31]. Although activated HSCs secrete TGF- β 1 during liver injury, our results showed that *Hic-5* deficiency did not alter the levels of TGF- β 1 expression in both mouse liver fibrosis models (BDL and CCl₄) and in culture-activated HSCs. In addition, *Hic-5* deficiency did not affect TGF- β 1-induced apoptosis in culture-activated HSCs (Supplementary Fig. 9C). Smad7 is well known as an important feedback inhibitor of TGF- β signaling, in part, involving TGF- β -mediated phosphorylation of Smad2 [7]. Our results showed that *Hic-5* interferes with the inhibitory effects of Smad7 on TGF- β signaling (Fig. 4), which is consistent with a previous report using a myofibroblast cell line [18], indicating that *Hic-5* serves as a novel antagonist of Smad7 in HSCs. Quiescent HSCs in culture display a functional negative feedback regulation of TGF- β signal transduction through a TGF- β -induced upregulation of Smad7 expression, which, however, is lost in activated HSCs (cultured for 7 days) [32]. Conversely, our results showed that *Hic-5* expression was significantly higher in activated HSCs (cultured for 7 days) while its expression was low in quiescent HSCs (cultured for 2 h) (Fig. 1H). These results

indicate that enhanced *Hic-5* expression in activated HSCs leads to suppression of Smad7, thereby accelerating TGF- β signaling. TGF- β signaling is upregulated by *Hic-5* and downregulated by Smad7. Thus, the balance between *Hic-5* and Smad7 is critical for TGF- β signaling.

Although HSC-derived myofibroblasts are the main ECM-producing cells in the injured liver [2], liver fibrogenesis is a complex interplay among different hepatic cell types including residents immune cells and infiltrated inflammatory cells [33]. We confirmed that *Hic-5* deficiency does not affect mRNA expression of pro-inflammatory cytokines, but alone it is unlikely to explain the whole inflammatory response in liver injury. Moreover, liver fibrogenesis following liver injury is induced by multiple factors. Although their cellular and molecular mechanisms remain unclear except for the involvement of TGF- β , an increasing number of studies have demonstrated that angiotensin II and reactive oxygen species such as H₂O₂ are involved in the activation of HSCs and the pathogenesis of liver fibrosis [34–37]. The relationship between angiotensin II- and TGF- β -induced cellular signaling pathways is under investigation, however, recent evidence indicates that they may likely share partial common pathways. Our previous study revealed that *Hic-5* expression was also induced by either angiotensin II or H₂O₂ in smooth muscle cell and fibroblasts [13,14,20]. Although the present study identified the role of *Hic-5* in TGF- β signaling in liver fibrosis, future studies should focus on the role of angiotensin II or H₂O₂ in TGF- β signaling and liver fibrosis.

It was once believed that fibrosis was irreversible, but accumulating evidence indicates that even advanced fibrosis may be a reversible condition. During liver injury, HSCs undergo activation and the key steps for the activation process have been identified as potential therapeutic targets. As a conclusion, our study identified *Hic-5* as a novel regulator of liver fibrosis through activation of HSCs during liver injury. These results indicate that *Hic-5* plays a key role in the process of liver fibrogenesis and its potential therapeutic application, which may be clinically useful in preventing or treating liver fibrosis. In addition, our findings could be applicable to fibrosis in other organ systems, since *Hic-5* is potentially involved in other fibrotic disorders [21–23].

Financial support

This work was supported by Grants-in-Aid for Young Scientists (26860588 to X.-F. Lei) and Scientific Research (26461149 to J.-r. Kim-Kaneyama; 26461368 to A. Miyazaki) from Japan Society for the Promotion of Science, a research grant from Showa University Medical Foundation (to J.-R. Kim-Kaneyama), a research grant from Takeda Science Foundation (to J.-R. Kim-Kaneyama and X.-F. Lei), a research grant from the Natural Science Foundation of China (81400657 to W. Fu). This work was also supported in part by the MEXT (Ministry of Education, Culture, Sports, Science and Technology)-Supported Program for the Strategic Research Foundation at Private Universities, 2012–2016.

Conflict of interest

The authors who have taken part in this study declared that they do not have anything to disclose regarding funding or conflict of interest with respect to this manuscript.

Calpain-6 confers atherogenicity to macrophages by dysregulating pre-mRNA splicing

Takuro Miyazaki,¹ Kazuo Tonami,² Shoji Hata,³ Toshihiro Aiuchi,⁴ Koji Ohnishi,⁵ Xiao-Feng Lei,¹ Joo-ri Kim-Kaneyama,¹ Motohiro Takeya,⁵ Hiroyuki Itabe,⁴ Hiroyuki Sorimachi,³ Hiroki Kurihara,² and Akira Miyazaki¹

¹Department of Biochemistry, Showa University School of Medicine, Tokyo, Japan. ²Department of Physiological Chemistry and Metabolism, Graduate School of Medicine, The University of Tokyo, Tokyo, Japan.

³Calpain Project, Department of Advanced Science for Biomolecules, Tokyo Metropolitan Institute of Medical Science, Tokyo, Japan. ⁴Division of Biological Chemistry, Department of Molecular Biology, Showa University School of Pharmacy, Tokyo, Japan. ⁵Department of Cell Pathology, Graduate School of Medical Sciences, Kumamoto University, Kumamoto, Japan.

Macrophages contribute to the development of atherosclerosis through pinocytotic deposition of native LDL-derived cholesterol in macrophages in the vascular wall. Inhibiting macrophage-mediated lipid deposition may have protective effects in atheroprone vasculature, and identifying mechanisms that potentiate this process may inform potential therapeutic interventions for atherosclerosis. Here, we report that dysregulation of exon junction complex-driven (EJC-driven) mRNA splicing confers hyperpinocytosis to macrophages during atherogenesis. Mechanistically, we determined that inflammatory cytokines induce an unconventional nonproteolytic calpain, calpain-6 (CAPN6), which associates with the essential EJC-loading factor CWC22 in the cytoplasm. This association disturbs the nuclear localization of CWC22, thereby suppressing the splicing of target genes, including those related to Rac1 signaling. CAPN6 deficiency in LDL receptor-deficient mice restored CWC22/EJC/Rac1 signaling, reduced pinocytotic deposition of native LDL in macrophages, and attenuated macrophage recruitment into the lesions, generating an atheroprotective phenotype in the aorta. In macrophages, the induction of CAPN6 in the atheroma interior limited macrophage movements, resulting in a decline in cell clearance from the lesions. Consistent with this finding, we observed that myeloid CAPN6 contributed to atherogenesis in a murine model of bone marrow transplantation. Furthermore, macrophages from advanced human atheromas exhibited increased CAPN6 induction and impaired CWC22 nuclear localization. Together, these results indicate that CAPN6 promotes atherogenicity in inflamed macrophages by disturbing CWC22/EJC systems.

Introduction

Atherosclerosis is a vascular disease characterized by intimal and subintimal cholesterol deposition in which cholesterol forms an initial fatty streak that is followed by an extended atheroma (1). Rupture of atherosclerotic plaques leads to lethal cardiovascular events, such as myocardial infarction and stroke, 2 primary causes of morbidity and mortality worldwide. Pharmacotherapy using statins is beneficial for the primary prevention of cardiovascular diseases, achieving a reduction in event rates of approximately 20%–40% in randomized, placebo-controlled clinical trials (2); however, statins are insufficient for lowering the number of recurrent events. For instance, lethal recurrent ischemic events following acute coronary syndrome occur in more than 20% of patients by 30 months despite optimal cholesterol-lowering therapy (3). Thus, a precise understanding of the pathogenesis of atherosclerotic diseases in vascular walls, including cholesterol deposition, is indispensable for next-generation antiatherosclerosis therapies.

Cholesterol deposition in vascular walls is mainly due to foam cell formation within monocyte-derived macrophages (4). Although many earlier investigations are based on the concept that foam cell formation in macrophages is driven by the uptake

of oxidized LDLs by scavenger receptors, some findings challenge this hypothesis. For instance, LDL isolated from human atherosclerotic vessels is insufficiently oxidized to be recognized by scavenger receptors (5). Furthermore, a deficiency of scavenger receptors does not abrogate foam cell formation in macrophages in atherogenic mice (6), implying that alternative mechanisms govern LDL uptake in macrophages. Recent advances have shown that scavenger receptor-independent uptake of native LDL in macrophages can drive foam cell formation. This phenomenon is known as fluid-phase pinocytosis (7). The pinocytotic uptake of native LDL is also independent of the degree of LDL oxidation and does not saturate, which is distinct from the properties of receptor-mediated uptake of modified LDL. Buono et al. reported that pinocytotic activity is potentiated in macrophages in murine atherosclerotic lesions (8). Although pinocytosis is mediated through Rho GTPase cytoskeletal dynamics (9, 10), little is known about its regulatory mechanisms.

In macrophage biology, growing evidence suggests that the posttranslational processing of functional proteins, in addition to their transcriptional regulation, defines their physiological and pathophysiological behavior. Calpain, an intracellular Ca²⁺-sensitive protease, plays a pivotal role in this process, thereby controlling endocytic signals in macrophages (11) and intracellular trafficking in platelets (12) as well as cytoskeletal dynamics (13). In terms of cholesterol regulation, calpain-1 (μ -calpain) reportedly proteolyzes

Conflict of interest: The authors have declared that no conflict of interest exists.

Submitted: December 4, 2015; **Accepted:** July 7, 2016.

Reference information: *J Clin Invest.* 2016;126(9):3417–3432. doi:10.1172/JCI85880.

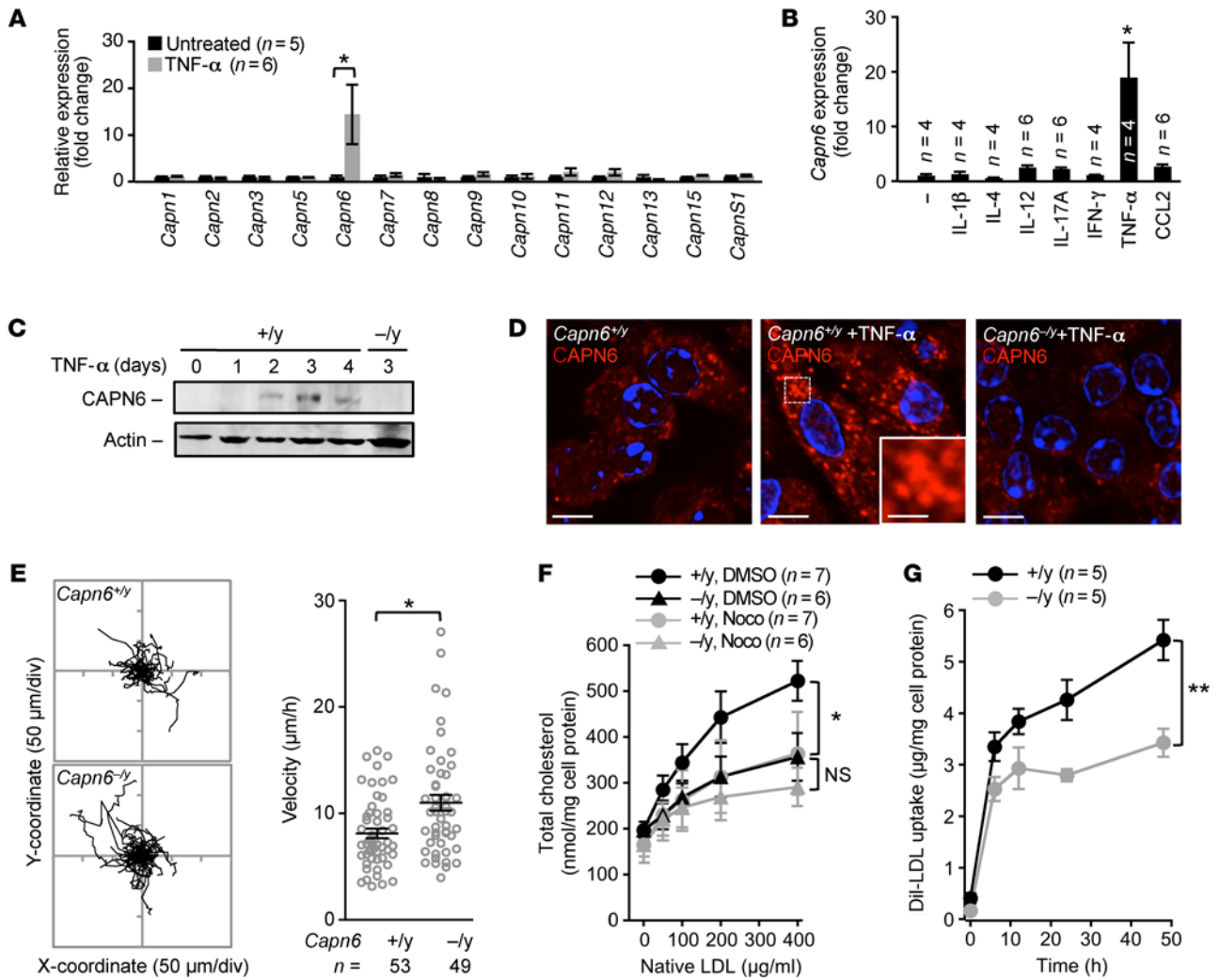


Figure 1. Loss of CAPN6 reduces the pinocytotic uptake of native LDL in macrophages. BMMs at day 4 of differentiation were used in these experiments. (A) Expression of calpain family members in BMMs in response to TNF- α stimulus. (B) Expression of *Capn6* mRNA in BMMs in response to variety of inflammatory stimuli. BM cells were stimulated with a variety of cytokines (IL-1 β , IL-4, IL-12, IL-17A, IFN- γ , TNF- α , 10 ng/ml; or CCL2, 50 ng/ml) together with M-CSF at 50 ng/ml for 4 days. (C) CAPN6 protein expression in TNF- α /M-CSF-primed BMMs. One representative result of 3 independent experiments is shown. (D) Subcellular distribution of CAPN6 in TNF- α /M-CSF-primed *Capn6*^{+y}*Ldlr*^{-/-} BMMs. *Capn6*^{-y}*Ldlr*^{-/-} BMMs served as a negative control. Scale bars: 10 μ m (D); 3 μ m (insets). (E) Cellular movements in BMMs. TNF- α /M-CSF-primed BMMs were tracked for 10 hours in the presence of CCL2 at 50 ng/ml. (F) Uptake of native LDL in TNF- α /M-CSF-primed *Capn6*^{+y}*Ldlr*^{-/-} or *Capn6*^{-y}*Ldlr*^{-/-} BMMs. Cells were treated with native LDL for 24 hours at the concentrations indicated, either in the presence of DMSO or nocodazole (Noco) at 1 μ mol/l. (G) Temporal changes in the uptake of DiI-labeled LDL in TNF- α /M-CSF-primed BMMs. ** $P < 0.01$; * $P < 0.05$, 1-way ANOVA followed by Bonferroni's test (A and B), Mann-Whitney *U* test (E), 2-way ANOVA (F and G). Error bars represent the mean \pm SEM.

the proteins ATP-binding cassette transporter subfamily A member 1 (ABCA1) and ATP-binding cassette transporter subfamily G member 1 (ABCG1), thereby preventing cholesterol efflux in cultured macrophages (14, 15). Earlier investigations by others and us have suggested that administering subtype-nonselective inhibitors of calpains suppresses atherosclerosis in mice without altering plasma dyslipidemia (16, 17). These atheroprotective actions may be due to the suppression of hyperpermeability induced by calpain-2 (m-calpain) in vascular endothelial cells and calpain-1-induced hyperinflammation in macrophages, whereas the proatherogenic roles of calpain in lipid handling in macrophages remain enigmatic. Moreover, considering that there are 15 homologues of the catalytic subunit of human calpain (13), the predominance of calpain family members in macrophage regulation remains unclear. Using

gene-targeting approaches, we herein investigated the impact of calpain family members on LDL uptake in proatherogenic macrophages. This study identifies calpain-6 (CAPN6), a unique nonclassical calpain without proteolytic activity, as an accelerator of the pinocytotic deposition of native LDL in macrophages and proposes a mechanism involving LDL metabolism in macrophages that is inducible by the disturbance of posttranscriptional mRNA splicing.

Results

CAPN6 modulates Rac1-dependent cellular dynamics and pinocytotic activity. To examine the involvement of calpains in macrophage regulation, we investigated the expression of calpain family members in murine BM-derived macrophages (BMMs) (Figure 1A). *Capn6* mRNA was selectively induced by supplementing the

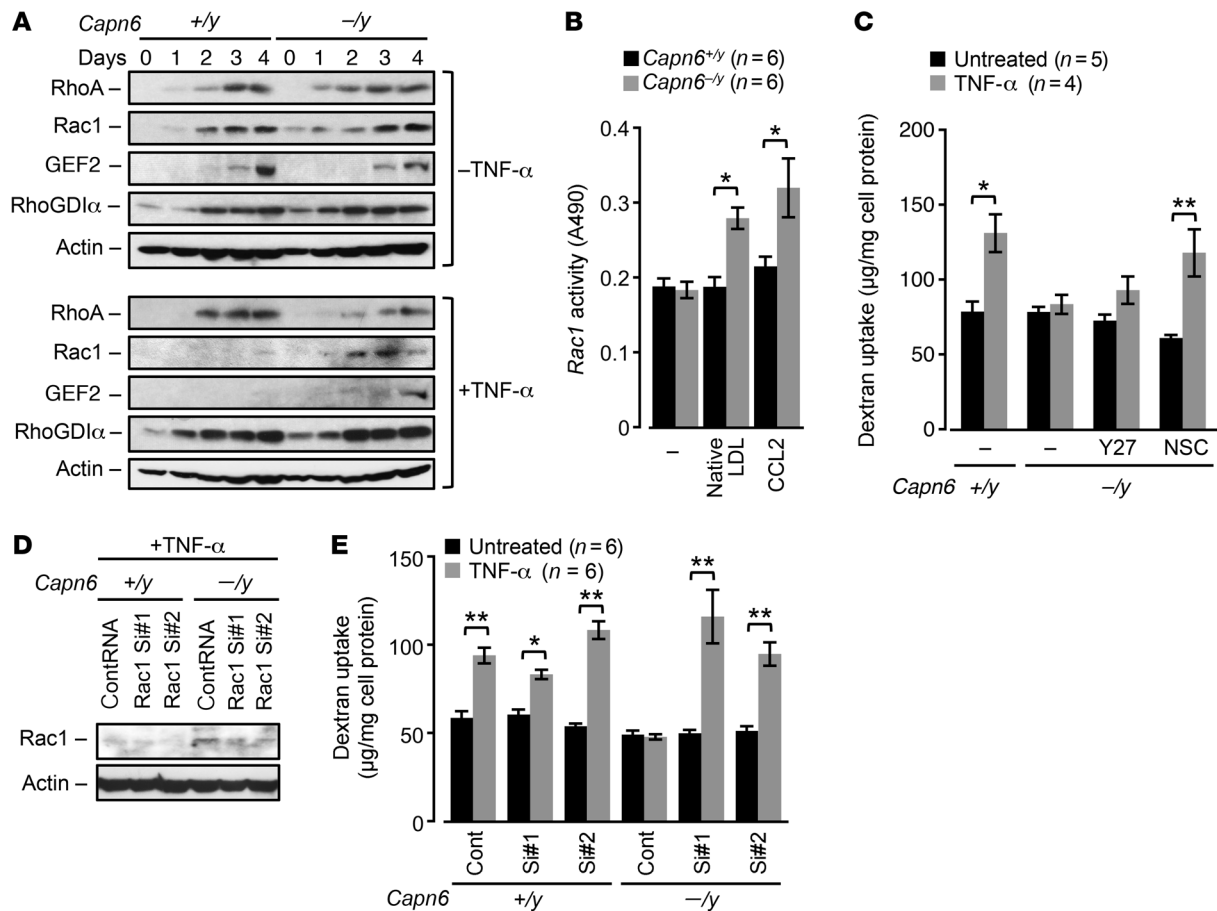


Figure 2. Recovery of *Rac1* by *CAPN6* deficiency antagonizes pinocytotic activity in macrophages. BMMs differentiated with M-CSF/TNF- α for 4 days were utilized in these experiments. (A) Expression of Rho GTPases and their regulatory molecules in *Capn6*^{+/-}*Ldlr*^{-/-} or *Capn6*^{-/-}*Ldlr*^{-/-} BMMs. Cells were stimulated with 10 ng/ml TNF- α for the indicated time periods. One representative result of 3 independent experiments is shown. (B) *Rac1* activity in *Capn6*^{+/-}*Ldlr*^{-/-} or *Capn6*^{-/-}*Ldlr*^{-/-} BMMs. TNF- α -primed BMMs were stimulated with CCL2 at 50 ng/ml or native LDL at 400 μ g/ml for 20 minutes. (C) Pinocytotic activity in *Capn6*-deficient BMMs. Cells were pretreated with γ -27632 at 10 μ mol/l or NSC23766 at 50 μ mol/l for 1 hour. (D) Silencing of endogenous *Rac1* protein by siRNA. One representative result of 3 independent experiments is shown. (E) Effects of *Rac1* silencing on pinocytotic activity in *Capn6*-deficient BMMs. ** $P < 0.01$; * $P < 0.05$, 1-way ANOVA followed by Bonferroni's test (B, C and E); error bars represent mean \pm SEM.

culture medium with TNF- α and macrophage CSF (M-CSF). Next, BMMs were stimulated with TNF- α , IFN- γ , IL-1 β , IL-4, IL-12, IL-17A, or chemokine (C-C motif) ligand 2 (CCL2, also known as monocyte chemoattractant protein-1), together with M-CSF (Figure 1B). *Capn6* mRNA was increased 2- to 3-fold by IL-12, IL-17A, or CCL2, whereas it was elevated 15- to 20-fold by TNF- α . *Capn6* mRNA expression in M-CSF/TNF- α -primed BMMs reflected the changes in its protein, which was abolished by a deficiency of *Capn6* (Figure 1C). Then TNF- α -stimulated expression of CAPN6 was induced in J774 macrophages and THP-1 cells (Supplemental Figure 1, A and B; supplemental material available online with this article; doi:10.1172/JCI85880DS1). Immunocytochemical analysis showed that CAPN6 in M-CSF/TNF- α -primed BMMs is located in clusters in the cytoplasm (Figure 1D). CAPN6 did not exist in major intracellular vesicles involving pinosomes, endosomes, or mitochondria, whereas a small portion of CAPN6-positive vesicles was overlapped with lysosomes (Supplemental Figure 1C).

DNA array analysis showed that mRNA expression levels in M-CSF/TNF- α -primed BMMs were not comprehensively altered by *Capn6* deficiency (Supplemental Figure 1D); indeed, the expres-

sion ratio (*Capn6*^{+/-}*Ldlr*^{-/-} versus *Capn6*^{-/-}*Ldlr*^{-/-}, where *Ldlr* indicates LDL receptor) of 93.3% of genes (55,359 of 59,305 genes) was within 2-fold. A PCR-based analysis confirmed that the expression levels of molecules related to the uptake of oxidized LDL (*Cd36*, *Msr1*, *Nr1h3*, *Abca1*, *Abcg1*, and *Acat1*) and markers for M1 (*Nos2*, *Tnf*, *Il1b*, and *Il6*) and M2 (*Arg1*) macrophages were comparable between *Capn6*^{+/-}*Ldlr*^{-/-} and *Capn6*^{-/-}*Ldlr*^{-/-} BMMs, even in the presence of M-CSF/TNF- α stimulus (Supplemental Figure 1E). In turn, *Capn6* deficiency accelerated cellular movements in M-CSF/TNF- α -primed BMMs in the presence of CCL2 (Figure 1E).

Next, we analyzed cholesterol handling in BMMs. The receptor-mediated uptake of oxidized LDL and engulfment of aggregated LDL in M-CSF/TNF- α -primed *Ldlr*^{-/-} BMMs were not influenced by *Capn6* deficiency (Supplemental Figure 1, F and G, respectively); conversely, the pinocytotic uptake of native LDL in the cells was significantly downregulated by *Capn6* deficiency (Figure 1F). We confirmed that the uptake of native LDL in *Capn6*^{+/-}*Ldlr*^{-/-} BMMs was prevented by nocodazole-induced microtubule disorganization, as noted in previous studies (18). Similar nocodazole-induced prevention was undetectable in *Capn6*^{-/-}*Ldlr*^{-/-}

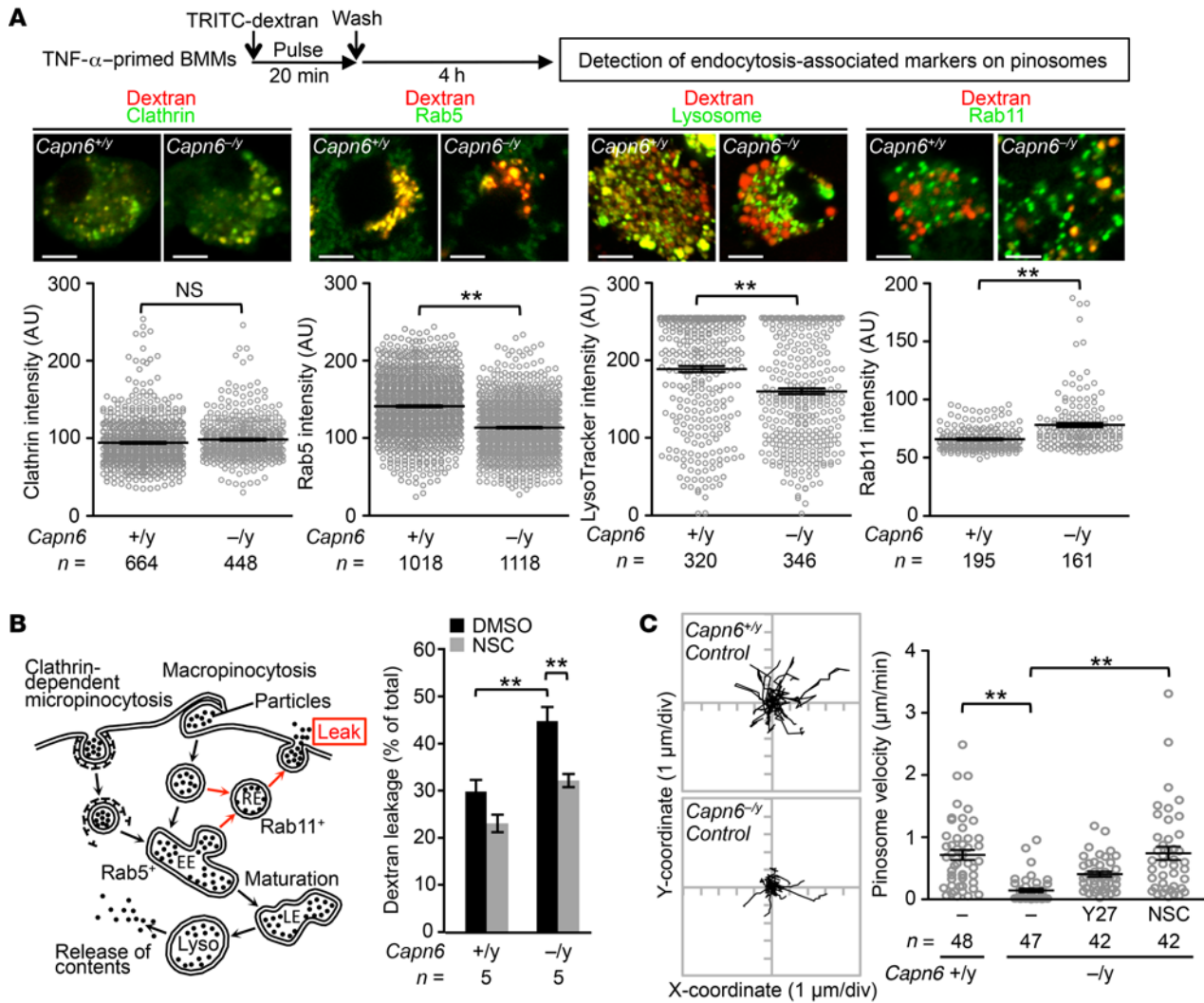


Figure 3. Loss of CAPN6 decelerates pinosome velocity and maturation and facilitates the leakage of pinocytotic particles in macrophages. (A) Pino-
some maturity in *Capn6*-deficient BMMs. BMMs were fixed following pulsed application of TRITC-labeled dextran at 5 mg/ml for 30 minutes, and fluores-
cence intensity in individual pinosomes was measured. Scale bars: 5 μ m. (B) Leakage of pinocytotic particles in BMMs. Spontaneous leakage of TRITC-
labeled dextran for 24 hours was measured in the presence or absence of NSC23766 at 50 μ mol/l. EE, early endosome; LE, late endosome; RE, recycling
endosome; Lyso, lysosome. (C) Pinosome velocity in *Capn6*-deficient BMMs. Cells were pretreated with γ -27632 at 10 μ mol/l or NSC23766 at 50 μ mol/l for
1 hour. **P < 0.01, Mann-Whitney U test (A) and 1-way ANOVA followed by Bonferroni's test (B and C); error bars represent mean \pm SEM.

BMMs. Consistently, uptake of Dil-labeled LDL in *Capn6*^{-y}*Ldlr*^{-y} BMMs was lower than that in *Capn6*^{+y}*Ldlr*^{-y} BMMs. It is likely that the uptake in *Capn6*^{-y}*Ldlr*^{-y} BMMs was saturated within 12 hours following administration (Figure 1G). *Capn6* deficiency increased cholesterol efflux in the presence or absence of apoA-I (Supplemental Figure 1H), indicating that CAPN6 potentially weakens spontaneous cholesterol efflux, but not apoA-I-induced efflux.

We sought to determine the mechanisms underlying the changes in pinocytotic activity in *Capn6*^{-y}*Ldlr*^{-y} BMMs. RhoA/Rac1 GTPases and their modulators, Rho/Rac guanine nucleotide exchange factor 2 (GEF2) and Rho GDP dissociation inhibitor α (RhoGDI α), were induced during differentiation in both *Capn6*^{+y}*Ldlr*^{-y} and *Capn6*^{-y}*Ldlr*^{-y} BMMs in the absence of TNF- α stimulus (Figure 2A). The induction of Rac1 and GEF2 in *Capn6*^{+y}*Ldlr*^{-y} BMMs, but not of RhoA and RhoGDI α , was abolished by TNF- α stimulus, whereas the induction of Rac1 and GEF2 was rescued by

Capn6 deficiency. *Capn6*^{-y}*Ldlr*^{-y} BMMs showed higher Rac1 activity in the presence of native LDL or CCL2 compared with *Capn6*^{+y}*Ldlr*^{-y} BMMs, whereas the baseline activity of Rac1 was unaltered by *Capn6* deficiency (Figure 2B). Rac1 protein expression was independent of its mRNA expression (Supplemental Figure 2A).

We measured the uptake of fluorescent dextran in isolated BMMs as an index of macropinocytosis (Figure 2C). Macropinocytosis in *Capn6*^{+y}*Ldlr*^{-y} BMMs was potentiated by TNF- α stimulus and attenuated by *Capn6* deficiency. This reduced pinocytotic activity in *Capn6*^{-y}*Ldlr*^{-y} BMMs was rescued by NSC23766-induced inhibition of Rac1, but not by Y27632-induced inhibition of RhoA/Rho kinase signaling. Similarly, siRNA-based silencing of Rac1 recovered declined macropinocytosis in *Capn6*^{-y}*Ldlr*^{-y} BMMs (Figure 2, D and E), while overexpression of wild-type Rac1 failed to decrease pinocytotic activity in *Capn6*^{+y}*Ldlr*^{-y} BMMs (Supplemental Figure 2B). Furthermore, uptake of Lucifer

Table 1. Candidate CAPN6-associated proteins detected by IP-LC-MS/MS analysis

	Gene name	Gene ID	Cover (%)
Calpain-6	<i>Capn6</i>	12338	30.1
ADP/ATP translocase 1	<i>Slc25a4</i>	11739	23.5
Runt-related transcription factor 3	<i>Runx3</i>	12399	20.5
Jumonji, AT rich interactive domain 2	<i>Jarid2</i>	16468	18.2
CWC22 spliceosome-associated protein homolog	<i>Cwc22</i>	80744	16.0
Lysine (K)-specific demethylase 3A	<i>Kdm3a</i>	104263	4.8
DEAD (Asp-Glu-Ala-Asp) box polypeptide 5	<i>Ddx5</i>	13207	3.9
Ring finger protein 38	<i>Rnf38</i>	73469	2.9

yellow in BMMs was partially inhibited by *Capn6* deficiency, suggesting that *Capn6* contributes to micropinocytosis as well as macropinocytosis (Supplemental Figure 2C). Forced *Capn6* expression accelerated macropinocytosis in M-CSF/TNF- α -stimulated J774 macrophages, which was prevented by the broad-range small GTPase inhibitor *Clostridium difficile* toxin B (Supplemental Figure 2D). Consistently, forced expression of *Capn6* downregulated Rac1 expression in J774 cells, thereby decelerating CCL2-driven cellular movement (Supplemental Figure 2, E and F). *Capn6* deficiency potentiated other Rac1-associated events in BMMs, including generation of oxidative stress and efferocytic engulfment of apoptotic cells (Supplemental Figure 2, G and H, respectively), while the cellular mitosis remained unchanged (Supplemental Figure 2I).

At the initial stage of pinocytosis, plasma membrane is internalized as clathrin-coated vesicles (for micropinocytosis) or noncoated vesicles (for macropinocytosis), which subsequently fuse with early/late endosomes. The endosomes finally fuse with lysosomes to digest interior particles, thereby releasing and accumulating the particles into cytoplasm. Importantly, a portion of intracellular vesicles refuses with the plasma membrane, allowing the vesicles to be recycled. During this process, interior particles are released to the extracellular spaces. To evaluate the fate of pinosome, we visualized endosome-related markers on dextran-labeled pinosomes (Figure 3A). We showed that intensity of the early endosome marker RAB5 and lysosomal labeling with LysoTracker (Thermo Fisher Scientific) on pinosomes was reduced by *Capn6* deficiency; conversely, that of clathrin, a marker for clathrin-coated vesicles, was unchanged by *Capn6* deficiency. In contrast, recycling endosome marker RAB11 on pinosomes was increased by *Capn6* deficiency. Consistently, deficiency of *Capn6* facilitated the spontaneous leakage of fluorescent dextran from BMMs in a Rac1-dependent manner (Figure 3B). Real-time tracking of pinosomes showed that their velocity was reduced by *Capn6* deficiency (Figure 3C). Pinosome velocity in *Capn6*^{-/-}*Ldlr*^{-/-} BMMs was recovered by NSC23766-induced inhibition of Rac1, but not by Y27632-induced inhibition of RhoA/Rho kinase signaling. Conversely, *Capn6* deficiency did not influence pinosome density (Supplemental Figure 3).

CAPN6 associates with CWC22, thereby interfering with the posttranscriptional regulation of Rac1 signaling. Next, we focused on how CAPN6 modulates Rac1 expression during macrophage

differentiation. IP-liquid chromatography-mass spectrometry/mass spectrometry (IP-LC-MS/MS) analysis identified several CAPN6-associated molecules, including CWC22 spliceosome-associated protein homolog, an essential loading factor of exon junction complex (EJC) (Table 1). Physical linkage between CWC22 and CAPN6 was validated by IP-immunoblotting analysis (Figure 4A). Organelle fractionation showed that *Capn6* deficiency enhanced nuclear localization of CWC22 in response to a second administration of TNF- α to BMMs at day 3 (Figure 4B). Immunocytochemical analysis showed that nuclear localization of CWC22 was induced by IL-1 β and IFN- γ in addition to TNF- α , whereas IL-4 elicited relatively weak nuclear localization (Figure 4C). CWC22 was uniformly expressed in the cytoplasm of M-CSF-primed BMMs, whereas it was clustered and colocalized with CAPN6-positive vesicles in the cytoplasm of M-CSF/TNF- α -primed BMMs (Figure 4D). Such TNF- α -induced clustering of CWC22 was canceled by *Capn6* deficiency (Figure 4E). A second administration of TNF- α to BMMs caused nuclear localization of CWC22, which was potentiated by *Capn6* deficiency (Figure 4E). In humans with atherosclerosis, significant nuclear localization of CWC22 in CD68-positive macrophages was detectable in mild-to-moderate atherosclerotic lesions; conversely, the localization was marginal in severe atherosclerotic lesions (Figure 5; clinicopathologic information is available in Supplemental Table 1). Thus, it is likely that the degree of CWC22 nuclear localization negatively correlates with the severity of atherosclerosis.

Because CWC22 is reportedly associated with EJC-mediated mRNA splicing (19), we assessed splicing efficiency in *Capn6*-deficient BMMs by a PCR-based analysis (Supplemental Figure 4 for detail). *Capn6* deficiency in M-CSF/TNF- α -primed BMMs elevated the ratio of spliced *Rac1*, *Arhgef2* (GEF2), and *Tpi1* mRNA to their pre-mRNAs, indicating improved mRNA splicing efficiency (Figure 6A); conversely, the splicing efficiency of *RhoA* and *Arhgdia* (RhoGDIa) mRNA remained unaffected. The elevation of *Rac1* splicing by *Capn6* deficiency was prevented by the siRNA-based silencing of *Cwc22* (Figure 6B). Accordingly, the induction of Rac1 protein in *Capn6*^{-/-}*Ldlr*^{-/-} BMMs was reduced by the silencing of *Cwc22* (Figure 6C). Furthermore, *Cwc22* silencing reversed the phenotypic changes evident in *Capn6*-deficient BMMs, including the downregulation of pinocytotic activity (Figure 6D) and upregulation of cellular movements (Figure 6E).

Deficiency of macrophage CAPN6 suppresses proatherogenic pinocytosis. We compared the aortic expression of catalytic subunits of the calpain family in chow-fed and high-fat diet-fed (HFD-fed) *Ldlr*^{-/-} mice. We found that the unconventional calpain genes *Capn6* and *Capn9* were induced in the aortas of HFD-fed mice in addition to the conventional *Capn2* (Figure 7A). Previously, we demonstrated that calpain-2 induction causes vascular endothelial cell hyperpermeability and subsequent atherosclerosis progression (16); thus, we attempted to focus on the roles of CAPN6 and CAPN9. *Capn6* deficiency in *Ldlr*^{-/-} mice significantly inhibited the development of atherosclerotic lesions in the aorta independently of the sex of the mice (Figure 7B and Supplemental Figure 5A), whereas *Capn9* deficiency did not yield these atheroprotective effects (Supplemental Figure 5, B and C). *Capn6* deficiency did not alter blood glucose homeostasis (Supplemental Figure 5D), population of peripheral blood cells (Supplemental Figure

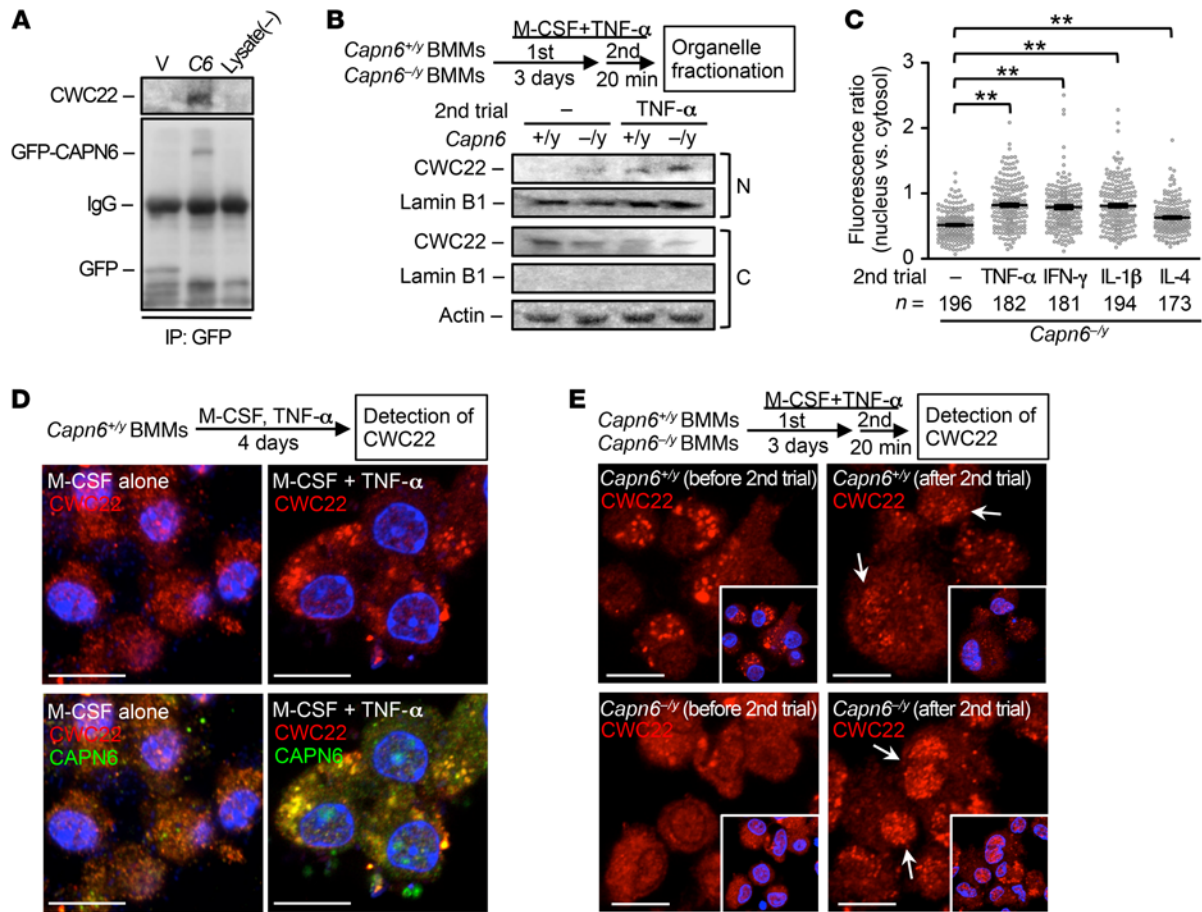


Figure 4. Nuclear localization of CWC22 in inflamed murine BMM is limited by the physical association between CAPN6 and CWC22. (A) CAPN6 associates with CWC22. Protein immunoprecipitates were detected by immunoblotting against CWC22 or GFP. One representative result of 3 independent experiments is shown. (B) *Capn6* deficiency potentiates nuclear localization of CWC22 in BMMs. After 20 minutes of a second administration of TNF- α /M-CSF, nuclear and cytoplasmic fractions were separated, and CWC22 was detected by immunoblotting. One representative result of 3 independent experiments is shown. N, nucleus; C, cytosol. (C) Nuclear localization of CWC22 in BMMs was induced by a variety of inflammatory cytokines. TNF- α -primed *Capn6*^{-/-} *Ldlr*^{-/-} BMMs were stimulated with a variety of cytokines for 20 minutes, and nuclear localization in individual cells was quantified. (D) Subcellular distribution of CWC22 in BMMs. BM cells were stimulated with M-CSF at 50 ng/ml in the presence or absence of TNF- α for 4 days; then CWC22 and CAPN6 were detected by immunocytochemistry. (E) *Capn6* deficiency potentiates nuclear localization of CWC22 in BMMs. BM cells were cultured in the presence of TNF- α at 10 ng/ml and M-CSF at 50 ng/ml for 3 days; then the culture medium was replaced with freshly prepared TNF- α /M-CSF-supplemented medium. Following 30-minute incubation, cells were fixed and CWC22 was detected by immunocytochemistry. Arrows represent nuclear localization of CWC22. ***P* < 0.01, 1-way ANOVA followed by Bonferroni's test (C); error bars represent mean \pm SEM. Scale bars: 10 μ m (D); 10 μ m (E).

5E), and oxidative stress in the lesions (Supplemental Figure 5F) and did not ameliorate plasma dyslipidemia (Figure 7C and Supplemental Figure 5G). Relative necrotic core in the lesions was slightly decreased by *Capn6* deficiency (Supplemental Figure 5H).

We investigated CAPN6 systemic expression in HFD-fed *Capn6*^{-/-}*Ldlr*^{-/-} mice using a LacZ reporter assay (Figure 7D), as the mice express LacZ under the *Capn6* native promoter (20). As a result, transcriptional activity of *Capn6* is restricted in atherosclerotic plaques, but not in other organs. Immunohistochemistry showed CAPN6 expression in macrophages in atherosclerotic lesions (Figure 7E), but not in other vascular component cells, including endothelial cells and smooth muscle cells (Supplemental Figure 5I). Next, we evaluated CAPN6 expression in human atheromas (Figure 8; clinicopathologic information is available in Supplemental Table 1 and Supplemental Table 2). CAPN6 expression was negligible in adventitial macrophages in the normal aorta (Figure 8A). Converse-

ly, CAPN6 was abundant in macrophages in severe coronary lesions. CAPN6 expression in human aortic atheromas was positively correlated with the severity of the lesions (Figure 8, B-D).

We assessed the contribution of myeloid *Capn6* to atherogenesis through BM transplantation experiments (Figure 9). PCR-based genotyping validated BM chimerism in recipient mice (*Capn6*^{+/-}*Ldlr*^{-/-} and *Capn6*^{-/-}*Ldlr*^{-/-}) transplanted with BM cells of different genotypes (Figure 9A). Transplantation of *Capn6*^{-/-}*Ldlr*^{-/-} BM cells significantly decreased HFD-induced aortic atherosclerotic lesions compared with transplantation of *Capn6*^{+/-}*Ldlr*^{-/-} BM cells independently of the recipient genotype (Figure 9B).

Using methods reported by Tacke et al. (21), we conducted in vivo labeling of circulating Ly-6C^{hi} monocytes to evaluate the recruitment of proatherogenic macrophages into the atherosclerotic lesions (Figure 10A). Subsequent to the transient depletion of preexisting monocytes by clodronate liposome, recruitment

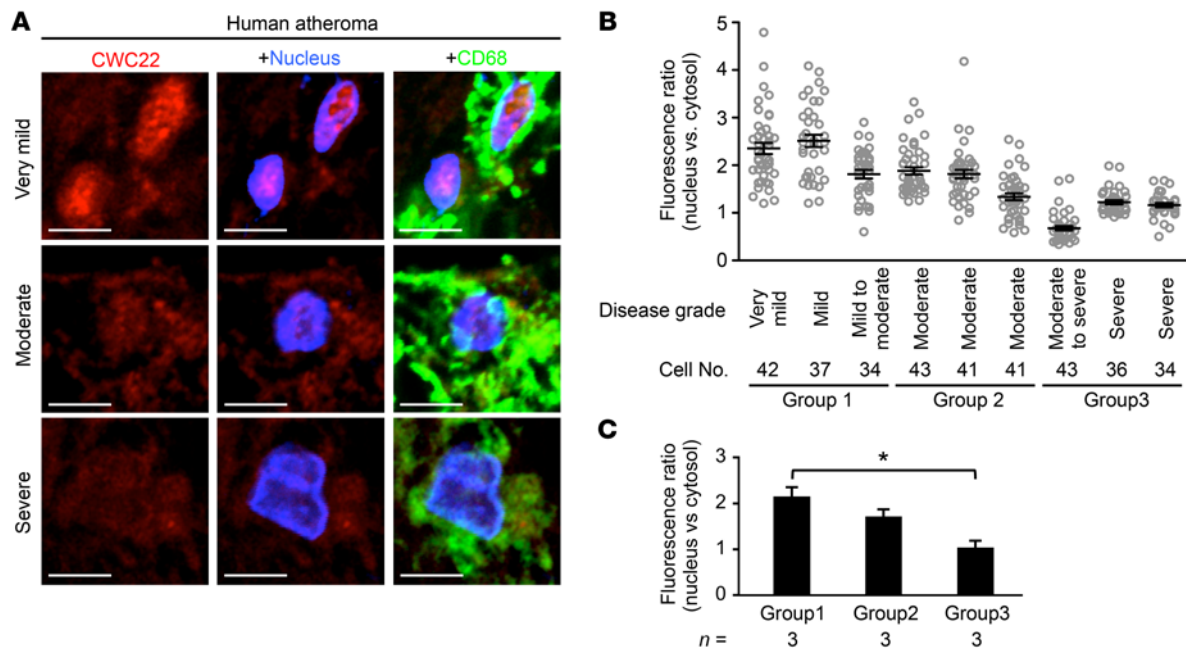


Figure 5. Nuclear localization of CWC22 in human macrophages/foam cells is negatively correlated with atherosclerosis grade. (A) Representative micrographs of CWC22 subcellular distributions in macrophages/foam cells in human atherosclerotic lesions in aorta. Scale bars: 5 μ m. (B) Nuclear localization of CWC22 in CD68-positive cells was quantified with respect to each specimen. (C) Statistical comparison of CWC22 nuclear localization in human macrophages/foam cells. Specimens were divided into 3 groups based on the atherosclerosis grade. * $P < 0.05$, 1-way ANOVA followed by Bonferroni's test (C); error bars represent mean \pm SEM.

of latex-positive monocytes into the aortic lesions was evaluated at day 3 following i.v. injection of latex beads. Whereas uptake of latex in circulating monocytes was equivalent between *Capn6*^{+/-} *Ldlr*^{-/-} and *Capn6*^{-/-} *Ldlr*^{-/-} mice (Figure 10A), the number of latex-positive cells in atherosclerotic lesions was reduced by *Capn6* deficiency (Figure 10B). Importantly, preexisting foam cell macrophages, but not newly recruited monocytes, abundantly express CAPN6 (Figure 10C and Supplemental Figure 6A), indicating that CAPN6 in monocytes/macrophages is induced after the cells infiltrate into lesions. Consistently, expression of the macrophage marker CD68 and macrophage accumulation in atherosclerotic lesions in the mice fed HFD for 12 weeks were reduced by *Capn6* deficiency (Figure 10, D and E), whereas the expression of the inflammatory molecules *Icam1*, *Vcam1*, *Sele*, *Tnfa*, *Il1b*, *Il6*, and *Ccl2* (Supplemental Figure 6B), as well as of the lymphocyte markers *Cd4* and *Cd8a1* (Figure 10D), remained unchanged. Filipin III-based cholesterol staining in macrophages in murine atheromas showed that *Capn6* deficiency reduced the amount of cholesterol in individual macrophages (Figure 10F), whereas it did not affect expression of genes related to the receptor-mediated uptake of oxidized LDL and its subsequent processing, including *Msr1*, *Cd36*, *Abca1*, *Abcg1*, and *Acat1* (Supplemental Figure 6C).

We assessed the in vivo uptake of fluorescent nanoparticles in macrophages as an index of pinocytotic activity (Figure 10G). Pinocytotic activity in macrophages in *Capn6*^{-/-} *Ldlr*^{-/-} atheromas was significantly lower than that in *Capn6*^{+/-} *Ldlr*^{-/-} lesions. Immunohistochemical analysis showed that nuclear localization of CWC22 was relatively frequent in macrophage foam cells in *Capn6*^{-/-} *Ldlr*^{-/-} atheromas than in *Capn6*^{+/-} *Ldlr*^{-/-} atheromas (Figure 11A). *Capn6* deficiency upregulated the splicing efficiency of

Rac1 and *Tpi1* mRNA but not of *Rhoa* mRNA in the proatherogenic aortas of *Ldlr*^{-/-} mice (Figure 11B), a phenomenon accompanied by the elevated *Rac1* protein expression in the whole aorta, while *RhoA* protein expression remained unchanged (Figure 11C). BM transplantation experiments showed that *Rac1* splicing upregulation was dependent on *Capn6* expression in myeloid cells (Supplemental Figure 6D). Immunohistochemical analysis demonstrated that *Capn6* deficiency upregulated *Rac1* protein expression in macrophages in atherosclerotic plaques (Figure 11D).

Discussion

Although it is established that macrophages uptake LDL and adopt foam cell properties, the specific mechanisms underlying the hyperpinocytosis of native LDL by macrophages evident under inflammatory conditions remain elusive. Our results show that pinocytotic activity, as well as cellular and intracellular dynamics in inflamed macrophages, depended on induction of CAPN6 (Figure 1, E and G, and Figure 3C). *Capn6* deficiency counteracted progression of atherosclerosis as well as macrophage pinocytotic ability and deposition in the lesions (Figure 7B and Figure 10, E and G); thus, CAPN6 conferred atherogenicity to the inflamed macrophages. Unexpectedly, CAPN6 failed to induce global changes in mRNA expression; however, *Capn6* deficiency elevated efficiency of mRNA splicing in certain genes. Consequently, for what we believe is the first time, we have shown that the CWC22/EJC posttranscriptional splicing system is disturbed by a physical interaction with CAPN6, which confers the ability to pinocytose LDL under inflammatory conditions to macrophages, resulting in cholesterol deposition in the athero-prone vascular wall (Figure 11E).

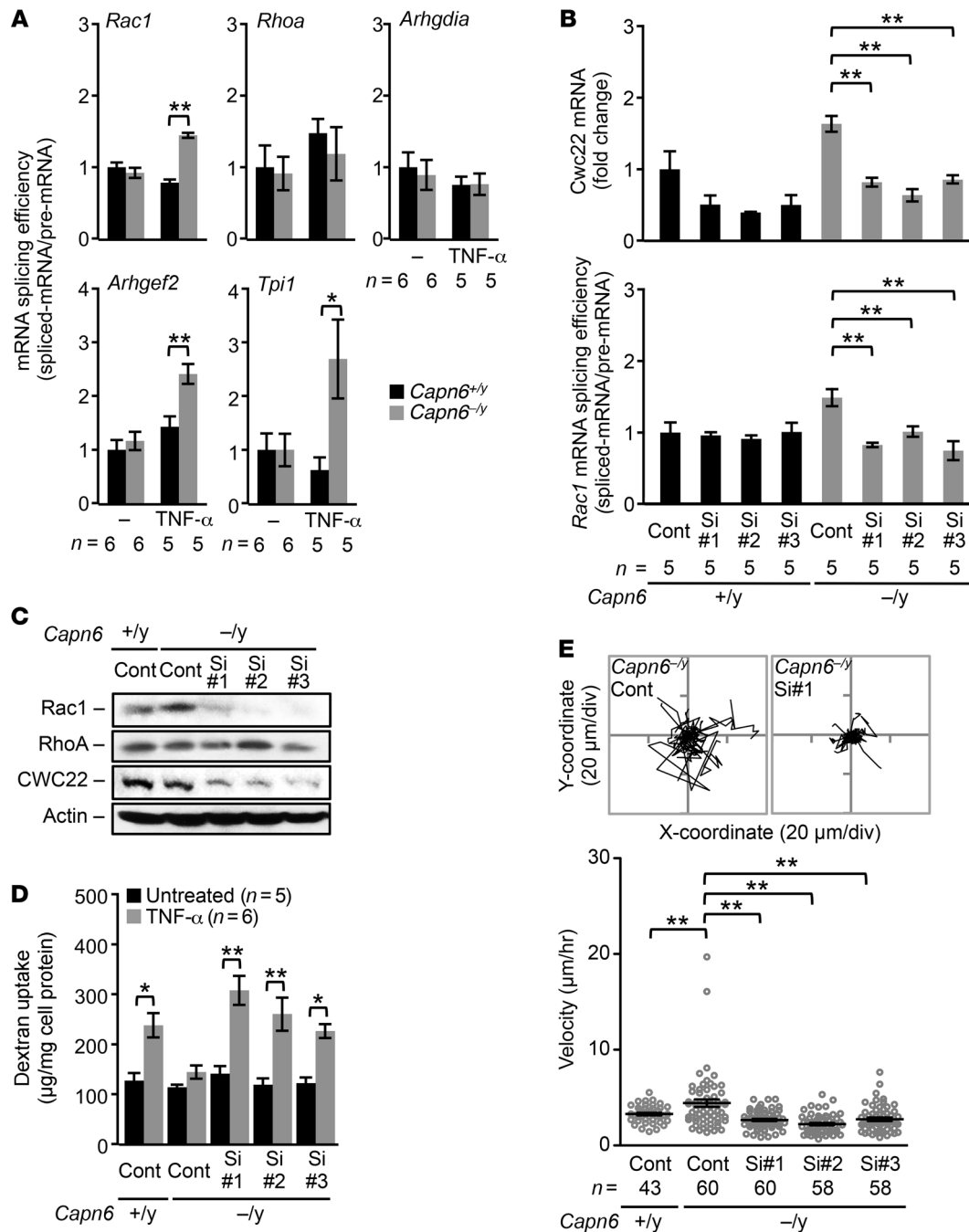


Figure 6. Rac1 downregulation in hyperpinocytotic macrophages is due to a disorder of CWC22-mediated mRNA splicing by CAPN6. BMMs differentiated with M-CSF/TNF-α for 4 days were used in these experiments. (A) Splicing of *Rac1*, *Arhgef2*, and *Tpi1* pre-mRNA but not of *RhoA* and *Arhgdia* pre-mRNA is upregulated by *Capn6* deficiency. Spliced mRNA, pre-mRNA ratio served as a statistical value. (B) siRNA-based silencing of *Cwc22* abrogates the upregulated *Rac1* splicing caused by *Capn6* deficiency. (C) Silencing of *Cwc22* cancels the upregulation of *Rac1* protein expression caused by *Capn6* deficiency. One representative result of 3 independent experiments is shown. Con, control; Si, siRNA. (D) Impaired pinocytotic activity in *Capn6*^{-y}*Ldlr*^{-y} BMMs is rescued by silencing of *Cwc22*. (E) Accelerated cellular motility in *Capn6*^{-y}*Ldlr*^{-y} BMMs is diminished by silencing of *Cwc22*. BMMs were stimulated with CCL2 at 50 ng/ml. ***P* < 0.01; **P* < 0.05, 1-way ANOVA followed by Bonferroni's test (A, B, D and E); error bars represent mean ± SEM.

CAPN6 is primarily expressed in the foam cell macrophages in the human and murine atherosclerotic lesions (Figure 7E and Figure 8). Actually, current BM transplantation experiments showed that *Capn6* in BM-derived cells, but not in other vascular component cells in the lesions, is responsible for atherogenesis (Figure 9B), suggesting the dominant contribution of macrophage CAPN6 to

atherogenesis. Reportedly, small GTPase signals orchestrate pinocytotic activity in certain cell types, including macrophages. Particularly, Rac1 GTPase mediates pinocytotic membrane transport (22) and membrane ruffling (23). Pharmacologic inhibition of Rho family GTPases by *C. difficile* toxin B diminishes the pinocytotic uptake of native LDL, even in macrophages (9, 18), whereas that of RhoA

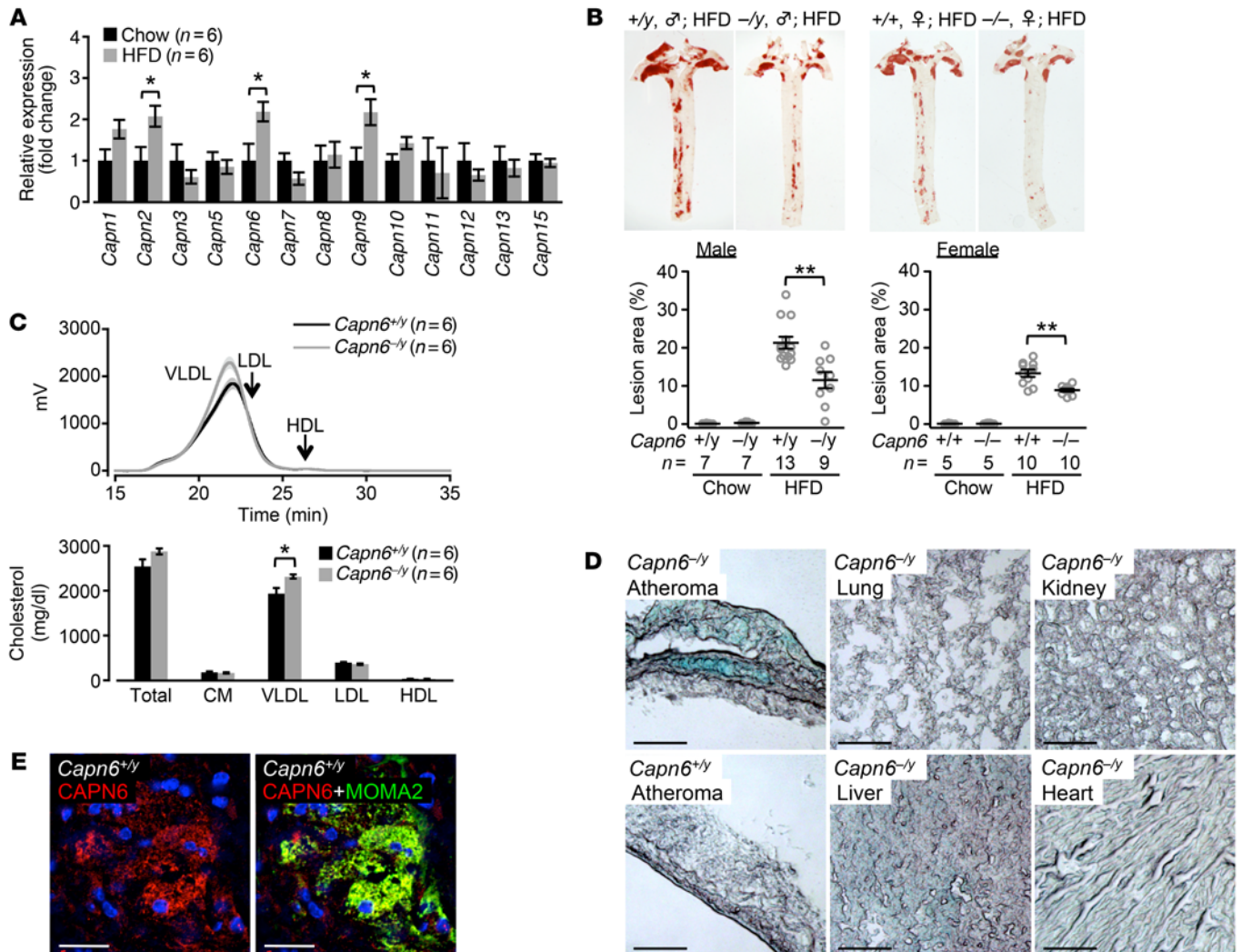


Figure 7. CAPN6 is induced in murine atheromas and exacerbates atherosclerotic diseases. (A) Aortic expression of calpain family genes in chow- or HFD-fed *Ldlr*^{-/-} mice. Mice received chow or HFD for 12 weeks. (B) Loss of *Capn6* reduces aortic atherosclerosis in *Ldlr*^{-/-} mice independently of sex. (C) *Capn6* deficiency does not ameliorate plasma dyslipidemia in *Ldlr*^{-/-} mice. (D) *Capn6* promoter is activated specifically in atherosclerotic lesions. *Capn6*^{-/y}*Ldlr*^{-/-} mice served as a negative control. (E) CAPN6 was localized in macrophages in murine atherosclerotic lesions. MOMA2 served as a macrophage marker. ***P* < 0.01; **P* < 0.05, 1-way ANOVA followed by Bonferroni's test (A, B and C); error bars represent mean ± SEM. Scale bars: 100 μm (D); 25 μm (E).

or Rac1 fails to abolish pinocytotic uptake in these cells (18); thus, the contribution of individual Rho GTPases to pinocytotic activity in macrophages remains unclear. Our data indicate that *Capn6* deficiency restores the reduced expression of the Rac1 and GEF2 proteins evident in M-CSF/TNF- α -primed BMMs without altering the expression of the RhoA and RhoGDI α proteins, leading to the recovery of Rac1 activity in cells (Figure 2, A and B). This is consistent with an earlier investigation indicating that siRNA-based silencing of CAPN6 in NIH3T3 cells potentiates Rac1 activity (24). This Rac1 system recovery appears to abrogate pinocytotic ability in *Capn6*^{-/y} *Ldlr*^{-/-} BMMs (Figure 2, C and E), while it slightly accelerates the production of oxidative stress and efferocytic activity in the cells (Supplemental Figure 2, G and H, respectively). It is noteworthy that the latter 2 phenotypes are likely to be pathophysiologically insignificant, since the changes in oxidative stress and the necrotic core by *Capn6* deficiency in the murine atherosclerotic lesion was marginal (Supplemental Figure 5, F and H, respectively). Importantly, Fujii

et al. noted that prolonged Rac1 activity impairs the integration of RAB21 into pinosomes in macrophages (10), suggesting that Rac1 signaling delays pinosome maturation. This is consistent with our finding that the recovery of Rac1 activity by *Capn6* deficiency suppressed the integration of RAB5 into pinosomes and their lysosomal transition without altering pinosome density (Figure 3A and Supplemental Figure 3). While *Capn6* deficiency abrogates the pinosomal maturation in BMMs, pinocytotic particles in *Capn6*^{-/y}*Ldlr*^{-/-} BMMs were preferentially transferred into RAB11-positive recycling vesicles (Figure 3A), which probably led to subsequent leakage of the particles to the extracellular space (Figure 3B). Our data further showed that the overexpression of wild-type Rac1 failed to decrease pinocytotic activity in BMMs (Supplemental Figure 2B), suggesting that Rac1 induction is necessary but insufficient for downregulation of pinocytotic activity in the cells. It is thought that the unknown mechanism or mechanisms that switch Rac1 into antipinocytosis action are activated by *Capn6* deficiency together with the Rac1

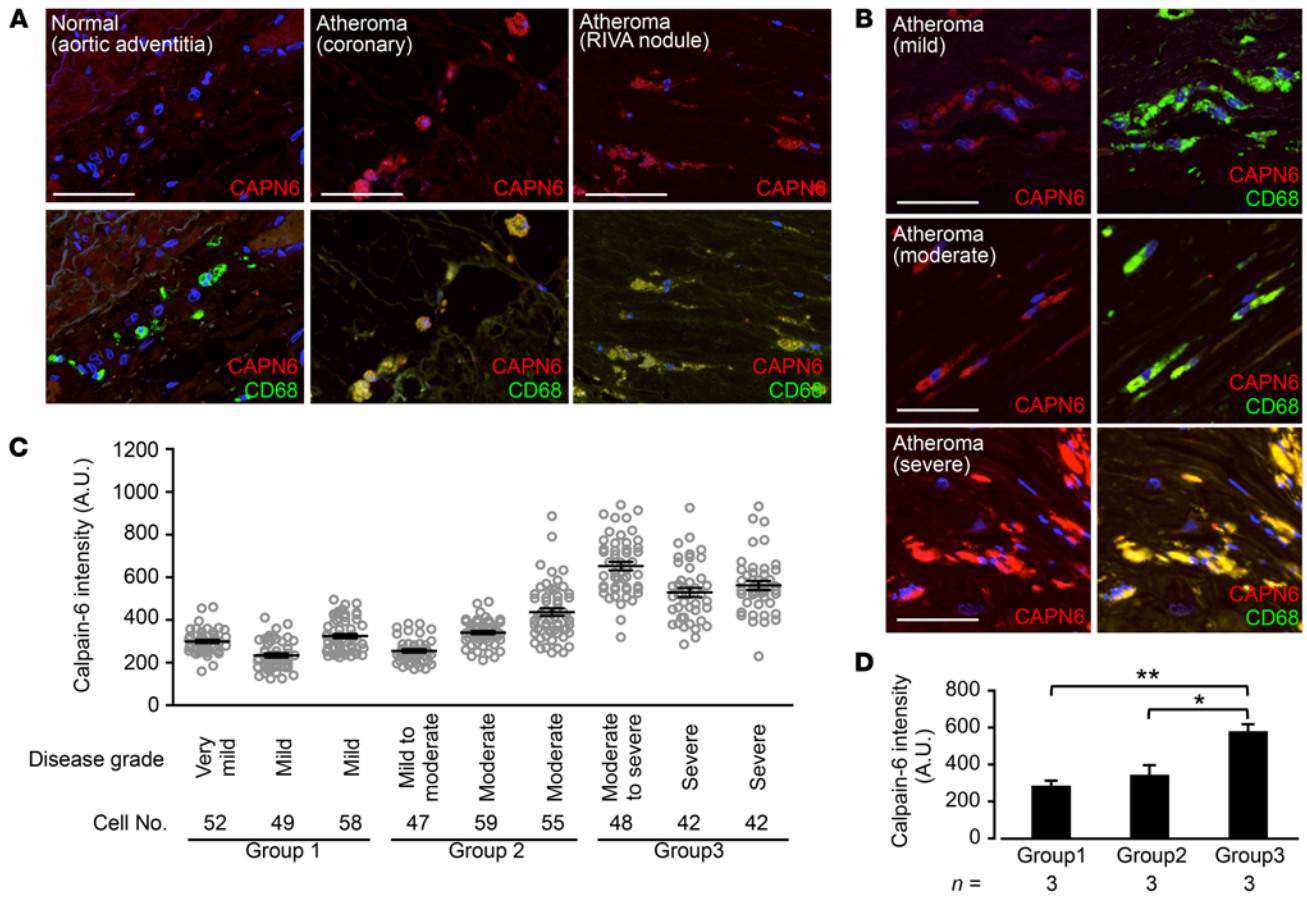


Figure 8. CAPN6 is localized in macrophages/foam cells in human moderate-to-severe atheromas. (A) CAPN6 expression in macrophages in human normal aorta and severe coronary atheromas. (B) CAPN6 expression in macrophages in human aortic atheromas. Scale bars: 50 μ m (A and B). (C) CAPN6 expression in CD68-positive cells was quantified with respect to each specimen. (D) Statistical comparison of CAPN6 expression in human macrophages/foam cells. Specimens were divided into 3 groups based on the atherosclerosis grade. CD68 served as a macrophage marker. Arrows represent CAPN6-positive macrophages. ** $P < 0.01$; * $P < 0.05$, 1-way ANOVA followed by Bonferroni's test (D).

inductions. In contrast, our pharmacologic data did not prove the contribution of RhoA signaling to pinocytotic activity in *Capn6*^{-/-} *Ldlr*^{-/-} BMMs (Figure 2C). Collectively, *Capn6* abrogates Rac1 signaling and accelerates pinosomal maturation in macrophages rather than participating in the pinosome formation. This may confer hyperpinocytosis on inflamed macrophages.

Although our present data showed that *Capn6* deficiency facilitated the movement of BMMs in response to CCL2 (Figure 1E), it inconsistently limited the recruitment and deposition of macrophages in murine atherosclerotic lesions (Figure 10, B, D, and E). It is noteworthy that the newly recruited monocytes in the atherosclerotic lesions did not express CAPN6, while preexisting foam cell macrophages were enriched with CAPN6 (Figure 10C and Supplemental Figure 6A), indicating that CAPN6 in monocytes/macrophages was induced after infiltration into the lesions. Thus, the recruitment of circulating monocytes may be independent of their endogenous CAPN6, while the exact mechanisms by which CAPN6 facilitated the recruitment are currently unclear. The abundance of CAPN6 in the preexisting macrophages, in turn, can limit their motility, thereby decelerating the emigration of the cells from the lesions. Therefore, it is possible for upregulation of CAPN6 to reduce the clearance of macrophages in atherosclerotic lesions.

Our in vitro DNA array and quantitative PCR (qPCR) analysis showed that the majority of the mRNA expression was comparable between *Capn6*^{-/-} *Ldlr*^{-/-} and *Capn6*^{-/-} *Ldlr*^{-/-} BMMs (Supplemental Figure 1, D and E). Similarly, the expression of *Icam1*, *Vcam1*, *Sele*, *Tnfa*, *Il1b*, *Il6*, *Ccl2*, *Msr1*, *Cd36*, *Abca1*, *Abcg1*, and *Acat1* in whole aorta was unchanged by *Capn6* deficiency, even with reducing macrophage number in the vessels (Supplemental Figure 6, B and C). Distinct changes in macrophage number and gene expression in the vessels indicated that the *Capn6*-driven proatherogenic macrophages have a negligible impact on the net gene expression in the vessels. A lack of global changes in gene expression in *Capn6*-deficient macrophages eliminated the possibility that their phenotypes were due to transcriptional regulation. Recent advances in macrophage biology revealed that the posttranscriptional processing of pre-mRNAs, in addition to their transcriptional regulation, modifies the fate of macrophages under inflammatory conditions (25). This pre-mRNA processing is driven by the spliceosome, a large ribonucleoprotein complex, and is mediated through RNA-binding proteins that form messenger ribonucleoprotein complexes (mRNPs) (26). A key regulatory element within mRNPs is EJC. EJC, which comprises 4 subunits — eIF4A3 (DDX48), MAGOH, Y14 (RBM8A), and BTZ (CASC3, MLN51; ref.

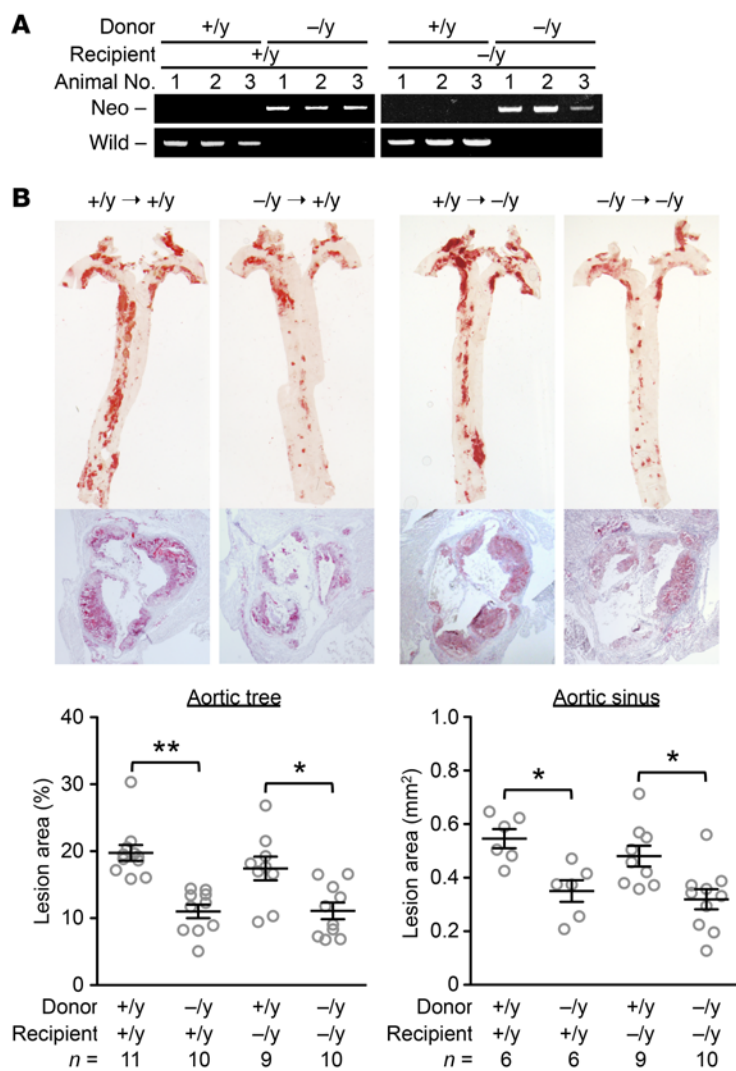


Figure 9. Myeloid *Capn6* is rate limiting for atherogenesis. (A) BM cells (1×10^7 cells/mouse) isolated from *Capn6*^{+/y}*Ldlr*^{-/-} or *Capn6*^{-/-y}*Ldlr*^{-/-} donor mice were i.v. injected into x-ray-irradiated (8 Gy) *Capn6*^{+/y}*Ldlr*^{-/-} or *Capn6*^{-/-y}*Ldlr*^{-/-} recipient mice. The *Capn6* genotype in BM cells from chimeric and nonchimeric mice was determined by a PCR-based analysis. (B) *Capn6* deficiency in BM cells, but not in resident cells, reduces atherosclerotic lesions. $**P < 0.01$; $*P < 0.05$, 1-way ANOVA followed by Bonferroni's test (B); error bars represent mean \pm SEM.

27) — is known to bind to CWC22, an essential EJC-loading factor (19). Although binding of CWC22 to the EJC is indispensable for EJC-mediated splicing, their roles in macrophage biology remain unclear. Through a comprehensive protein-protein interaction analysis, we identified that CAPN6 is a CWC22-associated protein (Table 1) and that CWC22 nuclear localization is limited by the physical cytoplasmic interaction between CAPN6 and CWC22 (Figure 4, B, D, and E). Furthermore, we revealed that CWC22 was enriched in the nucleus in response to many inflammatory stimuli (Figure 4C). Interestingly, Singh et al. noted that MAGOH, a core component of the EJC, is induced in lipopolysaccharide-stimulated macrophages (28), suggesting that inflammatory signaling modifies CWC22/EJC-mediated mRNA processing. Current cell-based experiments suggest that *Cwc22* silencing reverses the macrophage phenotypes induced by *Capn6* deficiency, such as the recovery of Rac1 signaling, reduction in pinocytotic activity, and promotion of cellular movements (Figure 6, C-E); thus, the CWC22/EJC system dominates the phenotypic changes in *Capn6*-deficient BMMs. Importantly, the nuclear localization of CWC22 was negatively correlated with atherosclerosis grade in human patients (Figure 5) and was almost imperceptible in macrophages in severe atherosclerotic lesions in which CAPN6 is

abundant (Figure 8). Thus, it is likely that CAPN6 limits the activity of the CWC22/EJC system in foam cells during atherogenesis, even in humans.

CAPN6 was first cloned by Dear et al. (29). CAPN6 expression is reportedly detectable in fetal skeletal muscle and in the placenta (20); however, its expression in skeletal muscle vanishes during growth. A gene-targeting study showed that CAPN6 limits the development and regeneration of skeletal muscle (20), although the physiologic and pathophysiologic role of this molecule remains unclear. Hong et al. noted that CAPN6 is induced during the differentiation of osteoclasts from BM-derived cells by receptor activator of NF- κ B ligand, thereby accelerating bone-resorptive activity (30), suggesting that CAPN6 may function in the monocyte/macrophage lineage under certain conditions. Our data also revealed that CAPN6 is induced by proatherogenic mediators (Figure 1B) and switches macrophages to a hyperpinocytotic and immobile phenotype through disturbance of the CWC22/EJC system (Figure 6, D and E). CAPN6 is robustly induced by TNF- α , whereas CWC22 is activated uniformly by multiple cytokine classes (Figure 4C); thus, it is likely that disturbance of the CWC22/EJC system occurs primarily in the presence of TNF- α . Considering the predominance of TNF- α in atherosclerotic diseases (31), it appears that CAPN6 acts as a molecular switch, conferring hyperpinocytosis on inflamed macrophages in atherosclerotic lesions.

27) — is known to bind to CWC22, an essential EJC-loading factor (19). Although binding of CWC22 to the EJC is indispensable for EJC-mediated splicing, their roles in macrophage biology remain unclear. Through a comprehensive protein-protein interaction analysis, we identified that CAPN6 is a CWC22-associated protein (Table 1) and that CWC22 nuclear localization is limited by the physical cytoplasmic interaction between CAPN6 and CWC22 (Figure 4, B, D, and E). Furthermore, we revealed that CWC22 was enriched in the nucleus in response to many inflammatory stimuli (Figure 4C). Interestingly, Singh et al. noted that MAGOH, a core component of the EJC, is induced in lipopolysaccharide-stimulated macrophages (28), suggesting that inflammatory signaling modifies CWC22/EJC-mediated mRNA processing. Current cell-based experiments suggest that *Cwc22* silencing reverses the macrophage phenotypes induced by *Capn6* deficiency, such as the recovery of Rac1 signaling, reduction in pinocytotic activity, and promotion of cellular movements (Figure 6, C-E); thus, the CWC22/EJC system dominates the phenotypic changes in *Capn6*-deficient BMMs. Importantly, the nuclear localization of CWC22 was negatively correlated with atherosclerosis grade in human patients (Figure 5) and was almost imperceptible in macrophages in severe atherosclerotic lesions in which CAPN6 is

We identified regulatory mechanisms underlying LDL metabolism in macrophages. This concept of CAPN6-induced disturbance of the CWC22/EJC system explains the mechanism activating pinocytotic abilities in macrophages in atherosclerotic lesions. Targeting CAPN6 to achieve normalization of the CWC22/EJC system may represent an efficient approach to suppressing proatherogenic pinocytosis because CAPN6 is specifically expressed in inflamed macrophages and CAPN6-induced disturbance of the CWC22/EJC system may be translatable into humans with atherosclerosis. To confirm the pathophysiologic significance of the CWC22/EJC system, future studies exploring the target genes of the CWC22/EJC system in response to inflammatory insults are necessary.

Methods

Reagents. All chemicals used were commercial products of the highest grade of purity available. The sources of these reagents are detailed in Supplemental Methods.

Mice. Mice were fed chow (CRF-1; Oriental Yeast Co.) or HFD (F2HFD1; CRF-1 supplemented with 16.5% fat, 1.25% cholesterol, and 0.5% sodium cholate; Oriental Yeast Co.) for 12 weeks from 8 weeks of

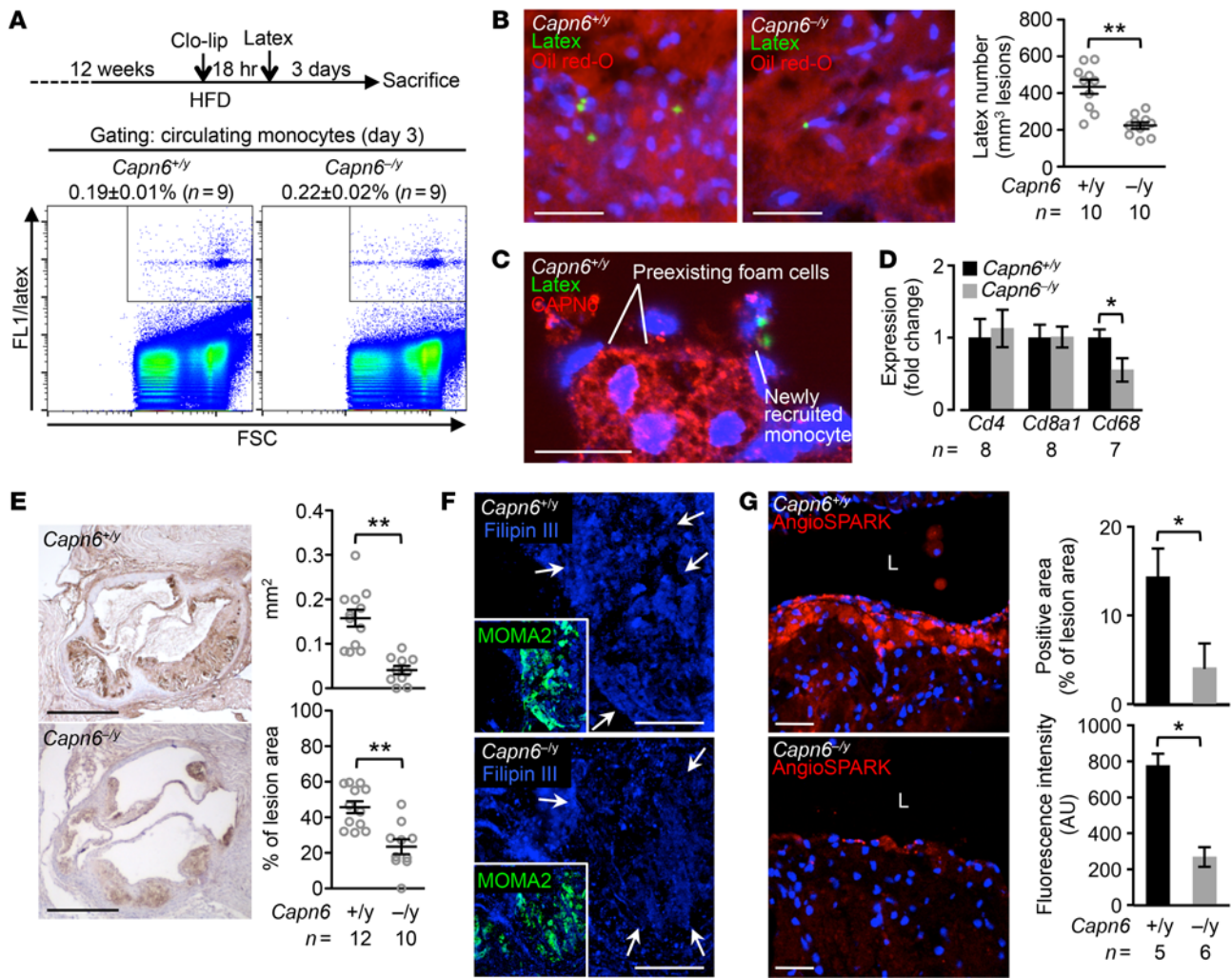


Figure 10. Ablation of CAPN6 diminishes the recruitment of macrophages and their pinocytotic ability in murine atherosclerotic lesions. (A) Uptake of latex beads in circulating monocytes at day 3 was equivalent between *Capn6*^{+/-}*Ldlr*^{-/-} and *Capn6*^{-/-}*Ldlr*^{-/-} mice. (B) Latex-positive monocytes in aortic atherosclerotic lesions were reduced by *Capn6* deficiency. (C) CAPN6 expression is abundant in preexisting foam cell macrophages, but not in newly recruited macrophages, in *Capn6*^{+/-}*Ldlr*^{-/-} atherosclerotic lesions. (D) PCR-based quantification of leukocyte markers in aortic atherosclerotic lesions in mice receiving HFD for 12 weeks. (E) Deposition of macrophages in atherosclerotic lesions is reduced by *Capn6* deficiency. MOMA2⁺ area in aortic sinus lesions in the mice receiving HFD for 12 weeks was quantified. (F) Cholesterol deposition in atherosclerotic plaques. Aortic sections were stained with Filipin III. Arrows indicate macrophage-enriched regions. (G) Pinocytotic activity in atherosclerotic lesions. AngioSPARK nanoparticles were i.v. injected as a pinocytotic activity marker. L, aortic lumen. ***P* < 0.01; **P* < 0.05; Student's *t* test (D, E, and G) and Mann-Whitney *U* test (B); error bars represent mean ± SEM. Scale bars: 50 μm (B); 20 μm (C); 500 μm (E); 100 μm (F); 40 μm (G).

age. Generation of *Capn6*^{-/-} and *Capn9*^{-/-} mice was performed as described previously (20, 32). *Capn6*^{-/-} mice express LacZ instead of CAPN6. *Ldlr*^{-/-} mice (C57/BL6J) were obtained from The Jackson Laboratory (stock no. 2207). *Capn6*^{-/-}*Ldlr*^{-/-} and *Capn9*^{-/-}*Ldlr*^{-/-} mice were generated by intercrossing *Capn6*^{-/-} and *Capn9*^{-/-} mice with *Ldlr*^{-/-} mice, respectively. *Capn6*^{+/-}*Ldlr*^{-/-}, *Capn6*^{-/-}*Ldlr*^{-/-}, *Capn9*^{+/-}*Ldlr*^{-/-}, and *Capn9*^{-/-}*Ldlr*^{-/-} mice were maintained by homozygous breeding, as they have a common genetic background; the genotypes were determined by standard PCR-based genotyping with specific primers (Supplemental Table 3). High-sensitivity lipoprotein profiling was performed on EDTA plasma with the LipoSEARCH system equipped with a specific cholesterol detector by Skylight Biotech Inc.

BMMs. The isolation of BMMs was performed as described in our previous study (33). Briefly, murine BM cells were collected by flushing femoral BM with culture medium; subsequently, the cells were incu-

bated in DMEM (Sigma-Aldrich) supplemented with 10% serum, penicillin-streptomycin-amphotericin B (Wako Pure Chemical Industries Ltd.), and M-CSF (50 ng/ml) for differentiation into macrophages in the presence or absence of the inflammatory cytokines TNF-α, IL-1β, IFN-γ, or IL-4 (10 ng/ml each). Unbound cells were removed by washing with medium; the culture medium was changed every other day.

Cellular movements. Measurement of cellular movements was described previously (34). Twenty thousand BMMs suspended in minimal essential medium were seeded on a 24-well culture plate. Then cellular movements in the presence of CCL2 (50 ng/ml) were monitored using a BioStation CT System (Nikon Instruments Inc.) at 37°C in a 5% CO₂ atmosphere under humidified conditions. Phase-contrast images were obtained at 60-minute intervals for 10 hours. Movement of cell centroids, calculated using ImageJ software (NIH), was measured to determine cell velocity as a statistical value.

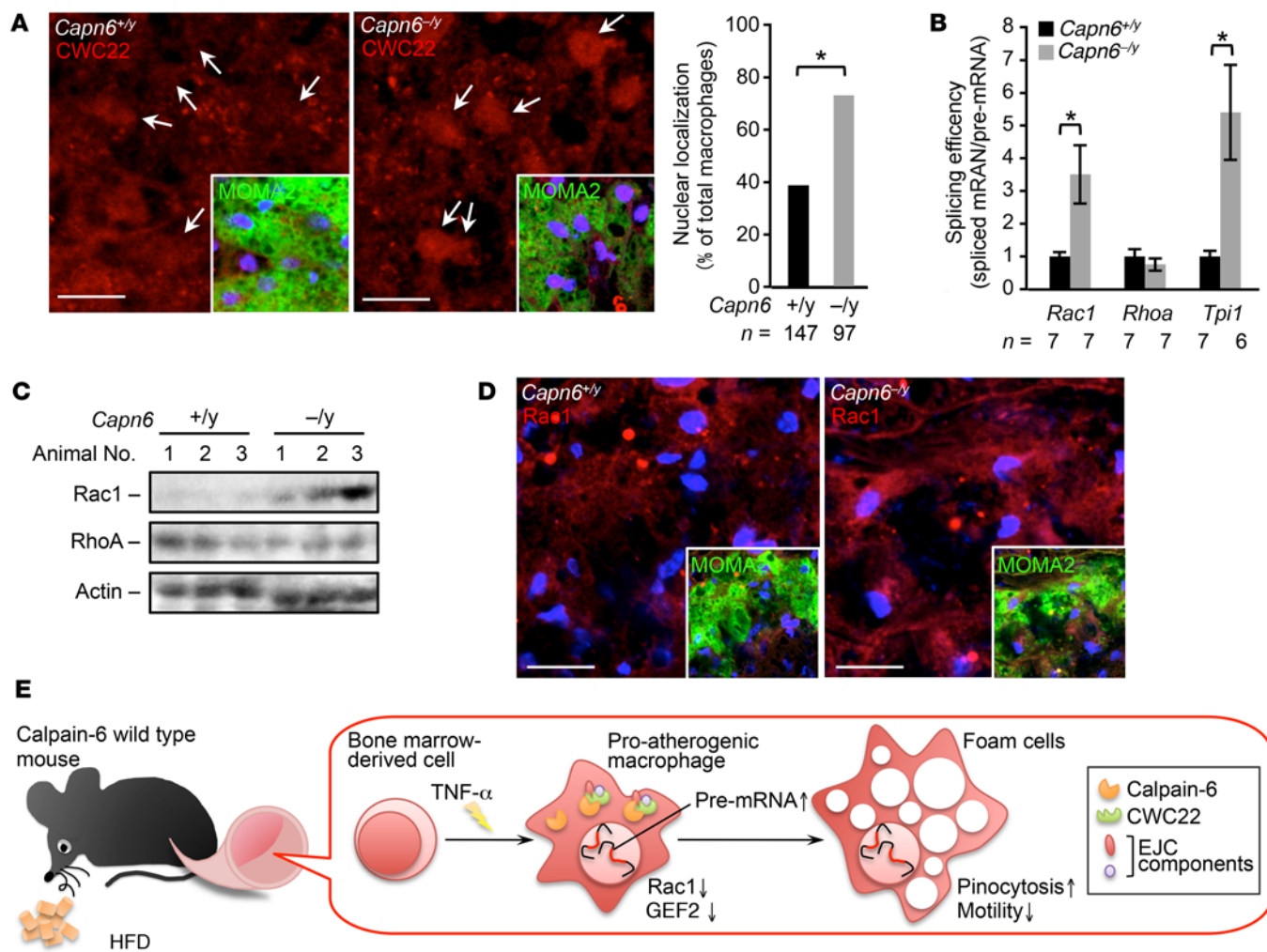


Figure 11. Loss of CAPN6 facilitates nuclear localization of CWC22 and subsequent *Rac1* splicing in macrophages/foam cells in murine atheromas. (A) Nuclear localization of CWC22 in macrophages in murine atheromas. MOMA2 served as a macrophage marker. Arrows represent nuclei. (B) Splicing of *Cwc22* mRNA is accelerated by loss of *Capn6*. Splicing efficiency in whole aorta was measured by a PCR-based analysis. (C) Protein expression of *Rac1* but not of *RhoA* in proatherogenic aorta. Protein expression in whole aorta was evaluated by immunoblotting. (D) Immunohistochemical distribution of *Rac1* protein in macrophages in atheromas. MOMA2 served as a marker for macrophages. (E) Schematic depiction of the CAPN6-mediated disturbance of posttranscriptional regulation in proatherogenic macrophages. CAPN6 was induced in *Capn6*^{+y} macrophages in response to TNF- α and was associated with CWC22 in the cytoplasm. This association disturbs the nuclear localization of CWC22, thereby suppressing posttranscriptional processing of *Rac1* and *Arhgef2* (the genes encoding *Rac1* and GEF2, respectively) and potentiates subsequent pinocytotic responses. Thus, CAPN6 induction in macrophages facilitates atherosclerotic development. * $P < 0.05$, Fisher's exact test (A) and 1-way ANOVA followed by Bonferroni's test (B); error bars represent mean \pm SEM. Scale bars: 10 μ m (A); 20 μ m (D).

In vitro uptake of native LDL and the pinocytosis assay. Human LDL ($d = 1.019\text{--}1.063$ g/ml) was prepared as described previously (16). To prepare oxidized LDL, native LDL (0.1 mg/ml) was incubated for 20 hours at 37°C with 5 μ mol/l CuSO₄, followed by the addition of 1 mmol/l ethylenediaminetetraacetic acid and cooling. To measure the uptake of LDL-derived cholesterol, TNF- α /M-CSF-primed BMMs (3×10^4 cells) were seeded on a 96-well culture plate. Next, native or oxidized LDL was added to the culture medium and incubated for 24 hours. After washing 3 times with HBSS, cellular lipids were extracted using hexane-isopropanol (v/v 3:2; 100 μ l/well). Then the extracts were transferred to another 96-well plate and dried. Cholesterol in the residue was quantified using a Cholesterol-E Kit (Wako Pure Chemical Industries Ltd.) and normalized against the total protein, which was measured by the bicinchoninic acid (BCA) method (Pierce Bio-

technology Inc.). To measure pinocytotic activity, BMMs or J774 macrophages were exposed to TRITC-labeled dextran (molecular weight, 70,000) at 5 mg/ml for 24 hours. To evaluate the temporal changes in Dil-LDL uptake, BMMs were subjected to the mixture of Dil-labeled LDL (Alfa Aesar) and unlabeled LDL (mixture ratio: w/w 1:20) at 400 μ g/ml. After washing 3 times with PBS, fluorescent dextran or Dil-labeled LDL uptake in the cells was measured using a microplate reader (Mithras LB 940; Berthold Technologies GmbH & Co. KG) or by confocal microscopy (A1; Nikon Instruments Inc.), as appropriate.

Rac1 activity. *Rac1* activity in BMMs was measured using a *Rac1* G-LISA Activation Assay Kit (Cytoskeleton, Inc.) according to the manufacturer's instructions. TNF- α /M-CSF-primed BMMs (2×10^5 cells) were stimulated with CCL2 at 50 ng/ml or native LDL at 400 μ g/ml for 20 minutes and lysed in lysis buffer. Subsequently, protein was quantified

using the BCA assay (Pierce Biotechnology, Inc.); protein aliquots (0.6 mg/ml) were loaded into the assay plate. Active Rac1 bound to plate walls was probed using an anti-Rac1 antibody and a horseradish peroxidase-labeled secondary antibody. After the chemiluminescent reaction, optical absorbance at 490 nm was measured as an index of Rac1 activity.

Pinosome dynamics and maturation. BMMs were seeded onto collagen I-coated cover slips; then 5 mg/ml TRITC-labeled dextran was added to the culture medium to label the pinosomes. After 30 minutes, cells were washed 3 times with HBSS, and pinosomes in individual cells were tracked for 30 minutes at 1-minute intervals using confocal microscopy (A1; Nikon Instruments Inc.). The velocity and density of pinosomes were determined using ImageJ (NIH).

Leakage of pinocytotic particles. BMMs were differentiated in the presence of 10 ng/ml TNF- α and 50 ng/ml M-CSF for 3 days and were seeded onto 48-well culture plate (2×10^5 cells/well). Subsequently, the cells were loaded with TRITC-labeled dextran at 5 mg/ml in the presence or absence of NSC23766 at 50 μ M. After 24 hours of incubation, cells were washed 3 times with RPMI medium and were incubated with RPMI medium supplemented with 10 ng/ml TNF- α and 50 ng/ml M-CSF in the presence or absence of NSC23766 at 50 μ M. Subsequent to the incubation for 24 hours, the culture medium was collected and cells were lysed by PBS containing 0.4% Triton X-100. Detached cells and unlysed debris in the culture medium and cell lysate were removed by centrifugation; then fluorescent dextran in the culture medium or cell lysates were measured using a microplate reader (Mithras LB 940; Berthold Technologies GmbH & Co. KG; Ex/Em: 530/590 nm). Dextran leakage was calculated from the following equation: dextran leakage = $[F_{media}/(F_{cell} + F_{media})] \times 100\%$, where F_{media} represents fluorescence intensity in the culture medium and F_{cell} denotes fluorescence intensity in cell lysate.

IP-LC-MS/MS. LC-MS/MS analysis was used as described previously (35). J774 cells were a gift from Masamichi Takami (Showa University School of Dentistry, Tokyo, Japan). J774 cells were transfected with vectors encoding GFP alone or GFP-fused *Capn6* using Lipofectamine 3000 (Invitrogen). Twenty-four hours after transfection, tagged proteins were collected by IP using anti-GFP antibody (Clontech Laboratories Inc.) and were eluted using citrate buffer (pH 2–3). The eluent was then blotted onto PVDF membranes, and the membranes were dried out. Subsequently, the membranes were incubated with a DTT-based reaction solution (80 mmol/l NH_4HCO_3 , 10 mmol/l DTT, and 20% acetonitrile) at 56°C for 1 hour. The reaction solution was then replaced with iodoacetamide solution (80 mmol/l NH_4HCO_3 , 55 mmol/l iodoacetamide, and 20% acetonitrile) and incubated at room temperature for 45 minutes in the dark. Following washing with distilled water and 2% acetonitrile, the membranes were incubated overnight with 1 μ g of trypsin dissolved into 30 mmol/l NH_4HCO_3 containing 70% acetonitrile. The tryptic digests were extracted twice with 70% acetonitrile/1% TFA and were dried out using a SpeedVac evaporator (Thermo Fisher Scientific). The residues were dissolved in 0.2% formic acid and analyzed using a Triple TOF5600 System (AB SCIEX). Data were analyzed by ProteinPilot Software (AB SCIEX) to explore the candidate CAPN6-associated proteins. Proteins that were precipitated similarly in GFP-expressing J774 lysates (GFP tag alone) were omitted from the candidate proteins.

PCR-based detection of mRNA splicing. To evaluate the efficiency of mRNA splicing, expression levels of pre-mRNAs and spliced mRNAs were measured by qPCR. The analytic principles and primer designs

are detailed in Supplemental Figure 4. The expression ratio of spliced mRNA to pre-mRNA served as an index of splicing efficiency. To avoid contamination with genomic DNA, total RNA was treated with DNase I (Invitrogen) before the reverse-transcription reaction.

BM transplantation. BM transplantation was conducted as previously described (33). To eliminate resident BM cells, recipient mice (*Capn6^{+/-}Ldlr^{-/-}* or *Capn6^{-/-}Ldlr^{-/-}*) were x-ray-irradiated at 8 Gy for 10 minutes using a soft x-ray system (OM-150HTS; OHMiC). The next day, BM cells (1×10^7 cells/animal) isolated from donor mice (*Capn6^{+/-}Ldlr^{-/-}* or *Capn6^{-/-}Ldlr^{-/-}*) were i.v. injected into recipient mice. Four weeks later, mice received HFD to induce atherosclerotic disease. Successful replacement of BM cells was validated by PCR-based genotyping of the BM.

In vivo tracking of circulating monocytes. In vivo labeling of circulating Ly-6C^{hi} monocytes was performed according to the previous literature by Tacke et al (21). Mice were fed HFD for 12 weeks, followed by i.v. injection of 200 μ l of clodronate liposome (FormuMax Scientific Inc.) into tail vein to transiently deplete circulating monocytes. Eighteen hours later, 1.0- μ m Fluoresbrite Plain YG Microspheres (w/v 2.5% solids; Polysciences Inc.) were diluted 1:25 in PBS, and 250 μ l of the solution was injected into the mice via tail vein. After 3 days, mice were sacrificed, and aortic sinus and whole blood with EDTA were collected. Erythrocytes in the whole blood samples were lysed with BD Pharm Lyse (BD Biosciences); then the samples were analyzed by using BD FACSVerse (BD Biosciences) to evaluate the uptake of fluorescence beads in monocyte population. Aortic sinus was cryosectioned at a thickness of 10 μ m and was stained with oil red O and DAPI. Latex beads in the atherosclerotic lesion sections were detected by using a conventional fluorescent microscope (IX70, Olympus) and were counted using ImageJ software (NIH).

In vivo pinocytosis activity. The detection of in vivo pinocytotic activity was performed as described previously (8). *Capn6^{+/-}Ldlr^{-/-}* and *Capn6^{-/-}Ldlr^{-/-}* mice that received a HFD for 12 weeks were used in these experiments. The mice were subjected to the i.v. administration of AngioSPARK 680 nanoparticles (PerkinElmer) at 80 mg/kg. After 24 hours, the mice were sacrificed; the aortic trees were dissected. The isolated aortas were cryosectioned; the uptake of fluorescent nanoparticles by the vascular wall was detected using confocal microscopy (A1; Nikon Instruments Inc.). Simultaneously, monocyte/macrophage antigen-2 (MOMA2) was immunohistochemically detected as a macrophage marker.

X-gal staining, immunohistochemistry, and quantification of atherosclerotic lesions. Because the targeted allele in *Capn6*-deficient mice contains the LacZ reporter, which is driven by the *Capn6* native promoter (20), we assessed the activity of *Capn6* using a β -Galactosidase Staining Kit (Takara Bio Inc.) according to the manufacturer's instructions. Briefly, isolated aortic tissues were immersed overnight in reaction buffer at 37°C. Subsequently, specimens were cryosectioned at 6- μ m thickness and photographed using light microscopy. For immunohistochemical analysis in mice, the isolated aortic trees and roots were fixed in 4% paraformaldehyde (PFA) in PBS and were subsequently frozen, sectioned at 6- μ m thickness, and mounted on glass slides as required. Target molecules were detected using immunofluorescence histochemistry or conventional immunohistochemistry with specific antibodies (Supplemental Table 4). To quantify atherosclerotic lesions, PFA-fixed aortic trees and roots were stained with oil red O in 60% isopropanol for 30 minutes. The specimens were washed with 60% isopropanol and photographed to calculate the staining-positive areas using ImageJ (NIH).

DNA array. BMMs from 4 different mice were pooled in each mouse line to minimize the individual differences and were lysed using TRIzol Reagent (Invitrogen). The DNA array was conducted using an Agilent Expression Array (Agilent Technologies) and a SurePrint G3 Mouse GE 8 × 60 K Microarray (Agilent Technologies) in the Dragon Genomics Center (Takara Bio Inc.). Data were deposited in the NCBI's Gene Expression Omnibus (GEO GSE83815).

Immunohistochemical analysis in humans. To evaluate the nuclear localization of CWC22 in macrophages, atherosclerotic lesions in human aortic segments, collected from 10 autopsied patients (men, 5; women, 5; age, 39–86 years; Supplemental Table 1), were graded based on the American Heart Association's criteria (36). Antigen retrieval was performed by heat-induced epitope retrieval using citrate buffer (Sigma-Aldrich) for 5 minutes at 121°C. The expression of CWC22 protein in the segments was detected by fluorescent immunohistochemistry with anti-CWC22 antibody (Sigma-Aldrich). Meanwhile, a commercially available cardiovascular tissue microarray (Provitro AG), as well as the specimens noted above, was employed for immunohistochemical detection of CAPN6 expression. Antigen retrieval was performed using proteinase K (DAKO) for 15 minutes at room temperature; CAPN6 protein expression was detected by fluorescent immunohistochemistry with anti-CAPN6 antibody (Abcam). Clinicopathological information regarding the tissue microarray is available in Supplemental Table 2.

Statistics. Our results are expressed as mean ± SEM; statistical analyses were performed using GraphPad Prism 5 (GraphPad Software Inc.). Two-tailed Student's *t* test was used to compare 2 groups with equal variances; alternatively, Mann-Whitney *U* test was applied for data with unequal variances. Multiple comparisons were conducted with 1- or 2-way nonrepeated measures ANOVA followed by post-hoc Bonferroni's test, as appropriate. *P* values of less than 0.05 were considered statistically significant.

Study approval. All experimental procedures involving animals were approved by the Institutional Animal Care and Use Committee

of Showa University and were conducted in conformity with the Animal Care and Use Committee Guidelines of Showa University. Use of human aortic autopsy specimens was approved by the Ethics Committee of Kumamoto University School of Medicine and was conducted in conformity with the Ethics Committee guidelines of Kumamoto University School of Medicine.

Author contributions

TM, KT, SH, HS, HK, and AM conceived the project and designed the experiments. TM conducted most of the experiments and data analyses. XFL and JRKK supported the experiments and data interpretations. KT generated *Capn6*^{-/-} mice. SH generated *Capn9*^{-/-} mice. KO and MT collected human autopsy specimens. TA and HI conducted IP-LC-MS/MS analysis. The manuscript was written and revised by TM and edited by AM.

Acknowledgments

The authors greatly appreciate Hideo Kataoka and Hirota Kuwata (Showa University School of Dentistry) for instruction on FACS analysis and valuable comments. This study was partially supported by the Japan Society for the Promotion of Science (JSPS) KAKENHI grant 26461368 (to AM), JSPS KAKENHI grant 15K09418 (to TM), CSTI-SIP BRAIN-NARO ID:14533567 (to HS), and research grants from the Takeda Science Foundation, the Banyu Life Science Foundation International, the NOVARTIS Foundation, the Ono Medical Research Foundation, a Hiroshi Iri-sawa, Aya Irisawa Memorial Research Grant from the Japan Heart Foundation and the Japan Heart Foundation & Astellas Grant for Research on Atherosclerosis Update (all to TM).

Address correspondence to: Takuro Miyazaki, Department of Biochemistry, Showa University School of Medicine, 1-5-8 Hatanodai, Shinagawa-ku, Tokyo 142-8555, Japan. Phone: 81.3.3784.8116; E-mail: taku@pharm.showa-u.ac.jp.

- Weber C, Noels H. Atherosclerosis: current pathogenesis and therapeutic options. *Nat Med*. 2011;17(11):1410–1422.
- Waters DD. What the statin trials have taught us. *Am J Cardiol*. 2006;98(1):129–134.
- Cannon CP, et al. Intensive versus moderate lipid lowering with statins after acute coronary syndromes. *N Engl J Med*. 2004;350(15):1495–1504.
- Brown MS, Goldstein JL. Lipoprotein metabolism in the macrophage: implications for cholesterol deposition in atherosclerosis. *Annu Rev Biochem*. 1983;52:223–261.
- Steinbrecher UP, Lougheed M. Scavenger receptor-independent stimulation of cholesterol esterification in macrophages by low density lipoprotein extracted from human aortic intima. *Arterioscler Thromb*. 1992;12(5):608–625.
- Manning-Tobin JJ, et al. Loss of SR-A and CD36 activity reduces atherosclerotic lesion complexity without abrogating foam cell formation in hyperlipidemic mice. *Arterioscler Thromb Vasc Biol*. 2009;29(1):19–26.
- Kruth HS. Receptor-independent fluid-phase pinocytosis mechanisms for induction of foam cell formation with native low-density lipoprotein particles. *Curr Opin Lipidol*. 2011;22(5):386–393.
- Buono C, Anzinger JJ, Amar M, Kruth HS. Fluorescent pegylated nanoparticles demonstrate fluid-phase pinocytosis by macrophages in mouse atherosclerotic lesions. *J Clin Invest*. 2009;119(5):1373–1381.
- Anzinger JJ, et al. Native low-density lipoprotein uptake by macrophage colony-stimulating factor-differentiated human macrophages is mediated by macropinocytosis and micropinocytosis. *Arterioscler Thromb Vasc Biol*. 2010;30(10):2022–2031.
- Fujii M, Kawai K, Egami Y, Araki N. Dissecting the roles of Rac1 activation and deactivation in macropinocytosis using microscopic photo-manipulation. *Sci Rep*. 2013;3:2385.
- Jeong SY, Martchenko M, Cohen SN. Calpain-dependent cytoskeletal rearrangement exploited for anthrax toxin endocytosis. *Proc Natl Acad Sci U S A*. 2013;110(42):E4007–E4015.
- Tsai JC, et al. The role of calpain-myosin 9-Rab7 pathway in mediating the expression of Toll-like receptor 4 in platelets: a novel mechanism involved in α -granules trafficking. *PLoS One*. 2014;9(1):e85833.
- Sorimachi H, Ono Y. Regulation and physiological roles of the calpain system in muscular disorders. *Cardiovasc Res*. 2012;96(1):11–22.
- Wang N, et al. A PEST sequence in ABCA1 regulates degradation by calpain protease and stabilization of ABCA1 by apoA-I. *J Clin Invest*. 2003;111(1):99–107.
- Hori N, Hayashi H, Sugiyama Y. Calpain-mediated cleavage negatively regulates the expression level of ABCG1. *Atherosclerosis*. 2011;215(2):383–391.
- Miyazaki T, et al. m-Calpain induction in vascular endothelial cells on human and mouse atheromas and its roles in VE-cadherin disorganization and atherosclerosis. *Circulation*. 2011;124(23):2522–2532.
- Subramanian V, Uchida HA, Ijaz T, Moorleghen JJ, Howatt DA, Balakrishnan A. Calpain inhibition attenuates angiotensin II-induced abdominal aortic aneurysms and atherosclerosis in low-density lipoprotein receptor-deficient mice. *J Cardiovasc Pharmacol*. 2012;59(1):66–76.
- Barthwal MK, Anzinger JJ, Xu Q, Bohnacker T, Wymann MP, Kruth HS. Fluid-phase pinocytosis of native low density lipoprotein promotes murine M-CSF differentiated macrophage foam

- cell formation. *PLoS One*. 2013;8(3):e58054.
19. Steckelberg AL, Boehm V, Gromadzka AM, Gehring NH. CWC22 connects pre-mRNA splicing and exon junction complex assembly. *Cell Rep*. 2012;2(3):454–461.
20. Tonami K, et al. Calpain-6 deficiency promotes skeletal muscle development and regeneration. *PLoS Genet*. 2013;9(8):e1003668.
21. Tacke F, et al. Monocyte subsets differentially employ CCR2, CCR5, and CX3CR1 to accumulate within atherosclerotic plaques. *J Clin Invest*. 2007;117(1):185–194.
22. Ridley AJ. Rho proteins: linking signaling with membrane trafficking. *Traffic*. 2001;2(5):303–310.
23. Ridley AJ, Paterson HF, Johnston CL, Diekmann D, Hall A. The small GTP-binding protein rac regulates growth factor-induced membrane ruffling. *Cell*. 1992;70(3):401–410.
24. Tonami K, et al. Calpain-6, a microtubule-stabilizing protein, regulates Rac1 activity and cell motility through interaction with GEF-H1. *J Cell Sci*. 2011;124(Pt 8):1214–1223.
25. Bhatt DM, et al. Transcript dynamics of proinflammatory genes revealed by sequence analysis of subcellular RNA fractions. *Cell*. 2012;150(2):279–290.
26. Rodríguez-Navarro S, Hurt E. Linking gene regulation to mRNA production and export. *Curr Opin Cell Biol*. 2011;23(3):302–309.
27. Tange TØ, Shibuya T, Jurica MS, Moore MJ. Biochemical analysis of the EJC reveals two new factors and a stable tetrameric protein core. *RNA*. 2005;11(12):1869–1883.
28. Singh KK, Wachsmuth L, Kulozik AE, Gehring NH. Two mammalian MAGOH genes contribute to exon junction complex composition and nonsense-mediated decay. *RNA Biol*. 2013;10(8):1291–1298.
29. Dear N, Matena K, Vingron M, Boehm T. A new subfamily of vertebrate calpains lacking a calmodulin-like domain: implications for calpain regulation and evolution. *Genomics*. 1997;45(1):175–184.
30. Hong JM, Teitelbaum SL, Kim TH, Ross FP, Kim SY, Kim HJ. Calpain-6, a target molecule of glucocorticoids, regulates osteoclastic bone resorption via cytoskeletal organization and microtubule acetylation. *J Bone Miner Res*. 2011;26(3):657–665.
31. Brånén L, Hovgaard L, Nitulescu M, Bengtsson E, Nilsson J, Jovinge S. Inhibition of tumor necrosis factor-alpha reduces atherosclerosis in apolipoprotein E knockout mice. *Arterioscler Thromb Vasc Biol*. 2004;24(11):2137–2142.
32. Hata S, et al. Calpain 8/nCL-2 and calpain 9/nCL-4 constitute an active protease complex, G-calpain, involved in gastric mucosal defense. *PLoS Genet*. 2010;6(7):e1001040.
33. Kigawa Y, et al. NADPH oxidase deficiency exacerbates angiotensin II-induced abdominal aortic aneurysms in mice. *Arterioscler Thromb Vasc Biol*. 2014;34(11):2413–2420.
34. Miyazaki T, et al. Calpastatin counteracts pathological angiogenesis by inhibiting suppressor of cytokine signaling 3 degradation in vascular endothelial cells. *Circ Res*. 2015;116(7):1170–1181.
35. Obama T, Kato R, Masuda Y, Takahashi K, Aiuchi T, Itabe H. Analysis of modified apolipoprotein B-100 structures formed in oxidized low-density lipoprotein using LC-MS/MS. *Proteomics*. 2007;7(13):2132–2141.
36. Stary HC, et al. A definition of advanced types of atherosclerotic lesions and a histological classification of atherosclerosis. A report from the Committee on Vascular Lesions of the Council on Arteriosclerosis, American Heart Association. *Circulation*. 1995;92(5):1355–1374.

Acknowledgement

We are deeply grateful to Dr. Kang Jong-Hon for his valuable discussions. We also thank Dr. Koji Ohnishi for his helpful comments in pathohistological assessment.

Supplementary data

Supplementary data associated with this article can be found, in the online version, at <http://dx.doi.org/10.1016/j.jhep.2015.08.026>.

References

Author names in bold designate shared co-first authorship

[1] Gines P, Cardenas A, Arroyo V, Rodes J. Management of cirrhosis and ascites. *N Engl J Med* 2004;350:1646–1654.

[2] Mederacke I, Hsu CC, Troeger JS, Huebener P, Mu X, Dapito DH, et al. Fate tracing reveals hepatic stellate cells as dominant contributors to liver fibrosis independent of its aetiology. *Nat Commun* 2013;4:2823.

[3] Friedman SL. Hepatic stellate cells: protean, multifunctional, and enigmatic cells of the liver. *Physiol Rev* 2008;88:125–172.

[4] Inagaki Y, Okazaki I. Emerging insights into Transforming growth factor beta Smad signal in hepatic fibrogenesis. *Gut* 2007;56:284–292.

[5] Schnabl B, Kweon YO, Frederick JP, Wang XF, Rippe RA, Brenner DA. The role of Smad3 in mediating mouse hepatic stellate cell activation. *Hepatology* 2001;34:89–100.

[6] Dooley S, ten Dijke P. TGF-beta in progression of liver disease. *Cell Tissue Res* 2012;347:245–256.

[7] Nakao A, Afrakhte M, Moren A, Nakayama T, Christian JL, Heuchel R, et al. Identification of Smad7, a TGFbeta-inducible antagonist of TGF-beta signalling. *Nature* 1997;389:631–635.

[8] Dooley S, Hamzavi J, Breitkopf K, Wiercinska E, Said HM, Lorenzen J, et al. Smad7 prevents activation of hepatic stellate cells and liver fibrosis in rats. *Gastroenterology* 2003;125:178–191.

[9] Kinoshita K, Iimuro Y, Fujimoto J, Inagaki Y, Namikawa K, Kiyama H, et al. Targeted and regulable expression of transgenes in hepatic stellate cells and myofibroblasts in culture and in vivo using an adenoviral Cre/loxP system to antagonise hepatic fibrosis. *Gut* 2007;56:396–404.

[10] Lan HY, Mu W, Tomita N, Huang XR, Li JH, Zhu HJ, et al. Inhibition of renal fibrosis by gene transfer of inducible Smad7 using ultrasound-microbubble system in rat UUO model. *J Am Soc Nephrol* 2003;14:1535–1548.

[11] Nakao A, Fujii M, Matsumura R, Kumano K, Saito Y, Miyazono K, et al. Transient gene transfer and expression of Smad7 prevents bleomycin-induced lung fibrosis in mice. *J Clin Invest* 1999;104:5–11.

[12] Shibanuma M, Mashimo J, Kuroki T, Nose K. Characterization of the TGF beta 1-inducible hic-5 gene that encodes a putative novel zinc finger protein and its possible involvement in cellular senescence. *J Biol Chem* 1994;269:26767–26774.

[13] Kim-Kaneyama JR, Wachi N, Sata M, Enomoto S, Fukabori K, Koh K, et al. Hic-5, an adaptor protein expressed in vascular smooth muscle cells, modulates the arterial response to injury in vivo. *Biochem Biophys Res Commun* 2008;376:682–687.

[14] Shibanuma M, Kim-Kaneyama JR, Ishino K, Sakamoto N, Hishiki T, Yamaguchi K, et al. Hic-5 communicates between focal adhesions and the nucleus through oxidant-sensitive nuclear export signal. *Mol Biol Cell* 2003;14:1158–1171.

[15] Kim-Kaneyama JR, Shibanuma M, Nose K. Transcriptional activation of the c-fos gene by a LIM protein, Hic-5. *Biochem Biophys Res Commun* 2002;299:360–365.

[16] Shibanuma M, Kim-Kaneyama JR, Sato S, Nose K. A LIM protein, Hic-5, functions as a potential coactivator for Sp1. *J Cell Biochem* 2004;91:633–645.

[17] Yang L, Guerrero J, Hong H, DeFranco DB, Stallcup MR. Interaction of the tau2 transcriptional activation domain of glucocorticoid receptor with a novel steroid receptor coactivator, Hic-5, which localizes to both focal adhesions and the nuclear matrix. *Mol Biol Cell* 2000;11:2007–2018.

[18] Wang H, Song K, Krebs TL, Yang J, Danielpour D. Smad7 is inactivated through a direct physical interaction with the LIM protein Hic-5/ARA55. *Oncogene* 2008;27:6791–6805.

[19] Kim-Kaneyama JR, Takeda N, Sasai A, Miyazaki A, Sata M, Hirabayashi T, et al. Hic-5 deficiency enhances mechanosensitive apoptosis and modulates vascular remodeling. *J Mol Cell Cardiol* 2011;50:77–86.

[20] Lei XF, Kim-Kaneyama JR, Arita-Okubo S, Offermanns S, Itabe H, Miyazaki T, et al. Identification of Hic-5 as a novel scaffold for the MKK4/p54 JNK pathway in the development of abdominal aortic aneurysms. *J Am Heart Assoc* 2014;3:e000747.

[21] Dabiri G, Tumbarello DA, Turner CE, Van de Water L. Hic-5 promotes the hypertrophic scar myofibroblast phenotype by regulating the TGF-beta1 autocrine loop. *J Invest Dermatol* 2008;128:2518–2525.

[22] Hornigold N, Craven RA, Keen JN, Johnson T, Banks RE, Mooney AF. Upregulation of Hic-5 in glomerulosclerosis and its regulation of mesangial cell apoptosis. *Kidney Int* 2010;77:329–338.

[23] Suga K, Kondo S, Matsuura S, Kinoshita Y, Urushihara M, Kagami S. Glomerular expression of hydrogen peroxide-inducible clone-5 in human and rat progressive mesangial proliferative glomerulonephritis. *Nephron Exp Nephrol* 2012;120:e59–e68.

[24] Maschmeyer P, Flach M, Winau F. Seven steps to stellate cells. *J Vis Exp* 2011;51:2710.

[25] Boers W, Aarrass S, Linthorst C, Pinzani M, Elferink RO, Bosma P. Transcriptional profiling reveals novel markers of liver fibrogenesis: gremlin and insulin-like growth factor-binding proteins. *J Biol Chem* 2006;281:16289–16295.

[26] **Ji J, Yu F, Ji Q**, Li Z, Wang K, Zhang J, et al. Comparative proteomic analysis of rat hepatic stellate cell activation: a comprehensive view and suppressed immune response. *Hepatology* 2012;56:332–349.

[27] Pignatelli J, Tumbarello DA, Schmidt RP, Turner CE. Hic-5 promotes invadopodia formation and invasion during TGF-beta-induced epithelial-mesenchymal transition. *J Cell Biol* 2012;197:421–437.

[28] Hornigold N, Johnson TS, Huang L, Haylor JL, Griffin M, Mooney A. Inhibition of collagen I accumulation reduces glomerulosclerosis by a Hic-5-dependent mechanism in experimental diabetic nephropathy. *Lab Invest* 2013;93:553–565.

[29] Gressner AM, Weiskirchen R, Breitkopf K, Dooley S. Roles of TGF-beta in hepatic fibrosis. *Front Biosci* 2002;7:d793–d807.

[30] Breitkopf K, Godoy P, Ciucan L, Singer MV, Dooley S. TGF-beta/Smad signaling in the injured liver. *Z Gastroenterol* 2006;44:57–66.

[31] Inagaki Y, Kushida M, Higashi K, Itoh J, Higashiyama R, Hong YY, et al. Cell type-specific intervention of transforming growth factor beta/Smad signaling suppresses collagen gene expression and hepatic fibrosis in mice. *Gastroenterology* 2005;129:259–268.

[32] Dooley S, Streckert M, Delvoux B, Gressner AM. Expression of Smads during in vitro transdifferentiation of hepatic stellate cells to myofibroblasts. *Biochem Biophys Res Commun* 2001;283:554–562.

[33] Bataller R, Brenner DA. Liver fibrosis. *J Clin Invest* 2005;115:209–218.

[34] Bataller R, Schwabe RF, Choi YH, Yang L, Paik YH, Lindquist J, et al. NADPH oxidase signal transduces angiotensin II in hepatic stellate cells and is critical in hepatic fibrosis. *J Clin Invest* 2003;112:1383–1394.

[35] Parola M, Robino G. Oxidative stress-related molecules and liver fibrosis. *J Hepatol* 2001;35:297–306.

[36] Bataller R, Gines P, Nicolas JM, Gorbic MN, Garcia-Ramallo E, Gasull X, et al. Angiotensin II induces contraction and proliferation of human hepatic stellate cells. *Gastroenterology* 2000;118:1149–1156.

[37] Garcia-Trevijano ER, Iraburu MJ, Fontana L, Dominguez-Rosales JA, Auster A, Covarrubias-Pinedo A, et al. Transforming growth factor beta1 induces the expression of alpha1(I) procollagen mRNA by a hydrogen peroxide-C/EBPbeta-dependent mechanism in rat hepatic stellate cells. *Hepatology* 1999;29:960–970.